FTD-HC-23-720-71

AD 740190

FOREIGN TECHNOLOGY DIVISION

AERODYNAMICS

by

A. M. Mkhitaryan

Approved for public release;
Distribution unlimited.

EDITED TRANSLATION

AERODYNAMICS

By: A. M. Mkhitaryan

English pages: 318

Source: Aerodinamika 1970, pp. 175-428

Translated under: F33657-71-D-0057

UR/0000-70-000-000

PREPARED BY:

TRANSLATION DIVISION
FOREIGN TECHNOLOGY DIVISION
WP-AFB, OHIO.

UNCLASSIFIED
Security Classification

DOCUMENT CONTROL DATA - R & D

(Security classification of title, body of abstract and indexing annotation must be entered when the overall report is classified)

1. ORIGINATING ACTIVITY (Corporate author) Foreign Technology Division Air Force Systems Command U. S. Air Force	2a. REPORT SECURITY CLASSIFICATION UNCLASSIFIED 2b. GROUP

3. REPORT TITLE

AERODYNAMICS

4. DESCRIPTIVE NOTES (Type of report and inclusive dates)

Translation

5. AUTHOR(S) (First name, middle initial, last name)

Mkhitaryan, A. M.

6. REPORT DATE	7a. TOTAL NO. OF PAGES	7b. NO. OF REFS
1970	318	71

8a. CONTRACT OR GRANT NO. b. PROJECT NO. F33657-71-D-0057 c. d. DIA Task No. T70-01-12	9a. ORIGINATOR'S REPORT NUMBER(S) FTD-HC-23-720-71 9b. OTHER REPORT NO(S) (Any other numbers that may be assigned this report)

10. DISTRIBUTION STATEMENT

Approved for public release; distribution unlimited.

11. SUPPLEMENTARY NOTES	12. SPONSORING MILITARY ACTIVITY
	Foreign Technology Division Wright-Patterson AFB, Ohio

13. ABSTRACT

This book deals with the fundamentals of aerodynamics in application to passenger aircraft configurations and includes the laws of motion of gases and bodies submerged in them, similarity laws for gas flows, and the fundamentals of finite-wing and boundary-layer theory. The characteristics of the earth's atmosphere are presented. Aerodynamic experiment techniques and equipment are described. The aerodynamic characteristics of wing profiles, wings and tails of various shapes, bodies of revolution, and the airplane as a whole are examined. Special chapters are devoted to the specific features of hypersonic aerodynamics and fundamentals of airscrew (puller and pusher) theory. This text is intended for the civil aviation college students but may also be recommended to a broad range of airline and industry engineers. Ori. art. has: 8 tables, 289 figures.

DD FORM 1 NOV 65 1473

UNCLASSIFIED
Security Classification

14. KEY WORDS	LINK A		LINK B		LINK C	
	ROLE	WT	ROLE	WT	ROLE	WT
Aerodynamic Characteristic Aerodynamic Lift Experiment Aerodynamics Aerodynamic Boundary Layer Aerodynamic Theory						

TABLE OF CONTENTS

CHAPTER XI

BOUNDARY LAYER THEORY FUNDAMENTALS

§11.1. The Boundary Layer Concept

It has been established experimentally that viscosity has a significant effect on gas flow only in a very thin layer near the surface of submerged bodies. Beyond the limits of this layer, the influence of viscosity can be neglected. The fluid layer adjacent to the submerged solid body, in which the internal friction forces are of the same order as the inertia forces, is termed the boundary layer.

Drag, lift, aerodynamic heating (at supersonic speeds), and so on depend to a considerable degree on the flow structure in the boundary layer. The air particles in the boundary layer are retarded under the action of the forces of adhesion with the solid surface and the viscous forces, which transfer this retardation from the wall some distance into the flow. The tangential stresses resulting from the viscous forces reduce the velocity of the air particles and cause them to rotate, forming vortices. Study of the flow structure in the boundary layer permits correct analysis of such important aerodynamic phenomena as flow separation from submerged bodies and

vortical wake formation behind a body, and also makes it possible to determine the air friction force on the body surface. Analysis of the flow in the boundary layer reduces to the solution of a system of complex differential equations.

Theoretical analyses of the boundary layer were initiated by Prandtl in 1904 and extended by Karman, Pohlhausen, Millikan, Blasius, Schlichting, and others. A large number of studies of Soviet scientists including L. S. Leybenzon, N. Ye. Kochin, A. A. Dorodnitsyn, V. V. Golubev, L. G. Loytsyanskiy, A. P. Mel'nikov, K. K. Fedyayevskiy, and others have been devoted to further development of boundary layer theory.

Soviet aerodynamicists have carried out several important theoretical and experimental investigations of the boundary layer and have developed efficient wing and fuselage forms having minimal drag.

Let us examine the flow of a viscous fluid about a flat plate of length L (Figure 11.1). Experiment shows that the fluid particles contacting the plate surface are completely retarded. As we move away from the plate, the flow velocity increases, approaching asymptotically the theoretical velocity corresponding to inviscid fluid flow past the plate. In the case in question this is the freestream velocity V_∞.

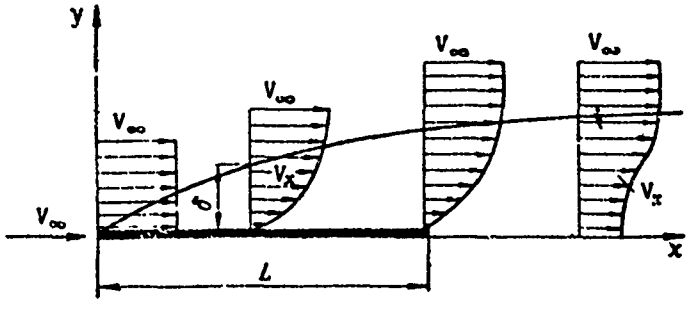

Figure 11.1. Schematic representation of boundary layer on a flat plate

Usually we take as the boundary layer thickness δ that (quite small) distance from the body surface at which the velocity V_x becomes equal to the outer flow velocity or differs from the latter by some small amount, for example by 1%. Other definitions of the boundary layer thickness are also frequently used.

If the submerged plate is sufficiently long, the flow structure in the boundary layer at different distances from the leading edge of the plate is different. Near the leading edge the flow within the boundary layer is laminar. Such a boundary layer is termed laminar. As we move away from the leading edge, the flow in the boundary layer becomes turbulent (Figure 11.2.). In the turbulent boundary layer the motion is turbulent except for a thin viscous sublayer immediately adjacent to the body surface. The distribution of the longitudinal velocity component in laminar and turbulent boundary layers is shown in Figure 11.3. We see from the figure that more rapid decrease of the velocity near the wall is observed in the turbulent boundary layer in comparison with the laminar.

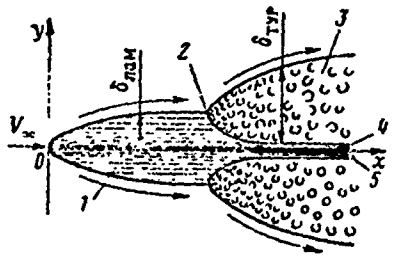

Figure 11.2. Boundary layer structure with transition from laminar to turbulent regime:

1 — laminar layer; 2 — transition point; 3 — turbulent layer; 4 — viscous sublayer; 5 — plate

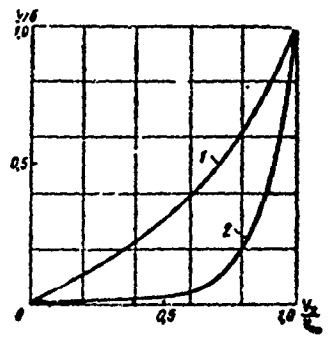

Figure 11.3. Comparison of velocity profiles in laminar and turbulent boundary layers:

1 — laminar layer; 2 — turbulent layer

The boundary layer on a submerged body has approximately the same structure as that on a flat plate. Downstream of the submerged body the boundary layers formed on the upper and lower surfaces come together and form the vortical wake (Figure 11.4), which "diffuses" with increasing distance from the body, and the velocities in this wake equalize and approach the freestream velocity.

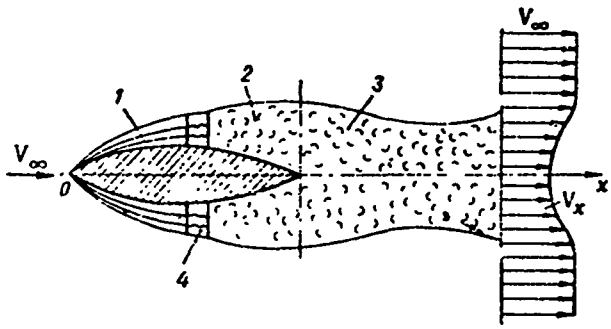

Figure 11.4. Schematic of viscous fluid flow past a body:

1 — laminar layer; 2 — turbulent layer; 3 — vortical wake; 4 — transition zone

§11.2. Integral Relation for Steady Incompressible Boundary Layer Flow

Let us examine fluid flow over a curvilinear surface of small curvature. In this case it is convenient to take the Ox coordinate axis to be curvilinear, locating it on the wetted surface along the flow (Figure 11.5). We shall apply the momentum theorem to the incompressible fluid within the elementary boundary layer segment ABCD, of length dx and width equal to unit length, located at the distance x from the coordinate origin. The fluid mass entering through section AB during the time dt, with velocity which is variable across the section, and the fluid mass leaving through section CD equal, respectively,

$$dt\varrho\int_0^\delta V_x dy \quad \text{and} \quad dt\varrho\left(\int_0^\delta V_x dy + dx\frac{\partial}{\partial x}\int_0^\delta V_x dy\right)$$

Hence the difference of the fluid masses entering and leaving will be

$$\varrho dt dx\frac{\partial}{\partial x}\int_0^\delta V_x dy$$

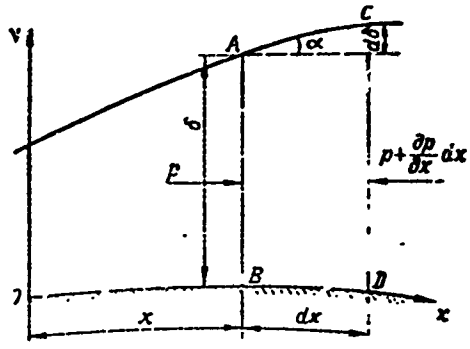

Figure 11.5. Derivation of integral relation for boundary layer in incompressible fluid

The projection on the Ox axis of the momentum of the fluid entering through section AB is

$$dt\varrho\int_0^\delta V_x^2 dy$$

and the projection of the momentum of the fluid leaving through section CD (considering this quantity a function of x) is

$$dt\varrho\left(\int_0^\delta V_x^2 dy + dx\frac{\partial}{\partial x}\int_0^\delta V_x^2 dy\right)$$

On the basis of mass conservation, a fluid mass must enter ABCD through the upper boundary AC which is equal to the difference of the fluid masses leaving through section CD and entering through section AB, i.e.,

$$\varrho dt dx\frac{\partial}{\partial x}\int_0^\delta V_x dy$$

This fluid brings into ABCD momentum equal to

$$\varrho V_0 dt dx\frac{\partial}{\partial x}\int_0^\delta V_x dy$$

where V_0 — is the velocity at the outer edge of the boundary layer.

Thus, the projection on the Ox axis of the increment during the time dt of the momentum of the fluid which is in the volume ABCD at the time t will be

$$\varrho dt\,dx\left(-V_0\frac{\partial}{\partial x}\int_0^\delta V_x\,dy+\frac{\partial}{\partial x}\int V_x^2\,dy\right) \qquad (a)$$

We consider the momentum introduced into the volume ABCD during the time dt to be negative, and that leaving the volume to be positive.

Now we calculate the projection of the sum of the impulses of the external forces acting during the time dt on the fluid within the elementary volume ABCD. The projections on the Ox axis of the external forces (pressure forces) acting on the faces AB, AC, and DC will be, respectively,

$$p\delta;\ \left(p+\frac{1}{2}dx\frac{\partial p}{\partial x}\right)ds\frac{d\delta}{ds}=p\,d\delta+\frac{1}{2}\frac{\partial p}{\partial x}dx\,d\delta;$$

$$-\left(p+\frac{\partial p}{\partial x}dx\right)\left(\delta+\frac{d\delta}{dx}dx\right)=-\left(p+\frac{\partial p}{\partial x}dx\right)(\delta+d\delta)$$

where $\frac{d\delta}{ds}$ — is the sine of the angle between the face AC and the Ox axis.

Neglecting small quantities of higher order and assuming that the projection on the Ox axis of the pressure of the wall element BD on the fluid equals zero, we find the sum of the projections of the pressure forces on the Ox axis

$$p\delta+p\,d\delta-\left(p+\frac{\partial p}{\partial x}dx\right)(\delta+d\delta)=p\delta+p\,d\delta-p\delta-p\,d\delta-$$

$$-\delta\frac{\partial p}{\partial x}dx-d\delta\frac{\partial p}{\partial x}dx\approx-\delta\frac{\partial p}{\partial x}dx.$$

The projection on the Ox axis of the pressure force impulse will be

$$-\delta\frac{\partial p}{\partial x}dx\,dt \qquad (b)$$

The impulse of the friction force applied to the face BD, whose area is dx · 1, is

$$-\tau_0 dx dt \qquad (c)$$

where τ_0 — is the friction force per unit area.

Equating the sum (a) to the sum of the expressions (b) and (c) and cancelling dxdt, we obtain

$$\varrho \frac{\partial}{\partial x}\int_0^\delta V_x^2 dy - \varrho V_0 \frac{\partial}{\partial x}\int_0^\delta V_x dy = -\delta \frac{\partial p}{\partial x} - \tau_0 \qquad (11.1)$$

This is then the integral relation for steady incompressible boundary layer flow. Assuming in view of stationarity that in (11.1.) all quantities depend only on x, the partial derivatives can be replaced by total derivatives

$$\varrho \frac{d}{dx}\int_0^\delta V_x^2 dy - \varrho V_0 \frac{d}{dx}\int_0^\delta V_x dy = -\delta \frac{dp}{dx} - \tau_0 \qquad (11.2)$$

The quantities V_0, $\frac{dp}{dx}$, and ρ are considered known, since if V_0 is known from the solution of the potential flow problem or from experiment we can find $\frac{dp}{dx}$ from the Bernoulli equation.

Thus, in this integral relation there are three unknowns: V_x, δ, and τ_0. Therefore we need two more relations to solve the problem, for example,

$$V_x = V_x(y) \quad \text{and} \quad \tau_0 = \tau_0(\delta)$$

§11.3. Use of Integral Relation to Calculate Laminar Flat Plate Boundary Layer and Drag

Let us examine the simplest case — longitudinal flow about a flat plate, since information on the boundary layer thickness and frictional drag for this case can be used for the approximate calculation of the thin profile and certain other profiles.

The integral relation (11.2) simplifies somewhat for the flat plate. At the upper edge of the boundary layer of such a plate

$$V_0 = V_\infty = \text{const.}$$

Then it follows from the Bernoulli equation (5.5) that p_∞ = const, and the integral relation takes the form

$$\varrho \frac{d}{dx}\int_0^\delta V_x^2 dy - \varrho V_\infty \frac{d}{dx}\int_0^\delta V_x dy = -\tau_0 \qquad (11.3)$$

The velocity distribution across the boundary layer section can be found approximately if we represent the function $V_x = f(y)$ in polynomial form, for example the second-order polynomial

$$V_x = a + by + cy^2 \qquad (11.4)$$

where a, b, and c — are constants defined from the boundary conditions.

For a flat plate the boundary conditions will be:

1) at the lower edge of the boundary layer, i.e., at the wall

$$\text{for} \quad y = 0 \quad V_x = 0$$

2) at the upper edge of the boundary layer

$$\text{for} \quad y = \delta \quad V_x = V_\infty$$

3) the friction forces are zero ($\tau = 0$) at the upper edge of the boundary layer and, consequently, on the basis of the Newton formula ($\tau = \mu \frac{\partial V_x}{y}$) for $y = \delta$

$$\frac{\partial V_x}{\partial y}=0$$

we find the values of the coefficients from these boundary conditions

$$a=0;\quad b=2\frac{V_\infty}{\delta};\quad c=-\frac{V_\infty}{\delta^2} \tag{11.5}$$

Then the velocity distribution across the boundary layer section is expressed by the formula

$$V_x=V_\infty\left(2\frac{y}{\delta}-\frac{y^2}{\delta^2}\right) \tag{11.6}$$

We use the Newton formula to find τ_0

$$\tau_0=\mu\left(\frac{\partial V_x}{\partial y}\right)_{y=0}. \tag{11.7}$$

From (11.7) and (11.6) we obtain the formula for the wall friction stress

$$\tau_0=2\mu\frac{V_\infty}{\delta} \tag{11.8}$$

Thus, we have obtained two additional relations (11.6) and (11.8), which together with the integral relation (11.3) make it possible to solve the problem of the boundary layer on a flat plate.

After finding the two integrals in (11.3), with account for (11.6) and (11.8), we obtain

$$\varrho\int_0^\delta V_x dy=\varrho\int_0^\delta V_\infty\left(2\frac{y}{\delta}-\frac{y^2}{\delta^2}\right)dy=\frac{2}{3}\varrho V_\infty\delta;$$

$$\varrho\int_0^\delta V_x^2 dy=\varrho\int_0^\delta V_\infty^2\left(2\frac{y}{\delta}-\frac{y^2}{\delta^2}\right)^2 dy=\frac{8}{15}\varrho V_\infty^2\delta$$

Substituting these expressions into (11.3), we obtain a differential equation in the form

$$\frac{2}{15}\rho V_\infty^2 \frac{d\delta}{dx} = 2\mu \frac{V_\infty}{\delta}$$

or, after separating the variables,

$$\delta\, d\delta = 15 \frac{\mu}{\rho V_\infty} dx$$

Integrating this equation, we obtain

$$\frac{1}{2}\delta^2 = 15 \frac{\mu}{\rho V_\infty} x + C \tag{11.9}$$

Setting $\delta = 0$ for $x = 0$ (boundary layer thickness zero at the leading edge of the plate), we find that $C = 0$. From (11.9) we find the boundary layer thickness

$$\delta = \sqrt{\frac{30\mu x}{\rho V_\infty}} \approx 5{,}48 \sqrt{\frac{\mu x}{\rho V_\infty}}$$

or

$$\delta = 5{,}48 \sqrt{\frac{\nu x}{V_\infty}} \tag{11.10}$$

This formula can be written as

$$\delta = 5{,}48 \frac{x}{\sqrt{\mathrm{Re}_x}} \quad \text{where} \quad \mathrm{Re}_x = \frac{V_\infty x}{\nu}$$

Substituting this value of δ into (11.8), we find

$$\tau_0 = 0{,}365 \sqrt{\frac{\mu \rho V_\infty^3}{x}} \tag{11.11}$$

The exact solution of the boundary layer problem, obtained by Blasius by integrating the differential equations of motion of a viscous fluid, yields the following expressions for δ and τ_0

$$\delta = 5{,}2 \sqrt{\frac{\nu x}{V_\infty}}; \quad \tau_0 = 0{,}332 \sqrt{\frac{\mu \rho V_\infty^3}{x}} \tag{11.12}$$

Comparing the approximate relations (11.10) and (11.11) with the exact expressions, we conclude that their agreement is good. We see from (11.10) that the boundary layer thickness is directly proportional to the square root of the kinematic viscosity ν and plate length x, and inversely proportional to the square root of the velocity at the outer edge of the boundary layer, which in the present case equals the freestream velocity V_∞.

The boundary layer thickness and friction stress are shown as functions of x in Figure 11.6.

Now let us calculate the frictional resistance force X_{fr} acting on one side of a flat plate of width b. The friction force on an elementary area will be $\tau b dx$. The total frictional resistance force on a plate of length l is

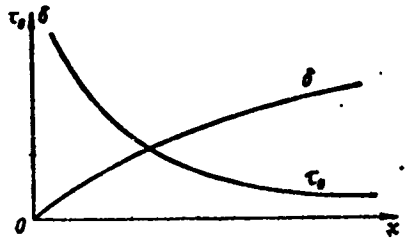

Figure 11.6. Variation of friction stress and boundary layer thickness along length of plate

$$X_{тр}=\int_0^b \tau_0 e\,dx$$

Substituting here the value of τ_0 from (11.12), we obtain

$$X_{тр}=0{,}664\,b\sqrt{\mu\varrho V_\infty^3 l}$$

Multiplying the numerator and denominator by $\sqrt{\rho l V_\infty}$, introducing the Reynolds number and considering that S = bl, we find

$$X_{тр}\approx\frac{1{,}3}{\mathrm{Re}^{\frac{1}{2}}}S\varrho\frac{V_\infty^2}{2} \qquad (11.13)$$

or

$$X_{тр}=c_{x\,тр}S\varrho\frac{V_\infty^2}{2} \qquad (11.14)$$

where

$$c_{x\,tp}=\frac{1.3}{\mathrm{Re}^{\frac{1}{2}}} \tag{11.15}$$

The quantity $c_{x\ fr}$ is the friction coefficient for a flat plate with laminar boundary layer. Thus, the larger Re, the smaller is this coefficient.

§11.4. Use of Integral Relation to Calculate the Turbulent Flat-Plate Boundary Layer and Drag

The integral relation (11.2) is also applicable to the turbulent boundary layer. However, the two additional conditions (11.6) and (11.8) are not suitable in this case, since the friction in the turbulent boundary layer obeys other and more complex governing relations. An exact theory has not yet been developed for turbulent flows; however, it has been established experimentally that for turbulent flow the velocity distribution in the boundary layer can be expressed in power-law form

$$V_x=V_\infty\left(\frac{y}{\delta}\right)^{\frac{1}{n}} \tag{11.16}$$

Experiment shows that for outer flow velocities which do not exceed half the speed of sound we can take n = 7. The magnitude of the coefficient n increases with increase of the flow velocity. To find the turbulent friction stress τ_0, we can use a formula obtained by analogy with pipe and flat-plate flows

$$\tau_0=0{,}0225\rho V_0^2\left(\frac{1}{\mathrm{Re}_\delta}\right)^{\frac{1}{4}} \tag{11.17}$$

where

$$Re_\delta = \frac{V_\infty \delta}{\nu} \tag{11.18}$$

Here we must bear in mind that an experimental relation is used for the friction stress in the turbulent fluid flow regime in a circular pipe. Calculations using (11.16) and (11.17) will be sufficiently exact for comparatively small values of Re δ.

Solving (11.3) with account for (11.16) and (11.17), we find the turbulent boundary layer thickness

$$\delta = 0{,}37\left(\frac{\nu}{V_\infty x}\right)^{\frac{1}{5}} x \tag{11.19}$$

or

$$\delta = 0{,}37\left(\frac{1}{Re_x}\right)^{\frac{1}{5}} x \tag{11.20}$$

and the frictional drag

$$X_{тр} = c_{x\,тр} S \rho \frac{V_\infty^2}{2} \tag{11.21}$$

where

$$c_{x\,тр} = \frac{0{,}072}{Re^{0{,}2}} \tag{11.22}$$

Under actual conditions some region near the leading edge of the plate is occupied by a laminar boundary layer. The turbulent boundary layer is located downstream of the laminar zone. If we assume that transition from laminar to turbulent flow takes place instantaneously, then we can speak of a transition point rather than a transition zone. The location of the transition point depends on several factors, primarily freestream turbulence and surface roughness. Surface roughness disturbs the laminar flow stability, and therefore the greater the roughness, the closer the transition point

will be to the leading edge. Increased freestream turbulence also favors early transition to turbulent flow in the boundary layer.

In addition to these factors, the location of the transition point also depends on the pressure distribution over the surface of the wing, which in turn depends on the wing geometric characteristics. Laminar flow is maintained only with negative pressure gradients along the streamlines. Therefore, in practice the boundary layer can be laminar on a profile only ahead of the maximal suction point. Laminar flow is also disturbed in the case of marked breaks in the contour of the profile, at locations of slots, protuberances, etc. and so on.

If a flat plate is aligned parallel to the freestream velocity vector, the pressure along the streamlines above the plate will be constant (zero-pressure-gradient flow). In this case the point of transition of the laminar flow to turbulent is determined by the critical Reynolds number Re_{cr}, which lies in the range $2 \cdot 10^5 - 5 \cdot 10^5$, depending on the plate roughness and freestream turbulence.

If part of the surface is covered by a laminar boundary layer and part by a turbulent layer, such a boundary layer is called mixed and the magnitude of the flat-plate friction drag coefficient for zero-pressure-gradient flow is found from the approximate formula

$$c_{x\,tp} = \frac{0.074}{Re}\left(Re - Re_{tp} + 37\,Re_{tp}^{\frac{5}{6}}\right)^{\frac{4}{5}} \qquad (11.23)$$

For $Re_{cr} = 0$, (11.23) takes the form (11.22) for the turbulent boundary layer, while for $Re_{cr} = Re$ it takes the form (11.13) for the laminar boundary layer.

Surface roughness has a significant effect on frictional drag in the case of turbulent flow in the boundary layer. The influence of roughness protuberances and Reynolds number on the frictional drag coefficient of a rough plate is shown in Figure 11.7. The

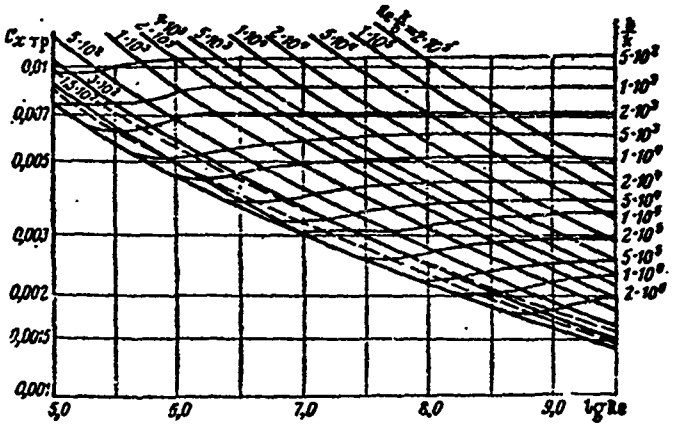

Figure 11.7. Frictional drag coefficient of rough plate as function of Re and surface roughness

sloping lines correspond to the values of $c_{x\ fr}$ for a constant value of the parameter $\mathrm{Re}\,\frac{k}{b}$ (for more detail see [56]), where $\mathrm{Re} = \frac{Vb}{\nu}$, while the horizontal lines are for a constant value of the relative roughness, equal to the ratio of the roughness protuberance height k to the plate chord b.

We see from the curves that the drag increases with increase of the roughness; for a definite value of the roughness, beginning with some value of Re the drag coefficient is independent of Re. In this case the frictional drag force is proportional to the velocity squared. This drag regime is termed the quadratic or self-similar regime, since modeling of the friction forces in the case of the quadratic drag law is provided by geometric similarity alone and does not require equality of the Reynolds numbers for the full-scale and model conditions.

Finally, it follows from the curves that the drag increase owing to roughness in comparison with the drag of a smooth plate

increases with increase of Re. Therefore, smooth surfaces are particularly important for high-speed airplanes.

§11.5. Boundary Layer Heating at High Gas Flow Velocities

At the lower edge of the boundary layer, i.e., at the wetted surface of the body, the air particles are brought to rest (V = 0). In the absence of heat exchange between these particles and the surrounding medium, the particle temperature will be equal to the stagnation temperature, which according to (9.3) is

$$T_0 = T_\infty \left(1 + \frac{k-1}{2} M_\infty^2\right)$$

for air with k = 1.4

$$T_0 = T_\infty (1 + 0{,}2 M_\infty^2) \tag{11.24}$$

where T_∞ and M_∞ are the freestream temperature and Mach number.

In reality, in the absence of heat exchange between the boundary layer, the surrounding medium, and the wetted surface, the actual gas temperature at the wetted surface, which is termed the recovery temperature and is denoted by T_r, differs somewhat from the theoretical value.

For a flat plate the recovery temperature can be found from the formula

$$T_r = T_\infty \left(1 + r \frac{k-1}{2} M_\infty^2\right) \tag{11.25}$$

where r — is the temperature recovery factor, characterizing how close the retardation in the boundary layer is to adiabatic retardation, for which r = 1.

For approximate calculations we can take r = 0.90 for the turbulent boundary layer and r = 0.85 for the laminar boundary layer.

We see from (11.25) that the recovery temperature at a thermally insulated wall increases markedly with increase of M_∞.

§11.6. Use of an Integral Relation to Calculate the Boundary Layer on a Curved Surface

In the case of flow past a curved surface, the velocity at the outer edge of the boundary layer is variable; therefore the pressure in the boundary layer varies along the flow, i.e., the longitudinal pressure gradient dp/dx is not equal to zero. In calculating the flow in the boundary layer over a curved surface, it is necessary to use the complete integral relation (11.2)

$$\rho \frac{d}{dx}\int_0^\delta V_x^2 dy - \rho V_0 \frac{d}{dx}\int_0^\delta V_x dy = -\delta \frac{dp}{dx} - \tau_0$$

We note that the following equality holds

$$\rho \frac{d}{dx}\left(V_0 \int_0^\delta V_x dy\right) = \rho V_0 \frac{d}{dx}\int_0^\delta V_x dy + \rho \frac{dV_0}{dx}\int_0^\delta V_x dy$$

hence

$$\rho V_0 \frac{d}{dx}\int_0^\delta V_x dy = \rho \frac{d}{dx}\left(V_0 \int_0^\delta V_x dy\right) - \rho V_0' \int_0^\delta V_x dy$$

Moreover, we have from the Bernoulli euqation (5.5)

$$\frac{dp}{dx} = -\rho V_0 \frac{dV_0}{dx} = -\rho V_0 V_0'$$

Then

$$\delta \frac{dp}{dx} = -\rho V_0 V_0' \int_0^\delta dy$$

With account for these relations (11.2) takes the form

$$\rho\frac{d}{dx}\int_0^\delta V_x(V_0-V_x)dy+\rho V_0'\int_0^\delta(V_0-V_x)dy=\tau_0 \qquad (11.26)$$

The quantity V_0, which is the velocity at the outer edge of the selected boundary layer cross section, is independent of y and therefore may be taken outside the integral sign.

The integral in the second term of the left side of this equation is the reduction of the mass flow rate through the boundary layer cross section of height δ and width equal to unit length owing to the influence of viscosity in comparison with the ideal fluid flow rate through the same section. This integral is represented graphically in the form of the area ObaO (shaded region in Figure 11.8). The quotient obtained by dividing this integral by the magnitude of the velocity at the outer edge of the boundary layer yields a linear quantity equal to

$$\delta^*=\int_0^\delta\left(1-\frac{V_x}{V_0}\right)dy \qquad (11.27)$$

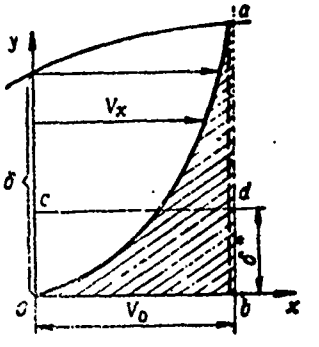

Figure 11.8. Geometric determination of displacement thickness

which is called the displacement thickness. The displacement thickness is numerically equal to the height of a rectangle equal in area to the area ObaO in Figure 11.8 and having the base V_0.

The integral in the first term of the left side of (11.26) is the magnitude of the momentum change in the boundary layer owing to the influence of viscosity. Therefore the quotient obtained by dividing it by the velocity V_0, having the linear dimension

$$\delta^{**}=\int_0^{\delta}\frac{V_x}{V_0}\left(1-\frac{V_x}{V_0}\right)dy \tag{11.28}$$

is called the momentum loss thickness.

Introducing the quantities δ^* and δ^{**}, we reduce (11.26) to the form

$$\varrho\frac{d}{dx}(V_0^2\delta^{**})+\rho V_0'V_0\delta^*=\tau_0$$

and

$$\varrho V_0^2\frac{d\delta^{**}}{dx}+2\varrho V_0V_0'\delta^{**}+\varrho V_0V_0'\delta^*=\tau_0 \tag{11.29}$$

Dividing this expression by ρV_{0^2}, we obtain the integral relation in dimensionless form

$$\frac{d\delta^{**}}{dx}+\frac{V_0'}{V_0}(2\delta^{**}+\delta^*)=\frac{\tau_0}{\varrho V_0^2} \tag{11.30}$$

or

$$\frac{d\delta^{**}}{dx}+\delta^{**}\frac{V_0'}{V_0}(2+H)=\frac{\tau_0}{\varrho V_0^2} \tag{11.31}$$

where

$$H=\frac{\delta^*}{\delta^{**}} \tag{11.32}$$

The integral relation in the form (11.31) with the parameters δ^* and δ^{**}, termed the Karman equation or the momentum equation, is used to calculate the boundary layer on curved profiles. Equation (11.31) is applicable for both laminar and turbulent boundary layers, since no assumptions were made concerning the concrete expression for the tangential stress in terms of the quantities δ^* and δ^{**}.

In the approximate solution of problems using (11.2), the shape of the velocity profile in the boundary layer is usually

specified and then this equation is used to find the friction stress τ_0 at the wetted surface, and also the boundary layer thickness δ, displacement thickness δ^*, and momentum loss thickness δ^{**}.

We note that the boundary layer thickness is somewhat greater than the displacement thickness δ^*, and the latter in turn is greater than the momentum loss thickness δ^{**}, i.e., $\delta > \delta^* > \delta^{**}$. We shall show this using the laminar boundary layer as an example.

To establish the connection between δ and δ^*, we substitute the value of V_x/V_0 from (11.6) into (11.27). Then we obtain

$$\delta^* = \int_0^\delta \left(1 - 2\frac{y}{\delta} + \frac{y^2}{\delta^2}\right) dy = \frac{\delta}{3}$$

Consequently, the displacement thickness in the laminar boundary layer on a flat plate amounts to about one third of the boundary layer thickness.

During flow over a curved surface, for example a wing surface, qualitatively new phenomena may occur which are not possible in the case of zero-pressure-gradient flow. At the leading edge of the profile the tangential velocity for potential flow equals zero, and the pressure is maximal in accordance with the Bernoulli formula. For points lying downstream the velocity increases and reaches a maximum at point m; the pressure decreases correspondingly and reaches a minimum at point m (Figure 11.9). The fluid particles in the boundary layer ahead of point m travel with a negative gradient $\frac{\partial p}{\partial x}$, while those behind this point will travel with a positive gradient. As the fluid particles enter the region downstream of point m, they are accelerated by the positive pressure gradient directed opposite the freestream velocity. Thus, near the solid surface the medium is retarded as it encounters the increasing pressure.

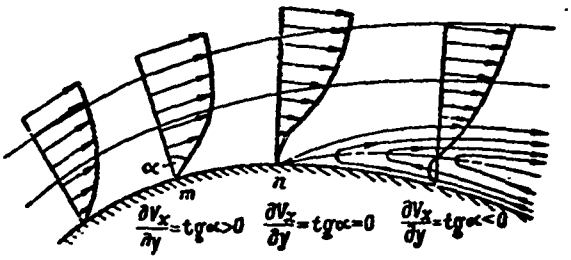

Figure 11.9. Schematic of flow with boundary layer separation

If we assume that the flow in the boundary layer is inviscid, the relation between the velocity and pressure near the surface is described by the Bernoulli equation, and the kinetic energy of the particles is sufficient to ensure their movement to the trailing edge against the increasing pressure. However, in reality the presence of friction in the boundary layer leads to more rapid reduction of the kinetic energy, so that at some point, termed the boundary layer separation point (n), not only the velocity at the wall but also its first derivative along the normal to the solid surface and therefore the friction stress become equal to zero

$$\left(\frac{\partial V_x}{\partial y}\right)_{y=0}=0;\quad \tau_0=\mu\left(\frac{\partial V_x}{\partial y}\right)_{y=0}=0$$

Under the influence of the increasing pressure downstream of the separation point, reverse flow develops in the boundary layer and leads to separation of the boundary layer from the body surface.

Outside the viscous zone behind the separation point, the pressure gradient decreases nearly to zero because of the reduction of the main flow cross section, so that the pressure on the aft part of the body decreases in comparison with the pressure obtained in the case of inviscid fluid flow past the body.

The reverse flow velocities are not large downstream of the separation point, but the tangential stress τ_0 changes markedly and may even change its sign. We might get the impression that the overall drag of the body decreases when boundary layer separation occurs. However, this is not really so.

The drag force is made up from the resistance associated with friction in the boundary layer and pressure drag owing to the difference of the pressures on the forward and aft parts of the submerged bodies. If the fluid is inviscid, the frictional drag is zero. But in this case the pressure drag, as was shown for the example of transverse flow past a cylinder (see Chapter VI), may also be zero (this is possible in the case of unseparated flow, when the pressure on the aft region will be the same as at the forward stagnation point).

In a viscid medium both frictional drag and pressure drag are always present. The relationship between these components depends on the shape of the body. If the body has large transverse dimensions in comparison with the longitudinal dimensions, boundary layer separation is always observed at the body surface and this leads to incomplete pressure recovery on the aft part of the body. The pressure on the aft part of the body is lower than on the forward part. The resultant pressure force retards body motion in the flow.

If the body has an elongated streamwise form with smooth contours, even if flow separation is observed it will be only on a small portion of the body surface and the frictional resistance makes up the major portion of the drag. Such bodies are termed <u>streamlined</u>, in contrast with those described above, for which pressure drag is dominant and which are termed <u>bluff bodies</u>. For the same cross sectional areas, the total drag of streamlined bodies may be many time less than that of bluff bodies. Therefore bodies (wing, fuselage, and so on) which are located in a stream are always

given a streamlined form, so that boundary layer separation is unlikely or the separated flow region is minimized.

The danger of boundary layer separation can be reduced by reducing the magnitude of the positive pressure gradient (this can be achieved by giving the body an elongated drop-like shape) or by influencing the nature of the flow in the boundary layer. Usually boundary layer separation takes place far from the nose portion of the body, in the zone of positive pressure gradients, where the boundary layer is turbulent. The greater the degree of turbulence of the boundary layer flow, the more intense is the momentum exchange between the outer and wall layers, and the larger the velocity near the surface and therefore the less the danger of separation.

The degree of turbulence in the boundary layer increases with increase of Re. This means that increase of Re reduces the danger of boundary layer separation. The degree of turbulence in the boundary layer increases with increase of the degree of turbulence of the outer flow. Unfortunately, we have no control over the degree of turbulence of the atmosphere. However, in internal problems (flow in a diffuser) we can increase the degree of turbulence to avoid the onset of boundary layer separation. Finally, we can cause boundary layer transition artificially by locating special protuberances — turbulence generators — on the surface of the body. In this case the frictional drag increase is compensated by the reduction of the pressure drag.

The influence of the degree of outer flow turbulence and turbulence generators on the drag of bodies is so large that the degree of wind tunnel turbulence is often determined on the basis of the magnitude of the drag coefficient of a sphere located in the tunnel working section. The higher the degree of turbulence, the smaller is the separation zone on the aft part of the bluff body, and this means that its drag coefficient is smaller. Figure 11.10 shows the influence of the degree of flow turbulence on the sphere drag coefficient. We see from the curves in Figure 11.11

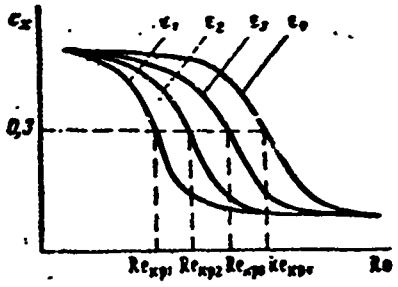

Figure 11.10. Effect of flow turbulence on sphere drag coefficient ($\varepsilon_1 > \varepsilon_2 > \varepsilon_3 > \varepsilon_4$)

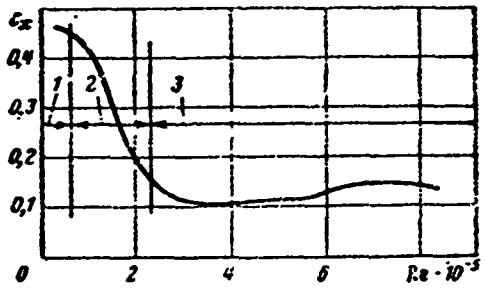

Figure 11.11. Sphere drag coefficient versus Re:

1 — subcritical zone; 2 — critical zone; 3 — supercritical zone

that with increase of Re, when the boundary layer becomes turbulent ahead of the separation point, there is a marked drag reduction, which can be explained by the reduction of the separation zone dimensions as a result of boundary layer turbulization, and this means more complete pressure recovery on the aft part of the body.

Techniques involving energetic influence on the stream, termed boundary layer control, are used to prevent boundary layer separation.

§11.7. Boundary Layer Control

As was shown above, boundary layer separation arises because of excessive retardation of the flow near the surface by the friction forces. Therefore, if we artificially increase the velocity near the surface we can avoid the onset of separation. Increase of the velocity can be achieved in two ways — either by sucking the

retarded flow layer into the submerged body, or by blowing off the retarded layer with the aid of a jet blown with high velocity along the surface in the direction of the stream. The first method is called boundary layer suction; the second is termed boundary layer blowing.

Boundary layer suction. Let us examine a cylinder in a fluid stream. Direct observations show that vortices separate periodically from the cylinder (at points A and B) and form a vortex street behind the cylinder (Figure 11.12). If we make slots at the separation points A and B and use a vacuum pump to suck off the boundary layer, then we can improve the flow past the cylinder markedly (Figure 11.13).

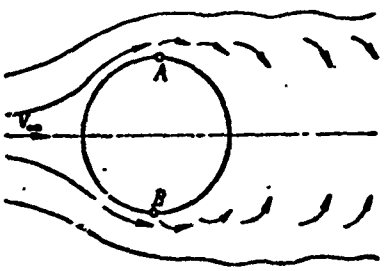

Figure 11.12. Schematic of flow past circular cylinder and formation of vortex street

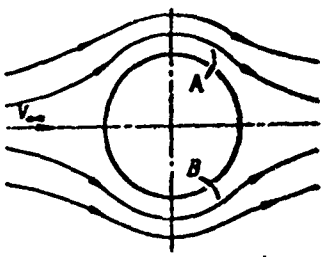

Figure 11.13. Separation-free flow past cylinder obtained by sucking boundary layer through slots A and B

The aerodynamics of an airplane wing can be improved similarly In fact, boundary layer suction through a slot located on the upper surface of the wing near the trailing edge (Figure 11.14) makes it possible to maintain separation-free flow over the wing clear up to the slot itself, even at high angles of attack.

Boundary layer suction has recently been used to reduce frictional drag, since the point of transition from the laminar to turbulent

boundary layer is shifted downstream. As a result, the flow is laminarized and thereby the friction is reduced, since the friction is less in the laminar boundary layer than in the turbulent.

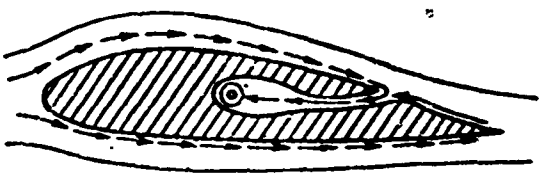

Figure 11.14. Separation-free flow past wing profile obtained by sucking boundary layer through a slot

We note that the favorable influence of suction amounts to the following. First, the fluid particles which are slowed down in the rising pressure region are removed from the boundary layer before they can separate from the wall. As a result, a new boundary layer which is capable of overcoming back pressure is created downstream of the slot. Second, laminar boundary layer suction creates velocity profiles in the layer which have a higher stability limit, i.e., higher critical Re, in comparison with the velocity profile in the boundary layer without suction.

Theoretical and experimental studies of this boundary layer control technique are being made at the present time. Of considerable interest is the attempt to use continuous suction along the entire wall through discrete holes or creation of a porous wall, through which suction can be performed more effectively.

Boundary layer blowing. The blowing method can also be used to achieve separation-free flow by supplying additional energy to the retarded fluid particles in the boundary layer (Figure 11.15). The additional energy is introduced by blowing an air jet into the boundary layer from inside the submerged body. In this case the velocity of the air particles in the layer adjacent to the wall is increased, eliminating the danger of separation.

We note that boundary layer control with the aid of blowing and suction can have a large effect in the sense of lift coefficient increase. However, constructional difficulties, and also the large energy expenditures required, prevent the use of blowing and suction in civil aviation practice at the present time.

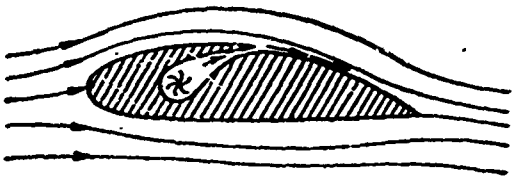

Figure 11.15. Separation-free flow past wing profile in presence of blowing

Other boundary layer control techniques also exist, for example, driving the wetted wall in the direction of motion; however, this technique involves still greater constructional difficulties. Experimental studies are being made of boundary layer control using vortex and electrodynamic techniques(1). However, these techniques are at the moment only of scientific and theoretical interest.

REVIEW QUESTIONS

1. What leads to the formation of a boundary layer on solid bodies submerged in a stream?

2. What factors influence the location of transition from laminar to turbulent boundary layers?

3. Describe the boundary layer control techniques.

Footnote (1) appears on page 29.

PROBLEMS

1. Find the friction drag coefficient and force of a smooth plate with dimensions l = 0.5 m, b = 3 m at α = 0. The flow velocity V = 12 m/sec. Assume the flow is a) laminar; b) turbulent. The air parameters correspond to the altitude H = 1000 m. Find the boundary layer thickness at the end of the plate.

Answer: a) $2c_f = 0.00417$, X = 0.51 N, δ = 4.65 mm;

b) $2c_f = 0.01135$, X = 1.36 N, δ = 14.1 mm.

2. Find the profile drag coefficient of a wing with relative thickness $\bar{c}$ = 14% and chord b = 3 m in flight at an altitude H = 600 m at a speed V = 600 km/hr. The boundary layer transition point is 20% of the chord from the profile nose.

Answer: $c_f = 0.0058$.

3. An airstream with velocity V = 30 m/sec flows past a thin flat plate aligned with the stream under standard atmospheric conditions. The plate length l = 200 mm. Taking an average value $5 \cdot 10^5$ of the critical Re based on boundary layer length, show that the boundary layer which forms on the plate will be laminar. Find the friction coefficient $c_{x\ fr}$. The kinematic viscosity of air at standard conditions is $\nu = 0.145 \times 10^{-4}$ m^2/sec

Answer: $c_{x\ fr} = 0.002$.

Footnotes

Footnote (1) on page 27: See, for example, Collection of Scientific Papers "Some Problems of Aerodynamics and Electrohydrodynamics," Vol. 1, KIIGA, 1964; Vol. 2, KIIGA, 1966; Vol. 3, KIIGA, 1968).

CHAPTER XII

WING PROFILES AND THEIR AERODYNAMIC CHARACTERISTICS

§12.1. Wing Profile Geometric Parameters

A body which creates in a fluid stream a lift force which exceeds considerably the drag force is called a wing. As a rule a wing has a from which is symmetric about a plane called the plane of symmetry.

Any section of a wing by a plane parallel to the wing plane of symmetry is termed the wing profile. The wing profile may be different in shape, size, and orientation at different sections.

One possible wing profile is shown in Figure 12.1. Point A is the profile leading edge. The line AB connecting the two most distant points of the profile, i.e., the leading and trailing edges of the profile, is termed the profile

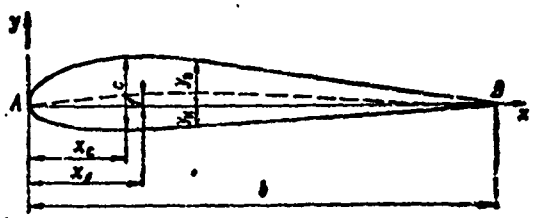

Figure 12.1. Profile geometric parameters

chord b. The chord divides the profile into two parts — upper and lower. The angle between the profile chord and the freestream flow direction is termed the angle of attack α if the freestream velocity vector is parallel to the profile plane. In the more general case, the angle of attack is measured by the angle between the profile chord and the projection of the freestream velocity on the profile plane.

In studying profile geometric characteristics, we use a rectangular coordinate system in which the origin coincides with the profile leading edge, the x axis is directed along the chord toward the trailing edge, and the y axis is directed upward.

In this coordinate axis system, the equations of the upper and lower profile contours have the form $y_u = f_1(x)$ and $y_l = f_2(x)$, respectively.

The profile thickness at any point of the chord is expressed as the difference of the ordinates of the points y_u and y_l. The maximal length of the segment perpendicular to the chord between the upper and lower profile contours, i.e., $y_u - y_l$, is called the profile maximal thickness or simply thickness and is denoted by c (see Figure 12.1).

The ratio of the profile maximal thickness c to the chord b is called the profile relative thickness

$$\frac{c}{b}=\bar{c},$$

or, in percent,

$$\frac{c}{b}100=\bar{c}\%.$$

The line connecting the midpoints of the segments $y_u - y_l$ constructed at different points of the chord is called the profile

mean camber line. In the particular case in which the profile is symmetric, the mean camber line coincides with the chord. The maximal ordinate of the mean camber line is called the profile camber f and its ratio to the chord is called the relative camber.

$$\frac{f}{b}=\bar{f},$$

or, in percent,

$$\frac{f}{b}100=f\%.$$

The abscissas of the profile maximal thickness and maximal camber are denoted by x_c and x_f, respectively (see Figure 12.1). The ratios of these quantities to the chord are termed respectively the relative thickness and camber abscissas

$$\bar{x}_c=\frac{\overline{x_c}}{b},\quad \bar{x}_f=\frac{x_f}{b}.$$

The values of $\bar{x}_c$ for subsonic profiles lie in the 25 - 30% range, while the values for supersonic profiles lie in the 40 - 50% range.

The radii of curvature at the "head" and "tail" of the profile (f_{head}, r_{tail}) are also referred to the chord and are often expressed in percent of the chord length. For example, the relative radius $\bar{r} = r/b$.

A series of profiles can be obtained by deforming some initial profile while holding one or more of the dimensionless parameters listed above constant. The quantities b, $\bar{c}$, $\bar{x}_c$, $\bar{x}_f$, $\bar{f}$, $\bar{r}$ are the basic profile geometric parameters, and they determine its aerodynamic characteristics. The relative thicknesses of the aerodynamic profiles of wings and propeller blades usually lie in the range from 3 - 4% up to 20 - 25%. The thin profiles are used at the tips of propeller blades and for wings of supersonic airplanes.

The relative camber of modern wing and propeller blade profiles usually does not exceed 2%. The camber of the airplane profiles of the 1920's and 1930's was considerably greater and reached 6 - 8%.

Modifications of wing profile shape associated with flight vehicle improvement and flight speed increase are shown in Figure 12.2.

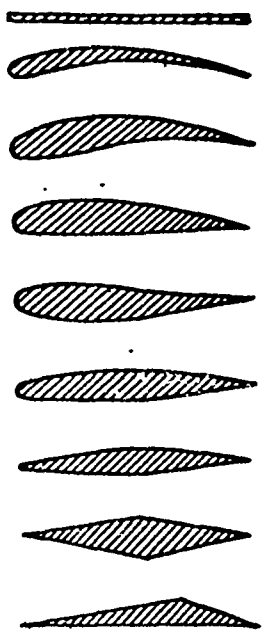

Figure 12.2. Aircraft profile forms (three lower profiles are supersonic)

§12.2. Aerodynamic Forces and Moments

The action of the air on the wing leads to the appearance of forces distributed continuously over the entire wing surface, which can be characterized by the magnitudes of the normal p and tangential τ stresses at every point on the wing surface.

We term the force R, the principal vector of the system of elementary aerodynamic forces distributed over the wing surface, the total aerodynamic force. However, frequently the total aerodynamic force R is taken to mean only the resultant of the normal forces, neglecting the friction forces.

The moment M_z of the total aerodynamic force about the wing leading edge is termed the longitudinal or pitching moment. The moment M_z is considered positive if it tends to rotate the wing in

the direction of increasing angles of attack, and negative if it is directed oppositely. A positive moment is called a climbing moment; a negative moment is called a diving moment.

In theoretical and experimental studies of the force interaction between a moving body and a medium, we usually use the components of the vector R in some coordinate system, rather than the vector R itself. Two coordinate systems are often used in aerodynamics: wing and body coordinates.

In the wing coordinate system, the Ox axis coincides with the velocity direction; the Oy axis is perpendicular to the Ox axis and lies in the plane of symmetry of the flight vehicle. The Oz axis forms a right-hand system with the Ox and Oy axes (directed along the right wing). The coordinate origin can be chosen arbitrarily. Most often the origin is located at the wing leading edge.

In the body coordinate system, the Ox_1 axis is directed along the wing chord or airplane longitudinal axis. The Oy_1 axis is perpendicular to the Ox_1 axis and lies in the plane of symmetry of the flight vehicle. The Oz_1 axis forms a right hand system with the Ox_1 and Oy_1 axes.

We shall denote the projections of the force R in the wing coordinate system by X, Y, Z and in the body coordinate system by X_1, Y_1, A_1 (Figure 12.3). In the solution of plane problems the aerodynamic force R is resolved into two components X, Y (X_1, Y_1).

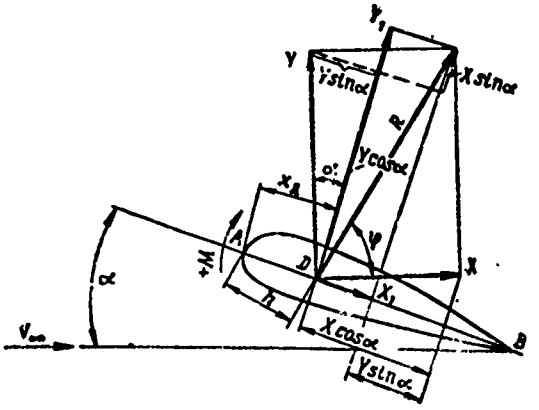

Figure 12.3. Components of total aerodynamic force in wing and body coordinate systems

In the body coordinate system the force components Y_1 and X_1 are called respectively the normal and tangential components.

In the wing coordinate system the projection of the force R on the direction perpendicular to the freestream velocity is called the lift force Y, and the projection of the force R on the direction of the wing (airplane) velocity is called the drag force X.

We have the following relations between the forces in the wing and body coordinate systems (see Figure 12.3)

$$\left.\begin{aligned} Y_1 &= Y\cos\alpha + X\sin\alpha, \\ X_1 &= X\cos\alpha - Y\sin\alpha \end{aligned}\right\} \tag{12.1}$$

or, conversely,

$$\left.\begin{aligned} Y &= Y_1\cos\alpha - X_1\sin\alpha, \\ X &= X_1\cos\alpha + Y_1\sin\alpha. \end{aligned}\right\} \tag{12.2}$$

Let us examine a cylindrical wing of infinite span in a fluid stream and identify as the characteristic length a segment of length l and as the characteristic area the area $S = lb$ (b is the chord length).

We assume that the Ox axis is directed along the profile chord, and the Oy axis coincides with the line of measurement of the maximal profile thickness (Figure 12.4). The elementary pressure force acting on the wing surface element $ds l$ is $pds l$. The projections of the elementary force on the Ox and Oy axes are

$$dY_1 = dslp\cos\beta = \pm lpdx;$$
$$dX_1 = dslp\sin\beta = lpdy.$$

The "plus" sign applies to the lower surface; the "minus" sign to the upper surface.

To find the forces X_1 and Y_1 it is necessary to sum the elementary components over the entire profile contour.

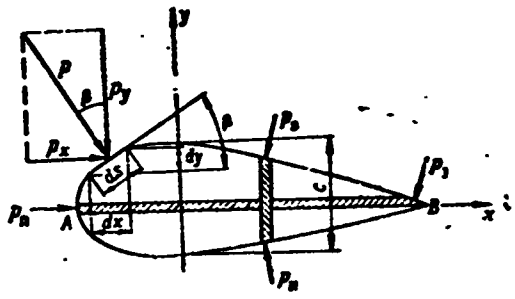

Figure 12.4. Illustration for calculating lift and drag

We make the summation along the x axis separately for the upper and lower profile surfaces. Then we obtain for the normal force

$$Y_1 = l \int_{(A,B)} (p_n - p_a)\, dx. \tag{12.3}$$

We make the summation along the y axis separately for the forward and aft parts of the profile. Denoting respectively the pressure on the forward part of the profile by p_f and on the aft part by p_a, we obtain

$$X_1 = l \int_{y_n}^{y_a} (p_n - p_a)\, dy. \tag{12.4}$$

In reality the force X_1 is greater than that defined by (12.4) by the magnitude of the resultant of the friction forces on the profile surface.

Knowing the forces Y_1 and X_1 for every angle of attack, we can use (12.2) to find the corresponding lift force Y and drag force X. The total aerodynamic force is

$$R = \sqrt{Y_1^2 + X_1^2}. \tag{12.5}$$

Experiment shows that the tangential force X_1 and the profile height are small in comparison with the normal force Y_1 and the

profile chord; therefore, the moment from the tangential force is usually neglected in view of its smallness.

The elementary moment from the normal force dY_1 is

$$dM=-dY_1x=-(p_н-p_в)lxdx.$$

Then the total moment is

$$M=-l\int_{(A,B)}(p_н-p_в)xdx. \tag{12.6}$$

§12.3. Profile Aerodynamic Coefficients and L/D

Formulas were presented in Chapter VII for finding the aerodynamic forces. We have the following formulas for the lift and drag

$$Y=c_yqS,\ X=c_xqS, \tag{12.7}$$

where $q=\rho\frac{V_\infty^2}{2}$ — is the velocity head or dynamic pressure;

c_y — is the lift coefficient;

c_x — is the drag coefficient;

S — is the wing lifting area;

V_∞ — is the freestream velocity or the wing (airplane) velocity.

The formulas for the normal and tangential forces have the form

$$Y_1=c_{y1}qS,\ X_1=c_{x1}qS, \tag{12.8}$$

where c_{y1}, c_{x1} — are the normal and tangential force coefficients.

If we denote the total aerodynamic force coefficient by c_R and the total moment coefficient by c_m, we can write

$$R=c_R qS,\ M=c_m qSb. \tag{12.9}$$

With account for (12.5) we obtain

$$c_R=\sqrt{c_{x1}^2+c_{y1}^2}. \tag{12.10}$$

If we express the forces in (12.1) and (12.2) in terms of their coefficients, we obtain

$$\left.\begin{aligned} c_{y1}&=c_y\cos\alpha+c_x\sin\alpha,\\ c_{x1}&=c_x\cos\alpha-c_y\sin\alpha \end{aligned}\right\} \tag{12.11}$$

or, conversely,

$$\left.\begin{aligned} c_y&=c_{y1}\cos\alpha-c_{x1}\sin\alpha,\\ c_x&=c_{x1}\cos\alpha+c_{y1}\sin\alpha. \end{aligned}\right\} \tag{12.12}$$

The angles of attack realized in flight are usually small; therefore we can set cos $\alpha \approx 1$, sin $\alpha \approx \alpha$. Considering that in practice the drag coefficient c_x is usually an order of magnitude smaller than the lift coefficient c_y, we can reduce (12.11) and (12.12) to the simpler and more frequently used form

$$\left.\begin{aligned} c_{y1}&=c_y,\\ c_{x1}&=c_x-c_y\alpha \end{aligned}\right\} \tag{12.13}$$

and

$$\left.\begin{aligned} c_y&=c_{y1},\\ c_x&=c_{x1}+c_{y1}\cdot\alpha. \end{aligned}\right\} \tag{12.14}$$

Using (12.3), we can write the formula for finding the normal force coefficient in the form

$$c_{y1}=\frac{Y_1}{q\frac{V^2}{2}b}=\int\limits_{(A,B)}\left(\frac{p_H-p_0}{q\frac{V^2}{2}}-\frac{p_B-p_0}{q\frac{V^2}{2}}\right)\frac{dx}{b}=\int\limits_0^1(\bar{p}_H-\bar{p}_B)\,d\bar{x},$$

where

$$d\bar{x}=\frac{dx}{b},\quad \bar{p}_H=\frac{p_H-p_0}{q\frac{V^2}{2}};\quad \bar{p}_B=\frac{p_B-p_0}{q\frac{V^2}{2}}.$$

We obtain similarly the formula for c_m

$$c_m = \int_0^1 (\bar{p}_n - \bar{p}_v)\bar{x}\,d\bar{x}.$$

For small angles of attack, this expression can also be used to find the lift coefficient

$$c_y = \int_0^1 (\bar{p}_n - \bar{p}_v)\,d\bar{x}. \tag{12.15}$$

Thus, knowing the pressure distribution on the upper and lower surfaces of the profile, we can obtain the value of the lift coefficient. To realize this method we must carry out an experiment with a pressure tapped profile model, providing flow conditions corresponding to infinite wing span (plane flow).

The aerodynamic coefficients are usually obtained by the force balance method. Special balances are used to measure directly the forces and moment acting on a wing model in a wind tunnel, and then the coefficients are found by calculation.

The profile efficiency K is used to evaluate the aerodynamic properties of the profile. The profile aerodynamic efficiency is the ratio of the lift to the drag

$$K = \frac{Y}{X}.$$

We see from Figure 12.3 that this quantity is the slope of the total aerodynamic force R to the freestream direction, i.e.,

$$K = \operatorname{tg}\varphi.$$

The lower the drag for the same lift, the higher is the efficiency. The dimensionless quantities c_x, c_y, c_m, c_R and K are the basic aerodynamic coefficients of the wing profile.

§12.4. Dependence of Aerodynamic Coefficients on Profile Angle of Attack. Profile Polar

The aerodynamic coefficients c_x, c_y, c_m are independent of one another, and the coefficients c_R and K are found from the corresponding formulas.

The total aerodynamic force coefficient c_R, and also its components c_x and c_y, the moment coefficient c_m, and the aerodynamic efficiency K depend on the profile form, angle of attack, similarity criteria Re and M, degree of turbulence, and so on. These coefficients are the same for dynamically similar flows and are therefore convenient to use. For this reason the results of experimental studies are presented in the form of relations for the aerodynamic coefficients. For a given profile and given Re and M, change of the angle of attack α leads to marked change of the profile aerodynamic coefficients.

The curve of aerodynamic lift coefficient c_y versus angle of attack α for low flow speeds, when gas compressibility can be neglected, is shown in Figure 12.5. The maximal value of c_y for $\alpha = \alpha_{cr}$ is denoted by $c_{y\ max}$. For the usual profiles $c_{y\ max}$ varies in the range 0.9 - 1.4. At the angle of attack $\alpha = 0°$ the modern profiles, having some camber, already have some lift force. The greater the profile camber $\bar{f}$, the further to the left the curve $c_y = f(\alpha)$ lies (see Figures 12.5). The angle of attack at which $c_y = 0$ is called the zero lift angle of attack and is denoted by α_0. It is usually negative and small (α_0 = −0.02 - −0.05 rad). For symmetric profiles $\alpha_0 = 0$.

Experiment and theory show that for separation-free flow past a profile the coefficients c_y and c_m depend linearly on the value of α over a wide range of angle-of-attack values

$$\left.\begin{aligned} c_y &= c_y^{\alpha}(\alpha - \alpha_0), \\ c_m &= c_{m0} + m c_y. \end{aligned}\right\} \qquad (12.16)$$

where c_{m0} — is the moment coefficient at zero lift;

$m = \frac{\partial c_m}{\partial c_y}$; $c_y^{\alpha} = \frac{\partial c_y}{\partial \alpha}$ — are constants for a given profile.

For angles of attack approaching α_{cr} the positive pressure gradient of the aft part of the profile increases so much that it leads to boundary layer separation — the flow around the wing is no longer smooth. As shown above in Chapter XI, separation of the laminar boundary layer occurs earlier than for the turbulent boundary layer for the same pressure gradient.

In level flight the airplane weight G is balanced by wing lift, i.e.,

$$G = Y = c_y \frac{\rho V^2}{2} S$$

or

$$V = \sqrt{\frac{2G}{\rho c_y S}}.$$

We see from this formula that the larger c_y, the lower is the airplane speed. The minimal value of the speed is obtained for $c_y = c_{y\,max}$.

The normal force coefficient c_{y1} changes with change of the angle of attack similarly to the coefficient c_y.

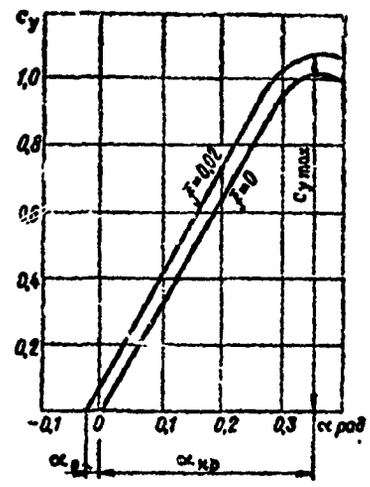

Figure 12.5. Aerodynamic coefficient c_y versus angle of attack α

With increase of angle of attack α, the profile drag coefficient c_x first changes slowly (Figure 12.6) and then, beginning at angles of attack somewhat less than α_{cr}, increases rapidly as a result of intensification of boundary layer separation. At an angle of attack close to the zero lift angle $c_x = c_{x\,min}$.

The nature of the variation of the coefficient c_{x1} differs markedly from the variation of c_x. The drag coefficient c_x is always positive, while the tangential force coefficient c_{x1} may become negative at large angles of attack, which is seen from (12.11).

The nature of the wing profile aerodynamic efficiency variation as a function of angle of attack is shown in Figure 12.7. The maximal value of the efficiency is $K_{max} = 25$ for wing profiles.

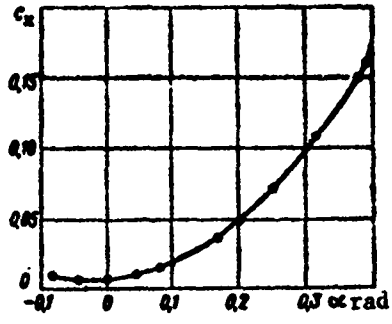

Figure 12.6. Aerodynamic coefficient c_x versus angle of attack α

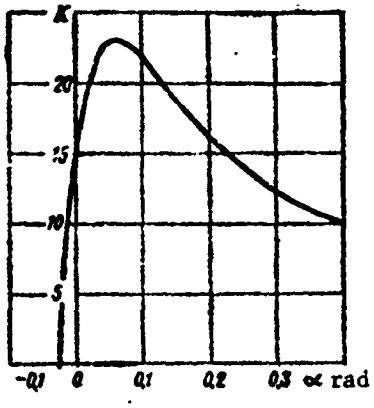

Figure 12.7. Wing profile efficiency versus angle of attack

The relations $c_y = f(c_x)$; $c_{y1} = f(c_{x1})$ are important in practice. The curve $c_y = f(c_x)$ is called type I polar (Figure 12.8); the curve $c_{y1} = f(c_{x1})$ is termed the type II polar (Figure 12.9).

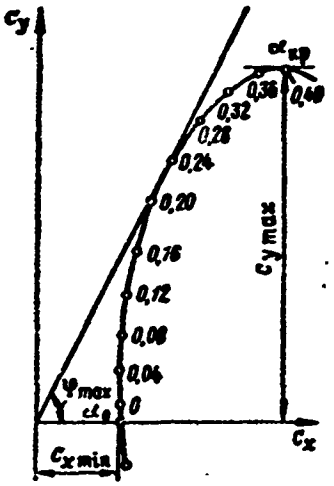

Figure 12.8. Type I polar

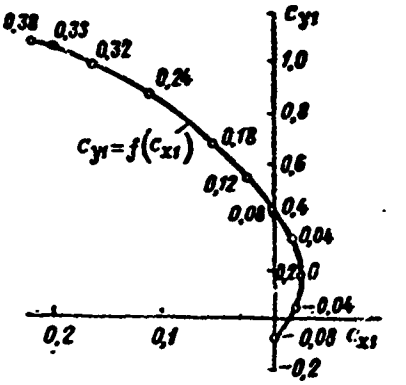

Figure 12.9. Type II polar

If in plotting the polar, the scales are taken to be the same along the c_x and c_y axes, then the vector connecting the coordinate origin with any point of the type I polar represents in magnitude and direction the resultant aerodynamic force coefficient corresponding to the given angle α. We obtain the angle of attack corresponding to the maximal efficiency K_{max} at the point of contact of the tangent drawn from the coordinate origin to the type I polar. We note that the scale along the c_x axis is usually 5 - 10 times larger than that along the c_y axis.

§12.5. Dependence of Aerodynamic Coefficients on Re, ε, and Profile Shape

For a given profile and constant M, ε (degree of turbulence), and angle of attack α the maximal lift coefficient and minimal drag coefficient depend to a considerable degree on Re. For profiles of

moderate relative thicknesses ($\bar{c}$ = 10 - 15%), $c_{y\ max}$ increases with increase of Re. For small values of Re, the coefficient $c_{y\ max}$ is determined by separation of the laminar boundary layer. With increase of Re the point of transition from laminar to turbulent boundary layer usually shifts upstream, and therefore separation of the turbulent boundary layer will take place. There is a reduction of the separation zone size and increase of the coefficient $c_{y\ max}$.

For thin profiles ($\bar{c}$ = 5 - 6%) and profiles with sharp leading edge the coefficient $c_{y\ max}$ remains nearly constant with change of Re, since flow separation for the thin profiles takes place near the profile leading edge and at low angles of attack. For thick profiles ($\bar{c}$ = 15 - 20%), the coefficient $c_{y\ max}$ decreases with increase of Re, since large pressure gradients develop on the aft portion of such profiles even at low angles of attack, leading to earlier separation of the boundary layer.

The minimal drag coefficient $c_{x\ min}$ is determined by the flat-plate friction coefficient c_x, which in turn depends on Re

$$c_x \sim \frac{1}{Re^n},$$

where n = 0.5 for the laminar boundary layer and n = 0.2 for the turbulent.

Hence we see that there is a reduction of the minimal drag coefficient $c_{x\ min}$ with increase of Re.

With increase of the initial degree of stream turbulence ε, the coefficient $c_{x\ min}$ increases, while the coefficient $c_{y\ max}$ of thin and thick profiles changes only slightly; the coefficient $c_{y\ max}$ for profiles of moderate thickness increases. This influence of initial stream turbulence on the profile aerodynamic characteristics is explained by the change of the location of the point of

transition from laminar layer to turbulent boundary layer with increase of the initial degree of turbulence ε.

The profile geometric parameters have considerable effect on the profile aerodynamic coefficients. Increase of the profile relative thickness $\bar{c}$ causes increase of the minimal drag coefficient $c_{x\ min}$. With increase of $\bar{c}$ in the range 5 - 12%, the maximal lift coefficient $c_{y\ max}$ increases, while in the range 12 - 20% it decreases.

With increase of the profile relative camber $\bar{f}$ the coefficients $c_{x\ min}$ (for profiles of moderate thickness) and c_m and the zero lift angle (in absolute magnitude) increase. Figure 12.10 shows the effect of camber $\bar{f}$ and of the abscissa $\bar{x}_f$ on the maximal lift coefficient $c_{y\ max}$ for a subsonic profile of large relative thickness.

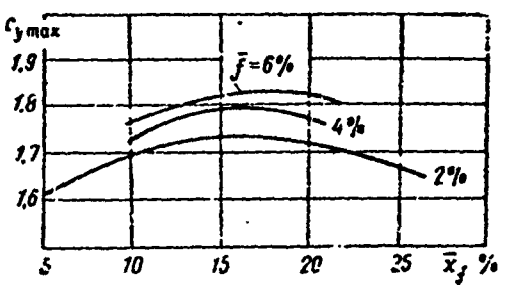

Figure 12.10. $c_{y\,max}$ as a function of $\bar{f}$ and the abscissa $\bar{x}_f$

§ 12.6. Center of Pressure. Profile Focus

The point O of intersection of the line of action of the aerodynamic force R with the wing chord is called the center of pressure (Figure 12.11). The ratio of its abscissa to the profile chord is denoted by $\bar{x}_D = x_D/b$. To find the abscissa of the aerodynamic force point of application, we must know the moment of the aerodynamic force about some point on the profile.

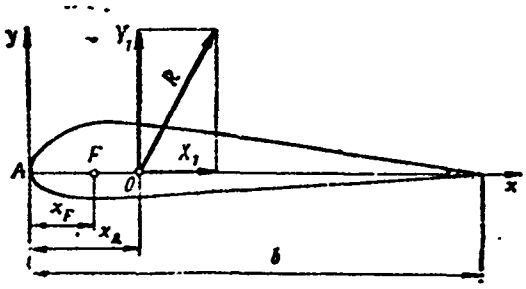

Figure 12.11. Definition of profile center-of-pressure and focus

The moment about the profile leading edge is

$$M_z = -Y_1 x_a = -(Y\cos\alpha + X\sin\alpha)x_a. \tag{12.17}$$

From (12.17) we find the abscissa of the center of pressure

$$x_a = -\frac{M_z}{Y_1}. \tag{12.18}$$

On the basis of (12.8), (12.9), (12.11) we have

$$\bar{x}_a = -\frac{c_m}{c_y\cos\alpha + c_x\sin\alpha} = -\frac{c_m}{c_{y1}}. \tag{12.19}$$

Now let us find the moment of force Y_1 about the point F on the profile (see Figure 12.11)

$$M_F = -Y_1(x_a - x_F) = M_z + Y_1 x_F.$$

Converting to coefficients and using (12.16), we find

$$c_{mF} = c_m + c_{y1}\bar{x}_F = c_{m0} + mc_{y1} + c_{y1}\bar{x}_F = \\ = c_{m0} + (m + \bar{x}_F)c_{y1}. \tag{12.20}$$

Hence we see that for $\bar{x}_F = -m$, $c_{mF} = c_{m0}$ and is independent of the angle of attack. The point having this property is called the profile focus.

The dimensionless coordinate of the profile focus determines the rate of change in moment coefficient about the profile leading edge. In fact, it follows from (12.16) and (12.20) that

$$\frac{\partial c_m}{\partial c_y} = m = -\bar{x}_F. \tag{12.21}$$

The moment coefficient relative to any other point B on the chord with the abscissa $\bar{x}$ can be found from the formula

$$c_{mB} = c_{m0} + (\bar{x} - \bar{x}_F) c_{y1}. \tag{12.22}$$

For most profiles at low Mach numbers (i.e., without account for compressibility) the coefficient m = −0.22 - −0.25; this means that $\bar{x}_F$ = −m = 0.22 - 0.25 or x_F = 0.22 - 0.25 b, i.e. the focus is located about one quarter chord from the leading edge. We note that a fixed position of the focus on the chord is possible only with a linear relation $c_m = f(c_y)$. For a symmetric wing profile the curves $c_m = f(\alpha)$ and $c_y = f(\alpha)$ pass through the coordinate origin (Figure 12.12).

Within the limits of the linear dependence, we can obtain from two triangles (see Figure 12.12)

$$-c_m = \alpha_1 \operatorname{tg} \varphi_1; \; c_y = \alpha_1 \operatorname{tg} \varphi_2.$$

Then the relative coordinate of the center of pressure

$$\bar{x}_A = -\frac{c_m}{c_y} = \frac{\operatorname{tg} \varphi_1}{\operatorname{tg} \varphi_2} = \text{const}. \tag{12.23}$$

Consequently, the position of the center of pressure remains constant for a symmetric wing profile.

For an asymmetric profile the center of pressure shifts along the chord or its extension from minus infinity to plus infinity with variation of the angle of attack. Substituting the value of c_m

from (12.16) into (12.19), we obtain

$$x_A = -\frac{c_m}{c_y} = -\frac{mc_y + c_{m0}}{c_y} = -m - \frac{c_{m0}}{c_y}. \qquad (12.24)$$

For thin and slightly cambered profiles the quantities c_y^α are nearly independent of the profile shape, while c_{m0}, conversely, depends markedly on the profile shape. We see from (12.24) that for the symmetric profiles, for which $C_{m0} = 0$, the profile center of pressure and focus coincide, i.e., they are at the same point. For asymmetric profiles at large positive and negative angles of attack α, $\bar{x}_D \to \bar{x}_F$, while for $\alpha = \alpha_0$ (which corresponds to cy = 0) $x_D = \pm \infty$, since in the absence of a lift force the aerodynamic effect on such a profile reduces to a couple.

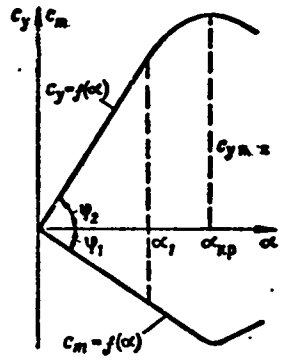

Figure 12.12. Aerodynamic coefficients c_y and c_m versus angle of attack α for symmetric profile

§12.7. Pressure Distribution Along the Profile

In strength analysis of the wing, in addition to the magnitudes of the coefficients c_x, c_y, c_m, we must know the pressure distribution along the profile. Pressure distribution diagrams for an asymmetric profile at different angles of attack α (α = −0.05 rad, 0.20 rad, 0.25 rad) are shown in Figure 12.13. These diagrams were obtained for low M, i.e., without account for compressibility of the fluid stream. The abscissa is the relative distance $\bar{x} = x/b$,

and the ordinate is the pressure coefficient $\bar{p} = \Delta p/q_\infty$, where

$$\Delta p = p_{loc} - p_\infty \text{ and } q_\infty = \rho \frac{V_\infty^2}{2}.$$

If $p_{loc} > p_\infty$, then $\bar{p} > 0$ and the pressure is called positive. If $\bar{p} < 0$ the pressure is termed negative or suction.

At angles of attack approaching α_{cr}, large pressure gradients develop on the wing surface and cause separation of the boundary layer.

A schematic of flow past a profile at the critical angle of attack and separation of the boundary layer from the upper profile surface, and also pressure diagrams for flow with and without separation of an incompressible fluid, are shown in Figure 12.14. Figure 12.15 shows the vector diagrams of the pressure distribution for different angles of attack. The relative pressure difference $\bar{p}$ is shown in the form of arrows — vectors plotted along the normal to the profile surface. For clarity the suction region is indicated by a "minus" sign and the positive pressure region by a "plus" sign, with suction shown by arrows directed along the outward normal and positive pressure by arrows directed along the inward normal. We see from the figure that at the angle $\alpha \approx \alpha_0$ there is on the upper surface of the profile near the leading edge a positive pressure, which then transitions into a suction. The reverse phenomenon occurs on the lower surface: near the leading edge there is suction, which transitions into a weak positive pressure.

At the point where the stream splits at the leading edge, where $V_{loc} = 0$, $\bar{p} = 1$ (for a compressible fluid the pressure difference is somewhat larger than $\rho \frac{V_\infty^2}{2}$ and $\bar{p} > 1$). At negative angles of attack this point lies on the upper surface of the profile, while for $\alpha > 0$

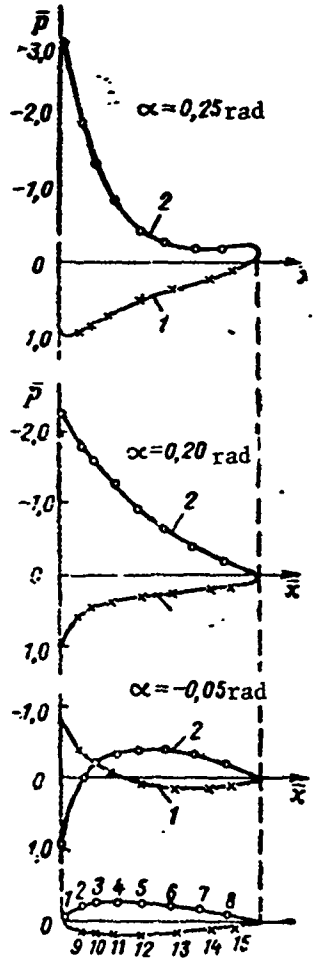

Figure 12.13. Pressure distribution diagrams for asymmetric profile at different angles of attack:

1 — lower surface; 2 — upper surface

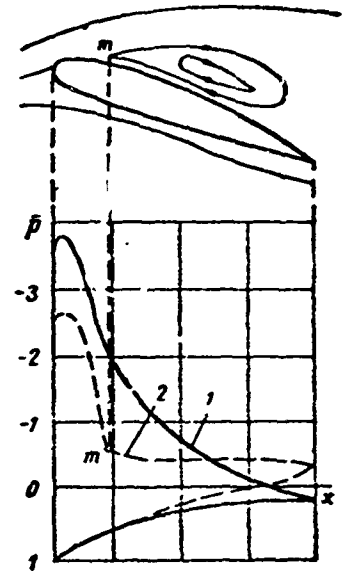

Figure 12.14. Flow over profile at stalling angle of attack:

1 — flow without separation; 2 — flow with separation (point m is point of boundary layer separation)

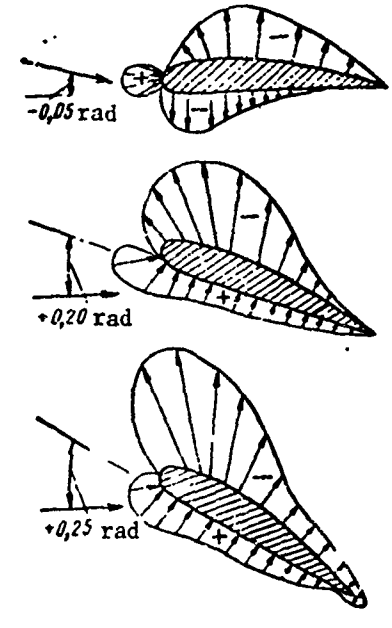

Figure 12.15. Vector diagrams of differential pressure distribution

it shifts to the lower side. At angles of attack greater than 0 - 0.5 rad, negative pressure extends over nearly the entire upper surface, and positive pressure over the entire lower surface.

At angles of attack near the stall, the suction on the upper surface reaches very large values ($\bar{p} = -2$ to -3 or less), while the positive pressure on the lower surface is characterized as before by a value $\bar{p} \leqslant 1$.

This implies that the wing lift force is created primarily by suction on the upper surface and to a lesser degree by positive pressure on the lower surface.

The minimal pressure point on the subsonic profiles which have been used in the past was located on the upper surface near the leading edge. This favors early transition of the laminar boundary layer into a turbulent layer, and at large pre-stall angles of attack α for profiles with a thin "nose" leads to flow separation.

The pressure diagrams make it possible to plot the distribution along the profile chord of the loading resulting from the pressure forces. In this case the vectors $\vec{p}$ are projected on the perpendicular to the chord, and these projections are laid off upward or downward relative to the chord depending on the direction of the vector $\vec{p}$. For example, the projections of the suction vectors on the upper surface and the positive pressure vectors on the lower surface are plotted above and below the chord, respectively.

Summation of the loads distributed along the chord yields the magnitudes of the aerodynamic force components X and Y and their coefficients c_x and c_y.

REVIEW QUESTIONS

1. Define wing profile. Write down the wing profile aerodynamic coefficients.

2. Define profile center-of-pressure and focus.

3. How is the optimal angle of attack found from the profile polar?

4. How does the lift coefficient c_y depend on the angle of attack for symmetric and asymmetric profiles?

5. Analyze the diagrams of the pressure distribution over the profile for different angles of attack.

PROBLEMS

1. Find the magnitude of the average circulation around the wing profile of an airplane with takeoff weight G = 588,000 N, flying at H = 8500 m and V = 828 km/hr. The wingspan l = 32 m.

Answer: $\Gamma_{av} = 161\ m^2/sec.$

2. The drag coefficient c_x of a new airplane was 0.019. During operation and after repairs to the skin the drag coefficient increased to 0.021. Find how much the drag force increased in flight at H = 6000 m and V = 648 km/hr. The airplane wing area $S = 140\ m^2$.

Answer: $\Delta X = 3020$ N.

3. During flight of an airplane with wing angle of attack $\alpha = 0.07$ rad the lift coefficient was 0.4. What is the zero lift angle if $\partial c_y/\partial\alpha = 5.3$.

Solution. According to (12.16)

$$c_y = c_y^{\alpha}(\alpha - \alpha_0),$$

hence

$$\alpha_0 = -\frac{c_y}{c_y^{\alpha}} + \alpha = -\frac{0,4}{5,3} + 0,07 = -0,0054 \text{ rad}.$$

CHAPTER XIII

AERODYNAMIC COEFFICIENTS OF PROFILE IN SUBSONIC FLOW

§13.1. Basic Equation of Gas Motion and Its Linearization by the Small Perturbation Method

To obtain the equation of motion of a barotropic gas and analyze the aerodynamic properties of wings at subsonic speeds with account for compressibility in steady plane-parallel flow, we write the two Euler Equations (5.3) and the continuity Equation (2.6') in the form

$$\left.\begin{aligned} -\frac{\partial p}{\partial x}&=\varrho\left(V_x\frac{\partial V_x}{\partial x}+V_y\frac{\partial V_x}{\partial y}\right);\\ -\frac{\partial p}{\partial y}&=\varrho\left(V_x\frac{\partial V_y}{\partial x}+V_y\frac{\partial V_y}{\partial y}\right);\end{aligned}\right\} \tag{13.1}$$

$$\frac{\partial(\varrho V_x)}{\partial x}+\frac{\partial(\varrho V_y)}{\partial y}=0. \tag{13.2}$$

Equation (13.2) after differentiation takes the form

$$\varrho\left(\frac{\partial V_x}{\partial x}+\frac{\partial V_y}{\partial y}\right)+V_x\frac{\partial\varrho}{\partial x}+V_y\frac{\partial\varrho}{\partial y}=0. \tag{13.3}$$

In this case in which p = p (ρ) and, conversely, ρ = ρ (p), the partial derivatives $\frac{\partial \rho}{\partial x}$ and $\frac{\partial \rho}{\partial y}$ in (13.3) with account for the formula $a=\sqrt{\frac{dp}{d\rho}}=\sqrt{\frac{\partial p}{\partial \rho}}$ for the speed of sound will have the form

$$\frac{\partial \rho}{\partial x}=\frac{\partial \rho}{\partial p}\frac{\partial p}{\partial x}=\frac{1}{a^2}\frac{\partial p}{\partial x};\quad \frac{\partial \rho}{\partial y}=\frac{\partial \rho}{\partial p}\frac{\partial p}{\partial y}=\frac{1}{a^2}\frac{\partial p}{\partial y}.$$

Substituting these expressions into (13.3), we obtain

$$\rho\left(\frac{\partial V_x}{\partial x}+\frac{\partial V_y}{\partial y}\right)+\frac{V_x}{a^2}\frac{\partial p}{\partial x}+\frac{V_y}{a^2}\frac{\partial p}{\partial y}=0,$$

or, with account for (13.1),

$$\rho\left(\frac{\partial V_x}{\partial x}+\frac{\partial V_y}{\partial y}\right)-\rho\left(\frac{V_x^2}{a^2}\frac{\partial V_x}{\partial x}+\frac{V_yV_x}{a^2}\frac{\partial V_x}{\partial y}\right)-$$
$$-\rho\left(\frac{V_yV_x}{a^2}\frac{\partial V_y}{\partial x}+\frac{V_y^2}{a^2}\frac{\partial V_y}{\partial y}\right)=0.$$

After transformation we have

$$\left(1-\frac{V_x^2}{a^2}\right)\frac{\partial V_x}{\partial x}+\left(1-\frac{V_y^2}{a^2}\right)\frac{\partial V_y}{\partial y}-\frac{V_xV_y}{a^2}\left(\frac{\partial V_x}{\partial y}+\frac{\partial V_y}{\partial x}\right)=0. \quad (13.4)$$

If we examine irrotational motion, the velocity components are expressed in terms of the velocity potential

$$V_x=\frac{\partial \varphi}{\partial x};\quad V_y=\frac{\partial \varphi}{\partial y};$$

$$\frac{\partial V_x}{\partial x}=\frac{\partial^2 \varphi}{\partial x^2};\quad \frac{\partial V_y}{\partial y}=\frac{\partial^2 \varphi}{\partial y^2}.$$

With account for these expressions, (13.4) takes the form

$$(V_x^2-a^2)\frac{\partial^2 \varphi}{\partial x^2}+(V_y^2-a^2)\frac{\partial^2 \varphi}{\partial y^2}+2V_xV_y\frac{\partial^2 \varphi}{\partial x\,\partial y}=0. \quad (13.5)$$

This equality is called the basic equation of motion of a compressible fluid in plane-parallel flow. It can be used for various theoretical studies of subsonic and supersonic gas flow past wings.

Equation (13.5) is a nonlinear partial differential equation, since the speed of sound, expressed in terms of the velocity components, depends on $\frac{\partial\phi}{\partial x}$ and $\frac{\partial\phi}{\partial y}$. It is difficult to find the general solution for such equations; therefore we resort to their linearization, i.e., we reduce the equations to a linear form by one method or another.

Exact solutions have been obtained only for a few simple flows. The most successful solution is that of Chaplygin, who converted in (13.5) to new variables (velocity hodograph variables) and after the relevant transformations obtained a linear equation. Several exact solutions for jet flow problems are obtained with the aid of the Chaplygin transformation. S. A. Khristianovich applied the Chaplygin method with success to wing profiles and solved the problem with account for the influence of air compressibility on the pressure distribution over the profile. We shall not discuss these methods further.

Let us turn to the approximate linearization of (13.5). In the case of flow about a thin profile at small angle of attack, the changes or perturbations of the gas parameters (velocity, density, pressure) will be small in comparison with the freestream parameters. Therefore in the equation of motion we can neglect terms containing products of the perturbations.

If we direct the flow along the Ox axis, for our case the velocity components, velocity, pressure, and density are expressed by the formulas

$$\left.\begin{aligned} V_x &= V_\infty + V'_x;\\ V_y &= V'_y;\\ V &= \sqrt{V_x^2 + V_y^2} \approx V_\infty + V'_x;\\ p &= p_\infty + p';\\ \rho &= \rho_\infty + \rho'. \end{aligned}\right\} \qquad (13.6)$$

where V'_x, V'_y, p', ρ' — are small perturbations at an arbitrary point caused by the flow past the profile.

Neglecting terms containing products of the perturbations, we find

$$\rho V_x = (\rho_\infty + \rho')(V_\infty + V'_x) \approx \rho_\infty V_\infty + \rho_\infty V'_x + \rho' V_\infty;$$
$$\rho V_y = (\rho_\infty + \rho') V'_y \approx \rho_\infty V'_y.$$

Substituting these values into the continuity equation (13.2), we obtain

$$V_\infty \frac{\partial \rho'}{\partial x} + \rho_\infty \frac{\partial V'_x}{\partial x} + \rho_\infty \frac{\partial V'_y}{\partial y} = 0. \tag{13.7}$$

This equation is the <u>linearized continuity equation</u>.

For isentropic flow we have

$$1 + \frac{p'}{p_\infty} = \left(1 + \frac{\rho'}{\rho_\infty}\right)^k.$$

Expanding into a series and neglecting small quantities of second order, we find $p' = a^2_\infty \rho$; hence $\rho' \approx \frac{p'}{a^2_\infty}$. Differentiating ρ' with respect to x and substituting $\partial\rho'/\partial x$ into (13.7), we obtain the continuity equation in a different form

$$\frac{V_\infty}{\rho_\infty a^2_\infty} \frac{\partial p'}{\partial x} + \frac{\partial V'_x}{\partial x} + \frac{\partial V'_y}{\partial y} = 0. \tag{13.8}$$

Now, linearizing the Bernoulli Equation (5.5)

$$\frac{dp}{\rho} + d\left(\frac{V^2}{2}\right) = 0.$$

and substituting herein the values of ρ and V from (13.6), at an arbitrarily chosen point A of the thin profile (Figure 13.1) we obtain

$$dp = -(\rho_\infty + \rho') d \frac{(V_\infty + V'_x)^2}{2}.$$

Neglecting small quantities of second order, we have

$$dp=-\varrho_\infty V_\infty dV'_x.$$

Integrating, we obtain

$$p=-\varrho_\infty V_\infty V'_x+C.$$

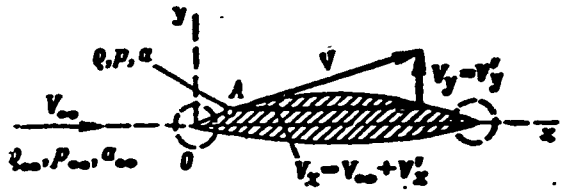

Figure 13.1. Thin profile in gas flow

Considering that far from the profile $V_x' = C$, we find the value of the constant of integration

$$C=p_\infty$$

Consequently

$$p=p_\infty-\varrho_\infty V_\infty V'_x. \tag{13.9}$$

With account for (13.6) and (13.9) we have

$$p'=-\varrho_\infty V_\infty V'_x. \tag{13.9'}$$

Equations (13.9) and (13.9') are called the linearized Bernoulli equations.

Substituting the value of p' into (13.8), we obtain

$$-\frac{V_\infty^2}{a_\infty^2}\frac{\partial V'_x}{\partial x}+\frac{\partial V'_x}{\partial x}+\frac{\partial V'_y}{\partial y}=0.$$

Considering that $\frac{V_\infty}{a_\infty} = M_\infty$, we have

$$(1-M_\infty^2)\frac{\partial V'_x}{\partial x}+\frac{\partial V'_y}{\partial y}=0.$$

Expressing the perturbation velocity components V_x' and V_y' for irrotational flow in terms of the velocity potential and substituting

their values into the last equation, we obtain the linearized equation or the velocity potential of the perturbed gas motion.

$$(1-M_\infty^2)\frac{\partial^2\varphi'}{\partial x^2}+\frac{\partial^2\varphi'}{\partial y^2}=0. \tag{13.10}$$

In contrast with (13.5), Equation (13.10) is a linear differential equation and is used to determine approximately the influence of compressibility on the aerodynamics of a profile in gas flow. This technique is called the linearization method, and the flow described by (13.10) is called a linearized flow.

§13.2. Connection between Gas Flow and Subsonic Incompressible Fluid Flow About a Thin Profile

Assume a thin profile (see Figure 13.1) whose form is given by the equation y = F(x) is in a gas flow. Let us suppose that the gas flow is irrotational and is defined by the velocity potential

$$\varphi=Vx+\varphi'(x, y),$$

where ϕ'' (x, y) — is the induced (perturbed) velocity potential. Equation (13.10) holds for a thin profile.

According to (2.1) the equation of a streamline for plane flow has the form

$$\frac{dx}{V_x}=\frac{dy}{V_y}. \tag{13.11}$$

Since the unseparated flow boundary condition is satisfied at the profile surface,

$$\left(\frac{V_y}{V_x}\right)_{\text{профиля}}=\left(\frac{dy}{dx}\right)_{\text{контура}}.$$

The boundary condition with account for (13.6) at points of the profile contour can be written as

$$V_y = V'_y = (V_\infty + V'_x)\left(\frac{dy}{dx}\right).$$

If we neglect the small quantity $V'_x \left(\frac{dy}{dx}\right)$ contour, with the aid of the perturbed flow velocity potential this boundary condition takes the form

$$\frac{\partial \varphi'}{\partial y} = V_\infty \frac{dy}{dx}. \qquad (13.12)$$

At an infinitely distant point

$$\varphi' \to 0 \quad \text{as} \quad (x^2 + y^2) \to \infty.$$

Equation (13.10) together with the boundary condition (13.12) defines the function ϕ' uniquely.

Equation (13.10) can be transformed into the Laplace equation if we introduce the new variables x_1 and y_1, connected with x and y by the relations

$$x = x_1;\ y_1 = y\sqrt{1 - M_\infty^2}.$$

In fact

$$\frac{\partial^2 \varphi'}{\partial x^2} = \frac{\partial^2 \varphi'}{\partial x_1^2};\ \frac{\partial^2 \varphi'}{\partial y^2} = \frac{\partial^2 \varphi'}{\partial y_1^2}(1 - M_\infty^2).$$

If in (13.10) we substitute in place of $\frac{\partial^2 \phi'}{\partial x^2}$ and $\frac{\partial^2 \phi'}{\partial y^2}$ their values, after cancelling out $(1 - M_\infty^2)$ we obtain the Laplace equation in the form

$$\frac{\partial^2 \varphi'}{\partial x_1^2} + \frac{\partial^2 \varphi'}{\partial y_1^2} = 0. \qquad (13.13)$$

The potential $\phi'(x, y)$, satisfying (13.13) corresponds to some incompressible fluid flow in the $x_1 O y_1$ coordinate plane. It is obvious that in this case the boundary condition (13.12) is violated

for the function $\varphi'=\varphi'\left(x, y\sqrt{1-M_\infty^2}\right)$. This means that the incompressible fluid flow obtained by such a change of variables flows past a profile of different form than the specified profile. It can be shown that this fictitious profile has a thickness which is $\frac{1}{\sqrt{1-M_\infty^2}}$ times greater than that of the original profile and is aligned in the flow at an angle of attack which is larger by a factor of $\frac{1}{\sqrt{1-M_\infty^2}}$. (1)

In order to restore the boundary conditions (13.12), i.e., to obtain the flow pattern about the original profile in the incompressible stream, we introduce the new velocity potential φ_1', connected with ϕ' by the relation

$$\varphi_1'=\varphi'\gamma,$$

where γ — is a constant.

The function ϕ_1' satisfies the Laplace equation, which can be easily verified by direct substitution into (13.13).

Let us find γ from the incompressible fluid flow condition past the original profile. The boundary condition in the gas flow at points of the profile contour has the form

$$\frac{\partial\varphi'}{\partial y}=V_\infty\frac{dy}{dx}.$$

The corresponding boundary condition in the incompressible fluid flow at points of the profile contour will be

---

Footnote (1) appears on page 71.

$$\frac{\partial \varphi_1'}{\partial y_1} = V_\infty \frac{dy_1}{dx_1}.$$

If we assume the contours to be the same in both flows, then at points of the contours $\frac{dy}{dx} = \frac{dy_1}{dx_1}$, and consequently the condition

$$\frac{\partial \varphi'}{\partial y} = \frac{\partial \varphi_1'}{\partial y_1}.$$

must be satisfied. Then

$$\frac{\partial \varphi'}{\partial y} = \frac{\partial \varphi_1'}{\partial y_1} = \gamma \frac{\partial \varphi'}{\partial y} \frac{dy}{dy_1}.$$

Hence we have

$$\gamma = \frac{dy_1}{dy} = \sqrt{1 - M_\infty^2}.$$

Thus, the incompressible stream flowing past the same contour as the gas stream must have the potential

$$\varphi_1' = \varphi' \sqrt{1 - M_\infty^2}.$$

This implies that the longitudinal components of the induced (perturbed) velocities in the incompressible fluid stream will be greater than in the gas stream

$$V'_{x\,\text{нс}} = V'_{x\,\text{сж}} \sqrt{1 - M_\infty^2}.$$

We have for the transverse components of the induced (perturbed) velocities

$$V'_{y\,\text{нс}} = \frac{\partial \varphi_1'}{\partial y_1} = \frac{\partial \varphi_1'}{\partial y} \frac{\partial y}{\partial y_1} = \frac{\partial \varphi'}{\partial y} \sqrt{1 - M_\infty^2} \frac{1}{\sqrt{1 - M_\infty^2}} = V'_{y\,\text{сж}}.$$

We shall express the pressure at point A in terms of M_∞, for which we use the Bernoulli equation in the form

$$\frac{a^2}{k-1} + \frac{V^2}{2} = \frac{a_0^2}{k-1}.$$

where a — is the sound speed at the considered point;

a_0 — is the sound speed in the gas at rest.

Substituting into the Bernoulli equation in place of V^2 its value from (13.6) and neglecting V'^2_x and V'^2_y as small quantities of second order, we obtain

$$a^2=a_0^2-\frac{k-1}{2}V_\infty^2-(k-1)V_\infty V'_x=a_\infty^2-(k-1)V_\infty V'_x.$$

Hence

$$\frac{a^2}{a_\infty^2}=1-(k-1)M_\infty^2\frac{V'_x}{V_\infty}. \qquad (13.14)$$

For an adiabatic process we can write

$$\frac{p}{p_\infty}=\left(\frac{a^2}{a_\infty^2}\right)^{\frac{k}{k-1}}.$$

Using the connection obtained between the pressure and the sound propagation velocity, on the basis of (13.14) we have

$$\frac{p}{p_\infty}=\left[1-(k-1)M_\infty^2\frac{V'_x}{V_\infty}\right]^{\frac{k}{k-1}}. \qquad (13.15)$$

Expanding the right side into a binomial series and neglecting small quantities of second order, we obtain

$$\frac{p}{p_\infty}=1-kM_\infty^2\frac{V'_x}{V_\infty}.$$

Hence

$$p=p_\infty-p_\infty kM_\infty^2\frac{V'_x}{V_\infty}.$$

The pressure coefficient at point A is

$$\bar{p}=\frac{p-p_\infty}{\frac{\varrho_\infty V_\infty^2}{2}}=-2\frac{kp_\infty}{\varrho_\infty}\frac{M_\infty^2}{V_\infty^2}\frac{V'_x}{V_\infty}=-2\frac{V'_x}{V_\infty}. \qquad (13.16)$$

If we use the relation expressing the connection between $V'_{x\ incom}$ and $V'_{x\ com}$, then on the basis of (13.16) we can obtain the connection between the pressure coefficients at corresponding points of the flows

$$\bar{p}_{сж}=\frac{\bar{p}_{нс}}{\sqrt{1-M_\infty^2}}. \qquad (13.17)$$

This formula expresses the familiar Prandtl-Glauert rule: the local pressure coefficient for a thin body in subsonic compressible flow with Mach number M_∞ is $\frac{1}{\sqrt{1-M_\infty^2}}$ times greater than the corresponding pressure coefficient for the same body in incompressible flow. This conclusion does not extend to those flow regions near the thin profile where the perturbation velocities cannot be considered small. Such regions include those near the stagnation points (these regions are circled in Figure 13.1). Specifically, for sufficiently small M_∞ the pressure coefficients at the stagnation point are connected with one another by the following relation to within small quantities of second order

$$\bar{p}_{сж.кр}=\bar{p}_{нс.кр}\left(1+\frac{M_\infty^2}{4}\right).$$

Let us derive the relation connecting the densities at point A and at an infinite distance from the profile. It is known that

$$\frac{\rho}{\rho_\infty}=\left(\frac{p}{p_\infty}\right)^{\frac{1}{k}}=\left(\frac{a^2}{a_\infty^2}\right)^{\frac{1}{k-1}}. \qquad (13.18)$$

Substituting herein the value of $\frac{a^2}{a_\infty^2}$ from (13.14), we expand the right side into a binomial series. Neglecting small quantities of

second order, we obtain

$$\frac{\rho}{\rho_\infty}=(1-M_\infty^2)\frac{V_x'}{V_\infty}. \tag{13.19}$$

§13.3. Influence of Compressibility on Profile Aerodynamic Characteristics

We shall use the previously obtained expressions for c_y and c_m (see Chapter XII)

$$c_y=\int_0^1(\bar{p}_u-\bar{p}_l)\,d\bar{x},\quad c_m=\int_0^1(\bar{p}_u-\bar{p}_l)\,\bar{x}\,d\bar{x}.$$

We assume that these expressions for c_y and c_m apply to the case of compressible fluid flow about a profile. Then, substituting in place of $\bar{p}_u$ and $\bar{p}_l$ their values from (13.17), we obtain

$$c_{y\,сж}=\frac{c_{y\,нс}}{\sqrt{1-M_\infty^2}}; \tag{13.20}$$

$$c_{m\,сж}=\frac{c_{m\,нс}}{\sqrt{1-M_\infty^2}}. \tag{13.21}$$

If we consider that in accordance with (12.21) the profile focus location is defined by the formula

$$\bar{x}_F=-\frac{dc_m}{dc_y},$$

then on the basis of (13.20) and (13.21) we obtain

$$\bar{x}_{F\,сж}=\bar{x}_{F\,нс}. \tag{13.22}$$

Thus, the profile lift and aerodynamic moment coefficients increase as a result of compressibility, while compressibility has no effect on the location of the aerodynamic center.

Formulas (13.20) and (13.21) make it possible to scale the values of the coefficients c_y and c_m obtained (by calculation or experiment) for flow of an incompressible medium past a thin profile to high subsonic gas flow past the same profile. These formulas are not suitable in the case of gas flow past a profile of considerable thickness, nor in the case in which M_∞ is close to one (for $M_\infty = 1$, $c_{y\ com}$ approaches infinity). The values of c_y as a function of M_∞, calculated using (13.20) and measured experimentally, are shown in Figure 13.2.

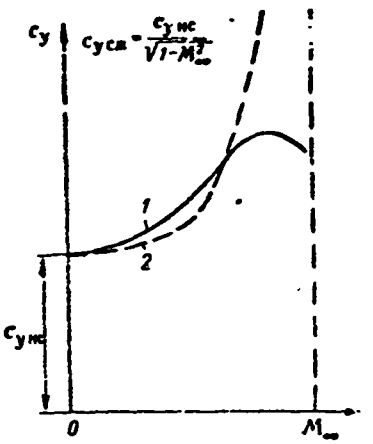

Figure 13.2. Comparison of actual values of c_y and those calculated using linear theory in the subsonic region: 1 — experimental values; 2 — theoretical values

The drag coefficient c_x for thin profiles is determined primarily by the friction forces. Therefore compressibility has a considerable influence on its magnitude, since it affects the gas flow conditions in the boundary layer.

Let us first examine the boundary layer on a flat plate, restricting ourselves to a purely qualitative evaluation of the effect of compressibility. At the plate surface, where the velocity vanishes, the gas temperature reaches the stagnation temperature T_0. Through the thickness of the boundary layer the gas temperature will vary in accordance with the velocity variation. The approximate temperature variation in laminar and turbulent boundary layers is shown in Figure 13.3. We can speak of some average temperature T in the boundary layer, which is greater than the temperature T_δ at the edge of the layer. Figure 13.4 shows the relation $\frac{T_{av}}{T_\delta} = f(M_\infty)$,

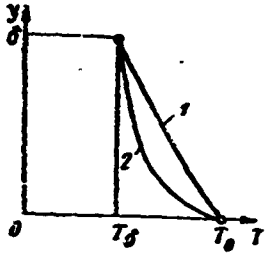

Figure 13.3. Temperature variation in boundary layer: 1 — laminar flow; 2 — turbulent flow

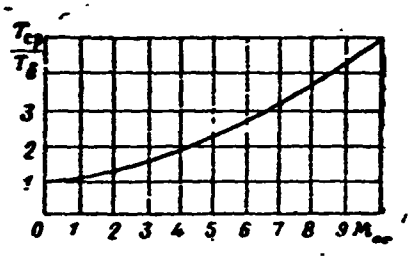

Figure 13.4. Temperature in turbulent boundary layer versus M_∞

calculated for a turbulent boundary layer with variation of the velocity across the boundary layer section following (11.16) with n = 7.

As a result of the temperature increase, the gas density in the boundary layer decreases, leading to increase of the boundary layer thickness. Figure 13.5 shows the boundary layer thickness as a function of M_∞. On the other hand, the gas viscosity increases as a result of the temperature increase in the boundary layer. The boundary layer thickness increase is of greater importance than the viscosity increase. Therefore, calculation shows that the friction coefficient of a flat plate in gas flow is less than in incompressible fluid flow.

The effect of M_∞ on the value of c_x is shown in Figure 13.6. The influence of compressibility on c_x can be evaluated using the G. F. Burago approximate formula

$$c_{x\,сж} = \frac{c_{x\,нс}}{\left(1 + \frac{1}{15} M_\infty^2\right)^{\frac{2}{3}}}.$$

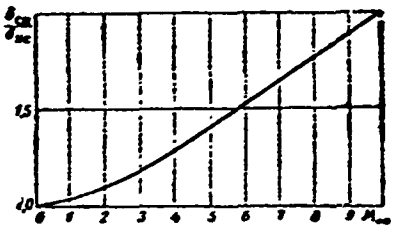

Figure 13.5. Turbulent boundary layer thickness versus M_∞

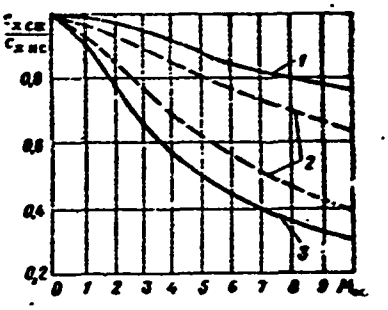

Figure 13.6. Flat plate drag coefficient versus M_∞:
1 — $\bar{x}_t = 1$; 2 — $0 < \bar{x}_t < 1$;
3 — $\bar{x}_t = 0$

In subsonic flow, when heating is not significant, the variation of c_x is evaluated quite accurately by the K. K. Fedyayevskiy formula

$$c_{x\,сж} = \frac{c_{x\,нс}}{\sqrt{1 + 0{,}2M_\infty^2}}.$$

In addition to friction drag, thick profiles experience pressure drag. Experiment shows that the pressure drag rises quite rapidly with increase of M_∞. This is a result of increase of the pressure gradient

$$\frac{d\bar{p}_{сж}}{dx} = \frac{d\bar{p}}{dx}\frac{1}{\sqrt{1 - M_\infty^2}}.$$

In the convergent region, where the boundary layer is laminar, increase of the negative pressure gradients leads to decrease of the boundary layer thickness. In the divergent region, where the boundary layer is usually turbulent, increase of the positive pressure gradients leads to thickening of the boundary layer. This implies that the degree of influence of compressibility on the profile viscous drag depends on the length x_t of the laminar portion of the boundary layer.

The profile drag coefficient depends on several basic factors: angle of attack, M_∞, Re, and relative profile thickness $\bar{c}$ (Figures 13.6, 13.7). For small relative profile thickness ($0 < \bar{c} < 0.05$) the pressure drag is small in comparison with the overall profile drag; therefore the drag coefficient decreases with increase of M_∞ (see Figure 13.6). For profiles of moderate thickness ($0.05 < \bar{c} < 0.12$) the drag first decreases and then for $M_\infty \approx 0.05 - 0.5$ begins to increase as a result of the pressure drag. Finally, the drag coefficient of thick profiles increases over the entire subsonic M_∞ range (see Figure 13.7).

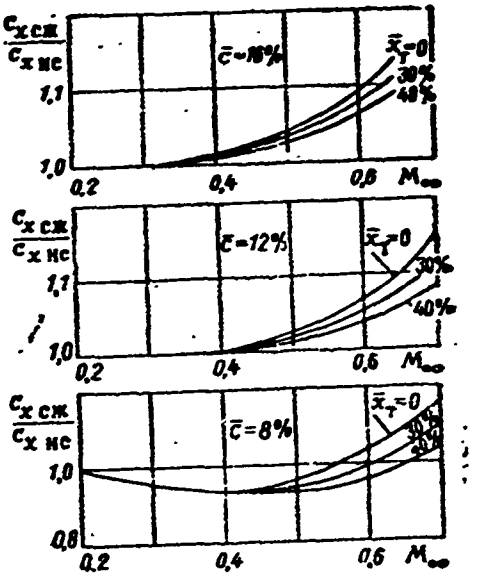

Figure 13.7. Effect of air compressibility on drag coefficient for several profiles of different thickness

REVIEW QUESTIONS

1. How do the coefficients c_x and c_y change with increase of M_∞? Describe their dependence on angle of attack for different M_∞.

2. How does compressibility affect the wing profile polar?

3. How does compressibility affect the position of the boundary layer separation point?

4. How does the pressure distribution along the profile contour change with increase of M_∞?

PROBLEMS

1. The profile lift coefficient $c_{y\ incom}$ for $M_\infty = 0$ is 0.3. Find the lift coefficient $c_{y\ com}$ for $M_\infty = 0.8$.

Solution. According to (13.20)

$$c_{y\,com} = \frac{c_{y\,inc}}{\sqrt{1-M_\infty^2}} = \frac{0{,}3}{\sqrt{1-0{,}8^2}} = 0{,}5.$$

Answer: $c_{y\ com} = 0.5$.

2. By what percent does the value of the lift coefficient c_y increase in flight at H = 500 m and V = 652 km/hr if compressibility is considered?

Answer: by 17.8%.

3. The lift force Y of a wing segment of infinite span and area S = 10 m^2 at $\alpha = 0.0434$ rad and flight speed V = 880 km/hr at sea level is 17,760 N. For the profile $\partial c_y/\partial\alpha = 5.40$. Find the zero lift angle α_0 and lift coefficient c_y for flight speed V = 720 km/hr and angle of attack $\alpha = 0.069$ rad.

Answer: $\alpha_0 = 0.0209$ rad; $c_y = 0.228$.

FOOTNOTES

Footnote (1) on page 61: In this connection, to obtain the aerodynamic characteristics of the profile at high subcritical values of M_∞ an experiment can be conducted under conditions of incompressible fluid flow past the thickened profile at the higher angle of attack.

CHAPTER XIV

WING PROFILE IN TRANSONIC FLOW

§14.1. Critical Mach Number Concept. Shock Waves

A wing profile in a gas stream displaces by its volume part of the gas and constricts the stream filaments flowing around it. The gas velocity first increases along the profile, reaching the maximal value V_{max} at the most constricted stream filament section, and then decreases.

In the case of adiabatic gas flow, the sound speed a in the gas decreases with increase of the gas velocity V. At the profile point where $V = V_{max}$, $a = a_{min}$. Consequently, the maximal value of the local Mach number $M = M_{max} > M_\infty$ is reached at the point where the stream filament section is minimal ($\omega = \omega_{min}$) (Figure 14.1). This point also corresponds to the minimal pressure and minimal value of the pressure coefficient ($\bar{p} = \bar{p}_{min}$). With increase of the gas velocity

$$M_{max} = \frac{V_{max}}{a_{min}} \to 1.$$

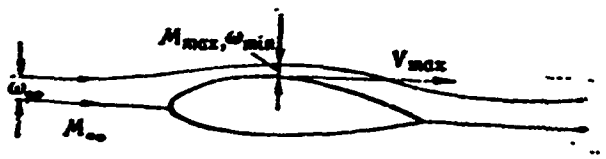

Figure 14.1. Wing profile in subsonic flow

At a definite value of V_∞ for a given profile the local gas velocity V at the profile surface becomes equal to the local speed of sound, in spite of the fact that the freestream velocity is still subsonic.

The value of M_∞ for which the local flow velocity at the profile surface equals the local speed of sound (the local Mach number equals one) is termed the critical Mach number and is denoted by M_{cr}. This number is always less than or equal to one, and depends on the profile shape and its angle of attack. The Mach number $M_\infty = M_{cr}$ is the upper limit of the values of M_∞ for which the relations obtained for completely subsonic flow are valid.

With further increase of V_∞, when $1 > M_\infty > M_{cr}$, at the surface of a profile in a subsonic gas stream there are formed regions of supersonic velocities; in the latter the gas parameter variation no longer obeys the subsonic flow laws.

The formulas of the preceding chapter which account for the influence of air compressibility on the aerodynamic characteristics of thin profiles contain the quantity $\sqrt{1-M_\infty^2}$, which vanishes for $M_\infty = 1$. These formulas are not valid for $M_\infty \to 1$ since the aerodynamic coefficients, which are inversely proportional to $\sqrt{1-M_\infty^2}$, increase without limit in this case, while this does not occur in reality.

The supersonic flow regions are usually closed by compression shocks (shock waves). The appearance of compression shocks causes additional mechanical energy losses in the flow around the body. This phenomenon is usually termed shock stall. In many cases the shocks also cause separation of the boundary layer.

At the instant of stall onset, $M_\infty = M_{cr}$ and sonic flow velocity appears on the profile at that point of its surface at which the pressure is minimal. S. A. Khristianovich[1] showed that M_{cr} for any profile is a function only of the magnitude of the minimal pressure coefficient, defined from the pressure distribution patterns along the contour for low incompressible fluid flow velocities past the profile (Figure 14.2). The relationships between M_{cr} and $\bar{p}_{min\ incom}$ for air, obtained using the Khristianovich and Burago methods, are shown as curves in Figure 14.3.

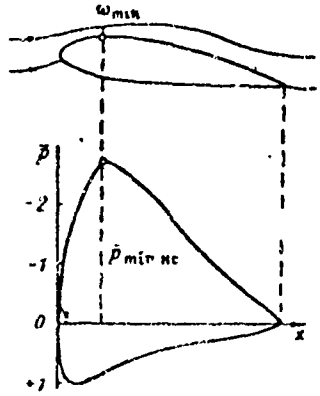

Figure 14.2. Variation of pressure coefficient $\bar{p}$ along profile contour in incompressible flow

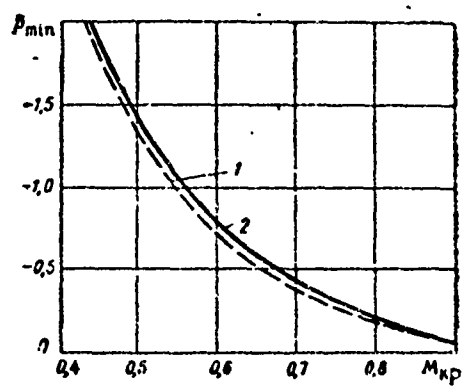

Figure 14.3. Minimal pressure coefficient versus M_{cr}:

1 — Khristianovich method: 2 — Burago method

Footnote (1) appears on page 86.

Thus for $M > M_{cr}$ there are on the wetted surface both subsonic and supersonic flow zones. The subsonic zones do not disappear immediately upon reaching supersonic flight speeds. Depending on the profile shape, this occurs at M = 1.2 - 1.4 or more. The flow regime in which there are both subsonic and supersonic zones in the flow around the profile is termed transonic. This regime includes Mach numbers in the range $M_{cr} < M < 1$ and in the low supersonic range.

§14.2. Effect of Angle of Attack and Profile Shape on M_{cr} and Flow Structure Around a Profile

Figure 14.4 shows the theoretical values of M_{cr} for a family of symmetric profiles as a function of relative thickness and angle of attack α. With increase of the angle of attack α, the constriction of the elementary stream filaments by the profile increases and consequently M_{cr} decreases. For an infinitely thin flat plate (c = 0) at zero angle of attack (α = 0), $M_{cr} = 1$; for all angles of attack α > 0, $M_{cr} = 0$. This is explained by the fact that near the leading edge of an infinitely thin flat plate there arise large local flow velocities and the local Mach numbers M > 1.

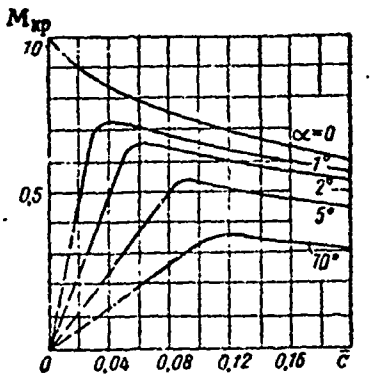

Figure 14.4. Effect of profile relative thickness and angle of attack on M_{cr}

With increase of the profile relative thickness, the local Mach numbers near the now rounded and thickened leading edge first

decrease and then increase, since further increase of the relative thickness, beginning with some value of $\bar{c}$, leads to constriction of the gas stream filaments downstream of the profile leading edge. Correspondingly, M_{cr} first increases and then decreases.

For an asymmetric profile at $\alpha = 0$ the local maximal velocities will be lower and the values of $\bar{p}_{min\ incom}$ will be larger, the thinner the profile. Consequently, M_{cr} increases with reduction of the profile relative thickness.

Judging by some experimental data, not only the profile relative thickness $\bar{c}$ but also the relative abscissa $\bar{x}_c$ has an effect on the pressure distribution (Figure 14.5). For small angles α (or for small values of c_y) M_{cr} increases with increase of $\bar{x}_c$, while for large angles of attack M_{cr} decreases.

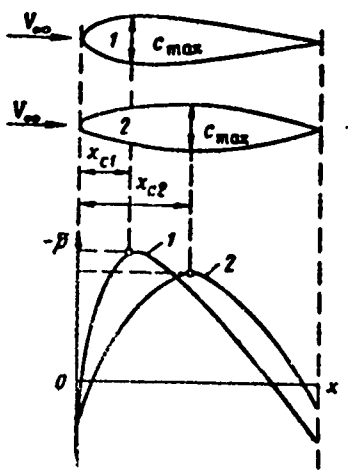

Figure 14.5. Effect of profile maximal thickness location on pressure distribution

For symmetric profiles the value of M_{cr} reaches a minimum at $\alpha = 0$ or at $c_y = 0$, and the maximal pressure reduction above and below the profile are equal. For asymmetric profiles the maximal value of M_{cr} is obtained at that angle of attack α (or for that value of c_y) for which the maximal pressure reductions above and below the profile are equal. Usually this occurs at small negative angles of attack. With increase of the profile camber, there is an increase of the value of c_y for which the maximal value of M_{cr} in reached.

Now let us examine the flow structure about a wing profile in a stream with $M_\infty > M_{cr}$. As was shown above, for $M_\infty > M_{cr}$ the flow velocity becomes equal to the local sound speed at some point of the profile surface, and the minimal value of the pressure coefficient is reached at this point. With further increase of M_∞ a supersonic flow zone is formed downstream of this point, usually closed by a compression shock. The location of the compression shock and the extent of the supersonic velocity zone depend on M_∞.

With increase of M_∞ the compression shocks, forming initially on the upper surface, displace together with the boundary of the supersonic velocity zone toward the trailing edge of the profile. Then a supersonic zone is also formed on the lower surface of the profile. The growth of the supersonic zone on the lower surface of the profile takes place more rapidly than on the upper surface. Therefore for some $M_\infty < 1$ the closing compression shock on the lower surface overtakes the compression shock on the upper surface as it travels toward the trailing edge of the profile. When M_∞ approaches one, the supersonic zones encompass nearly the entire surface of the profile.

The supersonic zone ahead of the compression shock, resting on the profile and bounded on the left by the subsonic flow velocity zone, is shown in Figure 14.6.

We note that the boundary layer, which forms on the wing surface as a result of friction, has an effect on the shape of the compression shock. It has been established experimentally that, if the boundary layer ahead of the compression shock is laminar, then near the boundary layer the normal shock splits and takes a sort of λ-shaped form (Figure 14.7). The forward leg of the lambda shock is an oblique compression shock while the aft leg is a continuation of the basic normal compression shock.

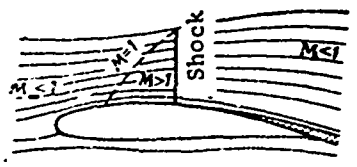

Figure 14.6. Air flow past profile for $M_\infty > M_{cr}$

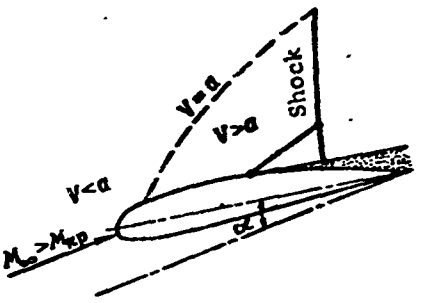

Figure 14.7. Flow past profile for $M_\infty > M_{cr}$ with transition of laminar boundary layer into turbulent

Upon increase of Re the laminar boundary layer becomes turbulent and the shock changes its shape. These changes lead to oscillations of the loads on the profile.

If the boundary layer ahead of the compression shock is turbulent, only a single normal compression shock is formed in the supersonic zone. In this case nearly the entire boundary layer is supersonic. The normal compression shock nearly rests on the wall and is most stable.

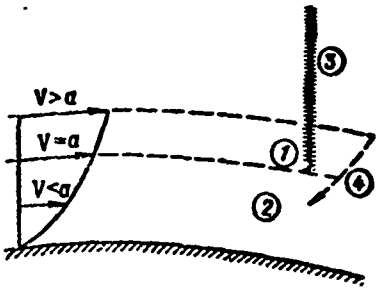

Figure 14.8. Division of boundary layer into subsonic and supersonic regions:

1 — boundary layer supersonic region; 2 — boundary layer subsonic region; 3 — high-pressure region; 4 — direction of pressure equalization

§14.3. Pressure Distribution Over Profile in Presence of Local Compression Shocks and Profile Wave Drag Calculation

Let us isolate a thin stream filament at the wing surface. In the absence of friction the flow in the stream filament can be likened to the flow in a Laval nozzle. We shall examine three characteristic flow cases (Figure 14.9).

1. For $M_\infty < M_{cr}$ the flow is subsonic along the entire stream filament. Up to the minimal (critical) section ω_{cr} the velocity increases while the pressure decreases; benind this section, conversely, the velocities decrease and the pressure increases.

2. For $M_\infty = M_{cr}$ the velocity at the critical section equals the local sound speed, while the flow is subsonic at all the other sections. The critical pressure (see Chapter X) is $p_{cr} = 0.528\, p_0$, where p_0 is the pressure at the profile forward stagnation point.

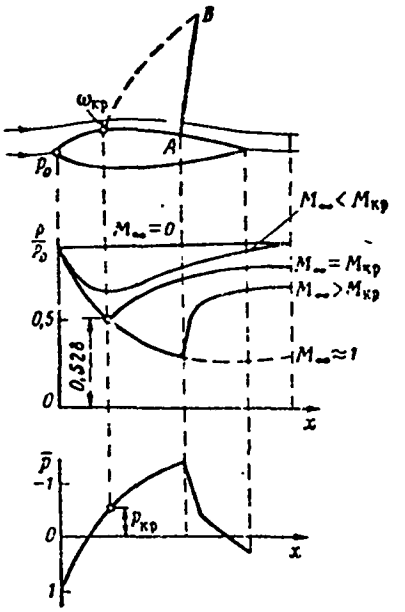

Figure 14.9. Pressure distribution over profile for different values of M_∞

3. For $M_\infty > M_{cr}$ a local zone with supersonic flow appears behind the critical section and is closed on the right side by the

normal compression shock AB. The pressure variation curve for $M_\infty > M_{cr}$ is shown in the lower figure.

Now let us turn to the calculation of the so-called wave drag. The shocks which form on the wing surface give rise to <u>wave drag</u> (which reaches significant magnitudes even for streamlined bodies), caused by energy dissipation in the compression shocks and friction variation in the boundary layer. The wave drag can be found by either the S. A. Khristianovich-Ya. M. Serebriyskiy or Burago methods.

We shall examine the Burago method. Let us assume that a local supersonic zone forms on the upper surface of the wing (Figure 14.10). We isolate in the flow an elementary stream filament passing through the compression shock, and we identify the two sections I and II in the flow at sufficiently great distance ahead of and behind the profile. We assume the gas parameters at these sections to be unperturbed and denote them respectively by the subscripts 1∞ and 2∞ (we denote the gas parameters ahead of and behind the shock by the subscripts 1 and 2, respectively). From the condition of flow continuity in the stream filament for the two sections, we can write

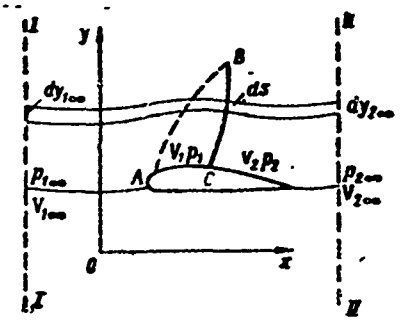

Figure 14.10. Scheme for calculating flow past wing profile in presence of normal shock

$$\rho_{1\infty} V_{1\infty} dy_{1\infty} = \rho_{2\infty} V_{2\infty} dy_{2\infty}. \qquad (14.1)$$

Assuming that $dy_{1\infty} = dy_{2\infty} = dy$, in accordance with the momentum theorem we have

$$\int_{-\infty}^{+\infty} \rho_{2\infty} V_{2\infty}^2 dy_{2\infty} - \int_{-\infty}^{+\infty} \rho_{1\infty} V_{1\infty}^2 dy_{1\infty} = \int_{-\infty}^{+\infty} (p_{1\infty} - p_{2\infty}) dy - X_a, \tag{14.2}$$

or, transforming (14.2) with account for (14.1), we obtain

$$X_a = \int_{-\infty}^{+\infty} (p_{1\infty} - p_{2\infty}) dy + \int_{-\infty}^{+\infty} \rho_{1\infty} V_{1\infty} (V_{1\infty} - V_{2\infty}) dy. \tag{14.3}$$

In the absence of compression shocks, i.e., for continuous isentropic gas flow past the profile, it follows from this formula that $X_w = 0$.

If we consider that the pressure p is recovered at the second section and takes the same value as at the first section, and that $V_{2\infty} = V_{1\infty}$ in all the stream filaments which do not cross the compression shock, then

$$\lim \int_{-\infty}^{+\infty} (p_{1\infty} - p_{2\infty}) dy = 0$$

and

$$\lim \int \rho_{1\infty} V_{1\infty} (V_{1\infty} - V_{2\infty}) dy = 0.$$

Then (14.3) takes the form

$$X_a = \int_{(s)} \rho_{1\infty} V_{1\infty} (V_{1\infty} - V_{2\infty}) dy + \int_{(s)} (p_{1\infty} - p_{2\infty}) dy, \tag{14.4}$$

where s — is the length of the compression shock.

If we follow Burago and assume that the velocities equalize behind the wing, i.e., $V_{1\infty} \approx V_{2\infty}$, and assume that $p_{1\infty}$ = const (unperturbed flow), then (14.4) can be reduced to the form

$$X_a = p_{1\infty} \int_{(s)} \left(1 - \frac{p_{2\infty}}{p_{1\infty}}\right) dy. \tag{14.5}$$

Since

$$\frac{p_{2\infty}}{p_{1\infty}}=\frac{p_{02}}{p_{01}}\left(\frac{1+\frac{k-1}{2}M_{1\infty}^2}{1+\frac{k-1}{2}M_{2\infty}^2}\right)^{\frac{k}{k-1}},$$

then for the same velocities

$$\frac{p_{02}}{p_{01}}=\frac{p_{2\infty}}{p_{1\infty}}=\sigma<1, \tag{14.6}$$

where σ — is the total head loss coefficient. For all the stream filaments which do not cross the compression shock $\sigma = 1$.

Considering (14.6) and noting that

$$\rho_{1\infty}V_{1\infty}dy_{1\infty}=\rho_1V_1ds,$$

or

$$dy_{1\infty}=dy=\frac{\rho_1V_1}{\rho_{1\infty}V_{1\infty}}\,ds,$$

we obtain the formula for finding the magnitude of the wave drag in the form

$$X_в=p_{1\infty}\int_{(s)}\frac{\rho_1V_1}{\rho_{1\infty}V_{1\infty}}(1-\sigma)\,ds. \tag{14.7}$$

We see from (14.7) that with decrease of σ the value of X_w increases. Since $\sigma < 1$ across the compression shock, the wave drag $X_w > 0$. With reduction of σ and increase of the compression shock length s, the value of X_w will increase.

The wave drag coefficient equals

$$c_{xв}=\frac{X_в}{\frac{\rho_{1\infty}V_{1\infty}^2}{2}b}. \tag{14.8}$$

Burago recommends the following formula for determining the wave drag coefficient in the first approximation

$$c_{x_0} = A(M_\infty - M_{cr})^3, \qquad (14.9)$$

where $M_\infty < M_{cr} + 0.15$;

A is a coefficient which depends on the profile type and pressure distribution. The average value of this coefficient for subsonic profiles is about 11.

The nature of the pressure distribution along a symmetric profile at zero angle of attack in the presence of a compression shock on the upper surface is shown in Figure 14.11. The pressure distribution corresponding to the flow pattern on the upper surface is shown on the lower surface of the profile. The pressure p_0 is maximal at the stagnation point. Further along the profile, the pressure decreases and reaches the value p_{cr} at the point A, where the velocity $V = a_{cr}$. In the supersonic zone AB the pressure decreases still further and only increases abruptly at the compression shock BC. Behind the compression shock the pressure continues to increase to the value of the stagnation pressure at the profile trailing edge (curve GH), and the flow velocity decreases.

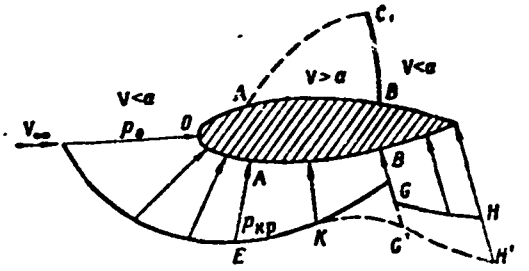

Figure 14.11. Pressure distribution over upper surface of profile for $1 > M_\infty > M_{cr}$

We note that, if the deceleration of the supersonic flow were to take place without compression shocks, then for the same velocities the pressure on the aft portion of the profile would be higher and would vary along curve KG'H'. Thus, in the presence of a compression shock the pressure on the aft portion of the

profile decreases in comparison with the shock-free flow case, which is the factor leading to the additional drag which is termed wave drag.

All the analytic techniques for determining the wave drag coefficient for $M_\infty > M_{cr}$ are very approximate. More exact results can be obtained only by experiments.

REVIEW QUESTIONS

1. Define the critical Mach number and list the factors on which M_{cr} depends.

2. What is the reason for the appearance of local compression shocks on a profile?

3. How do the coefficients c_x and c_y vary with increase of M? Show graphically the dependence of these coefficients on M_∞.

4. How does the profile aerodynamic center location vary for $M_\infty > M_{cr}$?

5. What is the physical meaning of wave drag? How do profile thickness, camber, and angle of attack affect the magnitude of the wave drag in the transonic flow regime?

PROBLEMS

1. For low-speed flow past a profile it is found that $\bar{p}_{\text{min incom}} = -0.75$. Find the critical Mach number for the profile.

Answer: $M_{cr} = 0.6$.

2. In low-speed flow past a profile, the maximal velocity at the surface was 125% of the freestream velocity. Find the value of M_{cr} and the corresponding flow velocity for flight at an altitude of 8000 m.

Answer: $M_{cr} = 0.65$, $V_{vc} = 720$ km/hr.

3. In the process of testing a wing profile in a high-speed wind tunnel with air temperature 260° K and freestream pressure $p_\infty = 6000$ N/m^2, it was found that $M_{cr} = 0.72$. Find the magnitude of the minimal pressure on the profile.

Solution. From the Khristianovich curve in Figure 14.3, we find the minimal static pressure coefficient: $\bar{p}_{min} = -0.4$.

According to (6.9)

$$\bar{p}_{min} = \frac{p_{min} - p_\infty}{\frac{\rho_\infty V_\infty^2}{2}}.$$

Hence

$$p_{min} = p_\infty + \bar{p}_{min} \frac{\rho_\infty V_\infty^2}{2}. \qquad \text{(a)}$$

To find the density we use the equation of state (1.2)

$$\rho_\infty = \frac{p_\infty}{RT_\infty}.$$

We find the magnitude of the velocity using (1.19) and (1.18)

$$V_\infty = M\sqrt{kRT_\infty}.$$

Substituting the values of ρ_∞ and V_∞ into (a), we obtain

$$p_{min} = p_\infty(1 + \bar{p}_{min} M^2 k) = 6000(1 - 0{,}4 \cdot 0{,}72^2 \cdot 1{,}4) = 1643 \text{ к/м}^2.$$

FOOTNOTES

Footnote (1) on page 74: Trudy TsAGI, No. 48, 181, 1940.

CHAPTER XV

WING PROFILE IN SUPERSONIC FLOW

§15.1. Characteristics of Supersonic Flow Past Bodies. Flat Plate in Supersonic Flow

The general problem of supersonic flow past bodies with a rounded nose, in which as a result of flow deceleration a curved (detached) compression shock forms ahead of the body, belongs to the class of "mixed" hydrodynamic problems, since there are regions in the stream with supersonic and subsonic flows. The complexity of the problem lies in the fact that the boundaries of the compression shocks cannot be determined in advance and, moreover, the supersonic gas flow behind the curved compression shock is rotational.

In contrast with the mixed problem, in the case of supersonic flow past a profile with sharp leading edge at small angle of attack, the bow shock is attached to the leading edge of the profile and breaks down into upper and lower oblique compression shocks. There are several methods of differing precision for the solution of problems of flow past such profiles, which make it possible to

obtain simple computational formulas. We shall restrict ourselves to consideration of the problem of the flow past a sharp-nosed profile at small angle of attack. We shall examine the simplest case: supersonic flow past a flat plate aligned at the angle of attack α (Figure 15.1).

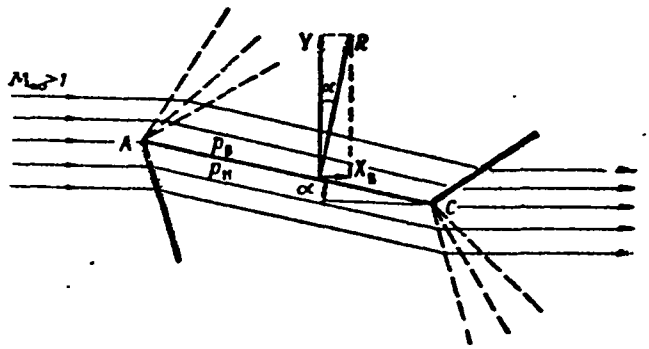

Figure 15.1. Supersonic flow past flat plate

The flow divides into two parts at the leading edge. The upper part of the flow is turned through the angle α and expands in a fan of characteristics (or weak disturbance lines). At the trailing edge the flow changes direction and tends to recover the initial direction, turning through the angle α and being compressed.

Thus, the upper part of the stream flows around a concave corner at the trailing edge and a compression shock develops here. The reverse picture is observed in the lower part of the stream. Near the leading edge of the flat plate a compression shock is formed, while near the trailing edge the flow expands in a fan of characteristics. For small angles α the expansion (or compression), as mentioned previously, takes place practically in a single characteristic, coinciding with the perturbation line.

If the angle α is positive, the pressure on the lower surface of the plate will be greater than that of the freestream flow,

i.e., $p_l > p_\infty$, while the situation is reversed on the upper surface.

The resultant force R, equal to the difference of the pressure forces, is perpendicular to the plate and for $\alpha > 0$ is directed upward. Thus, the resultant force per unit span of a plate with chord b is

$$R=(p_н-p_в)b\cdot 1.$$

The projection of the resultant force on the freestream velocity direction yields the drag force, termed the wave drag and denoted by X_w

$$X_в=(p_н-p_в)b\sin\alpha,$$

or, considering the smallness of α,

$$X_в=(p_н-p_в)b\alpha.$$

The wave drag results from the energy expenditures in forming wave disturbances in the flow.

The projection of the resultant force R perpendicular to the freestream velocity is the lift force Y

$$Y=(p_н-p_в)b\cos\alpha,$$

or, considering that for small angles $\cos\alpha \approx 1$,

$$Y=(p_н-p_в)b.$$

For positive and small angles α, we can find the pressure increase below the plate from (10.46)

$$p_в-p_\infty=\rho_\infty V_\infty^2\frac{\alpha}{\sqrt{M_\infty^2-1}} \qquad (15.1)$$

and the pressure reduction above the plate

$$p_0 - p_\infty = -\rho_\infty V_\infty^2 \frac{\alpha}{\sqrt{M_\infty^2 - 1}}. \tag{15.2}$$

Then we obtain the difference between the pressures on the lower and upper surfaces of the plate in the form

$$p_n - p_0 = \rho_\infty V_\infty^2 \frac{2\alpha}{\sqrt{M_\infty^2 - 1}}. \tag{15.3}$$

The lift and wave drag per meter of plate span are

$$Y = \rho_\infty V_\infty^2 \frac{2\alpha b}{\sqrt{M_\infty^2 - 1}}; \tag{15.4}$$

$$X_0 = \rho_\infty V_\infty^2 \frac{2\alpha^2 b}{\sqrt{M_\infty^2 - 1}}. \tag{15.5}$$

Considering that $S = b \cdot 1$, from (15.4) and (15.5) we find the formulas for the plate lift and wave drag coefficients

$$c_y = \frac{4\alpha}{\sqrt{M_\infty^2 - 1}}; \tag{15.6}$$

$$c_{x\,w\,i} = \frac{4\alpha^2}{\sqrt{M_\infty^2 - 1}} = c_y \alpha, \tag{15.7}$$

$$c_{x\,w\,i} = \frac{\sqrt{M_\infty^2 - 1}}{4} c_y^2. \tag{15.8}$$

We see from these formulas that the lift coefficient c_y is directly proportional to the angle of attack α and can change its sign depending on the sign of α; the wave drag coefficient $c_{x\,w\,i}$ depends quadratically on α and is always positive. Both the coefficients c_y and $c_{x\,w\,i}$ are inversely proportional to $\sqrt{M_\infty^2 - 1}$ and decrease with increase of M_∞.

Since the wave drag coefficient $c_{x\,w\,i}$ is proportional to the lift coefficient squared and equals zero for $c_y = 0$, it is termed the wave-induced drag[1].

We note that (15.6) and (15.7) are applicable in practice only when the compression shock extending downward from the nose part of the profile is a rectilinear attached shock with $\alpha > 0$. It is assumed that for M_∞ approaching unity the angle of attack α must approach zero. Otherwise the relations obtained will not be valid.

We should point out the fundamental differences between supersonic and subsonic flow past a flat plate. In supersonic flow the nose of the plate splits the flow and the streamlines are parallel to the plate; the differential pressure and the pressure coefficient are constant on the upper and lower surfaces of the plate and are equal in magnitude and opposite in sign (Figure 15.2). It is obvious that the center of pressure (point D) and focus of the flat plate are at the midpoint of the chord in this case.

In subsonic flow a sharp suction peak is created near the nose of the plate on the upper surface, and a large positive pressure on on the lower surface. The pressure varies along the length of the plate, and the center of pressure (D) and focus are located about 1/4 chord from the nose (Figure 15.3).

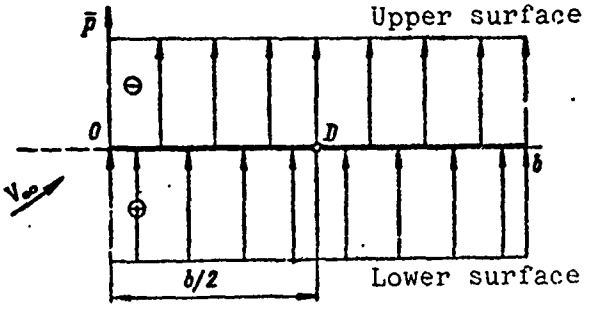

Figure 15.2. Pressure coefficient distribution over flat plate in supersonic flow

With account for friction, the drag coefficient of a plate of infinite span will be made up of two terms

Footnote (1) appears on page 107.

$$c_x = c_{x\,wi} + 2c_{xf} = \frac{4\alpha^2}{\sqrt{M_\infty^2 - 1}} + 2c_{xf}. \qquad (15.9)$$

where c_{xf} — is the flat plate friction drag coefficient calculated by the methods of boundary layer theory.

Substituting into (15.9) the value of $c_{x\,w\,i}$ from (15.8), we obtain the equation of the flat-plate polar

$$c_x = \frac{\sqrt{M_\infty^2 - 1}}{4} c_y^2 + 2c_{xf}. \qquad (15.10)$$

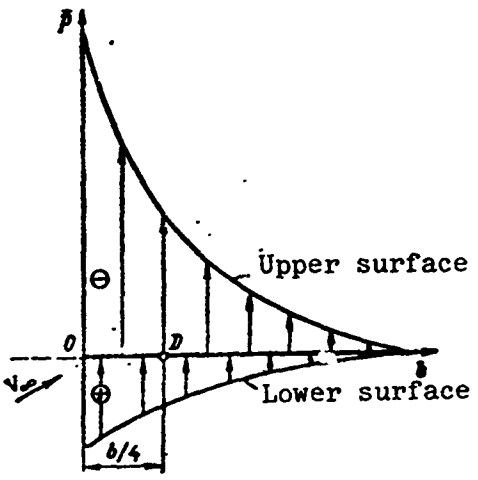

Figure 15.3. Pressure coefficient distribution over flat plate in subsonic flow

We see that the flat-plate polar is a quadratic parabola. For values of c_y differing from zero the polar will shift to the right with increase of M_∞.

§15.2. Pressure Distribution Along Profile

Let us examine the pressure distribution pattern on a symmetric profile in subsonic and supersonic flows.

In the case of subsonic flow about a symmetric profile (Figure 15.4a), the stream filaments first expand somewhat in the nose region, which leads to increase of the pressure and decrease of the velocity; and then they converge rapidly, as a result of which the pressure decreases and the velocity increases. Then in the aft region of the profile the stream filaments again expand, as a result of which there is a decrease of the velocity and increase of the pressure.

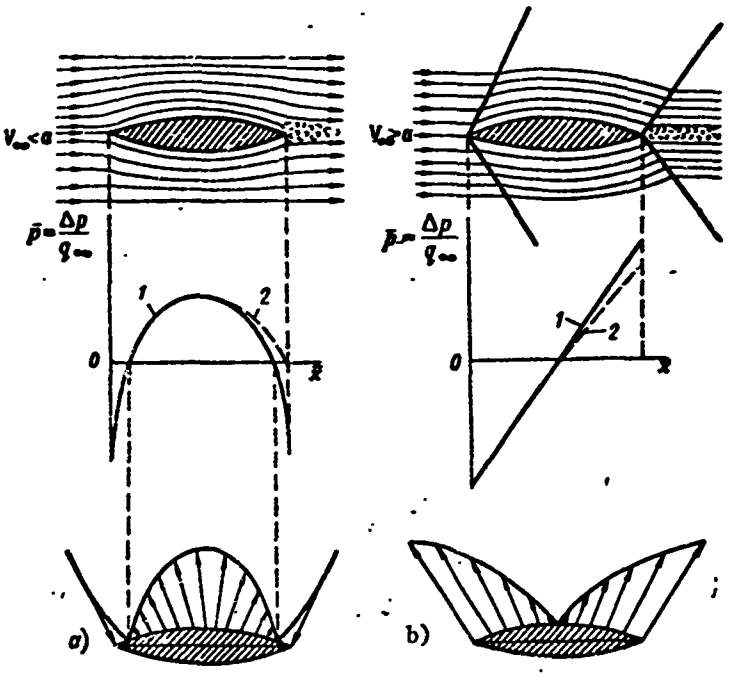

Figure 15.4. Comparison of subsonic and supersonic flow past profiles:

a — subsonic; b — supersonic; 1 — ideal fluid; 2 — viscous fluid

In the case of supersonic flow past a profile the pressure distribution pattern is somewhat different: upon reaching the bow compression wave, the stream filaments change their direction abruptly, which leads to decrease of the velocity and increase of the pressure (Figure 15.4b). Then the velocity gradually increases and the pressure decreases along the profile surface back to the trailing edge. The pressure increases abruptly in the tail shock wave, but this now has no effect on the pressure distribution along the profile.

Thus, in the subsonic flow case there is recovery of the pressure on the aft part of the profile, while in the supersonic flow case the pressure is not recovered prior to the trailing shock wave.

We see from the pressure distribution diagram that for subsonic ideal fluid flow past a profile the projection of the resultant aerodynamic force on the flow direction is equal to zero, while for supersonic flow past the profile this projection yields the so-called wave drag.

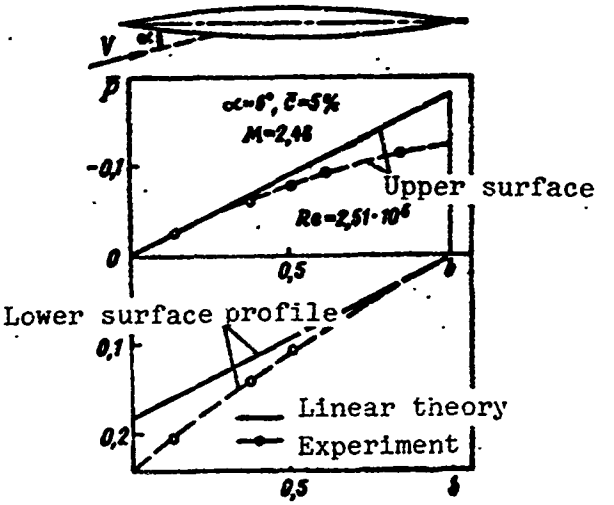

Figure 15.5. Comparison of theoretical and experimental values of pressure coefficients of a symmetric profile

If the fluid is viscous, an additional drag force appears owing to the friction force in the boundary layer. However, in this case the wave drag is again the basic part of the total profile drag, which can be represented in the form of the sum

$$X = X_в + X_{тр}.$$

Figure 15.5 shows a comparison of the theoretical and experimental values of the pressure coefficients $\bar{p}$. We see from the curves that linear theory yields values of the pressure coefficient which are too high in the low pressure region (on the upper side of the profile) as we move aft from the leading edge and values which are too low on the lower surface of the profile, particularly near the leading edge.

§15.3. Thin Profile in Supersonic Flow

Let us examine supersonic flow past a thin profile of arbitrary shape with chord b and span $l = 1$ at the angle of attack α (Figure 15.6).

We identify on the lower surface of the contour the elementary segment dl, whose inclinations to the Ox axis of the body coordinate system and to the freestream velocity direction are denoted by γ_l and and α_l:

$$\alpha_n = \alpha + \gamma_n.$$

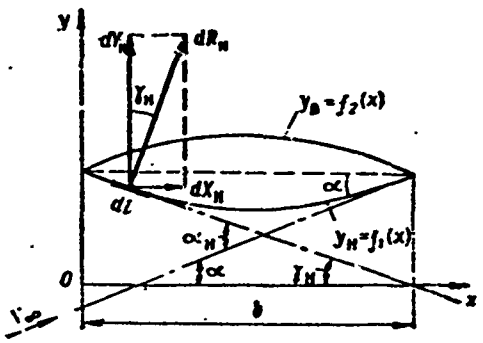

Figure 15.6. Supersonic flow past thin profile

According to (15.1) the differential pressure on the element dl is

$$\Delta p_n = p_n - p_\infty = \rho_\infty V_\infty^2 \frac{\alpha_n}{\sqrt{M_\infty^2 - 1}}.$$

If we denote the projections of dl on the coordinate axes by dy_l and $dx_l = dx$, we obtain

$$\sin \gamma_n \approx \operatorname{tg} \gamma_n = -\frac{dy_n}{dx}.$$

For a thin profile in view of the smallness of the angle γ_l, $\sin \gamma_l \approx \gamma_l$. Consequently

$$\gamma_n = -\frac{dy_n}{dx}. \tag{15.11}$$

The elementary differential pressure force applied normal to the lower surface element in question is

$$dR_n = \Delta p_n dl = \rho_\infty V_\infty^2 \frac{\alpha - \frac{dy_n}{dx}}{\sqrt{M_\infty^2 - 1}} dl.$$

Then the projections of this force on the coordinate axes and the elementary moment about the profile nose are, respectively,

$$dY_н = \Delta p_н dl \cos\gamma_н = \Delta p_н dx;$$

$$dX_н = \Delta p_н dl \sin\gamma_н = \Delta p_н \gamma_н dx = -\Delta p_н \frac{dy_н}{dx} dx;$$

$$dM_н = -dY_н x.$$

We neglect the moment of the projection dX_l by virtue of its smallness in comparison with dY_l.

The overall forces and moments for the lower surface of the profile are

$$Y_н = \int_0^b \Delta p_н dx = \frac{\rho_\infty V_\infty^2}{\sqrt{M_\infty^2 - 1}} \int_0^b \left(\alpha - \frac{dy_н}{dx}\right) dx,$$

$$X_н = \int_0^b \Delta p_н \gamma_н dx = -\frac{\rho_\infty V_\infty^2}{\sqrt{M_\infty^2 - 1}} \int_0^b \left(\alpha - \frac{dy_н}{dx}\right) \frac{dy_н}{dx} dx,$$

$$M_н = -\int_0^b \Delta p_н x dx = -\frac{\rho_\infty V_\infty^2}{\sqrt{M_\infty^2 - 1}} \int_0^b \left(\alpha - \frac{dy_н}{dx}\right) x dx.$$

We see from Figure 15.6 that the quantity $\int_0^b \frac{dy_н}{dx} dx = 0$. Then

$$Y_н = \frac{\rho_\infty V_\infty^2}{\sqrt{M_\infty^2 - 1}} ab;$$

$$X_н = \frac{\rho_\infty V_\infty^2}{\sqrt{M_\infty^2 - 1}} \int_0^b \left(\frac{dy_н}{dx}\right)^2 dx;$$

$$M_н = \frac{\rho_\infty V_\infty^2}{\sqrt{M_\infty^2 - 1}} \left(-\frac{a}{2} b^2 + \int_0^b \frac{dy_н}{dx} x dx\right).$$

Similar expressions can be obtained for the profile upper surface.

The forces and moment acting on both sides of the profile, defined in the body coordinate system, will be

$$Y_1 = Y_в + Y_н = -\frac{\rho_\infty V_\infty^2}{\sqrt{M_\infty^2 - 1}} 2ab;$$

$$X_1 = X_в + X_н = \frac{\rho_\infty V_\infty^2}{\sqrt{M_\infty^2 - 1}} \left[\int_0^b \left(\frac{dy_в}{dx}\right)^2 dx + \int_0^b \left(\frac{dy_н}{dx}\right)^2 dx \right];$$

$$M = M_в + M_н = \frac{\rho_\infty V_\infty^2}{\sqrt{M_\infty^2 - 1}} \left(-ab^2 + \int_0^b \frac{dy_в}{dx} x dx + \int_0^b \frac{dy_н}{dx} x dx \right).$$

Here the force Y_1 is normal to the profile chord; however, in view of the smallness of the angle of attack α it is essentially the lift force Y as well.

The lift coefficient

$$c_y = \frac{Y}{S \frac{\rho V^2}{2}}.$$

Considering that $S = b \cdot 1 = b$ and substituting the value of Y, we obtain

$$c_y = \frac{4\alpha}{\sqrt{M_\infty^2 - 1}}. \qquad (15.12)$$

This formula implies that the lift coefficient is independent of the profile form and thickness and depends only on the angle of attack, and for the same conditions is equal in magnitude to the flat-plate lift coefficient (15.6).

The drag X has the direction of the velocity V_∞. Projecting the forces Y_1 and X_1 on the direction of the freestream velocity V_∞ and considering that the angle α is small, we obtain

$$X = Y_1 \alpha + X_1. \qquad (15.13)$$

$$X=\frac{2\alpha^2\rho V_\infty^2 b}{\sqrt{M_\infty^2-1}}+\frac{\rho V_\infty^2}{\sqrt{M_\infty^2-1}}\int_0^b\left[\left(\frac{dy_в}{dx}\right)^2+\left(\frac{dy_н}{dx}\right)^2\right]dx.$$

Hence the wave drag coefficient is

$$c_{x\,в}=\frac{4\alpha^2}{\sqrt{M_\infty^2-1}}+\frac{B}{\sqrt{M_\infty^2-1}}, \qquad (15.14)$$

where

$$B=\frac{2}{b}\int_0^b\left[\left(\frac{dy_в}{dx}\right)^2+\left(\frac{dy_н}{dx}\right)^2\right]dx.$$

We represent the profile ordinates in terms of its thickness

$$y_в=c\bar{y}_в(x);\quad y_н=c\bar{y}_н(x).$$

Differentiating, we have

$$\frac{dy_в}{dx}=\frac{c}{b}\frac{d\bar{y}_в}{d\bar{x}};\quad \frac{dy_н}{dx}=\frac{c}{b}\frac{d\bar{y}_н}{d\bar{x}},$$

where

$$\bar{x}=x/b.$$

Then

$$B=K_1\bar{c}^2,$$

where

$$K_1=2\int_0^1\left[\left(\frac{d\bar{y}_в}{d\bar{x}}\right)^2+\left(\frac{d\bar{y}_н}{d\bar{x}}\right)^2\right]d\bar{x}.$$

The function K_1 depends only on the profile shape.

With account for the expression for B, (15.14) can be written as

$$c_{x\,в}=\frac{4\alpha^2}{\sqrt{M_\infty^2-1}}+\frac{K_1\bar{c}^2}{\sqrt{M_\infty^2-1}}=c_{x\,в\,1}+c_{x\,в\,0}. \qquad (15.15)$$

Thus, the profile wave drag coefficient is the sum of two drag coefficients: the wave drag coefficient c_{xwi} of a profile of zero thickness at the given angle of attack, and the minimal wave drag coefficient c_{xw0}, equal to $(c_{xw})_{\alpha = 0}$.

The wave drag coefficient of the profile of zero thickness ($\bar{c} = 0$) is also termed the wave-induced drag coefficient, since it depends on the profile lift coefficient

$$c_{xwi} = \frac{4\alpha^2}{\sqrt{M_\infty^2 - 1}} = c_y \alpha.$$

This implies that the coefficient c_{xwi} is independent of the profile form and thickness and is expressed by the same formula as is the flat-plate wave drag coefficient (15.7).

The minimal wave drag coefficient (for $\alpha = 0$) is

$$c_{xw0} = \frac{2\bar{c}^2}{\sqrt{M_\infty^2 - 1}} \int_0^1 \left[\left(\frac{d\bar{y}_u}{d\bar{x}} \right)^2 + \left(\frac{d\bar{y}_l}{d\bar{x}} \right)^2 \right] d\bar{x} = \frac{K_1 \bar{c}^2}{\sqrt{M_\infty^2 - 1}}. \qquad (15.16)$$

This coefficient for given M_∞ depends only on the profile form and relative thickness.

With account for the friction forces, the expression for the drag coefficient of a thin profile at small angle of attack has the form

$$c_x = c_{xwi} + c_{xf} = \frac{4\alpha^2}{\sqrt{M_\infty^2 - 1}} + c_{xw0} + c_{xf}, \qquad (15.17)$$

where c_{xf} — is the friction drag coefficient.

From (15.17) and (15.12) we can obtain the equation of the wing profile polar in the form

$$c_x = \frac{\sqrt{M_\infty^2 - 1}}{4} c_y^2 + c_{x0} + c_{xf}. \tag{15.18}$$

The profile moment coefficient about the leading edge is

$$c_m = \frac{M}{\frac{\rho V_\infty^2}{2} Sb} = -\frac{2\alpha}{\sqrt{M_\infty^2 - 1}} + c_{m0}, \tag{15.19}$$

where $S = b \cdot 1$;

c_{m0} — is the moment coefficient at zero angle of attack

$$c_{m0} = \frac{2}{b^2 \sqrt{M_\infty^2 - 1}} \int_0^b \left(\frac{dy_u}{dx} + \frac{dy_l}{dx} \right) x\, dx,$$

or

$$c_{m0} = \frac{2\bar{c}}{\sqrt{M_\infty^2 - 1}} \int_0^1 \left(\frac{d\bar{y}_u}{d\bar{x}} + \frac{d\bar{y}_l}{d\bar{x}} \right) \bar{x}\, d\bar{x}. \tag{15.20}$$

It follows from (15.20) that the coefficient c_{m0} depends on the profile shape. For the symmetric profile $\left(\frac{d\bar{y}_l}{d\bar{x}} = -\frac{d\bar{y}_u}{d\bar{x}} \right)$ $c_{m0} = 0$. Then

$$c_m = -\frac{2\alpha}{\sqrt{M_\infty^2 - 1}}.$$

Knowing the coefficients c_m and c_y, we can find the dimensionless abscissa of the profile focus

$$\bar{x}_F = \frac{x_F}{b} = -\frac{\partial c_m}{\partial c_y},$$

or

$$\bar{x}_F = -\frac{\frac{\partial c_m}{\partial \alpha}}{\frac{\partial c_y}{\partial \alpha}}.$$

Using (15.12) for c_y and (15.19) for c_m, we find that $\bar{x}_F = 0.5$. Consequently, the focus of the thin profile of arbitrary form in supersonic flow, just as for the flat plate, is located at the midpoint of the chord. According to (12.24) the center of pressure is at this same point, since for symmetric profiles $c_{m0} = 0$.

§15.4. Aerodynamic Coefficients for Some Typical Profile Forms

Let us examine a triangular profile in supersonic flow (Figure 15.7). The derivatives appearing in the integrals (15.16) and (15.20) will be numerically equal to the inclinations of the profile faces to its chord.

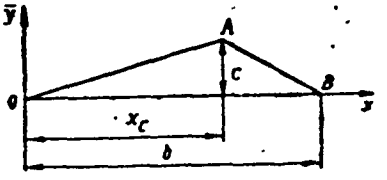

Figure 15.7. Asymmetric triangular profile

On the segment OA

$$\frac{dy_в}{dx} = \frac{c}{x_c};$$

then

$$\frac{d\bar{y}_в}{d\bar{x}} = \frac{b}{c}\frac{dy_в}{dx} = \frac{b}{x_c} = \frac{1}{\bar{x}_c}.$$

On the segment AB

$$\frac{dy_в}{dx} = -\frac{c}{b - x_c}; \text{ then } \frac{d\bar{y}_в}{d\bar{x}} = \frac{b}{c}\frac{dy_в}{dx} = -\frac{1}{1 - \bar{x}_c}.$$

Dividing the region of integration of the integrals (15.16) and (15.20) into two regions: $0 < \bar{x} < \bar{x}_c$ and $\bar{x}_c < \bar{x} < 1$ and substituting into each integral the corresponding value of the derivative $\frac{\overline{dyw}}{\overline{dx}}$, we obtain

$$c_{x\,w0}=\frac{2\bar{c}^2}{\sqrt{M_\infty^2-1}}\frac{1}{\bar{x}_c(1-\bar{x}_c)}; \tag{15.21}$$

$$c_{x0}=\frac{\bar{c}^2}{\sqrt{M_\infty^2-1}}. \tag{15.22}$$

It follows from (15.21) that for a given value of $\bar{c}$ the coefficient $c_{x\,w0}$ will be minimal when the value of the product

$$J=\bar{x}_c(1-\bar{x}_c)$$

becomes maximal.

To determine the value of $\bar{x}_c$ corresponding to J_{max}, we find the derivative $\frac{dJ}{d\bar{x}_c}$ and equate it to zero

$$\frac{dJ}{d\bar{x}_c}=1-2\bar{x}_c=0.$$

Hence we have

$$\bar{x}_c=\frac{1}{2}.$$

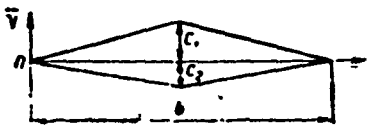

Figure 15.8. Asymmetric rhombic profile

Thus, a triangular profile for which the maximal relative thickness $\bar{c}$ is located at the midpoint of the chord will have the minimal value of $c_{x\,w0}$. For this profile the wave drag coefficient is expressed by the formula

$$c_{x\,w0}=\frac{8\bar{c}^2}{\sqrt{M_\infty^2-1}}. \tag{15.23}$$

Let us examine an asymmetric rhombic profile in supersonic flow. We can imagine that this profile consists of two triangular profiles with relative thicknesses $\bar{c}_1$ and $\bar{c}_2$ (Figure 15.8). Then the relative thickness of the rhombic profile is

$$\bar{c}=\bar{c}_1+\bar{c}_2.$$

By analogy with (15.22) and (15.23) we write the formulas for the coefficients $c_{x\,w0}$ and c_{m0}

$$\left.\begin{aligned} c_{x\,w0}&=\frac{8}{\sqrt{M_\infty^2-1}}(\bar{c}_1^2+\bar{c}_2^2);\\ c_{m0}&=\frac{\bar{c}_2-\bar{c}_1}{\sqrt{M_\infty^2-1}}. \end{aligned}\right\} \qquad (15.24)$$

Studying these formulas, we find that the minimal value of c_{xwo} will occur for $\bar{c}_1 = \bar{c}_2 = \frac{\bar{c}}{2}$, i.e., for the symmetric rhombic profile. In this case the formulas for the coefficients have the form

$$\left.\begin{aligned} c_{x\,w0}&=\frac{4\bar{c}^2}{\sqrt{M_\infty^2-1}};\\ c_{m0}&=0. \end{aligned}\right\} \qquad (15.25)$$

We see from the comparison of (15.23) and (15.25) that the coefficient $c_{x\,w0}$ of a rhombic profile is half the coefficient $c_{x\,w0}$ for the best triangular profile. Moreover, for the symmetric rhombic profile the coefficient $c_{m0} = 0$. This implies that the rhombic profile is more suitable than the triangular profile in supersonic flow.

Let us examine the lenticular profile with one-sided and two-sided convexity (Figure 15.9), described by the parabolic arcs.

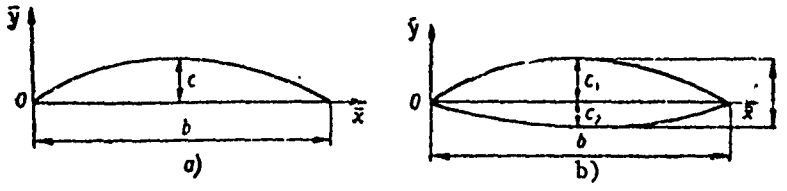

Figure 15.9. Lenticular profiles:
a — with one-sided convexity; b — with two-sided convexity

By analogy with the preceding derivations, we can obtain the formulas for finding the coefficients $c_{x\,w0}$ and c_{m0}.

For the one-sided convex lens

$$\left.\begin{aligned} c_{x\,w0} &= \frac{32}{3}\frac{\bar{c}^2}{\sqrt{M_\infty^2-1}}; \\ c_{m0} &= -\frac{4}{3}\frac{\bar{c}}{\sqrt{M_\infty^2-1}}. \end{aligned}\right\} \qquad (15.26)$$

For the two-sided convex lens

$$\left.\begin{aligned} c_{x\,w0} &= \frac{32}{3}\frac{\bar{c}_1^2+\bar{c}_2^2}{\sqrt{M_\infty^2-1}}; \\ c_{m0} &= -\frac{4}{3}\frac{\bar{c}_1-\bar{c}_2}{\sqrt{M_\infty^2-1}}. \end{aligned}\right\} \qquad (15.27)$$

In studying (15.27) we find that the minimal value of $c_{x\,w0}$ will occur in the case $\bar{c}_1 = \bar{c}_2 = \frac{\bar{c}}{2}$. For this profile

$$\left.\begin{aligned} c_{m0} &= 0; \\ c_{x\,w0} &= \frac{16}{3}\frac{\bar{c}^2}{\sqrt{M_\infty^2-1}}. \end{aligned}\right\} \qquad (15.28)$$

In comparing the symmetric lenticular profile with the symmetric rhombic profile of the same relative thickness, we find that the drag coefficient of the latter is 33% lower. Hence it is not difficult to conclude that the most rational wing profile form in supersonic flow is rhombic or a similar shape, since profiles with this form have minimal wave drag. However, with account for various requirements imposed on the profile (for example, minimal overall drag along with adequate strength and acceptable heating and so on) other wing profile forms may be more efficient.

We must also consider the viscous properties of the gas flowing over the wing, the existence of the boundary layer, and sometimes flow separation near the trailing edge.

In conclusion we note the following characteristics of the profile in supersonic flow: the lift and drag are not proportional to the velocity squared as in the case of subsonic flow. For example, from the formula

$$Y=\frac{2\rho_\infty V_\infty^2 S}{\sqrt{M_\infty^2-1}}\alpha=2\rho_\infty a_\infty \frac{V_\infty^2 S}{\sqrt{V_\infty^2-a_\infty^2}}\alpha$$

we see tha for $V_\infty > a_\infty$ the lift is proportional to the velocity to a power from 1 to 2, and for very large M_∞, when

$$V_\infty \gg a_\infty \text{ and } \sqrt{V_\infty^2-a_\infty^2}\approx V_\infty,$$

the lift is proportional to the first power of the velocity.

REVIEW QUESTIONS

1. Write the formulas for the lift and wave drag of a flat plate at the angle of attack α in supersonic flow.

2. Write the formula for the drag coefficient of a thin profile at small angle of attack.

3. What advantages do the symmetric profiles have at supersonic speeds? How does the profile thickness affect the magnitude of the wave drag at supersonic speeds?

PROBLEMS

1. By what factor is the minimal wave drag of the rhombic wing in supersonic flow less than that of the lenticular profile of the same thickness composed of circular arcs?

Answer: by a factor of 1.33.

2. Find the lift, wave drag, and moment coefficients for a flat plate at the angle of attack $\alpha = 0.06$ rad and $M_\infty = 2$.

Solution. We find the coefficients c_y, c_x, c_m from (15.6), (15.7), (15.8), respectively:

$$c_y = \frac{4\alpha}{\sqrt{M_\infty^2 - 1}} = \frac{4 \cdot 0{,}06}{\sqrt{2^2 - 1}} = 0{,}1385;$$

$$c_x = \frac{4\alpha^2}{\sqrt{M_\infty^2 - 1}} = \frac{4 \cdot 0{,}06^2}{\sqrt{2^2 - 1}} = 0{,}00831;$$

$$c_m = \frac{2\alpha}{\sqrt{M_\infty^2 - 1}} = \frac{2 \cdot 0{,}06}{\sqrt{2^2 - 1}} = 0{,}0692.$$

3. Find c_y and $c_{x\,w}$ for a rhombic profile of thickness 10.5% in air flow with $M_\infty = 1.53$ and $\alpha = 0.12$ rad.

Answer: $c_y = 0.413$; $c_{x\,w} = 0.038$.

FOOTNOTES

Footnote (1) on page 91: For more details on wave-induced drag see Chapter XVI, §16.4.

CHAPTER XVI

THEORY OF FINITE-SPAN WING IN INCOMPRESSIBLE FLOW

§16.1. Wing Geometric Characteristics

The flow which develops around a wing and determines its aerodynamic characteristics is a three-dimensional flow, whose degree of deviation from plane-parallel flow depends on the wing form and dimensions. The wings of modern airplanes are quite varied in their geometric characteristics. The plane of symmetry divides the wing into left and right sides. The projection of the wing on the plane perpendicular to the wing plane of symmetry in the x_1Oz_1 body coordinate system defines the wing planform. The most typical wing planforms are shown in Figure 16.1.

The area and span are the primary quantities defining wing size. By the wing area S we mean its area in plan view (Figure 16.2). The wing span l is the distance between the two most distant points of the wing along the Oz_1 axis.

The wing profile in the plane of symmetry is called the root profile. Profile obtained as a result of sectioning the wing by

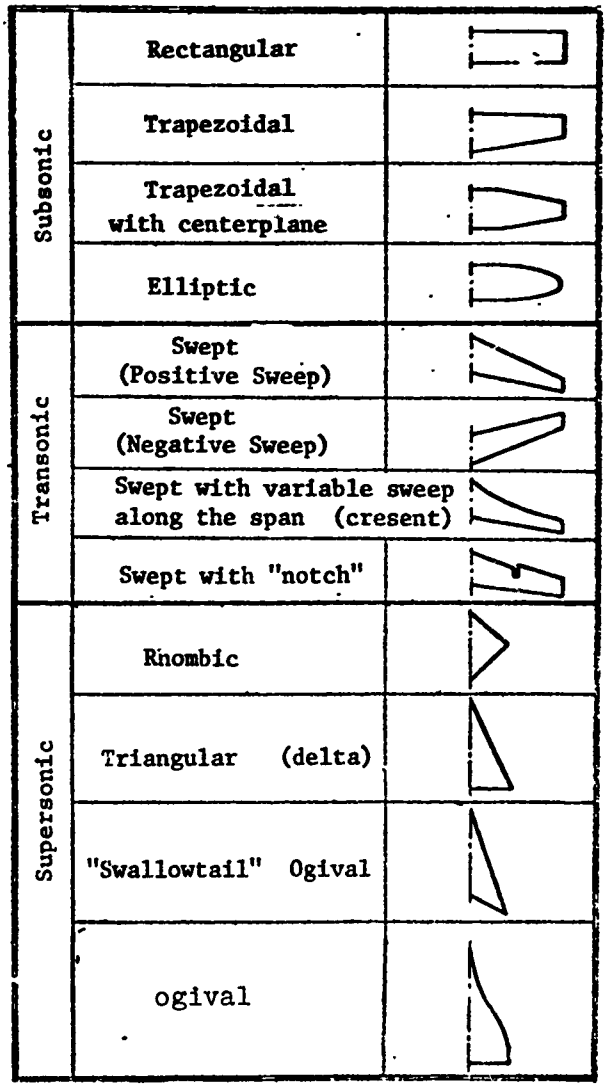

Figure 16.1. Characteristic wing planforms

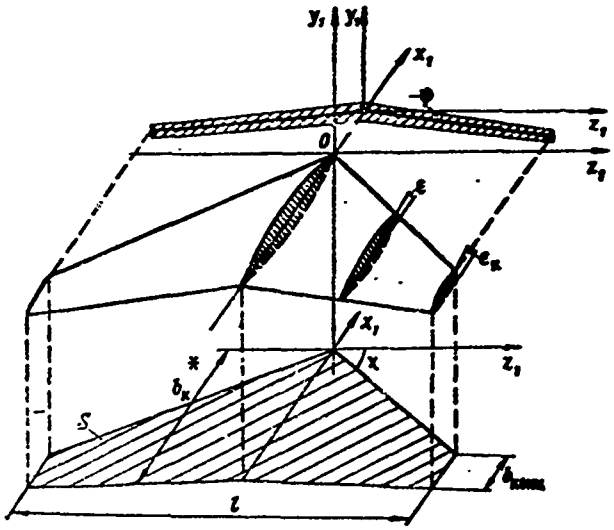

Figure 16.2. Wing geometric characteristics

planes parallel to the wing plane of symmetry in the general case vary along the span in form, dimensions, and chord inclination.

A wing is termed geometrically flat if the chords of all the sections are parallel to the x_1Oz_1 plane. If the profile chord forms some angle ε, whose magnitude varies from 0 at the root to ε_* at the tip section (see Figure 16.2), with the x_1Oy_1 plane we say the wing is geometrically twisted and the angle ε is the geometric twist angle. Twist may be either positive or negative. By positive twist we mean that in which the local angle of attack increases in comparison with the angle of attack of the root section. Usually negative twist is used in actual designs.

The wing projection on the plane parallel to the y_1Oz_1 plane may have a break at the root section. In this case we say that the wing has dihedral, which may be either positive or negative. The

*Translator's Note: This subscript should designate tip, not root as indicated in foreign text.

dihedral is characterized by the angle ψ between the direction of the Oz_1 axis and the projection of the wing leading edge on the y_1Oz_1 plane. The wing may have a form such that the angle ψ is variable along the span.

The ratio of wing area to span is called the mean aerodynamic chord

$$b_{cp}=\frac{S}{l}.$$

An important geometric characteristic of the wing is the aspect ratio λ, equal to the ratio of the wing span to the mean aerodynamic chord

$$\lambda=\frac{l}{b_{cp}}.$$

It is obvious that $\lambda = l^2/S$. The aspect ratio determines the degree of elongation of the wing along the span and has considerable influence on its aerodynamic characteristics. For subsonic airplanes $\lambda = 6 - 12$, and for supersonic $\lambda = 2 - 3$. The wing profile characteristics coincide with those of a hypothetical wing with $\lambda = \infty$.

The wing spanwise taper ratio is defined by the quantity

$$\eta=\frac{b_к}{b_{конц}},$$

where b_r and b_t are, respectively, the chords of the root and tip sections.

For a rectangular wing $\eta = 1$; for a triangular wing $\eta = \infty$. In the general case $1 \leqslant \eta \leqslant \infty$.

It is very difficult to give a general definition of the geometric parameters for all wings because of the great variety of

wing forms of modern flight vehicles. For example, all the parameters listed above are inapplicable for annular wings.

§16.2. Aerodynamic Model of Finite-Span Wing

In deriving the Zhukovskiy lift theorem we examined plane-parallel, potential, separation-free fluid flow past a cylindrical profile of infinite span. Since in accordance with the Zhukovskiy theorem the lift of a wing of infinite span is determined by the magnitude of the circulation around a contour enclosing the wing, in the first approximation with regard to the force effect on the free-stream the wing can be replaced by an infinitely long vortex filament with circulation about the contour enclosing the vortex filament equal to the circulation around the wing. Such a vortex filament is called a bound vortex. Thus, a rectilinear infinite vortex can serve as the aerodynamic model for a wing of infinite span.

For a finite-span wing the flow has a three-dimensional rather than plane-parallel nature, particularly near the wing tips. In this case the wing tips affect the pressure distribution over the entire wing surface.

Let us picture a wing of infinite span in rectilinear flight with constant velocity. If a lift force is developed on the wing, there is a low-pressure region above the wing and a high pressure region below the wing. The pressure difference leads to air cross-flow around the wingtips from the high-pressure region into the low-pressure region. Flow parallel to the span develops, with the flow below the wing being directed toward the wingtips and the flow above the wing directed toward the centersection (Figure 16.3).

As a result of interaction of the upper and lower flows, a vortex sheet is formed behind the wing. The vortex sheet consists of vortex filaments which originate at the trailing edge of the wing and remain in the stream.

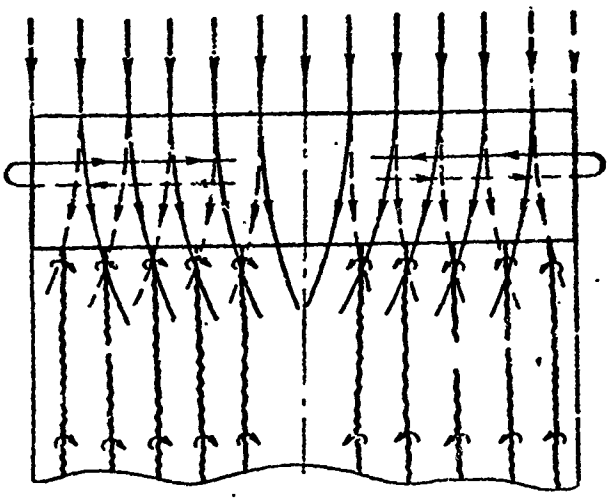

Figure 16.3. Vortex sheet formation behind finite-span wing

The vortex filaments which constitute the vortex sheet are termed free vortices. We can assume that every two symmetrically located free vortices are closed at the wing by a corresponding bound vortex (of the same intensity). Therefore the vortex sheet together with the bound vortices can be represented as an assemblage of horseshoe vortex filaments (Figure 16.4). Thus, an assembly of horseshoe vortices consisting of bound and free vortices can serve as the aerodynamic model of the finite-span wing.

The circulation $d\Gamma$ along each elementary horseshoe vortex filament is constant; however the circulation varies along the wing span.

Theoretical analysis and experiments show that the vortex sheet behind the wing is unstable; at some distance from the wing it rolls up into two powerful vortex lines (Figure 16.5). Such trailing vortices can be observed both under laboratory conditions and in flight (for example, during flight in fog or when spraying chemicals).

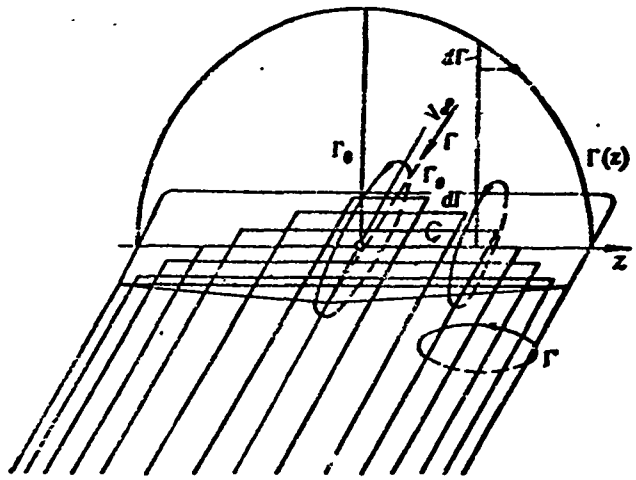

Figure 16.4. Vortex system of finite-span wing

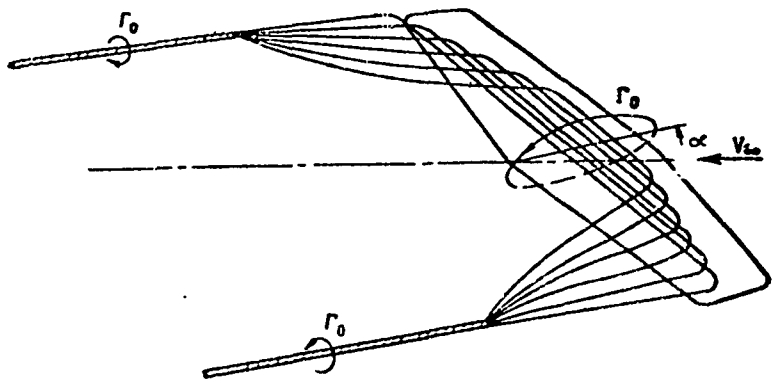

Figure 16.5. Transformation of vortex sheet into two trailing vortices

In approximate calculations the vortex system of a finite-span wing can be represented by two free vortices trailing from the wing-tips and closed by a single bound vortex (Figure 16.6). In this so-called horseshoe aerodynamic model of the wing, the circulation is constant along the wing span. In many cases this simplified aerodynamic model of the wing makes it possible to carry out calculations which are sufficiently accurate for practical purposes.

Chaplygin made one of the first studies devoted to finite-span wing theory. In his report Results of Theoretical Studies of Airplane Motion (1910) he noted the presence of vortices trailing from the finite-span wing. In 1912 Zhukovskiy in his report Vortex Theory of the Propeller (first article)

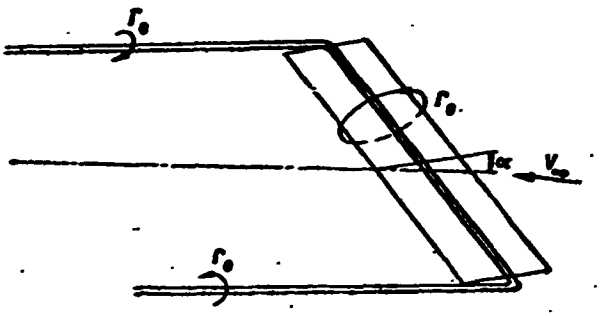

Figure 16.6. Simplest vortex scheme of finite-span wing

outlined the fundamental bases of propeller and finite-span wing theory. In 1913 in a work on finite-span wing theory Chaplygin obtained general expressions for the lift and drag of the finite-span wing. In the same year Zhukovskiy in his study Vortex Theory of the Propeller (second article) obtained the vortex scheme of a lifting body with continuous distribution of the circulation and vortex sheet behind the wing body. The vortex scheme with variable circulation was the basis for subsequent studies on wing and propeller theory.

The Zhukovskiy scheme was later used by many scientists, including Prandtl, who in 1918 obtained the equation defining the circulation variation along the wing span.

§16.3. Downwash at the Wing. Induced Drag

A characteristic feature of the flow past a finite-span wing is the presence near the wing of the so-called downwash: as the translational flow approaches the wing, it is deflected from its original direction. The flow deflection begins far ahead of the wing, growing gradually in the downstream direction. This deflection

is due to the system of free vortices, which in accordance with the Biot-Savart law induce a velocity field in the fluid mass surrounding the wing. The velocities V_y caused by the free vortices in the plane of the wing are directed vertically downward and vary both along the wing span and along its chord. The velocities V_y, combining geometrically with the approaching translational velocity V_∞, create a flow whose streamlines are curved in the vertical plane. At any wing section (Figure 16.7) the resultant velocity V_∞' is directed at the angle $\Delta\alpha$ to the original flow direction. Consequently, $\Delta\alpha$ is the downwash angle at this section. The downwash varies along the wing span, increasing toward the tips.

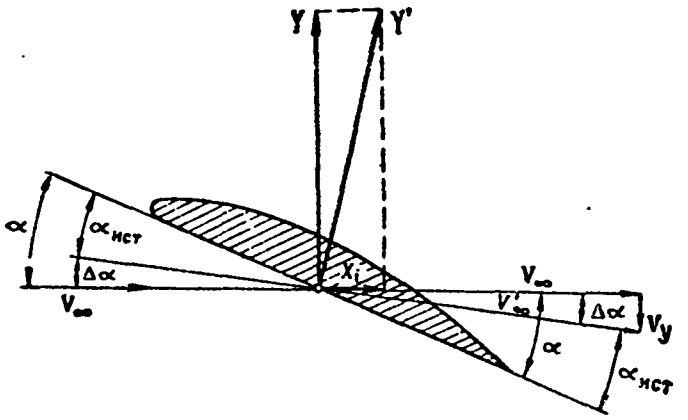

Figure 16.7. Velocity and force triangles for finite-span wing

We shall denote the average velocity V_y along the span by V_{yav}. Then the average downwash angle $\Delta\alpha_{av}$ is found from the relation

$$\operatorname{tg}\Delta\alpha_{cp} = -\frac{V_{y\,cp}}{V_\infty}.$$

Since the angle $\Delta\alpha$ is usually small, we can write

$$\operatorname{tg}\Delta\alpha_{cp} \approx \Delta\alpha_{cp} = -\frac{V_{y\,cp}}{V_\infty}. \qquad (16.1)$$

The true angle of attack of the wing, measured with respect to the actual direction of the approaching flow, will differ from the geometric angle of attack α by the magnitude of the downwash angle $\Delta\alpha_{av}$

$$\alpha_{\text{ист}}=\alpha-\Delta\alpha_{\text{ср}}. \tag{16.2}$$

According to the Zhukovskiy theorem, the force with which a plane-parallel ideal-fluid stream flowing over a wing presses on the wing is equal in magnitude to the product of the fluid density by the magnitude of the flow velocity at infinity and by the magnitude of the velocity circulation around the wing. The direction of this force is obtained if the velocity vector of the flow at infinity is rotated 90° opposite the direction of the circulation.

In accordance with the Zhukovskiy theorem, a force Y' perpendicular to the vector $\vec{V}_\infty$ must act on the wing.

The component of the force Y' perpendicular to the unperturbed flow direction

$$Y=Y'\cos\Delta\alpha_{\text{ср}}\approx Y', \tag{16.3}$$

is the wing lift force.

The component of the force Y' along the flow

$$X_i=Y'\sin\Delta\alpha_{\text{ср}}\approx Y\Delta\alpha_{\text{ср}} \tag{16.4}$$

is the wing induced drag.

Thus, when an ideal-fluid stream flows past a finite-span wing the presence of the free vortices trailing from the wing gives rise to a special sort of resistance which is not associated with viscosity — induced drag.

§16.4. Approximate Calculation of Induced Drag

We see from (16.4) that the wing induced drag is determined by the average downwash angle, whose magnitude in accordance with (16.1) is

$$\Delta\alpha_{cp}=-\frac{V_{y\,cp}}{V_\infty}.$$

For the approximate determination of the average downwash velocity V_{yav}, we replace the wing by the simplest vortex system — the horseshoe vortex. The action of this horseshoe vortex must cause the same lift and induced drag as the real wing (Figure 16.8).

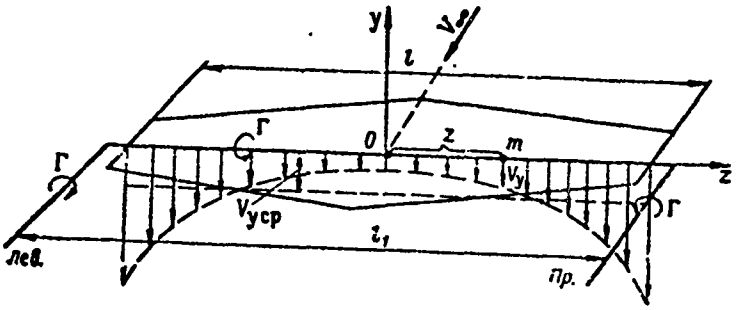

Figure 16.8. Illustration for calculating average downwash velocity

According to the Zhukovskiy theorem the formula for determining the lift force of the bound vortex, expressed in terms of the circulation Γ of the horseshoe vortex and the distance l_1 between the free vortices, has the form

$$Y=\rho V_\infty \Gamma l_1.$$

On the other hand, the wing lift can be expressed in terms of the wing lift coefficient c_y

$$Y=c_y\frac{\rho V_\infty^2}{2}S,$$

where S — is the wing area.
Equating the right sides, we obtain the so-called coupling equation

$$\Gamma=\frac{1}{2}c_y\frac{S}{l_1}V_\infty. \qquad (16.5)$$

Thus, the value of the horseshoe vortex circulation, i.e., the average circulation along the wing span, is found from the condition that the specified lift be provided.

A more detailed analysis (not presented here) shows that, for the induced drags of the horseshoe vortex and the real wing to be equal, it is necessary that the distance l_1 between the free vortices be somewhat greater than the wing span l

$$l_1=lk, \text{ where } k>1.$$

The quantity k depends on the wing planform and aspect ratio, and varies in the range from 1.02 to 1.04.

The average velocity across the span caused by the free vortices is

$$V_{y\,cp}=\frac{1}{l}\int_{-\frac{l}{2}}^{+\frac{l}{2}}V_y(z)dz.$$

We calculate the velocity $V_y(z)$ induced at an arbitrary point m, lying on the lifting vortex line (Figure 16.8), by the Biot-Savart law, applying it in turn to the left and right free vortices. Noting that the free vortices are semi-infinite, we can write for $V_y(z)$

$$V_y(z)=V_{y\,np}(z)+V_{y\,л}(z)=-\frac{\Gamma}{4\pi}\left(\frac{1}{\frac{l_1}{2}+z}+\frac{1}{\frac{l_1}{2}-z}\right).$$

This relation shows that as we approach the right vortex the quantity $V_y(z)$ grows as a result of the increase of V_{yr}, and at the same time V_{yz} decreases. With approach to the left vortex (here z is negative) $V_y(z)$ grows as a result of the increase of V_{yl}. Figure 16.8 shows the variation of V_y along the wing span.

Now let us substitute the value of $V_y(z)$ into the expression for V_{yav}

$$V_{y\,cp} = -\frac{\Gamma}{4\pi l}\left(\int_{-\frac{l}{2}}^{+\frac{l}{2}} \frac{dz}{\frac{l_1}{2}+z} + \int_{-\frac{l}{2}}^{+\frac{l}{2}} \frac{dz}{\frac{l_1}{2}-z}\right) =$$

$$= -\frac{\Gamma}{2\pi l} \ln \frac{l_1+l}{l_1-l}.$$

We have for the average downwash angle

$$\Delta\alpha_{cp} = -\frac{V_{y\,cp}}{V_\infty} = \frac{\Gamma}{2\pi l V_\infty} \ln \frac{l_1+l}{l_1-l}.$$

If we now substitute in place of the circulation Γ its Expression (16.5), we obtain

$$\Delta\alpha_{cp} = \frac{c_y S}{4\pi l l_1} \ln \frac{l_1+l}{l_1-l}.$$

Expressing l_1 in terms of l ($l_1 = lk$) and then replacing l^2/S by λ (aspect ratio), we obtain

$$\Delta\alpha_{cp} = \frac{c_y}{4\pi\lambda} \frac{1}{k} \ln \frac{k+1}{k-1}.$$

If we consider that k varies in the range 1.02 - 1.04 as a function of the wing planform, then $\frac{1}{k} \ln \frac{k+1}{k-1}$ amounts to a quantity somewhat greater than 4. Then

$$\frac{1}{k}\ln\frac{k+1}{k-1}=4(1+\Delta).$$

where Δ depends on the wing planform.

The formula for determining the average downwash angle takes the form

$$\Delta\alpha_{cp}=\frac{c_y}{\pi\lambda}(1+\Delta). \tag{16.6}$$

We see from this formula that the larger the aspect ratio λ, the smaller is the downwash angle $\Delta\alpha_{av}$. In the particular case of a wing of infinite span $\lambda \to \infty$, and therefore $\Delta\alpha_{av} \to 0$.

Substituting into (16.4) in place of $\Delta\alpha_{av}$ * its value from (16.6) and replacing Y, we obtain the expression for the induced drag

$$X_i=Y\Delta\alpha_{cp}=\frac{c_y^2}{\pi\lambda}\frac{\rho V_\infty^2}{2}S(1+\Delta).$$

Hence the induced drag coefficient is

$$c_{xi}=\frac{X_i}{\frac{\rho V_\infty^2}{2}S}=\frac{c_y^2}{\pi\lambda}(1+\Delta). \tag{16.7}$$

We see that the approximate calculation yields values of c_{xi} and $\Delta\alpha_{av}$ which are accurate to within the factor 1 + Δ, somewhat larger than one.

Analyzing the relations obtained, we can draw the following very important conclusions:

1. The magnitude of the induced drag is larger for larger c_y and varies parabolically as a function of c_y. The curve representing

*Translator's Note: Δ missing in original text.

this relationship is called the induced drag parabola (Figure 16.9). In real viscous fluid flow, in addition to the induced drag the wing also experiences resistance resulting from viscosity — profile drag. Therefore the total drag coefficient of the finite-span wing can be represented in the form of the sum

$$c_x = c_{xi} + c_{xp}.$$

If the wing polar is given, with the aid of the induced drag parabola we can separate the profile drag coefficient c_{xp} from the total drag coefficient c_x.

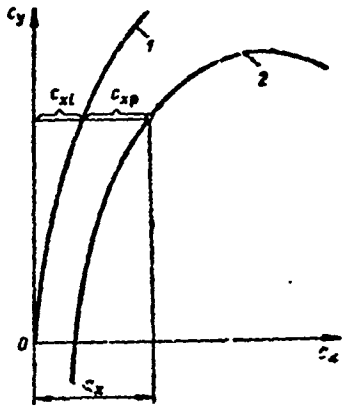

Figure 16.9. Induced drag parabola (1) and wing polar (2)

2. The magnitude of the induced drag depends markedly on the wing aspect ratio λ. For wings with large aspect ratios c_{xi} is smaller. In this connection, the wing aspect ratio is made as large as possible in order to obtain wings with large values of the aerodynamic efficiency $K = \frac{c_y}{c_x}$. We must bear in mind that this entire discussion relates to wings which do not have structural elements (endplates, for example) which reduce the induced drag. Since the induced drag is determined entirely by the presence of the free vortices, which appear as a result of air crossflow around the wingtips, the installation of endplates at the wingtips prevents this crossflow and reduces the induced drag.

§16.5. Calculation of Forces Acting on Finite-Span Wing with Variable Circulation

The theory of the finite-span wing presented above can be considered a first-approximation theory. In a more exact calculation of the forces acting on the wing, it is necessary to take into account the variation of the circulation and downwash angle along the span.

In deriving the computational formulas for the finite-span wing with variable circulation (vortex sheet scheme), we shall assume that:

a) the air flow around the wing is induced by a system of vortices;

b) the free vortices of the sheet are rectilinear and directed along the velocity of the undisturbed stream;

c) each wing section has its own angle of attack and is independent of the other sections.

These assumptions make it possible to apply the Zhukovskiy lift theorem to each of the wing elements. We imagine a wing of finite span in reversed flow (Figure 16.10). A vortex sheet with running intensity $q=\frac{d\Gamma}{dz}$, which is variable along the span, extends behind this wing. We isolate on the vortex sheet a narrow strip at the distance z_1 from the root section. The circulation around the contour enclosing this strip is

$$d\Gamma=\frac{d\Gamma(z_1)}{dz_1}dz_1.$$

At an arbitrary point B on the Oz axis, defined by the coordinate z, the vortex strip induces the velocity

$$dV_y(z)=\frac{\frac{d\Gamma(z_1)}{dz_1}dz_1}{4\pi(z_1-z)}.$$

The total velocity induced at the point B by the entire vortex sheet is(1)

$$V_y(z)=\frac{1}{4\pi}\int_{-\frac{l}{2}}^{\frac{l}{2}}\frac{\frac{d\Gamma(z_1)}{dz_1}dz_1}{z_1-z}. \qquad (16.8)$$

Hence we obtain the downwash angle at the section z (we neglect downwash angle variation along the wing chord)

$$\Delta\alpha(z)=-\frac{V_y(z)}{V_\infty}=-\frac{1}{4\pi V_\infty}\int_{-\frac{l}{2}}^{\frac{l}{2}}\frac{\frac{d\Gamma(z_1)}{dz_1}dz_1}{z_1-z}. \qquad (16.9)$$

Since the downwash angle is variable along the wing span, the true angle of attack will also be variable

$$\alpha_{\text{ист}}=\alpha-\Delta\alpha(z).$$

The geometric angle of attack at a given section can be represented in the form of the sum of the geometric angle of attack α_r of the root section and the geometric twist angle e(z)

$$\alpha=\alpha_r+e(z).$$

Then the true angle of attack at a given section has the expression

$$\alpha_{\text{ист}}=\alpha_r+e(z)-\Delta\alpha(z). \qquad (16.10$$

After determining the magnitude of the downwash angle at the individual wing sections, we can calculate the forces acting on the wing. These forces are determined as the geometric sum of the forces acting on the elementary sections of the wing.

Footnote (1) appears on page 147.

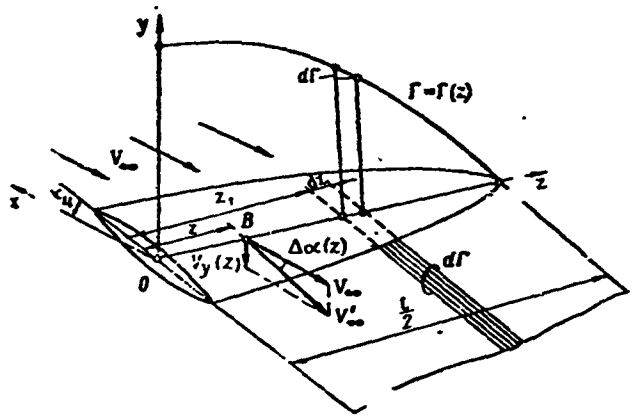

Figure 16.10. Definition of induced velocity at arbitrary wing section

In calculating the forces acting on a wing element, in accordance with the hypothesis of plane sections we shall assume that the given wing element operates like the corresponding element of a cylindrical wing of infinitely long span and that the forces acting on the wing element are completely defined by the value of the downwash angle at this element. The hypothesis of plane sections yields quite adequate accuracy for wings with $\lambda \geqslant 4$.

According to the Zhukovskiy theorem the force acting on a wing element is

$$dY' = \varrho \Gamma(z) V'_\infty dz,$$

where

$$\vec{V}'_\infty = \vec{V}_\infty + \vec{V}_y(z);$$

$\Gamma(z)$ — is the circulation around the contour enclosing the wing at the selected element section.

The force dY' is directed perpendicular to the direction of the vector $\vec{V}'_\infty$ (Figure 16.11). Resolving dY' into the corresponding

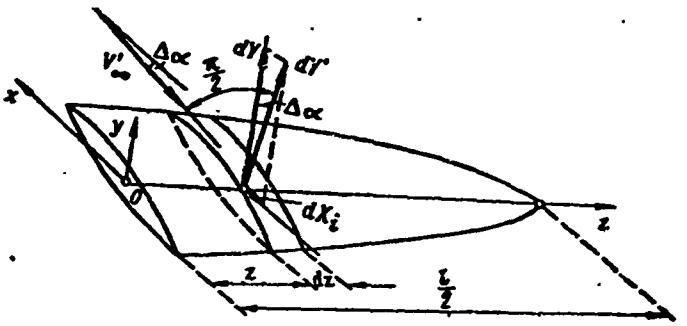

Figure 6.11. Calculation of forces acting on wing

components, we obtain the element lift

$$dY = \varrho\Gamma(z)V'_\infty \cos\Delta\alpha(z)\,dz$$

and induced drag

$$dX_i = \varrho\Gamma(z)V'_\infty \sin\Delta\alpha(z)\,dz.$$

Since the angle $\Delta\alpha(z)$ is small, these formulas may be written as

$$dY = \varrho\Gamma(z)V_\infty\,dz;$$
$$dX_i = \varrho\Gamma(z)V_\infty\Delta\alpha(z)\,dz = -\varrho\Gamma(z)V_y(z)\,dz.$$

Then the total lift is

$$Y = \varrho V_\infty \int_{-\frac{l}{2}}^{\frac{l}{2}} \Gamma(z)\,dz, \tag{16.11}$$

and the total induced drag

$$X_i = -\varrho \int_{-\frac{l}{2}}^{\frac{l}{2}} \Gamma(z)V_y(z)\,dz. \tag{16.12}$$

If we substitute into (16.12) in place of $V_y(z)$ its value from (16.8), we can write the expanded expression for the induced drag

$$X_i = -\varrho \int_{-\frac{l}{2}}^{\frac{l}{2}} \Gamma(z) \left[\frac{1}{4\pi} \int_{-\frac{l}{2}}^{\frac{l}{2}} \frac{\frac{d\Gamma(z_1)}{dz_1} dz_1}{z_1 - z} \right] dz. \qquad (16.13)$$

The expressions obtained for Y and X_i make it possible to calculate the forces acting on the wing in ideal-fluid flow with account for spanwise variation of the circulation and downwash angle.

In this case the accuracy of the calculation will depend on how close the actual wing operating conditions are to the assumptions made (possibility of using the hypothesis of plane sections, smallness of the downwash angle, neglecting the downwash angle variation along the wing chord).

§16.6. Determining Circulation Distribution Along Wing Span

To determine the wing lift and induced drag using (16.11), (16.13) we must find the circulation distribution $\Gamma(z)$ along the wing span.

Let us examine a wing element at an arbitrary spanwise location as a segment of a cylindrical wing of infinite span with the given profile (see Figure 16.11). We shall assume that the aerodynamic characteristics of the individual profile sections comprising the wing are known.

The lift force developed on the selected element can be expressed in terms of the circulation using the Zhukovskiy theorem or in terms of the coefficient c_y

$$dY=\varrho\Gamma(z)V_\infty dz;$$

$$dY=c_y(z)\frac{\varrho V_\infty^2}{2}b(z)dz,$$

where b(z) — is the wing chord at the given section.

Equating the right sides of the two expressions for dY, we obtain the coupling equation for the wing section

$$\Gamma(z)=\frac{1}{2}c_y(z)b(z)V_\infty. \qquad (16.14)$$

In accordance with (12.16) the expression for $c_y(z)$ can be written as

$$c_y(z)=c_y^\alpha(z)\alpha_a'(z), \qquad (16.15)$$

where $c_y^\alpha = \frac{\partial c_y}{\partial \alpha}$ in the range of angles of attack corresponding to the linear segment of the curve $c_y(z) = f(\alpha)$;

$\alpha_a'(z)$ — is the true angle of attack at the given section.

The true angle of attack (Figure 16.12) is expressed by the relation

$$\alpha_a'(z)=\alpha_a(z)-\Delta\alpha(z), \qquad (16.16)$$

where $\alpha_a(z)$ — is the aerodynamic angle of attack at the given section measured between the line-of-flight direction and the direction of the aerodynamic chord for the given section;

$\Delta\alpha(z)$ — is the downwash angle at the given section.

If we now substitute into (16.14) $c_y(z)$ from (16.15), replacing therein the true angle of attack $\alpha'_a(z)$ by its value from (16.16) with account for (16.9), we obtain

$$\Gamma(z)=\frac{1}{2}c_y^\alpha(z)b(z)V_\infty\left(\alpha_a(z)+\frac{1}{4\pi V_\infty}\int_{-\frac{l}{2}}^{\frac{l}{2}}\frac{\frac{d\Gamma(z_1)}{dz_1}dz_1}{z_1-z}\right). \qquad (16.17)$$

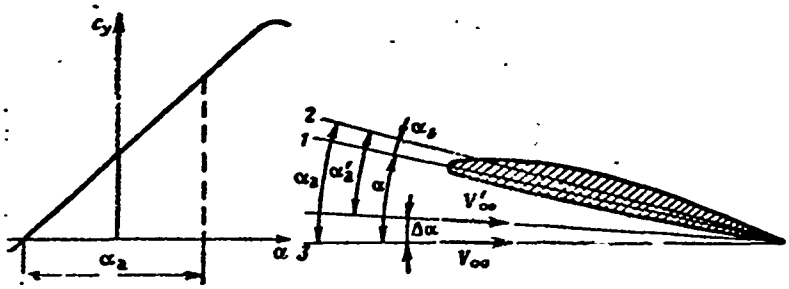

Figure 16.12. Determining true aerodynamic angle of attack: 1 — geometric chord direction; 2 — aerodynamic chord direction; 3 — direction of flight

This equation is termed the basic integrodifferential equation of the finite-span wing. This equation relates the unknown function $\Gamma(z)$ with known quantities and thus makes it possible to find the circulation distribution along the wing span.

In the general case it is very difficult to find the exact solution of (16.17). There are several approximate solutions of the basic equation, obtained by introducing simplifying assumptions or using various sorts of artificial methods (Glauert-Treffetz, Multhopp, B. N. Yur'yev, V. V. Golubev, G. F. Burago, S. G. Nuzhin, and other methods). An experimental method for solving (16.17) has also been proposed, based on the analogy between hydrodynamic and electrodynamic phenomena.

Most of the solution methods are based either on an approximate representation of the function $\Gamma(z)$ or the wing contour in series form. For example, the Glauert-Treffetz method involves representing the unknown function $\Gamma(z)$ in the form of a trigonometric sine series

$$\Gamma(z)=2lV_\infty\sum_{n=1}^{\infty}A_n\sin n\theta, \tag{16.18}$$

where θ — is a new variable, connected with the variable z (Figure 16.13) by the relation

$$z=-\frac{l}{2}\cos\theta;$$

A_n — are constant coefficients of the series, subject to determination.

Since the terms of the series (16.18) decay rapidly, to express the function $\Gamma(z)$ with a satisfactory degree of accuracy we need only take the sum of a comparatively small number m of terms rather than the series with an infinite number of terms

$$\Gamma(z)\approx 2lV_\infty \sum_{n=1}^{m} A_n \sin n\theta. \qquad (16.19)$$

To determine the m unknown coefficients, which must be such that $\Gamma(z)$ satisfies (16.17), we must write m algebraic equations. These equations can be obtained by substituting into (16.17) in place of $\Gamma(z)$ its value from (16.19) sequentially for m different wing sections. It can be shown that for a wing with symmetric circulation distribution along the span the terms of the series with even indices vanish, and in this case the required number of equations is reduced. The values of the series coefficients can be obtained by solving the system of algebraic equations.

Thus, the approximate expression for the circulation has the form

$$\Gamma\approx 2lV_\infty(A_1\sin\theta+A_3\sin 3\theta+\ldots+A_m\sin m\theta).$$

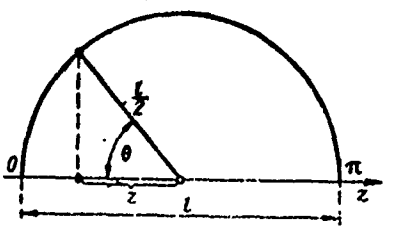

Figure 16.13. Geometric representation of connection between variables z and θ

§16.7. Wing Lift and Induced Drag Coefficients with Account for Circulation Distribution Along the Span

Knowing the circulation distribution along the span, we can find the forces acting on the wing. Converting in (16.11) from the variable z to the variable θ($dz = \frac{l}{2} \sin\theta d\theta$) and substituting in place of the circulation $\Gamma(z)$ its expression from (16.18), we obtain

$$Y = \varrho V_\infty^2 l^2 \sum_{n=1}^{\infty} A_n \int_0^{\pi} \sin n\theta \sin\theta \, d\theta.$$

Since

$$\int_0^{\pi} \sin n\theta \sin\theta \, d\theta = \begin{cases} \frac{\pi}{2} \text{ for } n=1 \\ 0 \text{ for } n \neq 1, \end{cases}$$

then

$$Y = \varrho V_\infty^2 l^2 \frac{\pi}{2} A_1.$$

Then the wing lift coefficient

$$c_y = \frac{Y}{\frac{\varrho V_\infty^2}{2} S} = \pi \frac{l^2}{S} A_1.$$

Replacing $\frac{l^2}{S}$ by λ, we finally obtain

$$c_y = \pi \lambda A_1. \tag{16.20}$$

This expression for c_y shows that the total lift developed by a finite-span wing is determined by the coefficient of the first term of the circulation expansion into a sine series. Substituting in place of the circulation, its expression (16.18) into the Formula (16.13) for determining induced drag and replacing the variables

z_1 and z by the variable θ, after straightforward but somewhat tedious transformations we obtain the expression for X_1 in the form

$$X_1=\varrho V_\infty^2 l^2 \frac{\pi}{2}\sum_{n=1}^{\infty} nA_n^2. \tag{16.21}$$

Hence the induced drag coefficient

$$c_{xi}=\frac{X_1}{\frac{\varrho V_\infty^2}{2}S}=\frac{\pi l^2}{S}\sum_{n=1}^{\infty} nA_n^2,$$

or

$$c_{xi}=\frac{\pi l^2}{S}A_1^2\left(1+\sum_{n=2}^{\infty}\frac{nA_n^2}{A_1^2}\right).$$

If we replace $\frac{l^2}{S}$ by λ and express A_1 in terms of c_y using (16.20), then the expression for the induced drag coefficient takes the form

$$c_{xi}=\frac{c_y^2}{\pi\lambda}(1+\delta), \tag{16.22}$$

where

$$\delta=\sum_{n=2}^{\infty}\frac{nA_n^2}{A_1^2}.$$

Expression (16.22) for c_{xi} coincides in form with the Expression (16.7) for c_{xi}, obtained without account for the variation of the circulation and downwash along the span. Account for the circulation and downwash angle distribution along the span makes it possible to refine the magnitude of the factor 1 + Δ. The magnitude of the planform correction coefficient δ is usually small in comparison with one, and in the general case depends on the wing geometric characteristics, angle of attack α, and c_y.

The expression for the average downwash angle has the form

$$\Delta\alpha_{c_p}=\frac{c_y}{\pi\lambda}(1+\tau), \tag{16.23}$$

where the magnitude of the aspect ratio correction factor τ depends on the circulation distribution along the span and equals

$$\tau=\sum_{n=2}^{\infty}\frac{A_n}{A_1}. \tag{16.24}$$

The factors $\frac{1+\tau}{\pi}$ and $\frac{1+\delta}{\pi}$ for wings of different planform are shown in Table 16.1.

TABLE 16.1.

Wing planform	$\frac{1+\tau}{\pi}$	$\frac{1+\delta}{\pi}$
Elliptic	0.318	0.318
Trapezoidal (η = 2 - 3)	0.318	0.318
Rectangular (λ = 5 - 8)	0.375	0.335
Rectangular with rounded tips	0.365	0.318

§16.8. Optimal Wing Planform

By optimal wing we mean the wing having the smallest induced drag coefficient for given values of the lift coefficient and wing aspect ratio. We see from (16.22) that the magnitude of the induced drag coefficient will be minimal for $\delta = 0$, i.e., for

$$\sum_{n=2}^{\infty}\frac{nA_n^2}{A_1^2}=0.$$

This means that all the coefficients of the expansion of $\Gamma(z)$ into a sine series, other than A_1, must vanish. In this case

$$\Gamma = 2lV_\infty A_1 \sin\theta. \tag{16.25}$$

Hence for $\theta = \frac{\pi}{2}$ (at the wing root section)

$$\Gamma_0 = 2lV_\infty A_1 = \Gamma_{max}.$$

Then (16.25) takes the form

$$\Gamma = \Gamma_0 \sin\theta. \tag{16.25'}$$

Converting from the coordinate θ to the coordinate $z(z = -\frac{l}{2}\cos\theta)$, we obtain

$$\Gamma = \Gamma_0 \sin\theta = \Gamma_0 \sqrt{1-\cos^2\theta} = \Gamma_0 \sqrt{1-\frac{z^2}{\left(\frac{l}{2}\right)^2}},$$

or

$$\frac{\Gamma^2}{\Gamma_0^2} + \frac{z^2}{\left(\frac{l}{2}\right)^2} = 1. \tag{16.26}$$

Thus, the optimal wing is a wing for which the circulation varies elliptically along the span (along the z axis) (Figure 16.14).

For the wing with elliptic circulation distribution, the induced drag coefficient is given by the formula

$$c_{xi} = \frac{c_y^2}{\pi\lambda},$$

and the downwash angle is

$$\Delta\alpha = \frac{c_y}{\pi\lambda}.$$

Consequently, c_{xi} and $\Delta\alpha$ do not vary along the span.

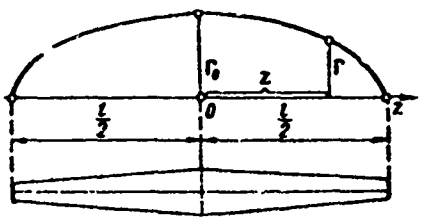

Figure 16.14. Elliptic circulation distribution along wing span

It follows from the coupling equation

$$\Gamma(z)=\frac{1}{2}c_y^{\alpha}(z)\alpha'_a(z)b(z)V_\infty$$

that an elliptic circulation distribution along the span can be achieved by varying the quantities $c^{\alpha}_{y}(z)$, α'_a, $b(z)$. To obtain an elliptic circulation distribution for the same values of c^{α}_{y} for all wing profile sections along the span and for the same true angle of attack $\alpha'_a(z)$, it is necessary that the chords vary in an elliptic fashion along the span, i.e., the wing must have an elliptic planform.

The same values of c_y^{α} for all the profile sections can be obtained by using the same profiles along the span, and the same values of α'_a can be obtained by using twist [see (16.16)].

For the wing of elliptic planform it is not mandatory that constant values of α'_a and c_y^{α} be obtained along the span — it is only necessary that their product $c_y^{\alpha}(z) \cdot \alpha'_a(z)$ be constant, which is achieved by a combination of twist and choice of the profiles along the span.

For the wing of rectangular planform (b = const along the span) an elliptic circulation distribution can be obtained only by providing an elliptic variation of the product $c_y^{\alpha}(z) \cdot \alpha'_a(z)$, which is achieved by a combination of twist and choice of the profiles. On modern wings elliptic or nearly elliptic circulation distribution is achieved by simultaneous variation of all three factors: $c_y^{\alpha}(z)$, α'_a, and $b(z)$.

We note that in those cases in which part of the wing is occupied by the fuselage, engine nacelles, and landing gear nacelles it is very difficult to obtain the optimal circulation distribution

along the span. In this case the value of δ may be quite large. We also note that for nonelliptic wings, profile selection and twist can provide an elliptic circulation distribution only at a particular angle of attack.

§16.9. Conversion of Wing Aerodynamic Characteristics from One Aspect Ratio to Another

It is known that the wing drag coefficient is

$$c_x = c_{xi} + c_{xp}.$$

The fact that the profile drag is independent of the aspect ratio and wing shape makes it possible to convert the known aerodynamic characteristics for a wing with aspect ratio λ_1 to a wing with aspect ratio λ_2, which facilitates considerably the use of wind tunnel test results of a stock model with standard λ (usually equal to 5).

Let us assume that the aerodynamic characteristics are known for a wing with aspect ratio λ_1. We need to convert the aerodynamic characteristics of the known wing with aspect ratio λ_1 to a wing made up of the same profiles but having different planform and different relative aspect ratio λ_2.

If the wings operate at the same average true angles of attack

$$\alpha_{ист1} = \alpha_{ист2} = \alpha_{ист},$$

the coefficients c_y are the same for the two wings.

Let $\Delta\alpha_1$ and $\Delta\alpha_2$ be the average downwash angles at the wings, then

$$\alpha_{ист} = \alpha_{ист1} = \alpha_1 - \Delta\alpha_1;$$

$$\alpha_{ист} = \alpha_{ист2} = \alpha_2 - \Delta\alpha_2.$$

Hence

$$\alpha_1-\alpha_2=\Delta\alpha_1-\Delta\alpha_2,$$

or

$$\alpha_2=\alpha_1-(\Delta\alpha_1-\Delta\alpha_2).$$

In accordance with (16.23)

$$\Delta\alpha_1=\frac{c_y}{\pi\lambda_1}(1+\tau_1);$$

$$\Delta\alpha_2=\frac{c_y}{\pi\lambda_2}(1+\tau_2),$$

where τ_1 and τ_2 — are the average values of τ, determined from (16.24) for both wings.

Then

$$\left.\begin{aligned}\alpha_1-\alpha_2&=\frac{c_y}{\pi}\left(\frac{1+\tau_1}{\lambda_1}-\frac{1+\tau_2}{\lambda_2}\right),\\ \text{hence}\qquad \alpha_2&=\alpha_1-\frac{c_y}{\pi}\left(\frac{1+\tau_1}{\lambda_1}-\frac{1+\tau_2}{\lambda_2}\right).\end{aligned}\right\} \qquad (16.27)$$

The smaller the aspect ratio, the larger the angles of attack must be to obtain the required value of the lift coefficient.

For wings with different aspect ratios but with the same planform, the zero lift angles α_0 are the same. This means that the curves of the functions $c_y = f(\alpha)$ for the different wings start from the same point on the abscissa axis but have different slopes — the smaller the aspect ratio, the flatter is the curve (Figure 16.15).

The slope of the linear part of the curve, equal to the derivative $dc_y/d\alpha$, can be found as follows. The equations of the linear parts of the curve for the wing of infinite span ($\lambda = \infty$) and for the wing with finite value of λ can be written in the form

$$\left.\begin{aligned}c_y&=c^{\alpha}_{y_{\lambda=\infty}}(\alpha-\alpha_0);\\ c_y&=c^{\alpha}_{y}(\alpha-\alpha_0+\Delta\alpha),\end{aligned}\right\} \qquad (16.28)$$

where $c^{\alpha}_{y} = \dfrac{\partial c_y}{\partial \alpha}$ for the wing with finite aspect ratio.

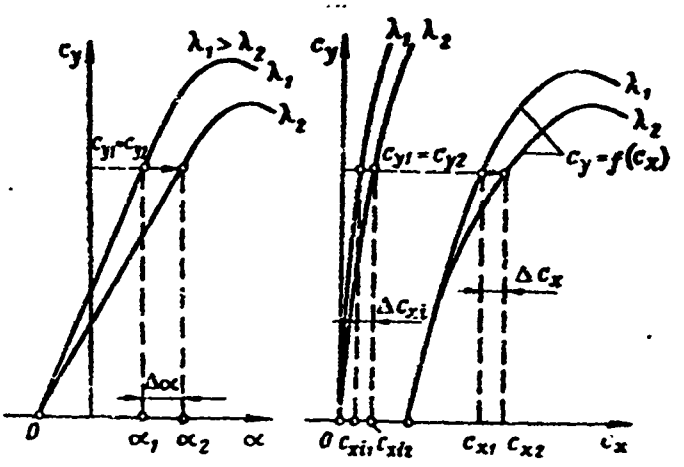

Figure 16.15. Conversion of wing aerodynamic characteristics to different aspect ratio

Considering that the magnitude $\Delta\alpha$ of the downwash angle is defined by (16.23) and excluding from (16.28) the quantity $\alpha - \alpha_0$, we obtain

$$c_y^\alpha = \frac{c_{y\lambda=\infty}^\alpha}{1 + \frac{c_{y\lambda=\infty}^\alpha}{\pi\lambda}(1+\tau)}. \tag{16.29}$$

Since the partial derivative c_y^α is the slope of the linear part of the curve $c_y = f(\alpha)$, from (16.29) we can conclude that with reduction of the wing aspect ratio λ the linear part of the relation $c_y = f(\alpha)$ becomes flatter.

The drag coefficients have the following expressions for the two wings

$$c_{x1} = c_{xp} + c_{xi1};$$
$$c_{x2} = c_{xp} + c_{xi2}.$$

Since the wings are made up of the same profiles, the profile part of the coefficient c_x is the same for both.

Then

$$c_{x1}-c_{x2}=c_{xi1}-c_{xi2},$$

or

$$c_{x2}=c_{x1}-(c_{xi1}-c_{xi2}).$$

In accordance with (16.22) the induced drag coefficients equal

$$c_{xi1}=\frac{c_y^2}{\pi\lambda_1}(1+\delta_1);$$

$$c_{xi2}=\frac{c_y^2}{\pi\lambda_2}(1+\delta_2).$$

Hence

$$\Delta c_{xi}=c_{xi1}-c_{xi2}=\frac{c_y^2}{\pi}\left(\frac{1+\delta_1}{\lambda_2}-\frac{1+\delta_2}{\lambda_1}\right),$$

or

$$c_{x2}=c_{x1}-\frac{c_y^2}{\pi}\left(\frac{1+\delta_1}{\lambda_1}-\frac{1+\delta_2}{\lambda_2}\right). \qquad (16.30)$$

Figure 16.15 shows a typical construction illustrating the use of (16.27), (16.30) to convert the aerodynamic characteristics from the aspect ratio λ_1 to the aspect ratio λ_2 ($\lambda_1 > \lambda_2$). We note that this technique can also be used to obtain the characteristics of the wing of infinite aspect ratio (profile).

§16.10. Moment of Wing of Arbitrary Planform

The moment of an airplane wing differs from the moment of the profile, since the wing planform (sweep, aspect ratio, taper ratio,

etc.) and geometric twist affect the magnitude of its moment. The wing may be composed of different profiles (aerodynamic twist).

The longitudinal moment M_z of the aerodynamic forces acting on the wing under actual conditions is defined relative to the Oz axis, passing through the airplane center of mass. However, in the design process and in several other cases the position of the mass center is not known. Therefore the wing longitudinal moment is calculated about an axis passing thorugh some arbitrary coordinate origin, for example, coinciding with the leading edge of the wing root section.

Let us calculate the longitudinal moment M_{z1} of a wing about the Oz_1 axis of the body coordinate system with origin located at the leading edge of the root section (Figure 16.16).

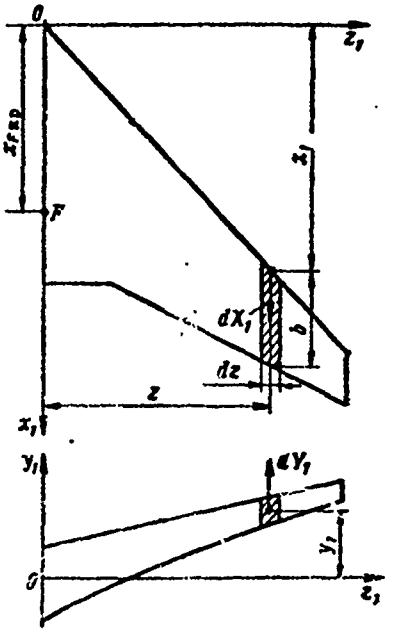

Figure 16.16. Determining wing longitudinal moment

On a wing element of width dz and chord b, located at the distance z from the root chord, there act the longitudinal moment $dM_z = c_m qbdS$ and also the lift $dY_1 = c_{y1} qdS$ and drag $dX_1 = c_{x1} qdS$, applied at the leading edge of the wing element. The arm of the lift force about the Oz_1 axis is x_1 and that of the drag force is y_1.

Considering that

$$dS = bdz;\ c_m = c_{m0} + mc_y;$$
$$c_y \approx c_{y1},$$

where b, c_{m0}, m, c_y vary along the span and depend on z, and defining a climbing moment, tending to raise the wing leading edge, as a positive and a diving moment, tending to lower the wing leading edge, as negative, we obtain the expression for finding the total longitudinal moment about the Oz_1 axis in the form

$$M_{z1}=\int_{-\frac{l}{2}}^{\frac{l}{2}} c_m q b^2 dz-\int_{-\frac{l}{2}}^{\frac{l}{2}} c_{y1} q x_1 b\, dz+$$

$$+\int_{-\frac{l}{2}}^{\frac{l}{2}} c_{x1} q y_1 b\, dz=q\left(\int_{-\frac{l}{2}}^{\frac{l}{2}} c_{m0} b^2 dz+\right.$$

$$\left.+\int_{-\frac{l}{2}}^{\frac{l}{2}} c_{y1}(m_{ce_v} b-x_1) b\, dz+\int_{-\frac{l}{2}}^{\frac{l}{2}} c_{x1} b y_1 dz\right). \qquad (16.31)$$

The wing focus, just like the profile focus, is the point of application of the wing lift increment when the angle of attack is changed within the linear part of the relation

$$c_y=f(\alpha).$$

If we shift the total aerodynamic force to the wing focus (point F in Figure 16.16), the expression for finding the wing longitudinal moment takes the form

$$M_{z1}=M_{z0}-Y_1 x_{F\,кр}+X_1 y_{F\,кр}. \qquad (16.32)$$

Equating the last two terms in the right sides of (16.31) and (16.32) and expressing the lift and drag respectively in terms of c_{y1} and c_{x1}, we obtain the focus coordinates in the adopted coordinate system

$$\left.\begin{aligned} x_{F\,wp} &= \frac{1}{S}\int_{-\frac{l}{2}}^{\frac{l}{2}} \frac{c_{yl}}{c_{yl\,wp}}(x_1+x_F)b\,dz; \\ y_{F\,wp} &= \frac{1}{S}\int_{-\frac{l}{2}}^{\frac{l}{2}} \frac{c_{xl}}{c_{xl\,wp}} b y_1 dz. \end{aligned}\right\} \qquad (16.33)$$

Here $x_F = -mb$ at each wing section.

For a flat wing with constant profile $c_{yl\,w} \approx c_{yl}$ and $c_{xl\,w} \approx c_{xl}$, then (16.33) take the form

$$\left.\begin{aligned} x_{F\,wp} &= \frac{1}{S}\int_{-\frac{l}{2}}^{\frac{l}{2}} (x_1+x_F)b\,dz; \\ y_{F\,wp} &= \frac{1}{S}\int_{-\frac{l}{2}}^{\frac{l}{2}} y_1 b\,dz. \end{aligned}\right\} \qquad (16.34)$$

For a wing with straight leading edge $x_1 = 0$ in (16.33) and (16.34); for wings with positive sweep, $x_1 > 0$ and the focus shifts aft. These formulas do not take into account the mutual influence of the sections and the influence of tip effects on wing focus location.

Experiment shows that for the wing of infinite span $x_F \approx 0.25$ b, while at the tip sections of the finite-span wing the position of the focus changes with change of the sweep, taper, and aspect ratio.

In aerodynamic calculations the profile moment characteristics, as shown in Chapter XII, are evaluated with the aid of the longitudinal moment coefficient m_z, obtained from the relation

$$M_z = m_z qSb.$$

For the wing of arbitrary planform, the chord is variable along the span. Therefore, in order to compare the moment characteristics of different wings we need a standard approach to the definition of the magnitude of the chord b for determining the moment coefficient. For this purpose we use the so-called mean aerodynamic chord b_A, equal to the chord of a plane rectangular wing which is equivalent to the original wing, i.e., having the same area, the same forces Y_1 and X_1, and the same longitudinal moment M_{z1}.

We shift the aerodynamic forces to the leading edge of the equivalent wing. Then the moment relative to the axis (Figure 16.17), passing through the leading edge of the root section of the equivalent wing, is

$$M_{z1}=c_{m\,кр}qSb_A-c_{y1кр}\times \\ \times qSx_A+c_{x1кр}qSy_A$$

or, considering that

$$c_{m\,кр}=c_{m0кр}+m_{кр}c_{y1кр},$$
$$M_{z1}=c_{m0кр}qSb_A- \\ -c_{y1}qS\,(x_A-m_{кр}b_A)+ \\ +c_{x1кр}qSy_A. \qquad (16.35)$$

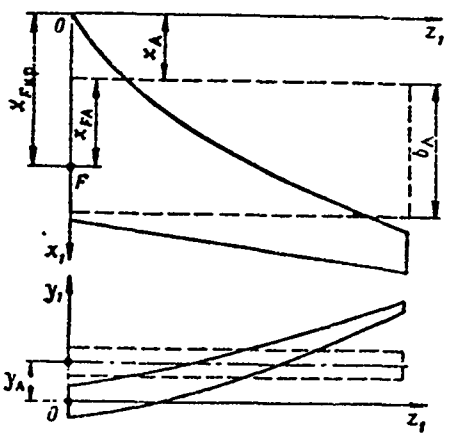

Figure 16.17. Mean aerodynamic chord (b_A)

Equating term-by-term the right sides of (16.31) and (16.35), we obtain the magnitude of the mean aerodynamic chord b_A and the coordinates of its leading edge in the adopted coordinate system

$$\left.\begin{aligned} b_A &= \frac{1}{S}\int_{-\frac{l}{2}}^{\frac{l}{2}} \frac{c_{m0}}{c_{m0xp}} b^2\,dz; \\ x_A - m_{xp}b_A &= \frac{1}{S}\int_{-\frac{l}{2}}^{\frac{l}{2}} \frac{c_{y1}}{c_{y1xp}}(x_1+x_F)b\,dz = x_{F\,xp}; \\ y_A &= \frac{1}{S}\int_{-\frac{l}{2}}^{\frac{l}{2}} \frac{c_{x1}}{c_{x1xp}} by_1\,dz = y_{F\,xp}. \end{aligned}\right\} \qquad (16.36)$$

It follows from the last two relations that the focuses of the given wing and its equivalent wing coincide.

In the first approximation we can assume that

$$\frac{c_{m0}}{c_{m0xp}} = \frac{c_{y1}}{c_{y1xp}} = \frac{c_{x1}}{c_{x1xp}} = 1.$$

Then (16.36) takes the form

$$\left.\begin{aligned} b_A &= \frac{2}{S}\int_0^{\frac{l}{2}} b^2\,dz; \\ x_A - m_{xp}b_A &= x_{F\,xp} = \frac{2}{S}\int_0^{\frac{l}{2}} b(x_1+x_F)\,dz; \\ y_A &= y_F = \frac{2}{S}\int_0^{\frac{l}{2}} by_1\,dz. \end{aligned}\right\} \qquad (16.37)$$

Analysis of (16.37) from the geometric viewpoint makes it possible to obtain a quite simple technique for determining the magnitude and coordinates of the mean aerodynamic chord (Figure

16.18). For example, laying off on the lower extension of the root chord the magnitude of the tip chord and on the upper extension of the tip chord, the root chord, we connect the ends of the resulting segments and find the point of intersection of this line with the line connecting the midpoints of the root and tip chords. The chord drawn through the resulting point of intersection is then the MAC.

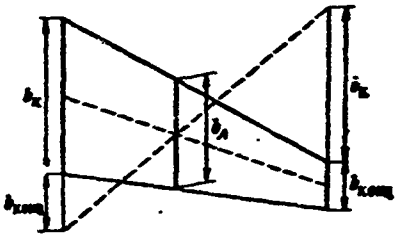

Figure 16.18. Geometric technique for finding MAC

REVIEW QUESTIONS

1. Explain the nature of induced drag. How does wing aspect ratio affect the magnitude of the induced drag?

2. Explain how the induced drag depends on angle of attack.

3. For what circulation distribution along the span is minimal induced drag obtained? What planform must the flat wing have in this case?

4. What methods do you know for the approximate solution of the integrodifferential equation of the finite-span wing?

PROBLEMS

1. Plot the wing polar in the range $0 < c_y < 1$. The wing aspect ratio $\lambda = 10$, profile drag coefficient $c_{xp} = 0.008$, and the coefficient $\delta = 0.03$.

2. For the conditions of the preceding problem, find graphically and analytically the maximal wing aerodynamic efficiency, optimal angle of attack, and the relation between the profile and induced drags in the case in which $\partial c_y/\partial\alpha = 5.0$ and the zero lift angle $\alpha_0 = 0°$.

Answer: $K_{max} = 30.9$; $\alpha_{opt} = 5.66°$; $c_{xp} = c_{xi}$.

3. An airplane polar for small angles of attack is given by the equation $c_x = 0.022 + 0.078\, c_y^2$. Find the lift coefficient, drag coefficient corresponding to the optimal angle of attack, and also the maximal efficiency of the airplane.

Solution. At the optimal angle of attack the efficiency $K = \frac{c_y}{c_x}$ is maximal and the reciprocal efficiency $\frac{1}{K} = \frac{c_x}{c_y}$ is minimal. The minimum of the quantity $1/K$ is found from the condition

$$\frac{d\left(\frac{1}{K}\right)}{d\alpha} = \frac{d\left(\frac{1}{K}\right)}{dc_y}\frac{dc_y}{d\alpha} = 0.$$

Since $\frac{dc_y}{d\alpha} \neq 0$, then

$$\frac{d\left(\frac{1}{K}\right)}{dc_y} = \frac{\frac{dc_x}{dc_y}}{c_y} - \frac{c_x}{c_y^2} = 0.$$

Using the problem conditions, we have

$$0{,}156 - \frac{0{,}022 + 0{,}078c_{y\,\text{кв}}^2}{c_{y\,\text{кв}}^2} = 0.$$

Hence

$$c_{y\,\text{кв}} = \sqrt{\frac{0{,}022}{0{,}078}} = 0{,}531;$$

$$c_{x\,\text{кв}} = 0{,}022 + 0{,}078 \cdot 0{,}282 = 0{,}044;$$

$$K_{max} = \frac{c_{y\,\text{кв}}}{c_{x\,\text{кв}}} = \frac{0{,}531}{0{,}044} = 12{,}07.$$

FOOTNOTES

Footnote (1) on page 124: This integral is improper; however its principal value can be obtained from the relation

$$V_y(z) = \frac{1}{4\pi} \lim_{\varepsilon \to 0} \left[\int_{-\frac{l}{2}}^{z-\varepsilon} \frac{\frac{d\Gamma(z_1)}{dz_1} dz_1}{z_1 - z} + \int_{z+\varepsilon}^{\frac{l}{2}} \frac{\frac{d\Gamma(z_1)}{dz_1} dz_1}{z_1 - z} \right].$$

This operation is justified physically by the fact that we neglect the effect of the vortex element on itself.

CHAPTER XVII

SWEPT WINGS IN SUBSONIC FLOW

§17.1. Concept of Wing Sweep and Its Effect

Experimental data and also actual flight data have shown the advantage of swept wings in overcoming the shock stall problem and reducing wave drag.

A swept wing is one in which the line of focuses, located approximately one quarter of the chord from the leading edge, forms with the normal to the wing plane of symmetry the angle χ, termed the sweep angle (Figure 17.1).

Sometimes in calculations the sweep angle is measured, not from the line of focuses, but rather from some other line, for example, from the leading or trailing edge of the wing, and so on. For definiteness of sweep angle notation a subscript is attached to the letter χ to show the line relative to which this angle is measured. For example, χ_0 is the leading edge sweep; χ_c refers to the line of maximal thickness, $\chi_{1/4}$ is for the line of focuses, $\chi_{1/2}$ is for the midpoint of the chord, χ_1 is for the trailing edge, and so on (see Figure 17.1).

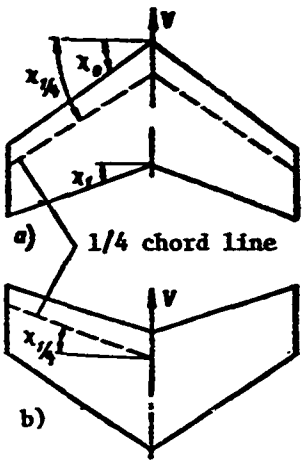

Figure 17.1 Swept wing: a - positive sweep; b - negative sweep.

As a rule wing sweep is positive (see Figure 17.1a), and less frequently negative (see Figure 17.1b). In the case of negative sweep the wing tips are displaced forward in the direction of flight (in this case the angle χ is negative). If the wing edges have breaks or are curved, the sweep angle changes at various segments along the wing span.

One of the characteristic features of swept wing operation in an air stream is the utilization of the sideslip effect. Assume the air flow approaches a rectangular wing of infinite span with the velocity V_1, perpendicular to the wing leading edge (Figure 17.2a). In this case, as the air flows past the wing we obtain a definite pressure distribution along the chord, which has an effect on the wing aerodynamic coefficients.

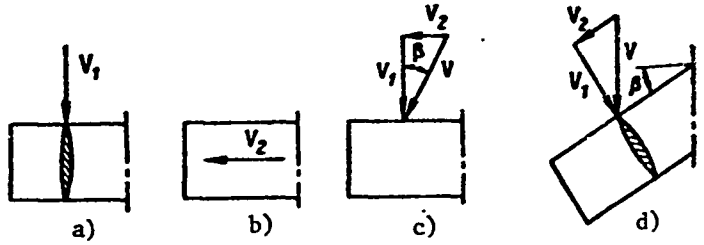

Figure 17.2. Illustrating sideslip effect.

Now let us assume that the given wing is subjected to flow in the direction along the span by another stream with the velocity V_2 (Figure 17.2b). This velocity V_2 has no effect on the pressure distribution over the wing surface or on its other characteristics (It is true that in the viscous flow case friction develops in the boundary layer, which we shall ignore here).

Under simultaneous action of both flows the velocity vectors $\vec{V}_1$ and $\vec{V}_2$ on the wing combine. The resultant velocity is

$$\vec{V}=\vec{V}_1+\vec{V}_2$$

It is obvious that the resultant velocity V is directed at the angle β to the wing plane of symmetry (Figure 17.1c), termed the sideslip angle. The picture is the same if the resultant velocity is parallel to the original velocity V_1 and the subject wing is rotated through the angle β (Figure 17.2d). In this case we obtain the flow pattern about a yawed wing with the sideslip angle β. Thus, flow past a yawed wing is equivalent to oblique flow over a rectangular wing.

The normal and tangential velocity components are, respectively

$$V_1=V\cos\beta,\quad V_2=V\sin\beta$$

We note that in the yawed case the flow about the wing profile in the section normal to the wing generator is defined not by the velocity V, but rather by its component V_1, which is less than the velocity V by the factor cos β. If we now maintain the same angle of attack for the profile as we had for the straight wing, the pressure distribution along the profile of the yawed wing becomes, for the flight velocity V, the same as it would be for a straight wing at a velocity V_1, equal to V cos β.

Since for the same flow velocity past the straight and yawed wings the local velocities at the surface of the yawed wing are less, the shock stall on the yawed wing will occur at higher flight speeds. For small yaw angles the magnitude of the critical Mach number for the yawed wing of infinite span can be determined in the first approximation from the relation

$$M_{кр.ск}=M_{кр.пр}\sec\beta=\frac{M_{кр.пр}}{\cos\beta} \qquad (17.1)$$

The operation of swept wings has a complex nature and the sideslip effect is not fully utilized. On a swept wing of sufficiently large aspect ratio we can arbitrarily define the regions I, II, and III (Figure 17.3).

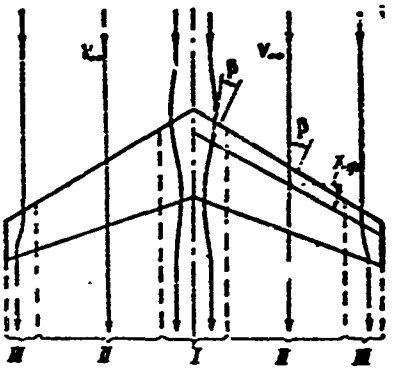

Figure 17.3. Schematic of flow around swept wing.

In the central part of the wing (I) (near the plane of symmetry) the local yaw angle β diminishes and becomes equal to zero over some region as a result of mutual influence of the wing sections. This phenomenon, termed the centerline effect, reduces the yaw effect somewhat and influences the aerodynamic characteristics of the swept wing. The yaw effect is also significantly decreased at the tip part of the wing (III), where there is considerable deviation of the streamlines on the surface of the wing.

In region II, with more uniform flow along the span, the streamlines are deflected only slightly from the xOy plane and the magnitude of the yaw angle β is close to the sweep angle χ. The existence of a region with flow which is uniform over a large part of the span makes it possible in studying the swept wing to represent this region as a corresponding part of an infinitely long cylindrical wing placed in the flow at the sweep angle, i.e., a yawed wing.

§17.2. Physical Picture of Flow Past Swept Wing

In order to clarify the physical essence of the flow over a swept wing, we shall analyze the behavior of the streamlines on its surface. Figure 17.4 shows a schematic of part of a swept wing. We assume that the freestream velocity $\vec{V}_\infty$ approaching the wing is parallel to the wing axis of symmetry. We resolve this velocity into two components: $\vec{V}_n$ normal to the wing leading edge and $\vec{V}_t$ tangent to the leading edge, i.e.,

$$\vec{V}_\infty = \vec{V}_n + \vec{V}_t$$

The tangential component of the velocity on the swept wing has practically the same magnitude $V_t = V_\infty \sin \chi$ at neighboring sections, while the normal component V_n varies as a function of the section profile shape (and angle of attack). Therefore the streamline curvature

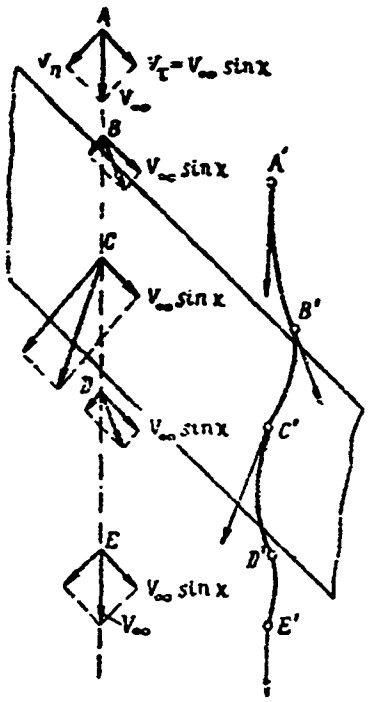

Figure 17.4. Variation of velocity and streamline direction near surface of yawed wing.

depends basically on the magnitude of the normal velocity component.

At point A (Figure 17.4) we have undisturbed flow with the velocity V_∞. As we approach the leading edge of the wing, the flow velocity decreases and right at the leading edge $V_n = 0$. Further along the chords normal to the wing generator the velocity increases, reaching a maximal value at the point C of minimal pressure. Behind point C the velocity again decreases, passing through a second minimum at the trailing edge, and then again increases to the magnitude of the undisturbed flow velocity at point E. The direction of the streamline near the wing (line A'B'C'D'E' in Figure 17.4) changes in accordance with the changes of the resultant velocity vector $\vec{V}_\infty$ (the velocity V equals the sum of the constant tangential velocity and the variable normal velocity).

This unique variation of the velocities in magnitude and direction leads to significant differences between the pressure distribution pattern on the surface of the swept wing and that on the straight wing, for which the pressure distribution pattern is nearly the same at all sections. The pressure distribution along the upper surface of different longitudinal sections (in the streamwise direction) of a swept wing, confirming the existence of the centerline and tip effects, is shown in Figure 17.5.

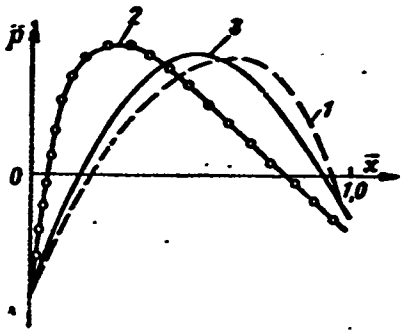

Figure 17.5. Pressure distribution at different sections of swept wing (in streamwise direction): 1 - root section; 2 - tip section; 3 - intermediate section.

§17.3. Connection Between Parameters of Swept and Straight Wings

Figure 17.6 shows a wing of infinite span placed at the sweep angle χ to the stream — a yawed wing. The chord b_n in the section normal to the wing generator can be expressed in terms of the chord b of a streamwise section

$$b_n = b\cos\chi.$$

We denote the angle of attack in the normal section by α_n, then

$$\sin\alpha_n = \frac{h}{b_n} = \frac{h}{b\cos\chi} = \frac{\sin\alpha}{\cos\chi}$$

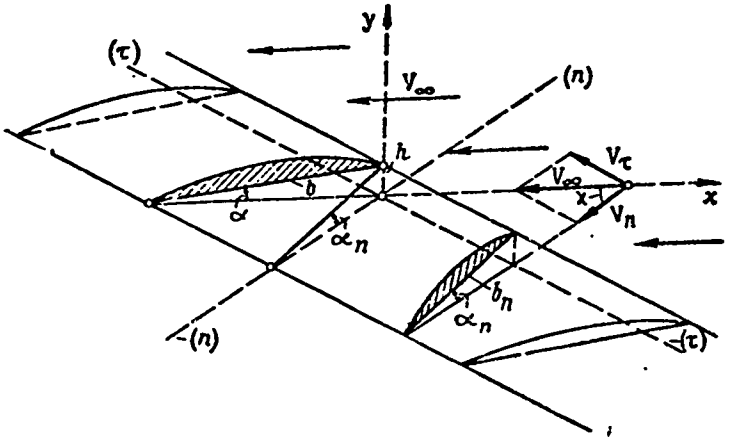

Figure 17.6. Yawed wing of infinite span.

Since the angles of attack usually have a small magnitude, this formula for moderate sweep can be rewritten as

$$\alpha_n = \frac{\alpha}{\cos\chi} \qquad (17.2)$$

The relative thickness of the normal section is

$$\bar{c}_n = \frac{c}{b_n} = \frac{c}{b}\frac{b}{b_n} = \frac{\bar{c}}{\cos\chi} \qquad (17.3)$$

The relative curvatures of the normal and streamwise sections have the same relationship

$$\bar{f}_n = \frac{\bar{f}}{\cos\chi}$$

Thus, we can conclude that the normal flow passes around a cylindrical, infinitely long wing with somewhat thicker and more highly cambered profile than the yawed wing at the angle of attack α_n.

Let us examine the yawed wing and some straight wing (Figure 17.7) which is equivalent in form to the yawed wing (both wings have the same chord, profile sections, and streamwise angles of attack). The transverse stream, approaching the yawed wing with the velocity $V_n = V_\infty \cos\chi$, creates the lift

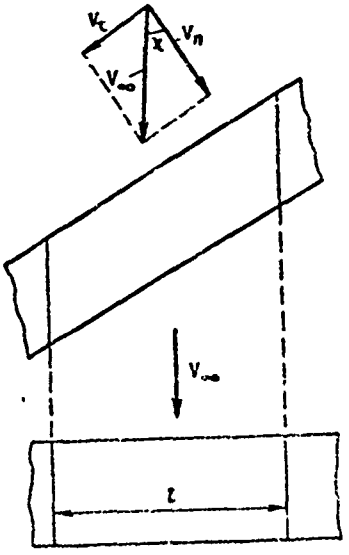

Figure 17.7. Swept wing and equivalent straight wing to it

$$Y_n = c_{yn}\frac{\rho V_\infty^2 \cos^2\chi}{2} S \qquad (17.4)$$

where S is the area of a wing segment of length l along the span (see Figure 17.7).

On the basis of (17.4) the lift coefficient of the yawed wing is

$$c_{y\,ск} = c_{yn}\cos^2\chi \qquad (17.5)$$

We know from wing profile theory that at small angles of attack the lift coefficients for a symmetric profile are connected by the relation

$$c_{y1} = c_{y2}\frac{\alpha_1}{\alpha_2}$$

On this basis and with account for (17.2) we can write

$$c_{y_n}=c_y\frac{1}{\cos\chi}$$

Substituting the value of c_{yn} into (17.5), we obtain

$$c_{y\,ск}=c_y\cos\chi \tag{17.6}$$

Thus we conclude that the lift coefficient of the yawed wing is less than that of the equivalent straight wing.

Differentiating (17.6), we obtain the expression for c_y^α of the yawed wing

$$c^\alpha_{y\,ск}=c^\alpha_y\cos\chi \tag{17.7}$$

We can obtain the corresponding derivative for the finite-span swept wing by substituting into (16.29) in place of c_y^α the quantity $c_y^\alpha \cos\chi$ in accordance with (17.7). After several transformations we obtain

$$c^\alpha_{y\,стр}=\frac{c^\alpha_{y\lambda=\infty}}{\sqrt{1+tg^2\chi}+\frac{c^\alpha_{y\lambda=\infty}}{\pi\lambda}(1+\tau_{стр})} \tag{17.8}$$

where τ_{sw} accounts for aspect ratio, taper, sweep, and the circulation distribution along the wing span. On the average τ_{sw} equals 0.2; with increase of λ and decrease of η, the quantity τ_{sw} increases somewhat (to about 0.3).

Typical curves of $c_y = f(\alpha)$ for a finite-span, straight-wing profile, for the profile of a swept wing of the same aspect ratio, and for a wing of infinite span are shown in Figure 17.8. Comparison of the curves shows that c_y^α is less for the swept wing than for the straight line.

For the swept wing the average downwash angle can be represented by an expression analogous to (16.23) for the straight wing

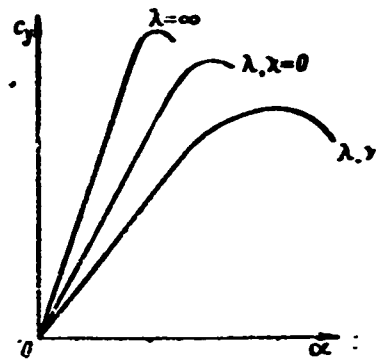

Figure 17.8. Relation $c_y = f(\alpha)$ for wing of infinite span (profile) and also for straight and swept wings of finite span having different aspect ratio.

$$\Delta\alpha_{cp}=\frac{c_y}{\pi\lambda}(1+\tau_{crp}) \qquad (17.9)$$

The induced drag coefficient of the swept wing is determined similarly to that of the straight wing from the formula

$$c_{xi}=\frac{c_{y\,crp}^2}{\pi\lambda}(1+\delta_{crp}) \qquad (17.10)$$

For the swept wing the pressure drag coefficient component is less than for the equivalent straight wing, while the friction drag coefficient component is larger. If we also consider the change of the induced drag coefficient, we find that in the first approximation we can write

$$c_{x\,crp}=c_{x\,np} \qquad (17.11)$$

The pitching moment of the swept wing resulting from the aerodynamic forces, like the lift force, is proportional to cos χ, since both the lift and the pitching moment are created basically by the pressure forces. Therefore we can write the following formula for the moment coefficient of an element of a swept wing relative to the leading edge

$$c_{m\,crp}=c_{m\,np}\cos\chi$$

Substituting herein the value of $c_{m\ str}$ from (12.16), we obtain

$$c_{m\,crp}=c_{m0}\cos\chi+mc_y\cos\chi=c_{m0}\cos\chi+mc_{y\,crp} \qquad (17.12)$$

or, introducing the notation $c_{m0}\cos\chi = c_{m0\ sw}$, we have

$$c_{m\,crp}=c_{m0\,crp}+mc_{y\,crp} \qquad (17.13)$$

To find the moment coefficient of the entire wing we must take into account the longitudinal displacement of the individual elements.

We note that many studies are now available which yield an exact solution of the swept wing problem. These studies are based on one method or another for accounting for the induced velocities generated by the bound vortices of the two halves of the wing. In particular, techniques have been developed to calculate the circulation distribution along the span of the swept wing. One of these methods involves first finding the circulation distribution along the span of the equivalent straight wing, in which the circulation is represented in the form of the sum of trigonometric terms, and then a sweep correction is introduced into the coefficients of the terms of this sum.

§17.4. Small Aspect Ratio Wings

Wings with comparatively large aspect ratios were used in airplane design up to the 1950's. Even the tail surfaces had aspect ratios λ exceeding 4. Large aspect ratio wings were used to reduce the induced drag. The maximal magnitude of wing aspect ratio was limited primarily by requirements of wing strength and stiffness.

After the 1950's airplane speeds began to increase particularly rapidly, and rocketry developed tremendously. At these high speeds quite small values of c_y were required and the role of the flight vehicle induced drag, which depends on c_y, in the overall drag balance became very small. Wings of very small aspect ratio (λ = 0.5-3), which are more favorable at the high speeds, began to be used more and more. Particularly small aspect ratio wings were used on the cruise-type missiles. Attempts to apply to these wings the highly developed classical theory of the large aspect ratio wing were unsuccessful: in many cases the theory did not yield even qualitative agreement with experiment.

In fact, the basic assumptions of large aspect ratio wing theory are not applicable to the small aspect ratio wing: the hypothesis of

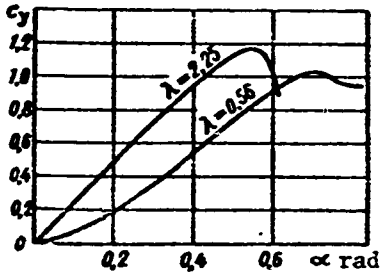

Figure 17.9. Curves $c_y = f(\alpha)$ for wings of large and small aspect ratio.

plane sections, replacement of the wings by a vertical lifting line, neglect of the downwash angle variation along the wing chord. Of considerable importance for the small aspect ratio wing is the transverse flow over the wing, which leads to marked three dimensionality of the flow and the appearance of a very complex pressure field on the wing surface. The wing planform has a particularly great influence on the aerodynamic characteristics of the small aspect ratio wing.

Experiment is of great importance in studying small aspect ratio wings. Many semi-theoretical (semi-emperical) methods for analysis of small aspect ratio wings have also been proposed. The primary difference between these methods lies in the vortex models which are used to replace the wing and the flow in the region of the wing. As a rule, these methods make it possible to calculate the forces acting on the wing for very small angles of attack.

The primary features of the aerodynamic characteristics of the small aspect ratio wings are the following.

1. For small aspect ratio wings, the curve $c_y = f(\alpha)$ does not have the rectilinear segment characteristic of the large aspect ratio wings (Figure 17.9). The curve $c_y = f(\alpha)$ for $\lambda < 2$ has an S-shape. This form of the curve $c_y = f(\alpha)$ is explained as follows. For small α, as a result of the intense crossflow of air around the tips of small aspect ratio wings, the pressure on the upper and lower surfaces of the wing equalizes, and this leads to reduction of c_y. With increase of α, powerful vortices begin to separate from the tips and these lead to reduction of the pressure on the upper surface and therefore to increase of c_y.

2. For small aspect ratio wings α_{st} is considerably larger than for large aspect ratio wings. Here the value of α_{st} for wings with aspect ratio $\lambda < 2$ retains about the same value, close to 0.6 rad. The increase of α_{st} for the low aspect ratio wings is explained by the equalization of the pressure along the wing chord above its upper surface, which is a result of the intense crossflow around the wing tips.

3. The induced drag of the low aspect ratio wings depends to a marked degree on the wing planform and is larger in magnitude than for the large aspect ratio wings (for the same values of c_y). The coefficient c_{xi} for the low aspect ratio wing can be represented by a relation analogous to (16.22) for the large aspect ratio wing

$$c_{xi} = \frac{c_y^2}{\pi\lambda}(1+\delta)$$

where the parameter δ depends on the wing planform and angle of attack and is determined experimentally.

Experiment shows that for the low aspect ratio swept wings for values of $c_y < 0.6$, $\delta = 0.05 - 0.15$, i.e., it has the same values as for large aspect ratio wings. For triangular (delta) wings the parameter δ is considerably larger (0.4 - 1.0).

When the design of small aspect ratio wings is necessary, reliable experimental data should be used, with particular attention being devoted to the similarity of the test and full-scale vehicles.

REVIEW QUESTIONS

1. What is the effect of sweep?

2. Explain the physical nature of the flow past a swept wing.

3. Write the formulas connecting the parameters of swept and straight wings.

4. How does wing sweep affect the magnitude of the lift coefficient c_y and $c_{y\ max}$?

5. What are the peculiarities of the aerodynamic characteristics of the small aspect ratio wings?

PROBLEM

1. Find the angle of attack of a flat wing with constant profile along the span with aspect ratio $\lambda = 8$ and sweep angle $\chi = 0.6$ rad if the lift coefficient $c_y = 0.6$, zero lift angle $\alpha_0 = -0.06$ rad. Moreover, we know that $\tau = 0.12$ and $c^{\alpha}_{y\lambda=\infty} = 5.2$.

Solution. From (17.8) we find

$$c^{\alpha}_{y\,cp} = \frac{c^{\alpha}_{y\lambda=\infty}}{\sqrt{1+\operatorname{tg}^2\chi} + \frac{c^{\alpha}_{y\lambda=\infty}}{\pi\lambda}(1+\tau_{cp})} = 3{,}62$$

From (12.16) we have

$$\alpha = \frac{c_y}{c^{\alpha}_{y\,cp}} + \alpha_0 = 0{,}106 \text{ rad} = 6°04'$$

CHAPTER XVIII

MAXIMAL LIFT COEFFICIENT. WING MECHANIZATION

§18.1. Flow Separation from Wing Surface

When a wing operates at high angles of attack, the flow over its upper surface separates. Flow separation occurs at comparatively small angles of attack, on the order of 10 - 12°, and initially has a local nature. As the angle of attack is increased, the separation zone gradually expands more and more, extending forward along the chord and laterally along the wing span. Separated flows on the upper surface of the wing are the result of boundary layer separation, which takes place at large pressure gradients.

The separated flow regime over the wing has considerable influence on the wing aerodynamic characteristics, particularly the lift coefficient. This influence results from the fact that reduction of the rarefaction in the separation zone disrupts the linear dependence of the lift coefficient on the angle of attack (segment AB in Figure 18.1). The lift coefficient corresponding to point A is sometimes termed $c_{y\ buffet}$, since airplane flight is usually accompanied by buffeting when the separated zone appears on the wing.

At some critical angle of attack α_{cr}, flow separation extends to most of the wing surface, and the lift force decreases beginning at this angle of attack. The values of $c_{y\ max}$ and α_{st} depend to a considerable degree on the geometric characteristics of the wing and on the Reynolds number Re. The region of separation onset and further growth of the separation zone depend on the wing planform. Let us examine the influence of the wing geometric characteristics on the development of the separation phenomena.

Influence of Wing Planform

For each section of a geometrically plane wing of infinite span with constant profile, the lift coefficient is limited to the value $c_{y\ max\ sec}$. The value $c_{y\ max\ sec}$ (see Chapter XII) for a given profile depends on $Re = Vb_{sec}/\nu$. If we determine $c_{y\ max\ sec} = f(\bar{z})$ for a given wing, we can plot a curve which is the upper limit of the variation of $c_{y\ sec}$. At any point along the wing span, the value of $c_{y\ sec}$ cannot exceed the value defined by this curve. In Figures 18.2 and and 18.3 this straight line 1 is plotted for straight and trapezoidal wings.

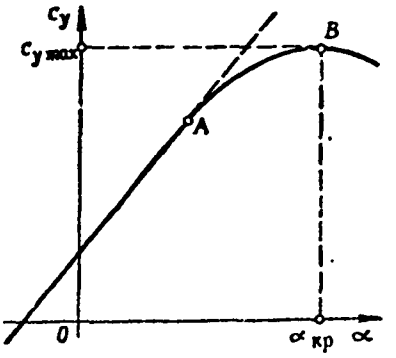

Figure 18.1. Lift coefficient of asymmetric profile versus angle of attack

Now let us plot the $c_{y\ sec}$ distribution along the span, corresponding to some angle of attack. In accordance with the coupling Equation (16.14) we have

$$c_{y\,sec} = \frac{2\Gamma(\bar{z})}{V_\infty b(\bar{z})}, \qquad (18.1)$$

where $\Gamma(\bar{z})$ is the value of the circulation around a contour enclosing the given wing section at the given angle of attack.

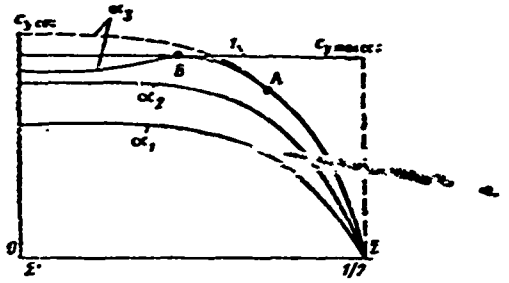

Figure 18.2. Change of spanwise $c_{y\ sec}$ distribution for rectangular planform wing with increase α

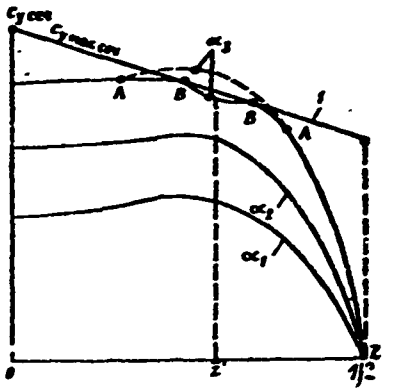

Figure 18.3. Change of spanwise $c_{y\ sec}$ distribution for trapezoidal wing with increase of α

In the central part of a rectangular planform wing the circulation is nearly constant, while it drops off markedly toward the tips. Since the chord is constant in the present case, the nature of the c_y variation along the span is the same as the Γ variation, i.e., for a straight wing the coefficient $c_{y\ sec}$ is practically constant (see Figure 18.2) over a large portion of the span in the central region.

On the trapezoidal wing the circulation decreases toward the tips along the entire wing semispan — for the trapezoidal wing the free vortices trail more uniformly from the trailing edge of the wing. In this connection we would expect a more uniform decrease of $c_{y\ sec}$ along the span of the trapezoidal wing in comparison with the rectangular wing. However, in accordance with the coupling Equation (18.1), because of the chord reduction as we move away from the root section, there is initially some increase of $c_{y\ sec}$ and then $c_{y\ sec}$ decreases at the tip sections, where the circulation decreases markedly (see Figure 18.3).

This variation of $c_{y\ sec}$ along the span of a trapezoidal wing can be explained in another way if we consider the nature of the effective section angle of attack variation along the span. In fact, if we examine some arbitrary wing section, the value of $c_{y\ sec}$ will be determined by the effective local angle of attack, which depends on the wing angle of attack (we are considering a plane wing) and the downwash angle.

On the straight wing the free vortices are concentrated primarily at the tips (Figure 18.4) and the downwash angle increases smoothly along the span. Consequently, the effective angle of attack gradually decreases as we approach the wing tips, vanishing at the tips. On the trapezoidal wing the free vortices are distributed along the span approximately as shown in Figure 18.4.

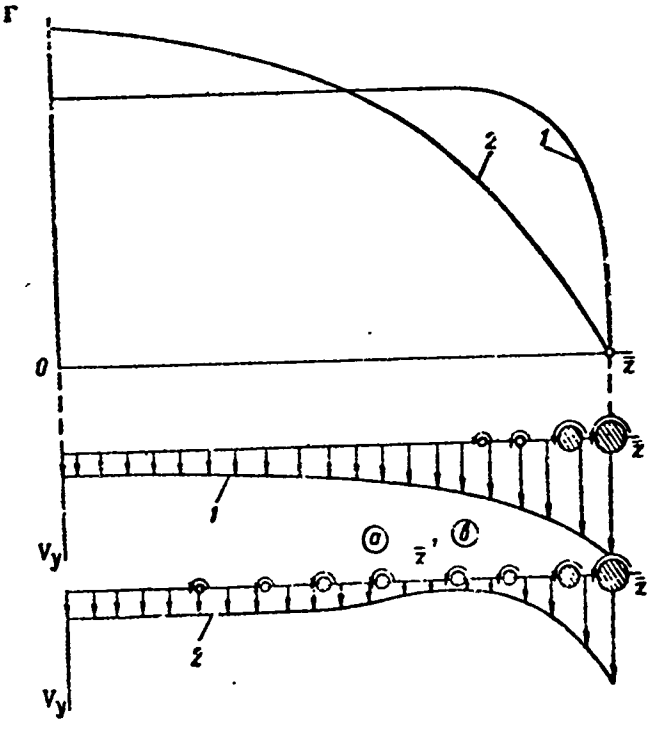

Figure 18.4. Change of circulation and velocities induced by free vortices along span for straight (1) and trapezoidal (2) wings

This figure also shows the spanwise variation of the velocity V_y induced by the free vortices. We see from the figure that the induced velocities will have a minimal value at some section $\bar{z}'$, since here the velocity is induced simultaneously by both vortices located to the right of the section (vortices b) and vortices located to the left of the section (vortices a). It is obvious that the effective angle of attack and c_y reach their maximal values for the plane wing at the section $\bar{z}'$.

With increase of the angle of attack, the circulation and $c_{y\ sec}$ increase at each section. In this case, there will be a linear increase of $c_{y\ sec}$ at all sections if the flow does not separate at any of the sections.

Upon reaching some angle of attack, separation of the boundary layer begins at that wing section where the ordinates of the curve $c_{y\ sec}$ are closest to the ordinates of the curve $c_{y\ max\ sec}$ (section $\bar{z}'$ in Figure 18.3). On the wing of rectangular planform, flow separation begins in the wing root region and rapidly extends to a large portion of the span. On the trapezoidal wing separation begins near the tips because of the rapid decrease of $c_{y\ max\ sec}$ toward the tips (because of the small values of Re), and also as a result of the nature of the $c_{y\ sec}$ variation described above. At those sections where separation occurs, the values of $c_{y\ sec}$ will not increase in proportion to α as the angle of attack is increased further, as a result of which the $c_{y\ sec}$ distribution pattern is deformed.

Distributions of $c_{y\ sec}$ for the angle of attack α_3, corresponding to separated flow on the upper part of the wing, are shown in Figures 18.2 and 18.3. The dashed curves show the distributions which would occur with separation-free flow, while the continuous curves are with account for separation. For the angle of attack α_3 separation takes place on the segment AA (see Figure 18.3). On the segment AB the values of c_y have not yet reached the values $c_{y\ max\ sec}$, while the segment BB is a region of developed flow separation, corresponding to supercritical local angles of attack.

The variation of the $c_{y\ sec}$ distribution along the span of the trapezoidal swept wing with increase of the angle of attack is shown in Figure 18.5. Characteristic for the swept wing is the marked decrease of $c_{y\ sec}$ in the root region, which is explained by decrease of the effective angles of attack at these sections because of the local increase of the downwash. We see from Figure 18.5 that for the swept plane wing with constant profile the lift coefficient is distributed very nonuniformly along the span, reaching its maximal values at sections located near the wingtips. Just as in the case of the straight trapezoidal wing, this leads to the appearance of separation phenomena at these sections.

Moreover, characteristic for the swept wing is piling up and increase of the boundary layer thickness near the tips as a result of the flow velocity component along the span (Figure 18.6), which leads to premature flow separation at the wingtips. To prevent premature flow separation, use is made of so-called fences — plates on the upper wing surface which prevent flow of the boundary layer toward the tips (possible locations for such fences are shown dashed in Figure 18.6).

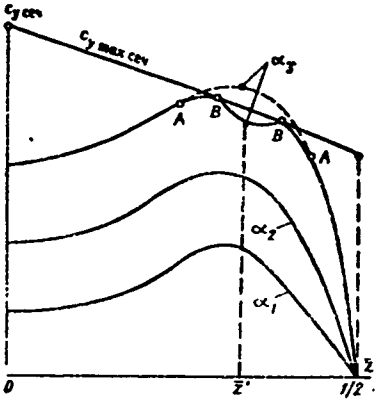

Figure 18.5. Change of spanwise $c_{y\ sec}$ distribution for swept wing with increase of α

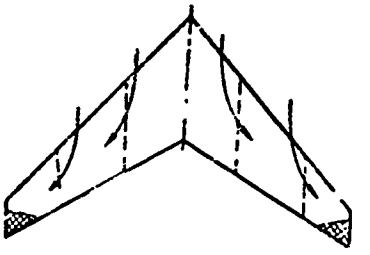

Figure 18.6. Regions of premature flow separation on swept wing owing to boundary layer pileup

Thus we can draw the following conclusions. The wing planform has a very significant influence on the location where separation phenomena begin on the wing. For the wing of rectangular planform, separation phenomena begin in the center region and extend rapidly to the entire span. On the trapezoidal and swept wings, flow separation begins near the tips. The use of aerodynamic fences makes it possible to avoid this early flow separation on the swept wing; in this case, the swept wing behaves approximately the same as a straight wing.

We note that the wing planform, which determines the location where flow separation begins along the wing span, has a major influence on airplane behavior in a spin.

Effect of Profile Section Shape and Wing Twist

For a wing of given planform, assembled from profiles which differ along the span, $c_{y\ max\ sec}$ depends not only on Re but also on the profile form: for the same values of Re the coefficient $c_{y\ max}$ depends on the relative thickness, camber, and maximal thickness position along the chord.

On the other hand, use of different profiles leads to redistribution of the circulation along the span and therefore to change of the curves $c_{y\ sec} = f(\bar{z})$. By assembling the wing from different profiles, we can alter the nature of the $c_{y\ max\ sec}$ and c curves and thereby control the location of the zone where flow separation starts on the wing.

For example, by using profiles providing more lift, i.e., profiles with a large value of $c_{y\ max}$, in the region of expected separation initiation we can obtain practically simultaneous onset of the separation phenomena over the entire wing span.

To ensure transverse flight stability at high angles of attack, it is usually required that the separation phenomena begin at the root sections. In this connection profiles with higher $c_{y\ max}$ are

used at the wing tip sections and profiles with lower lifting properties are used at the root section — even profiles with negative camber.

The lifting properties of a wing can be improved by using geometric twist, for which the profile sections are rotated without altering their form, so that the local angles of attack are less in the regions of expected flow separation than on the remaining portions of the wing. If the tip part of a trapezoidal or swept wing is given a negative twist, the separation zone can be shifted toward the root section.

Simultaneous use of twist and different profiles along the wing span makes it possible to obtain the required wing lifting qualities at high angles of attack.

Effect of Wing Aspect Ratio

In the case of high wing aspect ratios, flow separation occurs at angles of attack close to α_{st} for the given profile. For wings of low aspect ratio ($\lambda < 3$) flow separation usually occurs at considerably higher angles of attack. The delay of flow separation on wings with low aspect ratio is explained by the lesser pressure reduction on the upper surface as a result of air cross-flow around the wing tips, and also as a result of the influence on the boundary layer of the powerful tip vortices trailing from the wing.

§18.2. Calculation of Maximal Lift Coefficient

The maximal lift coefficient is one of the most important aerodynamic characteristics of the wing. The maximal value of c_y determines the minimal airplane level flight speed. The lower the level flight speed, the lower is value of the landing speed which can be achieved. The magnitude of the landing speed must be as low as possible, since it defines the required runway length and safety in the most critical phase of airplane flight — the landing.

We note that exact determination of the value of wing $c_{y\ max}$ involves several difficulties. It is difficult to perform a model experiment for finding $c_{y\ max}$ in the wind tunnel, since it is not always possible to obtain the required Reynolds numbers. A factor which alleviates the situation somewhat is the fact that, since the value of $c_{y\ max}$ must be known to calculate the airplane takeoff and landing characteristics, the velocity and therefore the Reynolds number will have comparatively low values. However, for the modern large commercial airplanes difficulties of a technical nature arise in obtaining the required values of Re for their models in wind tunnels.

It is also difficult to obtain an adequately exact determination of $c_{y\ max}$ by calculation, since spanwise variation of the profiles, the use of twist and complex planforms (variable taper along the span, variable sweep, and so on) are characteristic for the wings of modern airplanes. The complex wing shape in plan and cross section makes it difficult to calculate the distribution of $c_{y\ sec}$ along the span, and this is what leads to the primary difficulty in determining wing $c_{y\ max}$.

The method developed at TsAGI* for calculating wing $c_{y\ max}$ is suitable for straight and trapezoidal wings of comparatively large aspect ratio, composed of identical profiles without geometric twist or sweep. This method is based on the assumption that the wing stalling angle of attack is reached at the instant the value of $c_{y\ sec}$ reaches the value $c_{y\ max\ sec}$ at any one section as the angle of attack is increased. In this approach it is assumed that a linear dependence of $c_{y\ sec}$ on the local angle of attack is maintained at all sections right up to this instant, and in this connection the curves representing the spanwise $c_{y\ sec}$ distribution are not deformed at the location where flow separation starts. In Figure 18.7 the dashed curve shows the actual $c_{y\ sec}$ distribution, while the continuous curve shows the distribution obtained by the method just described.

---

*Translator's Note: This designates the Central Institute of aerohydrodynamics imenii N. Ye. Zhukovskiy.

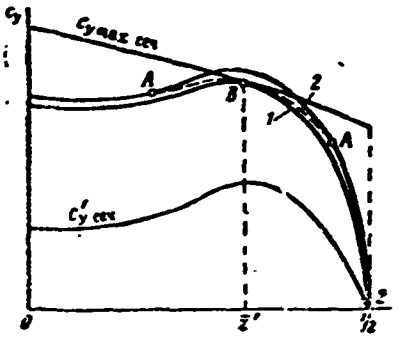

Figure 18.7. Illustration for calculation of wing $c_{y\ max}$: 1 - variation of $c_{y\ sec}$ used in calculation under assumption that $c_{y\ sec} = c_{y\ max\ sec}$ at the section $\bar{z}'$; 2 - actual variation of $c_{y\ sec}$ at the angle of attack for which $c_{y\ sec} = c_{y\ max\ sec}$ at section $\bar{z}'$

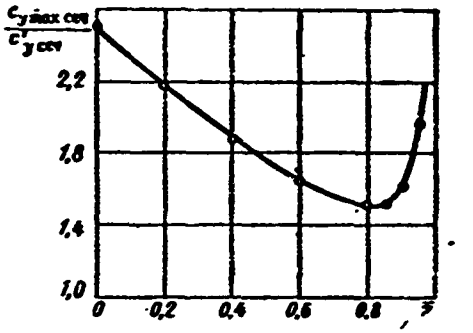

Figure 18.8. Curve of $c_{y\ max\ sec}/c'_{y\ sec} = f(\bar{z})$

If we assume that the wing $c_{y\ max}$ corresponds to the case shown in Figure 18.7, we can show that the following formula holds

$$c_{y\,max\,sp} = \left(\frac{c_{y\,max\,sec}}{c'_{y\,sec}}\right)_{min},$$

where $c'_{y\ sec}$ is the value of $c_{y\ sec}$ for the angle of attack corresponding to the value $c_{y\ st} = 1$.

To calculate $c'_{y\ sec} = f(\bar{z})$ we must know the circulation distribution along the wing span. In this case, $c_{y\ max\ st}$ is determined graphically (Figure 18.8).

Data on the circulation distribution along the span for wings of different planform are presented in the reference literature.

For an approximate estimate of the value of $c_{y\ max}$ for wings of large aspect ratio ($\lambda > 3$) we can use the approximate empirical formula

$$c_{y\ max\ xp} = c_{y\ max\ sec} k_\eta \frac{1 + \cos \chi_c}{2},$$

where $c_{y\ max\ sec}$ is the maximal lift coefficient of the wing profile with chord equal to the average wing chord at a Reynolds number corresponding to the landing speed;

χ_c — is the wing sweep angle along the maximal thickness line;
k_η — is a coefficient depending on the wing taper ratio η;

η	k_η	η	k_η
1	0,90	3	0,93
2	0,94	4	0,92

For triangular wings of small aspect ratios, $c_{y\ max\ st}$ is determined approximately as a function of the wing aspect ratio:

λ	1	2	4
$c_{y\ max\ xp}$	1,28	1,2	1,0

§18.3. Wing Mechanization

In modern aviation swept wings of comparatively small area with profiles of very low camber and relative thickness are used in order to increase the flight speed. Such wings cannot provide high lift forces under landing conditions because of early flow separation. The problem of increasing the lifting qualities of the modern wings at high angles of attack is a very urgent question at the present time in order to reduce takeoff and landing distances. For this purpose the wings are equipped with special structural elements which

make it possible to increase the magnitude of the wing lift coefficient in the critical angle of attack region. These elements operate only in the takeoff and landing regimes and are termed wing mechanization. Wing mechanization includes split flaps, trailing-edge flaps, slats, leading-edge flaps, spoilers, and so on.

The split flap is a portion of the wing lower surface near the trailing edge which deflects through the angle δ_f. The deflection may take place either about a fixed hinge (simple split flap, Figure 18.9a) or about a sliding hinge (extending split flap, Figure 18.9b). The flap chord amounts to 15 to 30% of the wing chord. The maximal deflection angle δ_f may reach $\pi/3$. Split flaps are located in the central part of the wing and occupy from 40 to 60% of the entire wing span.

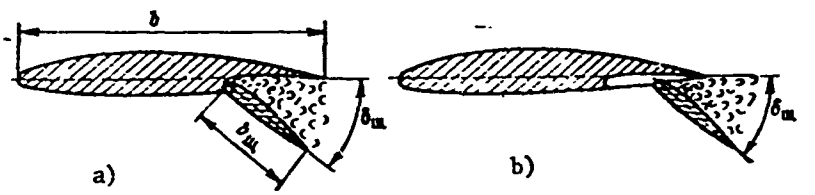

Figure 18.9. Split flaps:
a - simple; b - extending

We see from Figure 18.10 that deflection of the flaps of a straight wing of large aspect ratio causes considerable increase of the lift coefficient, since flap deflection leads to increase of the pressure on the lower surface of the wing, while a low-pressure zone is formed between the flap and the wing. This low pressure leads to decrease of the pressure and increase of the velocity over the upper surface of the wing. With increase of the angle δ_f, the curves $c_y = f(\alpha)$ shift to the left. As a result of the aspirating action of the flap there is a marked increase of $c_{y\ max}$ (its value may double in certain cases). The effect increases when a sliding flap is used since in this case there is also an increase of the wing area.

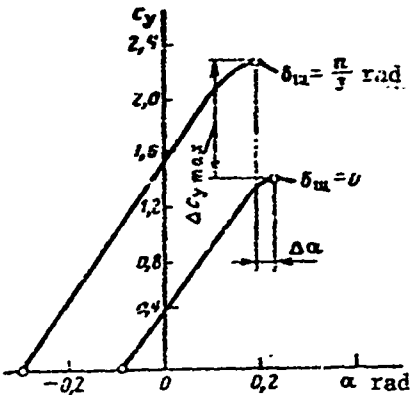

Figure 18.10. Wing lift coefficient c_y versus angle of attack α for split flap deflections $\delta_f = 0$ and $\delta_f = \pi/3$ rad

Flap effectiveness is evaluated by the magnitude Δc_y of the lift coefficient increase. We note that the flap deflection angle δ_f, relative flap chord b_f/b, relative flap length l_f/l, and finally the wing planform affect the magnitude of Δc_y and $\Delta c_{y\,max}$. The effect of the quantity b_f/b on the coefficient $\Delta c_{y\,max}$ is shown in Figure 18.11. Flaps which cover the entire span will obviously have the largest values of Δc_y.

We note specifically that flaps increase the drag coefficient as well as the lift coefficient. The aerodynamic efficiency $K = c_y/c_x$ of wings with deflecting flaps is less than for wings without flaps. The drag coefficient increase plays a favorable role during the airplane landing procedure. However, during takeoff it is necessary that the drag coefficient be as low as possible, while increasing the lift coefficient. Therefore, the flaps are deflected only partially, usually 0.4 - 0.5 rad, during takeoff.

When δ_f is increased, there is also an increase in the wing pitching moment coefficient. Curves showing the dependence of c_{m0} on the flap deflection angle in the simple split flap and sliding split flap ($b_f/b = 0.3$; $l_f/l = 1$) cases are shown in Figure 18.12.

Trailing-edge flaps are a deflecting aft portion of the wing. When trailing-edge flaps are deflected, a profiled slot (Figure 18.13) is usually formed between the wing and the leading edge of the flap, through which air flows at high velocity over the upper surface of the trailing-edge flap. This stabilizes the separation-free flow in

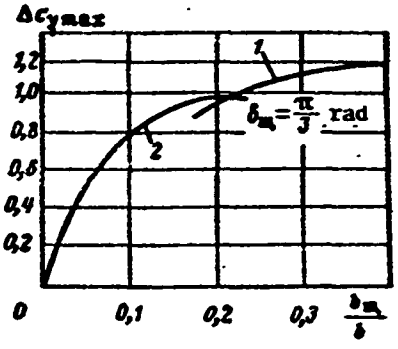

Figure 18.11. $\Delta c_{y\max}$ versus relative split flap chord:

1 - extending split flap;
2 - simple split flap

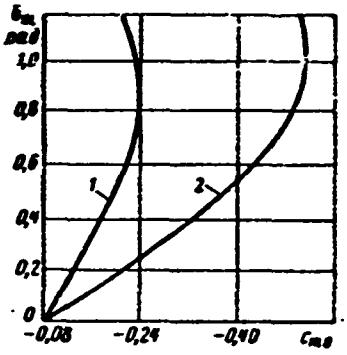

Figure 18.12. Effect of split flap deflection angle on wing moment characteristics:

1 - simple split flap;
2 - extending split flap

the boundary layer and makes it possible to deflect the flaps through large angles while retaining their effectiveness.

Trailing-edge flap deflection leads to about the same effects as does deflection of split flaps; however, the drag coefficient will be smaller in the trailing-edge flap case. The trailing-edge flap chord does not usually exceed 20 - 25% of the wing chord, since trailing-edge flap effectiveness increases only slightly with further increase of b_f/b.

The quantity $\Delta c_{y\ max}$ increases with increase of the flap deflection angle. The maximal trailing-edge flap effectiveness is obtained with $\delta = 0.7 - 0.8$ rad, i.e., with somewhat less deflection than for the split flap. In addition to increasing $\Delta c_{y\ max}$ and the drag coefficient, trailing-edge flaps also increase the diving moment coefficient c_m. The variation of c_y with c_m for a straight wing with different trailing-edge flap deflection angles for $l_f/l = 1$ is shown in Figure 18.14. We note that deflection of both the split and trailing-edge flaps has very little effect on the location of the wing aerodynamic center.

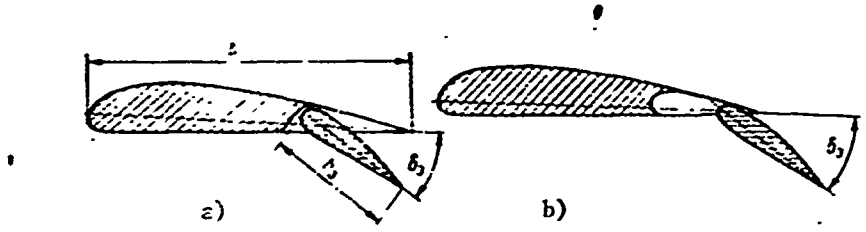

Figure 18.13. Trailing edge flaps:
a - simple; b - extending

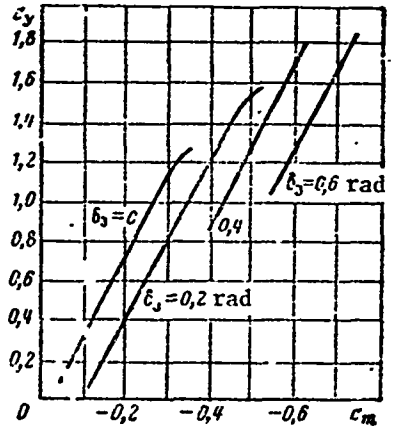

Figure 18.14. c_y versus c_m for wing with different trailing-edge flap deflections (l_f/l = 1)

Usually the trailing-edge flaps, like split flaps, occupy about 60% of the span, since part of the wing is used for the ailerons. Therefore, the effect of both the split and trailing-edge flaps is reduced correspondingly. Sometimes the ailerons are also used as trailing-edge flaps in order to increase the effectiveness, both ailerons being deflected down during the landing process for this purpose.

For a comparison of the effectiveness of the use of split flaps and various types of trailing-edge flaps covering the entire span, Table 18.1 shows the aerodynamic characteristics of a straight wing (λ = 5). The extending trailing-edge flaps are most effective.

Leading-edge flaps and slats. The leading-edge flap with sharp leading edge has found use on supersonic airplanes as a form of wing mechanization (Figure 18.15). When deflected at high angles of attack, the leading-edge flap prevents premature flow separation from the sharp leading edge of the supersonic profile and thereby increases $c_{y\ max}$.

TABLE 18.1

Type of mechanization	$c_{y\ max}$	$\Delta c_{y\ max}$	α_{st}, rad
Split flap ($\delta_f = \pi/3$; $b_f = 0.3\ b$)	2.16	0.87	0.24
Trailing-edge flap without profiled slot ($\delta_f = \pi/4$; $b_f = 0.3\ b$)	1.95	0.66	0.21
Slotted trailing-edge flap ($\delta_f = \pi/4$, $b_f = 0.35\ b$)	1.98	0.69	0.21
Extending trailing-edge flap ($\delta_f = \pi/4$; $b_f = 0.4\ b$)	2.42	1.13	0.26

The slat has a winglike shape and is located along the leading edge of the wing. At high angles of attack a profiled slot is formed between the wing and the slat (Figure 18.16). The effect of the slat lies in the fact that it deflects the jet leaving the profiled slot downward and thus aids in holding the flow on the upper surface of the wing. The gradual narrowing of the slot causes the air velocity to increase. The jet discharging at high velocity through the slot shifts the point of boundary layer separation on the upper surface of the wing downstream and prevents flow separation with further increase of the angle of attack.

Figure 18.15. Leading-edge flap

As a result of the slat action there is an increase of the wing stalling angle of attack and the coefficient $c_{y\ max}$. The curves $c_y = f(\alpha)$ for a wing with and without slats are shown in Figure 18.17. These curves show that $c_{y\ max}$ for the wing with slats increases significantly (by 50% on the average), and there is

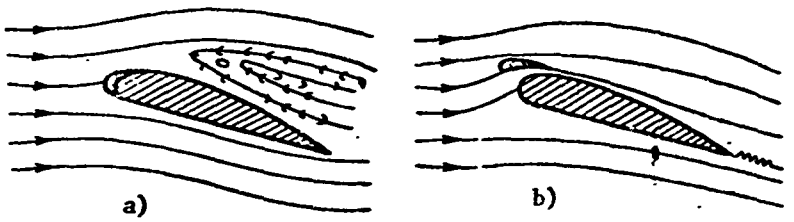

Figure 18.16. Flow around wing at high angle of attack with undeflected (a) and deflected (b) slats

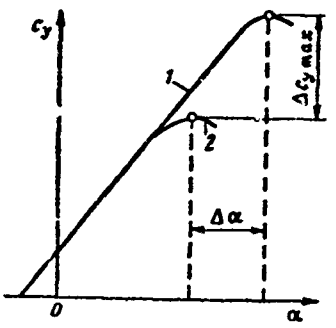

Figure 18.17. Curve $c = f(\alpha)$ for wing with and without slats:

1 - wing with slats;
2 - wing without slats

a considerable increase of the stall angle of attack. This latter factor prevents complete utilization of the slat effect, since this would lead to increase of the landing angle of attack and complication of the airplane landing and takeoff process. For this reason, on most airplanes slats are used only near the wing tips in order to increase aileron effectiveness at high angles of attack.

Multislotted wings. Negative pressure ($\bar{p} < 0$) is formed on the upper surface of the wing at high angles of attack and positive pressure on the lower surface ($\bar{p} > 0$). If we make one or more slots in the wing, then as a result of the pressure difference part of the air will flow through the slots from the lower surface of the wing to the upper surface. The discharging jets lead to downstream shift of the boundary layer separation point. The effect will be the greater, the more the jet contracts in the direction of the flow (Figure 18.18).

Multislotted wings increase c_y by a factor of 2.5 - 3 or more. However, it is difficult to use slotted wings on real flight vehicles

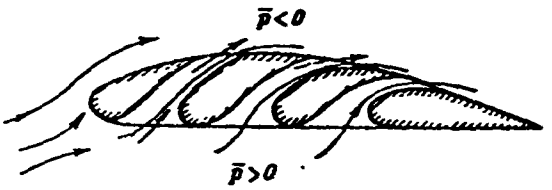

Figure 18.18. Profile of "slotted" (multislotted) wing

because of structural complexity.

Jet flaps and slats. Studies have recently been initiated of the so-called jet flaps and slats. A strong jet is blown into a narrow slot located along the trailing edge of the wing (jet flap) or near the leading edge of the wing (jet slat), as a result of which there is improvement of the flow around the wing and at the same time a reactive force is created by the jet (in the jet flap case). As a result, there is considerable increase of the coefficient $c_{y\ max}$ (without increase of the angle α_{st}), which makes it possible to perform landings at comparatively low speeds.

Spoilers or flow interrupters consist of flat or slightly curved plates, located along the span, which can be extended through slots in the wing approximately along the normal to the wing surface. Spoilers are capable of causing boundary layer transition or even flow separation from the wing surface, depending on the spoiler extension height. This phenomenon is accompanied by redistribution of the pressure over the profile. In this case, the pressure changes considerably not only on that side of the profile where the spoiler is extended, but also on the opposite side. In many cases the pressure redistribution caused by the spoiler leads to change of the coefficients c_x, c_y, c_m. The magnitude and sign of the pressure coefficient change depends not only on spoiler height but also on spoiler location along the chord.

Spoiler operation has a decelerating effect on the flow ahead of it: the local velocities ahead of the spoiler decrease and the pressure increases. The pressure decreases behind the spoiler, and

a suction region is created. Sometimes the spoilers are made comb-like (intermittent) in order to maintain smooth flow over the wing and reduce separation drag.

Effect of wing planform on mechanization effectiveness. The deflection of split or trailing-edge flaps has practically no effect on the derivatives $c_y^\alpha = \frac{\partial c_y}{\partial \alpha}$ and $\frac{\partial c_m}{\partial c_y}$ within the limits of linear relations $c_y = f(\alpha)$ and $c_m = f(c_y)$, but does affect markedly the value of the angle α for $c_y = 0$. The change of the magnitude of the angle of attack α_{0f} for $c_y = 0$ resulting from deflection of split or trailing edge flaps is determined by the type and geometric parameters of the mechanization.

For swept wings c_y^α is considerably lower than for unswept wings of large aspect ratio. Consequently, with increase of the sweep angle the lift increment Δc_y owing to mechanization decreases (Figure 18.19).

The mechanization effectiveness decreases sharply for swept wings at angles of attack near the stall. For example, for $\chi=\pi/4$; $\eta=4$; $\lambda=4,5$ flap deflection through an angle $\delta=\pi/3$ yields practically no increase of c_y.

For sweep angles $\chi_{0.4}$ larger than 0.9 rad, the split and trailing-edge flaps nearly always lose their effectiveness at the stalling angles of attack. Wing aspect ratio has a similar effect on mechanization effectiveness: the mechanization effectiveness decreases with decrease of the aspect ratio.

The unfavorable influence of high sweep and low aspect ratio on flap effectiveness and wing lift makes it necessary to use more effective mechanization techniques, for example, extending split flaps, extending trailing-edge flaps, and so on. In addition, use is made of increased taper ratio; in this case, the relative area of the trailing-edge flaps is increased, and there is an associated increase of their effectiveness. Sometimes aerodynamic fences are located on the upper surface of swept wings in the areas where the trailing-edge

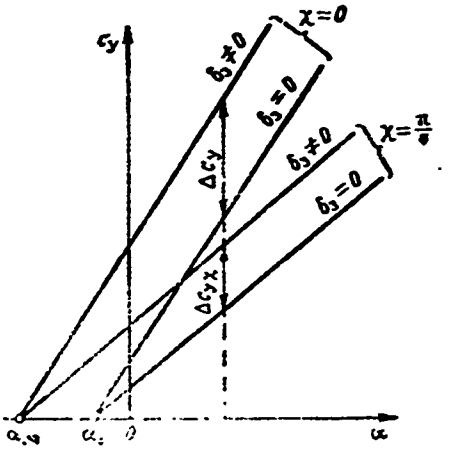

Figure 18.19. Effect of wing planform on mechanization effectiveness

flaps are located. In this case, the flow approaches plane-parallel flow, and there is an increase of the flap effectiveness. Boundary layer control by blowing and suction is very effective, and use is also made of jet flaps.

§18.4. Influence of Ground Effect on Maximal Lift Coefficient and Wing Polar

When the airplane travels near the ground (during takeoff and landing) the physical conditions of the flow around the wing change, since the ground surface restricts the flow. In this case, the downwash behind the wing cannot develop as it does at higher altitudes.

As a result of the pressure increase below the wing, the velocity near the leading edge of the wing increases markedly, which leads to redistribution of the pressure on the profile (Figure 18.20). Since there is an increase of the positive pressure gradient, this redistribution tends to cause the boundary layer on the upper surface of the wing to separate. As a result of the pressure redistribution on the upper and lower wing surfaces, the lift coefficient increases for a given α, but the stalling angle of attack decreases. In this case, there is a decrease of the maximal lift coefficient (Figure 18.21a).

The drag decreases somewhat because of the ground effect. The reason for the drag reduction is the appearance of a suction force,

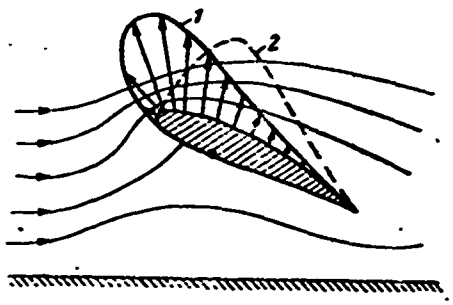

Figure 18.20. Influence of ground effect on pressure distribution over profile:

1 - near ground; 2 - far from ground

which arises as a result of pressure reduction near the leading edge and downwash reduction behind the wing (the ground surface prevents downward deflection of the flow). The first factor leads to reduction of the pressure drag — the wing polar shifts to the left — while the second factor leads to reduction of the induced drag — the polar has lower slope (Figure 18.21b). This pressure redistribution has a still more marked nature for a wing with flaps deflected (see Figure 18.21a). A wing leading edge which can be deflected downward may be used to improve the flow around the wing near the ground.

The induced drag reduction during landing and takeoff is evaluated by introducing a fictitious aspect ratio, defined from the formula

$$\lambda_\phi = \frac{\lambda \cdot \phi}{2,23}\left(\frac{\pi l}{8h}+2\right),$$

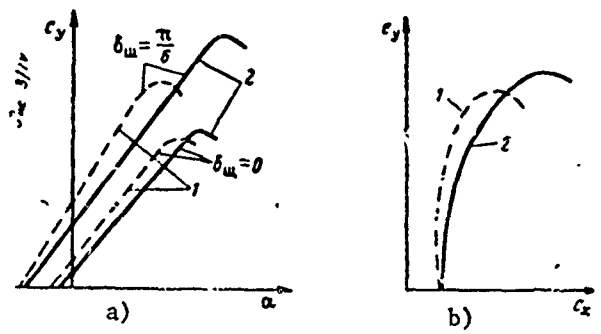

Figure 18.21. Change of wing aerodynamic characteristics under influence of ground effect:

1 - near ground; 2 - far from ground.

where λ_{eff} is the effective wing aspect ratio;
l is the wing span;
h is the distance between the wing focus and the ground with the airplane parked.

REVIEW QUESTIONS

1. What factors affect the magnitude of the maximal lift coefficient, and to what degree?

2. Where does boundary layer separation begin at high angles of attack on straight, trapezoidal, and swept wings?

3. What measures are used to prevent boundary layer separation in the tip regions of the swept wing?

4. Show graphically the dependence of c_y on the angle of attack for a wing with slats and for a wing with trailing-edge flaps. What is the difference between these relations?

5. Draw the polar of a wing without mechanization and with deflected trailing edge flaps. How do the lift, drag, and efficiency of the wing vary as the flaps are deflected? How does flap deflection affect the stalling angle of attack?

PROBLEMS

1. Find the maximal lift coefficient of a wing with trapezoidal planform with elliptical circulation distribution along the span if the wing area $S = 32\ m^2$, wing aspect ratio $\lambda = 8$, taper ratio $\eta = 5$, maximal section lift coefficient $c_{y\ max\ sec} = 1.72$.

Solution. We shall use the TsAGI method, for which we first find the wing geometric dimensions and circulation distribution.

The wing span

$$l=\sqrt{\lambda S}=\sqrt{8\cdot 32}=16\ м.$$

The wing area

$$S=2\,\frac{b_{конц}+\eta b_{конц}}{2}\,\frac{l}{2}=\frac{b_{конц}l}{2}(\eta+1).$$

Hence we find the tip chord length:

$$b_{конц}=\frac{2S}{l(\eta+1)}=\frac{2\cdot 32}{16(5+1)}=\frac{2}{3}=0{,}67\ м.$$

The root chord

$$b_к=\eta b_{конц}=5\cdot\frac{2}{3}=3{,}33\ м.$$

The mean aerodynamic chord

$$b_{ср}=\frac{S}{l}=\frac{32}{16}=2\ м.$$

By assumption, the circulation distribution is elliptic, so that

$$\left(\frac{\Gamma}{\Gamma_{max}}\right)^2+\left(\frac{z}{l/2}\right)^2=1.$$

Using the formula for the area of an ellipse, we express the maximal circulation in terms of the spanwise average

$$\Gamma_{max}=\frac{2}{\pi}\Gamma_{ср}.$$

We obtain for the circulation distribution

$$\bar{\Gamma}^2+\bar{z}^2=1, \qquad (а)$$

where

$$\bar{\Gamma}=\frac{\Gamma}{\Gamma_{max}};\ \ \bar{z}=\frac{z}{l/2}.$$

We find the quantity $c_{y\ max\ st}$ from the relation

$$c_{y\,max\,kp}=\left(\frac{c_{y\,max\,cec}}{c'_{y\,cec}}\right)_{min}, \qquad (b)$$

where $$c'_{y\,cec}=\bar{\Gamma}\frac{b_{cp}}{b}.$$

This formula is obtained if we use the coupling Equation (16.14), setting $c_{y\ sec}$ and $c_{y\ st}$ = 1. We summarize the calculations in a table.

$\bar{z}$	0	0.2	0.4	0.6	0.8	0.85	0.9	0.95	1.0
Γ/Γ_{cp}	1.130	1.110	1.035	0.903	0.677	0.615	0.502	0.352	0
b/b_{cp}	1.67	1.40	1.14	0.87	0.60	0.54	0.47	0.40	0.33
$c'_{y\,cec}$	0.677	0.793	0.908	1.04	1.13	1.14	1.07	0.88	0
$c_{y\,max\,cec}/c'_{y\,cec}$	2.51	2.17	1.89	1.65	1.52	1.51	1.61	1.95	∞

Then we use Figure 18.8 to find graphically

$$c_{y\,max\,kp}=1{,}51.$$

2. For the conditions of the preceding problem, plot the wing polar if the flight speed at sea level V = 456 km/hr, profile relative thickness c = 0.14, point of transition of laminar boundary layer to turbulent $\bar{x}_T=0.2$, $\partial c_y/\partial\alpha=4.6$, $\delta=0.06$, and zero lift angle $\alpha_0=-0.026$ rad. Also plot the lift coefficient versus angle of attack and note the angles of attack on the wing polar.

CHAPTER XIX

WING AERODYNAMIC COEFFICIENTS AT SUBSONIC AND TRANSONIC SPEEDS

§19.1. Effect of Compressibility on Aerodynamic Characteristics of Finite-Span Wing in Subsonic Flow

It was shown in Chapter 13 that in the first approximation the aerodynamic characteristics of a profile in subsonic flow are connected with the aerodynamic characteristics of the profile in incompressible flow by relations obtained on the basis of linearization of (13.10)

$$c_{y\,\text{сж.сеч}} = \frac{c_{y\,\text{нс.сеч}}}{\sqrt{1-M_\infty^2}}; \tag{19.1}$$

$$c_{m\,\text{сж.сеч}} = \frac{c_{m\,\text{нс.сеч}}}{\sqrt{1-M_\infty^2}}. \tag{19.2}$$

To evaluate the effect of compressibility on the characteristics of the finite-span wing, we use the hypothesis of plane sections, assuming that the aerodynamic properties of the individual wing sections are completely determined by the flow conditions at these sections (velocities and angles of attack). Comparison of theoretical and experimental data shows that the hypothesis of plane sections is applicable for wings of comparatively large aspect ratio ($\lambda > 3$).

The expression for the coefficient c_y of the finite-span wing has the form

$$c_y=\frac{1}{S}\int_{-\frac{l}{2}}^{\frac{l}{2}} c_{y\,сеч}b(z)dz.$$

If we use (19.1) for $c_{y\ sec}$, on the basis of the hypothesis of plane sections we obtain

$$c_{y\,сж}=\frac{c_{y\,нс}}{\sqrt{1-M_\infty^2}}. \tag{19.3}$$

We obtain similarly the relation

$$c_{m\,сж}=\frac{c_{m\,нс}}{\sqrt{1-M_\infty^2}}. \tag{19.4}$$

Formulas (19.3), (19.4) make it possible to calculate approximately the aerodynamic characteristics of a wing in compressible flow if the wing characteristics in incompressible flow are known.

Applying the hypothesis on the analogy between swept and yawed wings, we obtain the connection between c_{yn} for sections normal to the wing axis

$$c_{y_n\,сж}=\frac{c_{y_n\,нс}}{\sqrt{1-M_\infty^2\cos^2\chi}}. \tag{19.5}$$

Assuming that $c_{y\ sw}$ depends linearly on α, we can calculate $c^{\alpha}_{y\ sw}$ for compressible flow

$$c^{\alpha}_{y\,стр.сж}=\frac{c^{\alpha}_{y_\lambda\,\infty}}{\sqrt{1+\operatorname{tg}^2\chi-M_\infty^2}+\frac{c^{\alpha}_{y_\lambda\,\infty}}{\pi\lambda}(1+\tau_{стр})}. \tag{19.6}$$

As $M_\infty \to 0$ we obtain (17.8) from (19.6).

At angles of attack near the stall, compressibility affects the lifting capabilities of the wing. As a result of compressibility there is an increase of the pressure gradient on the upper surface of

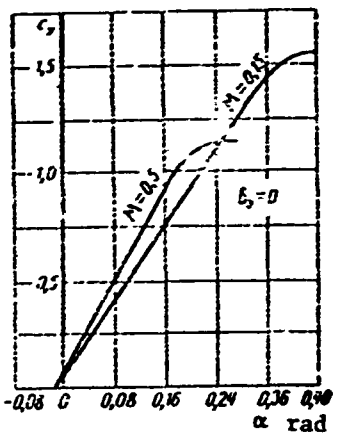

Figure 19.1. Wing lift coefficient c_y of An-24 airplane versus α.

the wing and increase of the boundary layer thickness. The increase of the pressure gradient and the simultaneous increase of the boundary layer thickness lead to premature separation of the compressible fluid flow in comparison with incompressible fluid flow: $c_{y\ max}$ and α_{st} decrease.

Figure 19.1 shows curves of $c_y = f(\alpha)$ for the An-24 airplane wing at M = 0.15 and M = 0.5. We see from the figure that c_y will be larger at the same angles of attack for the wing in the higher speed flow, i.e., with the larger Mach number. The stalling angle of attack α_{st} and the coefficient $c_{y\ max}$ decrease with increase of the Mach number, since at the higher speed boundary layer separation begins at a lower angle of attack.

The expression for the drag coefficient of the finite-span wing has the form

$$c_x = \frac{1}{S}\int_{-l/2}^{l/2} c_{x\,сеч} b(z)\,dz,$$

where

$$c_{x\,сеч} = c_{xp\,сеч} + c_{xi\,сеч},$$

or

$$c_x = c_{xp} + c_{xi}.$$

In the case of flow without separation, the wing profile drag coefficient is independent of c_y and is equal to the drag coefficient for $c_y = 0$

$$c_{xp} = c_{x0}.$$

The wing induced drag coefficient is found from the formula

$$c_{xi}=\frac{c_y^2}{\pi\lambda}(1+\delta).$$

The equation of the wing polar for subsonic flow has the form

$$c_x=c_{x0}+\frac{c_y^2}{\pi\lambda}(1+\delta). \qquad (19.7)$$

The effect of M_∞ on the induced drag is accounted for by the presence in (19.7) of the quantity c_y, which depends on M_∞. The effect of M_∞ on the profile drag is accounted for by the additional coefficient $\eta_M=\frac{c_{x\,com}}{c_{x\,incom}}$, which can be found from the curves of Figures 13.6 and 13.7.

§19.2. Critical Mach Number of Finite-Span Wing

Just as for a profile, the critical Mach number of a wing is that freestream Mach number at which local supersonic zones appear on the wing surface.

The critical Mach number separates the subsonic regime of flow around the wing from the mixed (transonic) flow regime, in which there are both subsonic and supersonic local velocities.

The methods for determining $M_{cr\ prof}$ make it possible to determine the value of M_{cr} which is applicable only for a straight wing of infinite span. The value of M_{cr} for real wings may differ significantly from $M_{cr\ prof}$ because of the existence of sweep and low aspect ratio, which lead to flow having a three-dimensional nature. Exact methods for calculating M_{cr} for the swept wing have not yet been developed because of the complexity in accounting for the influence of the centerline and tip effects on the nature of the flow Therefore, for practical purposes experimental data are most reliable for determining the effect of wing sweep on the value of M_{cr}.

The increment $\Delta M_{cr\lambda}$ of the critical Mach number M_{cr} when the sweep angle measured along the maximal thickness line is varied is shown in Figure 19.2. We see from this figure, first of all, that

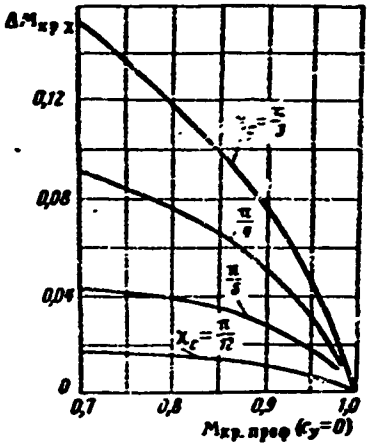

Figure 19.2. $\Delta M_{cr\chi}$ versus $M_{cr\ prof}$ $(c_y = 0)$ and wing sweep angle along maximal thickness line.

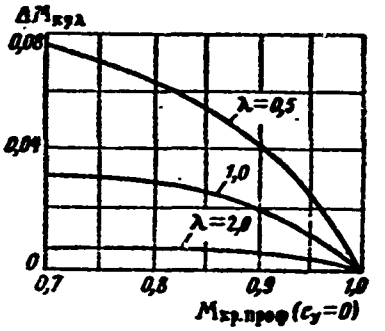

Figure 19.3. $\Delta M_{cr\lambda}$ versus $M_{cr\ prof}$ $(c_y = 0)$ and wing aspect ratio.

there is a very marked influence of sweep, particularly for comparatively small M_{cr}; secondly, we can see that no sweep angle increase can make it possible to obtain a value of M_{cr} exceeding one, i.e., M_{cr} is always less than one. This follows from the fact that as $M_\infty \to 1$ we can always find near the wing surface a zone within the limits of which the local velocity will be greater than the freestream velocity. It is from this zone that the shock stall begins to develop when the local speed becomes equal to the critical velocity α_{cr}.

Decrease of the wing aspect ratio λ affects the value of M_{cr} just as increase of the sweep does. For low aspect ratio wings the tip crossflow effects encompass nearly the entire wing surface, reducing the local underpressures, which in accordance with the Khristianovich theory (see Chapter 14) leads to increase of M_{cr}. To determine the increment $\Delta M_{cr\lambda}$, we can use the curves of Figure 19.3, which show that for an aspect ratio greater than two this correction does not reach one percent and can be neglected.

Since the aspect ratio of modern passenger airplane wings is a quantity of order 8-12, the aspect ratio for these airplanes does not affect the value of M_{cr} significantly. A quite different situation is

seen in supersonic aviation, where wings with aspect ratio $\lambda < 2$ may frequently be encountered.

Thus, the relation for the wing M_{cr} can be written in the form

$$M_{кр} = M_{кр.проф} + \Delta M_{кр\lambda} + \Delta M_{кр\lambda}. \qquad (19.8)$$

§19.3. Wing Aerodynamic Characteristics at Transonic Flight Speeds

Exceeding M_{cr} in flight always involves the appearance of supersonic zones, which are closed by compression shocks. As M_∞ is increased the supersonic zones develop, extending quite rapidly to the trailing edge of the wing and comparatively slowly to the leading edge. At $M_\infty = 1$ the subsonic zone is retained primarily only at the leading edge of the wing.

When $M_\infty > 1$ a normal compression shock develops ahead of the rounded leading edge of the wing. Further from the wing the normal shock front becomes curved and transitions into an oblique shock. As M_∞ is increased, the shock approaches the leading edge and the subsonic zone becomes smaller. The bow shock becomes an oblique shock and "attaches" to the leading edge at Mach numbers $M_\infty = 1.3 - 1.4$ for wings with sharp leading edge and at $M_\infty = 2$ or more for blunt leading edges. Beginning at this moment the transonic flow regime around the wing becomes supersonic. The relations which are valid for transonic flows are supplanted by the supersonic relations only when the velocities become supersonic over the entire wing surface.

Transonic flow theory makes possible basically only a qualitative analysis in view of the exceptional complexity of transonic flow description.

The lift coefficients of a wing with symmetric profile in the transonic flow regime are determined with the aid of the equation

$c_y = c_y^{\alpha}(\alpha - \alpha_0)$, which is valid on the linear part of the curve $c_y = f(\alpha)$. The quantity c_y^{α} is usually found from curves plotted on the basis of experimental data, which yield the relation

$$\frac{c_y^{\alpha}}{\lambda} = f\left(\lambda\sqrt{1-M_{\infty}^2},\ \lambda \operatorname{tg}\chi,\ \eta,\ \lambda\sqrt[3]{\bar{c}}\right),$$

where $\lambda\sqrt{1-M_{\infty}^2}$, $\lambda \operatorname{tg}\chi$, η, $\lambda\sqrt[3]{\bar{c}}$—are the similarity parameters in the transonic regime, established by similarity theory.

Figure 19.4 shows the relation

$$\frac{c_y^{\alpha}}{\lambda} = f\left(\lambda\sqrt{1-M_{\infty}^2},\ \lambda\sqrt[3]{\bar{c}}\right).$$

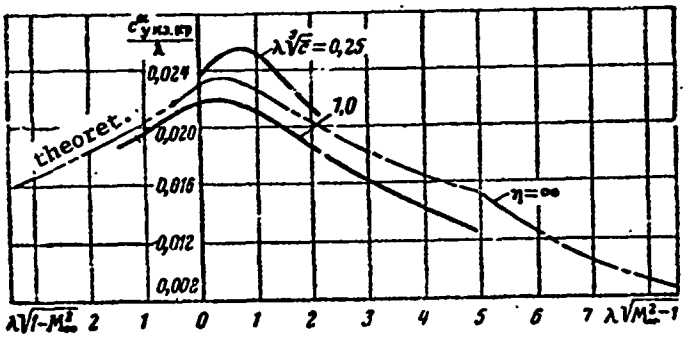

Figure 19.4. Curves for calculating lift coefficients of isolated wings ($\lambda \operatorname{tg} \chi_c = 3$)

The continuous curves are experimental results, averaged with respect to η in view of the weak influence of the taper ratio.

Wing drag in transonic flow differs from the drag in subsonic flow by the magnitude of the additional drag, termed wave drag.

The wing drag coefficient is determined from the usual formula

$$c_x = c_{x0} + c_{xi}. \qquad (19.9)$$

The first term c_{x0} is independent of lift and is made up from the boundary layer friction drag $c_{x0\ fr}$ and the wave drag $c_{x0\ w}$

$$c_{x0}=c_{x0\,fr}+c_{x0\,w}. \tag{19.10}$$

The friction drag coefficient $c_{x0\ fr}$ is found with the aid of the formulas and graphs which are valid for the subsonic flow regimes. The coefficient $c_{x0\ w}$, which accounts for the wave drag for $c_y = 0$, is determined experimentally.

The second term c_{xi} in (19.9) is the drag which depends on the lift coefficient. Since there are both subsonic and supersonic flow zones on the wing, the magnitude of this drag component occupies an intermediate position between the induced drags for the subsonic and supersonic regimes.

The approximate method developed by Kuznetsov for determining induced drag amounts to the following. The larger the lift coefficient, the smaller is the corresponding M_{cr} and, conversely, if we assume a value of M_{cr}, then as c_y increases the shock stall develops at a quite definite value of c_y, which we term $c_{y\ cr}$. The connection between M_{cr} and $c_{y\ cr}$ for the upper surface of the wing is shown in Figure 19.5.

If $c_y \leq c_{y\ cr}$ the induced drag appears as a result of the downwash angle $\Delta\alpha$ and is found from the formula

$$c_{xi}=\frac{c_y^2}{\pi\lambda}(1+\delta). \tag{19.11}$$

When $c_y > c_{y\ cr}$ additional lift and drag increase takes place because of the presence of the supersonic zones. In this case we assume that the additional aerodynamic force ΔR, in accordance with the supersonic flow laws (see Chapter 15), will be perpendicular to the wing chord, i.e., it will form the angle α with the normal to the flow direction (Figure 19.6).

Projecting the forces R and ΔR on the coordinate axes in the wind system and assuming $\cos\alpha \approx \cos\Delta\alpha \approx 1$, $\sin\alpha \approx \alpha$, in view of the smallness

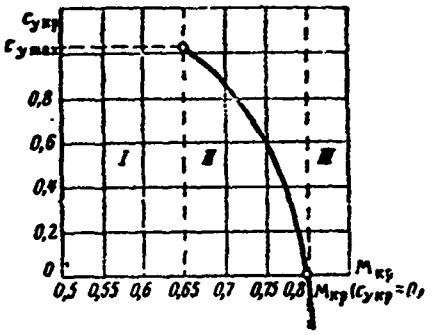

Figure 19.5. M_{cr} versus $c_{y\,cr}$ for upper surface of wing.

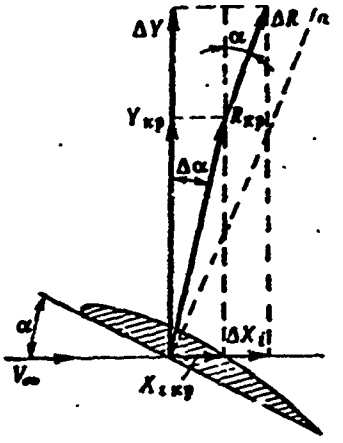

Figure 19.6. Illustration for constructing wing polar for $M_\infty > M_{cr}$.

of the angle of attack and the downwash angle, we obtain the formulas for wing lift and induced drag in the form

$$Y = Y_{кр} + \Delta Y = R + \Delta R;$$
$$X_i = X_{i\,кр} + \Delta X_i = X_{i\,кр} + \Delta R\alpha$$

or, converting to the aerodynamic coefficients, we have

$$\left.\begin{aligned} c_y &= c_{y\,кр} + \Delta c_y, \\ c_{xi} &= c_{xi\,кр} + \Delta c_y \alpha. \end{aligned}\right\} \qquad (19.12)$$

Here $c_{xi\,cr}$ is the induced drag coefficient, defined by (19.11) for $c_y = c_{y\,cr}$.

Excluding Δc_y from (19.12) and replacing $c_{xi\,cr}$ using (19.11), we obtain

$$c_{xi} = \frac{c_{y\,кр}^2}{\pi\lambda}(1+\delta) + (c_y - c_{y\,кр})\alpha. \qquad (19.13)$$

Assuming that the relation $c_y = c_y^\alpha \alpha$ holds in the transonic regimes, (19.13) can be reduced to the form

$$c_{xi} = \frac{c_{y\,кр}^2}{\pi\lambda}(1+\delta) + \frac{(c_y - c_{y\,кр})\,c_y}{c_y^\alpha}. \qquad (19.14)$$

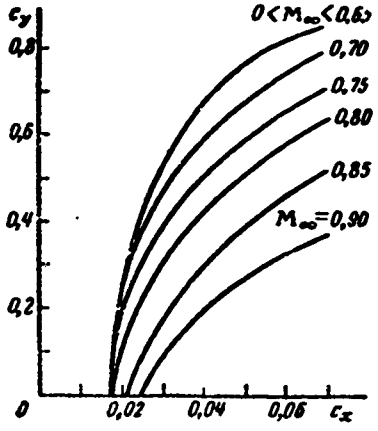

Figure 19.7. Wing polars for different M_∞ ($\lambda = 7$; $\bar{c} = 0.09$; $\chi_c = 0.52$ rad).

The quantity $c_{y\ cr}$ is determined from a graph for each flight Mach number. Calculations show that the values found using (19.14) are quite close to the values obtained experimentally. We note that for $c_y < c_{y\ cr}$ there is no shock stall and in this case (19.11) should be used.

The equation of the polar can be obtained if in (19.9) we substitute the value of the induced drag coefficient from (19.14)

$$c_x = c_{x0} + \frac{c_{y\,кр}^2}{\pi\lambda}(1+\delta) + \frac{c_y - c_{y\,кр}}{c_y^*} c_y. \qquad (19.15)$$

The wing polars in the coordinates c_y and c_x for various M_∞, plotted using (19.15), are shown in Figure 19.7.

The nature of the polars for different M_∞ can be analyzed with the aid of the curve of Figure 19.5. We divide the area of the figure into three zones. In zone I there is no wave drag over the entire range of values of c_y, and the wing polars at these M_∞ are expressed by the equation of the polar for subsonic flow. We see from Figure 19.7 that zone I ends at $M_\infty = 0.65$. In zone II, corresponding to $0.65 < M_\infty < 0.8 = M_{cr}$ ($c_y = 0$), the shock stall begins when the value $c_y = c_{y\ cr}$ is reached. For small values of c_y, the polars for M_∞ in this range coincide with the wing polar in subsonic flow, while beginning with $c_y = c_{y\ cr}$ they deviate to the right. In zone III there will be wave drag even for $c_y = 0$. With increase of M_∞, beginning with M_{cr} ($c_y = 0$), the polars shift to the right and do not coincide with the wing polar in subsonic flow for any values of c_y.

§19.4. Wing Moment Characteristics

The wing moment coefficient about an axis passing through the leading edge of the equivalent rectangular wing is defined, just as for subsonic flows, by the relation

$$c_m = c_{m0} - \bar{x}_F c_y, \tag{19.16}$$

where $\bar{x}_F$ is the ratio of the distance from the leading edge to the wing focus to the MAC length.

Sufficient experimental data have now been obtained to evaluate the location of the wing focus for quite a wide range of flow conditions. Experiment shows that the similarity criteria obtained from linear theory make it possible to treat the experimental data quite well in the form of the relations

$$\bar{x}_F = f\left(\lambda\sqrt[3]{1-M_\infty^2},\ \lambda \operatorname{tg}\chi,\ \eta,\ \lambda\sqrt[3]{\bar{c}}\right).$$

Figure 19.8 shows two plots — for straight and swept wings with symmetric profile ($\bar{x}_F = \bar{x}_D$). The curves shown on both plots correspond to the values $\lambda\sqrt[3]{\bar{c}}=0{,}5$ [31]. When the value of the parameter $\lambda\sqrt[3]{\bar{c}}$ is changed, the wing focus location changes. We see from the figures that for wings with small taper ratio η, and particularly for straight wings, the focus shifts forward as M_∞ approaches M_{cr}. For most wings it is characteristic that the focus, located for $M_\infty < M_{cr}$ at about one quarter of the chord from the leading edge, shifts aft at large values of M_∞, nearly reaching the midpoint of the chord.

The experimental curves in Figure 19.8 make it possible to conclude that very large fore and aft shifts of the focus are possible in the transonic M_∞ range. It is likely that this can be explained by the earlier development of the supersonic zone on the upper surface and then on the lower surface of the wing. Experiments show that with increase of the angle of attack in the transonic regime the focus shifts aft, particularly for a small value of the parameter $\lambda \operatorname{tg} \chi$.

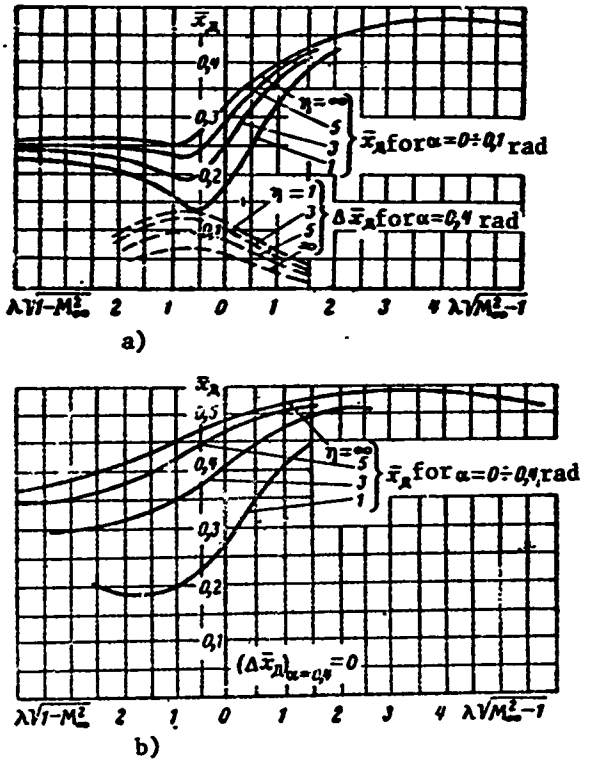

Figure 19.8. Plot for determining center of pressure coordinates of isolated wings with symmetric profile: a - straight ($\lambda tg\chi_c = 0$); b - swept ($\lambda tg\chi_c = 3.0$).

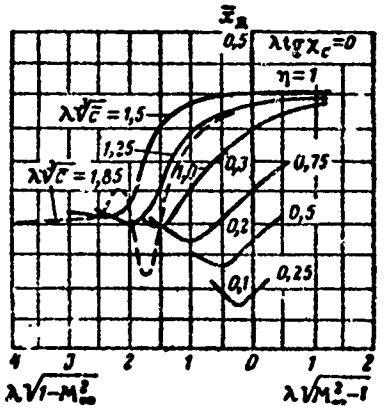

Figure 19.9. Effect of parameter $\lambda\sqrt[3]{\bar{c}}$ on straight wing center of pressure location.

Considering that in the first approximation the variation of $\bar{x}_F$ with α in the angle of attack range 0.1 rad < α < 0.4 rad is linear, we can determine the value of the focus dimensionless coordinate in this range from the formula

$$\bar{x}_F = (\bar{x}_F)_{\alpha=0,1} + \frac{\alpha-0,1}{0,3}(\Delta\bar{x}_F)_{\alpha=0,4}. \quad (19.17)$$

The quantities $(\bar{x}_F)_{\alpha=0.1}$ and $(\Delta\bar{x}_F)_{\alpha=0.4}$ are determined with the aid of graphs.

The effect of the transonic similarity parameter on the location of the center of pressure of a straight wing with symmetric profile is shown in Figure 19.9.

REVIEW QUESTIONS

1. How does the wing M_{cr} depend on its geometric parameters?

2. Write the equation of the wing polar for different M_∞.

3. Analyze the wing moment characteristics.

PROBLEMS

1. Find M_{cr} for an airplane under the following conditions: $M_{cr\ prof} = 0.78$, wing sweep angle $\chi = 0.78$ rad, wing aspect ratio $\lambda = 2$.

Answer. $M_{cr} = 0.867$.

2. Find c_y^α for a swept wing in compressible flow if

$$c^a_{y\lambda=\infty}=4{,}7; \quad \chi=0{,}58 \text{ rad}; \quad \lambda=5{,}6;$$
$$\tau_{стр}=0{,}1; \quad M_\infty=0{,}8.$$

Solution. According to (19.6)

$$c^a_{y\,стр.сж}=\frac{c^a_{y\lambda=\infty}}{\sqrt{1+\operatorname{tg}^2\chi-M^2_\infty}+\frac{c^a_{y\lambda=\infty}}{\pi\lambda}(1+\tau_{стр})}=$$
$$=\frac{4{,}7}{\sqrt{1+0{,}4225-0{,}64}+\frac{4{,}7\cdot 1{,}1}{3{,}14\cdot 5{,}6}}=4.$$

CHAPTER XX

AERODYNAMICS OF WING IN SUPERSONIC FLOW

§20.1. Effect of Wing Planform on Nature of Supersonic Flow Past Wing

Just as in the case of subsonic velocities, in supersonic flow the wing planform has a significant effect on the nature of the flow and this leads to differences between the aerodynamic characteristics of the finite-span wing and those of the profile in supersonic flow. However, we note that the influence of tip effects, sweep, and magnitude of the aspect ratio at supersonic speeds will be different in comparison with the influence of these factors on the nature of the flow about the wing at subsonic speeds.

The influence of the wing tips on the flow over the central part of a straight wing is illustrated in Figure 20.1. In supersonic flow the disturbance zone generated by the wing tips is bounded by two disturbance cones with apexes at the lateral leading edges. The cone halfangle is found from the relation

$$\sin\mu=\frac{1}{M_\infty}. \tag{20.1}$$

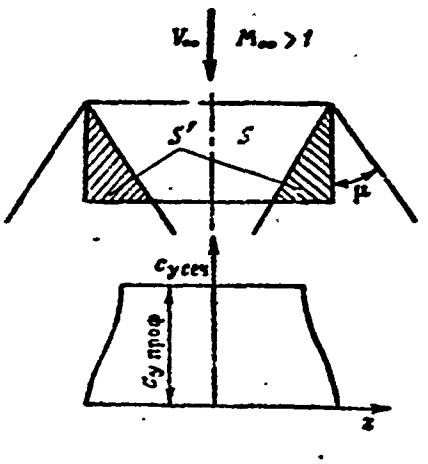

Figure 20.1. Influence of wing tips for supersonic flow around wing.

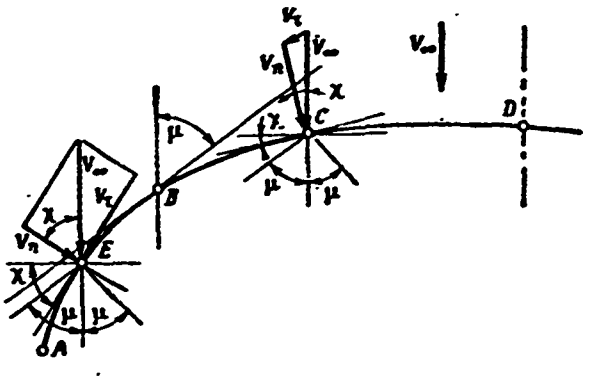

Figure 20.2. Supersonic flow past wing of arbitrary planform.

Outside the disturbance cones the flow is not disturbed and the influence of the tip effects is not felt. While in subsonic flow the tip effects encompass the entire wing surface $S = bl$, at supersonic speeds the influence of the tips is felt only on the area S'.

For the straight wing

$$S' = \frac{b^2}{\sqrt{M_\infty^2 - 1}}.$$

The area ratio

$$\frac{S'}{S} = \frac{b^2}{bl\sqrt{M_\infty^2 - 1}} = \frac{1}{\lambda\sqrt{M_\infty^2 - 1}}.$$

Consequently, the influence of the tip effects on the magnitude of the aerodynamic coefficients depends on the quantity $\lambda\sqrt{M_\infty^2 - 1}$. The larger the wing aspect ratio λ or the Mach number M_∞, the smaller is the fraction of the disturbed zones S' in the overall wing area S, and this means that the influence of the tips on the wing aerodynamic characteristics is less.

The alignment of the leading edge relative to the freestream velocity vector has a marked influence on the nature of the flow around the wing. To see this we examine how the flow approaches a wing of arbitrary planform (Figure 20.2). We assume that the wing is thin and is at a small angle of attack in the flow. In this case we can suppose that any point on the wing surface, including any point on the leading edge, is a source of small disturbances. These disturbances propagate from each point within a cone with halfangle μ, defined by (20.1).

On the segment BD the leading edge is in undisturbed flow, since none of the disturbances extend foward ahead of the leading edge (see, for example, the disturbances at point C). The presence of the wing is not felt in the approaching stream up to the leading edge itself. The velocity, pressure, and density in the stream do not change prior to contact of the stream with the leading edge. This nature of the flow is typical for supersonic flow over a profile. In this case the leading edge is called supersonic.

On the segment AB the stream passes through the disturbance zone prior to reaching the leading edge. Here the velocity and parameters of the air begin to change ahead of the wing in a fashion similar to that associated with subsonic flow. In this case the leading edge is termed subsonic. If the leading edge is subsonic, the flows on the upper and lower surfaces of the wing interact with one another.

It can be shown that for a subsonic leading edge the normal component of the velocity will be less than the speed of sound, while for a supersonic leading edge this component will be greater than the speed of sound. We see from the flow conditions at point E (Figure 20.2) that the following relation holds between the angles χ and μ

$$\chi > \frac{\pi}{2} - \mu. \qquad (20.2)$$

It follows from (20.2) that

$$\cos\chi < \sin\mu = \frac{1}{M_\infty}. \tag{20.3}$$

Hence

$$M_\infty \cos\chi < 1,$$

or

$$V_\infty \cos\chi < a.$$

Since $V_\infty \cos \chi = V_n$, we have

$$V_n < a. \tag{20.4}$$

Consequently, for a subsonic leading edge in supersonic flow the relation (20.4) is valid. However, in the following we shall use a different, simpler relation which is obtained from (20.2)

$$\operatorname{tg}\chi > \sqrt{M_\infty^2 - 1}. \tag{20.5}$$

If (20.5) is satisfied the leading edge will be subsonic.

For a supersonic leading edge (point C in Figure 20.2), we have

$$\chi + \mu < \frac{\pi}{2}.$$

Hence with account for (20.1) we find that the following condition must be satisfied for the supersonic leading edge

$$\operatorname{tg}\chi < \sqrt{M_\infty^2 - 1}, \tag{20.6}$$

which is equivalent to the statement that the normal component of the velocity for the supersonic leading edge is always greater than the speed of sound in the undisturbed flow.

In the case in which the disturbance lines pass along the leading edge, i.e., when

$$\operatorname{tg}\chi = \sqrt{M_\infty^2 - 1}, \tag{20.7}$$

the leading edge is termed sonic.

If we multiply both sides of (20.5) by the value of the wing aspect ratio λ, we obtain for the subsonic leading edge

$$\lambda \operatorname{tg} \chi_0 > \lambda \sqrt{M_\infty^2 - 1}, \qquad (20.8)$$

where χ_0 is the sweep angle along the wing leading edge. The condition for subsonic nature of the leading edge flow is encountered most frequently in this form. This is explained by the fact that the expressions λ tg χ and $\lambda\sqrt{M_\infty^2 - 1}$ are the supersonic similarity criteria, which follows from supersonic flow wing theory[1]. The quantity λ tg χ is called the reduced sweep and $\lambda\sqrt{M_\infty^2 - 1}$ is called the reduced aspect ratio.

It is obvious that the following inequality holds for the supersonic leading edge

$$\lambda \operatorname{tg} \chi_0 < \lambda \sqrt{M_\infty^2 - 1}. \qquad (20.9)$$

In calculations we sometimes encounter subsonic and supersonic trailing edges, maximal thickness lines, and so on. In this case the sweep angle in (20.8) and (20.9) is measured relative to the corresponding lines.

The pressure distribution along the wing chord, and also the magnitudes of the aerodynamic coefficients are quite different for wings with subsonic and supersonic leading edges.

The stream approaching a supersonic leading edge remains undisturbed right up to the oblique compression shocks or the expansion waves, which rest on the leading edge (Figure 20.3a). The leading edge separates the stream into upper and lower parts, i.e., the stagnation point lies on the leading edge.

In the subsonic leading edge case (Figure 20.3b), flow which has already been disturbed approaches the wing, and therefore there are no

Footnote (1) appears on page 214

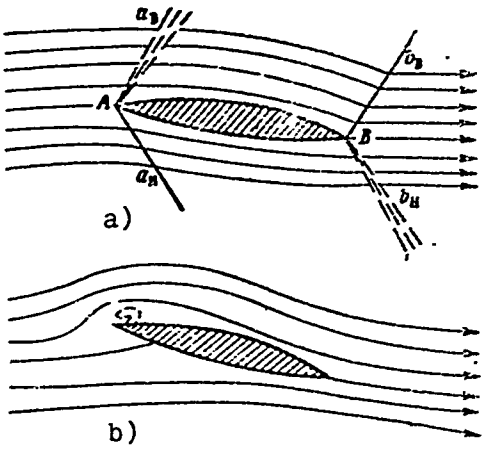

Figure 20.3. Flow past infinite-span wing with supersonic (a) and subsonic (b) leading edges.

shocks immediately ahead of the leading edge. The stagnation point is shifted downward relative to the wing leading edge; the stream filaments flow around the leading edge with high velocity; therefore, a marked underpressure develops on the upper surface of the wing near the leading edge and creates the so-called suction force, which is directed forward and reduces the wing drag.

The suction force develops only in the case in which the leading edge is subsonic and at angles of attack at which $c_y \neq 0$, i.e., the suction force arises only in the presence of a lift force. In order to increase the suction force, in the subsonic leading edge case the wing profile has a blunted and rounded nose, just like the subsonic profiles, which makes it possible to obtain the maximal suction force, other conditions being the same. The stalling angles of attack for wings with rounded nose are considerably higher than for wings with sharp nose, and this is of great importance in providing low takeoff and landing speeds.

§20.2. Lift Force

Because of the wing planform influence, the magnitude of the lift force and therefore the magnitude of the lift coefficient of the finite-span wing differ from the analogous quantities for the profile at the same angle of attack α. Theoretical calculations have been made only for comparatively simple wing planforms and, as a rule, for supersonic leading edges.

For the wings of supersonic airplanes the lift coefficient is proportional to the angle of attack

$$c_y = c_y^{\alpha}\alpha. \tag{20.10}$$

The lift coefficient of the straight wing of infinite span can be found from (15.12), obtained for the profile,

$$c_y = \frac{4\alpha}{\sqrt{M_\infty^2 - 1}}. \tag{20.10'}$$

This formula is also valid for the yawed wing of infinite span if we use the "normal" flow characteristics. In this case we must consider that

$$\alpha_n = \frac{\alpha}{\cos\beta}; \quad M_n = M_\infty \cos\beta.$$

Then we have

$$c_{y_n} = \frac{4\alpha}{\cos\beta\sqrt{M_\infty^2\cos^2\beta - 1}}.$$

Assuming that the lift coefficients of the yawed and straight wings are connected with one another by the relation (17.5), we obtain

$$c_y = \frac{4\cos\beta}{\sqrt{M_\infty^2\cos^2\beta - 1}}\alpha = \frac{4\alpha}{\sqrt{M_\infty^2 - 1 - \mathrm{tg}^2\beta}}. \tag{20.11}$$

Since yawing reduces the "normal" flow Mach number, the lift coefficient also increases with increase of the yaw angle. This is valid provided the leading edge of the yawed wing is supersonic. The increase of the yawed wing lift coefficient in supersonic flow is a consequence of the fundamental difference between the subsonic and supersonic flow characteristics. (In subsonic flow, as we already know from Chapter XVII, yaw reduces the lift coefficient).

The following formulas have been obtained for the triangular wing with supersonic leading edge

$$c_y = \frac{4\alpha}{\sqrt{M_\infty^2 - 1}} \quad \text{or} \quad c_y^{\alpha} = \frac{4}{\sqrt{M_\infty^2 - 1}}, \tag{20.12}$$

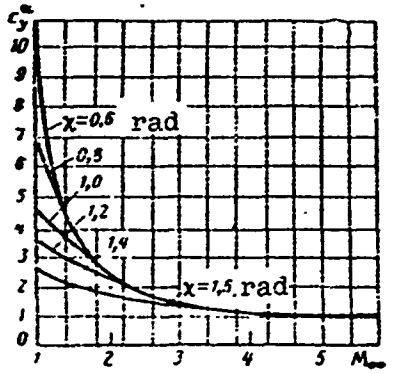

Figure 20.4. $c_y^\alpha = f(M_\infty, \chi)$ for triangular wing calculated by the method of conical sections.

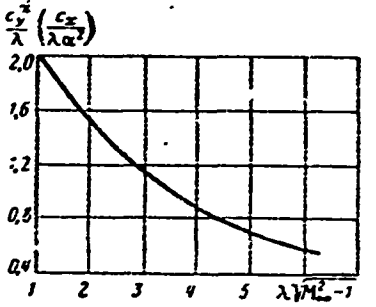

Figure 20.5. $\frac{c_y^\alpha}{\lambda}\left(\frac{c_x}{\lambda\alpha^2}\right)$ as a function of $\lambda\sqrt{M_\infty^2-1}$ for straight wing.

i.e., the same formulas as for the profile (the lift force is independent of the sweep angle). Incidentally, for the triangular wing the reduced sweep is a constant quantity, namely $\lambda \operatorname{tg} \chi_0 = 4$, which is easily seen from geometric constructions. Consequently this similarity criterion is satisfied automatically when molding triangular wings.

While for a triangular wing with supersonic leading edge the quantities c_y and c_y^α depend only on M_∞, sweep plays a very significant role for subsonic leading edges. Figure 20.4 shows the relation $c_y^\alpha = f(M_\infty, \chi)$, calculated for a triangular wing by the method of conical sections [2]. The extreme right-hand curve, which is the envelope, corresponds to the supersonic leading edge.

For a wing of rectangular planform theoretical constructions [4] lead for $\lambda\sqrt{M_\infty^2-1} > 2$ to the result

$$\frac{c_y^\alpha}{\lambda} = \frac{1}{\lambda\sqrt{M_\infty^2-1}}\left(1-\frac{1}{2\lambda\sqrt{M_\infty^2-1}}\right). \qquad (20.13)$$

Footnote (2) appears on page 214

The quantity $\lambda\sqrt{M_\infty^2-1}$ (one of the supersonic similarity criteria) is the determining factor for the straight wing. The curve plotted from (20.13) is shown in Figure 20.5.

All three similarity criteria

$$\frac{c_y^a}{\lambda}=f\left(\lambda\sqrt{M_\infty^2-1};\ \lambda\operatorname{tg}\chi;\ \eta\right). \qquad (20.14)$$

must be taken into consideration for other wing planforms in determining the lift. Usually graphs constructed on the basis of experimental data are used for practical purposes; one such graph is shown in Figure 19.4, where the sweep is taken along the maximal thickness line.

§20.3. Wave-Induced Drag

The drag coefficient of a wing in supersonic flow is made up of two components, one of which c_{x0} is independent of the lift, while the other c_{xi} depends on the lift

$$c_x=c_{x0}+c_{xi}. \qquad (20.15)$$

The component c_{xi} has a different nature for subsonic and supersonic velocities, being basically vortical for the former and wave for the latter.

The drag coefficient c_{xi} depends very little on the profile shape and its origin can be explained as follows. When an infinitely thin wing interacts with a supersonic stream at the angle of attack α, different pressures develop on the upper and lower surfaces of the wing. The resultant R of the pressure forces for a thin wing with supersonic leading edge will be perpendicular to the wing chord plane (Figure 20.6), and this means that in the wind coordinate system it can be resolved into two mutually perpendicular components — lift and induced drag.

$$Y=R\cos\alpha\approx R;$$
$$X_i=R\sin\alpha\approx R\alpha\approx Y\alpha.$$

Converting to coefficients, we have

$$c_{xi}=c_y\alpha, \tag{20.16}$$

or, in accordance with (20.10'),

$$c_{xi}=\frac{4}{\sqrt{M_\infty^2-1}}\alpha^2. \tag{20.16'}$$

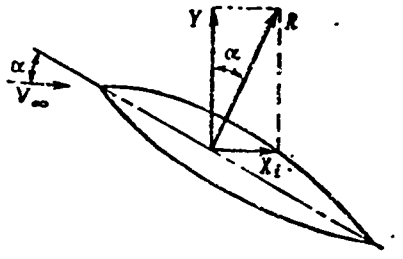

Figure 20.6. Illustration for determining induced drag of thin-profile wing in supersonic flow.

In contrast with the subsonic regimes, in supersonic flow the induced drag of an infinite-span wing is not equal to zero if the lift force is not equal to zero, since in this case the induced drag develops from sources other than tip effects.

Using (20.16) and knowing the wing lift coefficient, we can find the induced drag coefficient. Relation (20.16) is valid only for wings with supersonic leading edge; otherwise the aerodynamic force R will be inclined somewhat forward relative to the normal to the wing chord as a result of the influence of the suction force, which reduces the induced drag.

We obtain the induced drag coefficient of a yawed wing in accordance with (20.11) and (20.16) in the form

$$c_{xi}=\frac{\sqrt{M_\infty^2-1-\mathrm{tg}^2\beta}}{4}c_y^2, \tag{20.17}$$

or

$$c_{xi}=\frac{4}{\sqrt{M_\infty^2-1-\mathrm{tg}^2\beta}}\alpha^2. \tag{20.17'}$$

Comparing (20.16'), valid for the straight wing of infinite span, with (20.17') for the yawed wing, we obtain

$$\frac{c_{xi}}{(c_{xi})_{\beta=0}}=\frac{\sqrt{M_\infty^2-1}}{\sqrt{M_\infty^2-1-tg^2\beta}}>1.$$

Consequently, the induced drag of a yawed wing is greater than that of a straight wing for the same angles of attack, since the lift coefficient of the yawed wing is greater than that of the straight wing. It is more proper to compare the drag for the same values of c_y; then the induced drag coefficient of the yawed wing will be lower.

The induced drag of a triangular wing with supersonic leading edge will be the same as for a straight wing of infinite span. This follows from (20.12)

$$c_{xi}=\frac{4\alpha^2}{\sqrt{M_\infty^2-1}},$$

or

$$c_{xi}=\frac{\sqrt{M_\infty^2-1}}{4}c_y^2. \qquad (20.18)$$

The lift coefficient for the straight wing is defined by (20.13). Then we can write for the induced drag

$$\frac{c_{xi}}{\lambda\alpha^2}=\frac{4}{\lambda\sqrt{M_\infty^2-1}}\left(1-\frac{1}{2\lambda\sqrt{M_\infty^2-1}}\right). \qquad (20.19)$$

A plot of the relation $\frac{c_{xi}}{\lambda\alpha^2}=f\left(\lambda\sqrt{M_\infty^2-1}\right)$ is shown in Figure 20.5.

§20.4. Wing Wave Drag For $c_y = 0$

The wing drag for $c_y = 0$ is made up of the profile drag c_{xp}, which arises basically as a result of viscous friction in the boundary layer and the wave-profile drag $c_{xp\,w}$, which arises as a result of energy dissipation in the compression shocks. Frequently the wing drag for $c_y = 0$ is called the minimal drag.

The profile drag coefficient c_{xp} is found by the methods described in Chapter XVII. As for the wave-profile drag, relations for this drag have been obtained both experimentally and theoretically. However, the experimental studies are more reliable.

In the general case the results of the theoretical and experimental studies are conveniently represented in the form of the wave-profile drag coefficient $c_{xp\ w}$ as a function of the supersonic similarity criteria

$$\frac{c_{xpW}}{\lambda \bar{c}^2} = f\left(\lambda\sqrt{M_\infty^2-1},\ \lambda \operatorname{tg}\chi,\ \eta,\ \text{profile shape}\right). \qquad (20.20)$$

Comparison of the results of theoretical and experimental studies for a triangular wing ($\eta = \infty$) is shown in Figure 20.7. The theoretical curves 1 and 2 correspond to two values of the maximal thickness line location: $\bar{x}_c = 0.5$; $\bar{x}_c = 0.3$. The experimental curve 3 corresponds to $\bar{x}_c = 0.5$.

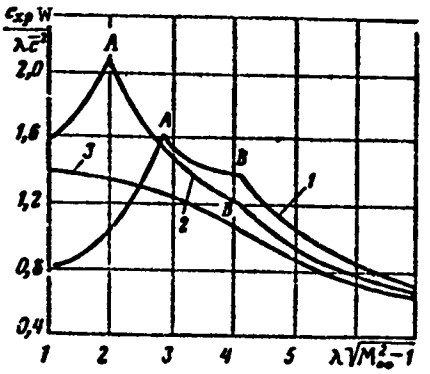

Figure 20.7. Influence of maximal profile thickness location on wave-profile drag: 1 - theoretical curve ($\bar{x}_c = 0.5$); 2 - theoretical curve ($\bar{x}_c = 0.3$); 3 - experimental curve ($\bar{x}_c = 0.5$).

The presence of the discontinuity points A and B on the theoretical curves is explained by the fact that for corresponding values of M_∞ the maximal thickness line ($\bar{x}_c$) and the leading edge become supersonic at these points, i.e., the relations

$$\sqrt{M_A^2-1} = \operatorname{tg}\chi_c;\quad \sqrt{M_B^2-1} = \operatorname{tg}\chi_b.$$

hold for these points.

For other wing shapes the curves are plotted in accordance with (20.20). Curves of this sort for trapezoidal wings with rhombic profile and taper ratio $\eta = 5$ are shown in Figure 20.8. The broken curves are theoretical results. The continuous curves are experimental results, which approach the theoretical curves in the region of large values of $\lambda\sqrt{M_\infty^2-1}$.

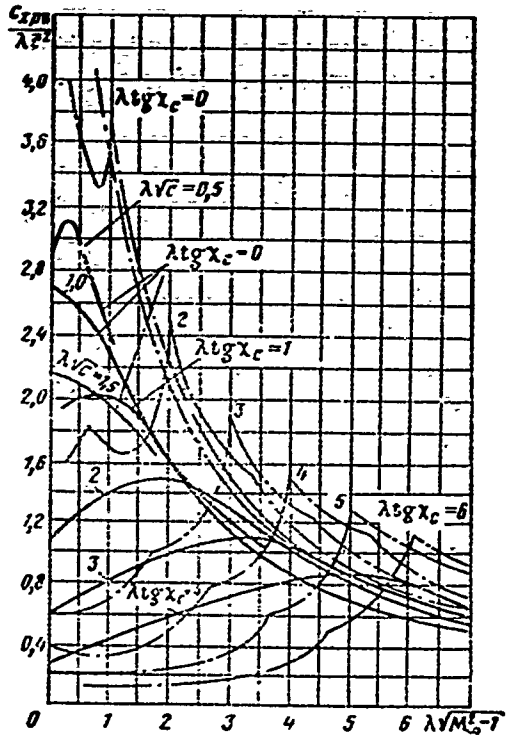

Figure 20.8. Graph for calculating wave drag of trapezoidal wing with rhombic profile ($\bar{x}_c$ = 0.5; η = 5).

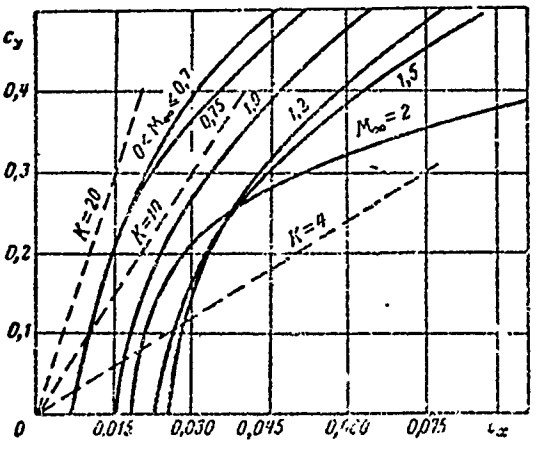

Figure 20.9. Wing polars for transonic and supersonic M_∞ range.

Experiment shows that the profile shape has a marked effect on the wave-profile drag only when the maximal thickness line becomes supersonic, i.e., when $\lambda tg\chi_c<\lambda\sqrt{M_\infty^2-1}$. If the maximal thickness line is subsonic, the profile shape has nearly no influence on the wave-profile drag.

Analysis of the minimal wing drag coefficient variation for different M_∞ shows that its increase, beginning at M_∞ equal to the critical value, continues approximately up to the moment when the maximal thickness line becomes supersonic. For the supersonic leading edge the coefficient $c_{xp\ w}$ decreases with increase of M_∞ (see Chapter XV), as a result of which the wing minimal drag coefficient also decreases.

Increase of the angle of attack leads to increase of the wing induced drag coefficient and therefore to increase of the drag coefficient

$$c_x=c_{x0}+c_{xi}=c_{xp}+c_{xpw}+c_{xi}. \quad (20.21)$$

Wing polars constructed in accordance with (20.21) are

shown in Figure 20.9. The polar shape is typical for the transonic and supersonic M_∞ range.

§20.5. Moment Characteristics of Wing in Supersonic Flow

The wings of supersonic airplanes usually have a symmetric profile. Therefore the pitching moment coefficient is zero for $\alpha = 0$ and is proportional to the angle of attack for comparatively small values of α. To find the moment coefficient of a triangular wing about the axis passing through its apex, we use the fact that the center-of-pressure coincides with the center of gravity of the triangle, i.e.,

$$x_A = \frac{2}{3} b_0.$$

Then the pitching moment is

$$M_z = -Yx_A = \frac{2}{3} c_y \frac{\rho V_\infty^2}{2} S b_0.$$

On the other hand, calculating the pitching moment with the aid of the moment coefficient, we have

$$M_z = c_m \frac{\rho V_\infty^2}{2} S b_0.$$

Comparing these expressions for M_z, we obtain

$$c_m = -\frac{2}{3} c_y, \tag{20.22}$$

or, replacing c_y by its value from (20.12), we have

$$c_m = -\frac{8}{3} \frac{\alpha}{\sqrt{M_\infty^2 - 1}}. \tag{20.23}$$

Using (20.22) and (20.23), we note that the coefficient c_m is referred to the central chord b_0 of the triangular wing.

For a wing of rectangular planform with reduced aspect ratio , the magnitude of the moment coefficient about the leading edge and the center-of-gravity location are defined on the basis of

linear theory by the equalities

$$c_m = -\frac{2\alpha}{\sqrt{M_\infty^2-1}}\left(1-\frac{2}{3\lambda\sqrt{M_\infty^2-1}}\right); \qquad (20.24)$$

$$\bar{x}_A = \frac{x_A}{b} = -\frac{c_m}{c_y} = \frac{1}{6}\left(3-\frac{1}{2\lambda\sqrt{M_\infty^2-1}-1}\right). \qquad (20.25)$$

It follows from (20.25) that as M_∞ is increased in the supersonic range the center-of-pressure shifts aft to the midpoint of the wing chord. Increase of the aspect ratio λ has the same effect (Figure 20.10).

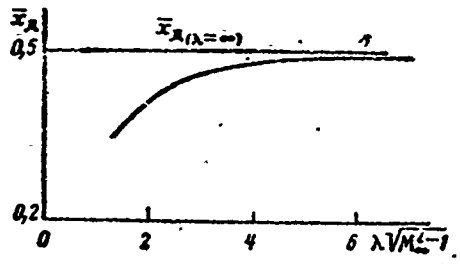

Figure 20.10. Influence of M_∞ and aspect ratio λ on center-of-pressure location.

For swept and triangular wings, the center-of-pressure location can be found from curves similar to those shown in Figure 19.9. In the general case the center-of-pressure coordinate is expressed by the relation

$$\bar{x}_A = f\left(\lambda\sqrt{M_\infty^2-1},\ \lambda\operatorname{tg}\chi,\ \eta\right).$$

It follows from the curves that for large M_∞ taper has very little effect on the center-of-pressure location.

REVIEW QUESTIONS

1. What is the difference between subsonic and supersonic wing leading edges?

2. Explain the cases in which a suction force can arise in supersonic flow past a wing.

3. How do the aerodynamic coefficients c_x, c_y, c_m vary with increase of M_∞?

4. What wing planform provides the least wave drag?

5. How does the induced drag change when passing from transonic to supersonic speeds?

PROBLEMS

1. Find the angle of attack of a plane thin wing of an airplane flying at H = 10,000 m and V = 473 m/sec if the wing area S = 15 m^2 and the airplane weight G = 49,000 N. Find the thrust expended in overcoming the wing wave drag.

Answer: $\alpha \approx 0{,}0225$ rad, $P = 1100$ N.

2. An airplane wing sweep angle is 1 rad. Find the airplane flight speed at which the wing leading edge will be subsonic, sonic, and supersonic.

Solution. According to (20.7), the wing leading edge coincides with the flow disturbance characteristics for

$$M_\infty = \sqrt{1 + \operatorname{tg}^2 \chi} \approx 1{,}85.$$

Consequently, for flight speeds corresponding to $M_\infty < 1.85$ the leading edge will be subsonic, and for $M_\infty > 1.85$ it will be supersonic.

FOOTNOTES

Footnote (1) appears on page 202

Aerodynamic Components of Aircraft at High Speeds, edited by A. F. Donovan and H. R. Lawrence, IL, 1959.

Footnote (2) appears on page 205

See, for example, Aerodynamic Components of Aircraft at High Speeds, edited by A. F. Donovan and H. R. Lawrence, IL, 1959.

CHAPTER XXI

AERODYNAMIC CHARACTERISTICS OF BODIES OF REVOLUTION

§21.1. Geometric and Aerodynamic Characteristics of Bodies of Revolution

The study of methods for determining the aerodynamic characteristics of bodies of revolution is of great importance, since the fuselages of modern airplanes, external fuel tanks, engine pods, missile and rocket bodies usually have the shape of bodies of revolution or nearly so.

The body of revolution of the usual form (Figure 21.1) can be divided into the forward (head or nose), middle (cylindrical), and aft (tail or rear) parts.

The nose section, as a rule, has the form of a conical, ogival (formed by a circular arc of some radius), or parabolic body. The nose part of the body of revolution is characterized by the apex angle τ and the fineness ratio λ_{nose}

$$\lambda_{нос} = \frac{l_{нос}}{D_{мид}} \qquad (21.1)$$

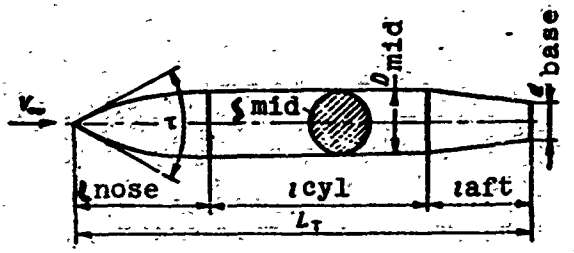

Figure 21.1. Basic geometric dimensions of body of revolution.

where l_{nose} is the distance from the nose of the body to its midsection;

D_{mid} is the midsection diameter.

By midsection we mean the section perpendicular to the longitudinal axis of the body having the maximal area. If the body has a cylindrical portion, as shown in Figure 21.1, then the midsection is the cylinder cross section area and l_{nose} is the distance from the nose of the body to its cylindrical part. In the general case the midsection diameter is the diameter of a circle which is equivalent in area to the midsection. The cylindrical part of the body of revolution is also characterized by the fineness ratio

$$\lambda_{цил}=\frac{l_{цил}}{D_{мид}} \tag{21.2}$$

The geometric parameters of the aft part of the body of revolution are the fineness ratio

$$\lambda_{корм}=\frac{l_{корм}}{D_{мид}} \tag{21.3}$$

and the taper ratio

$$\eta_{корм}=\frac{d_{кон}}{D_{мид}} \tag{21.4}$$

where d_{base} is the base diameter (see Figure 21.1).

When bodies of revolution have no base $\eta_{aft} = 0$.

The fineness ratio of a body of revolution is equal to the sum of the fineness ratios of its individual parts

$$\lambda=\lambda_{нос}+\lambda_{цил}+\lambda_{корм}=\frac{L_т}{D_{мид}} \tag{21.5}$$

where L_b is the total body length.

The quantity which is the reciprocal of the fineness ratio is called the relative thickness of the body of revolution.

$$\bar{d}=\frac{1}{\lambda} \qquad (21.6)$$

The ducted body of revolution is wetted by the flow both externally and internally. An example of a ducted body of revolution is an engine pod.

Just as in studying wing aerodynamic characteristics, the aerodynamic forces acting on the body of revolution are examined in wind or body coordinate systems. In the wind coordinate system the formulas for the lift and drag have the form

$$\begin{aligned} Y&=c_y q S_{\text{мид}};\\ X&=c_x q S_{\text{мид}}, \end{aligned} \qquad (21.7)$$

where c_y and c_x are the lift and drag coefficients of the body of revolution.

$q=\frac{\rho V^2}{2}$ is the velocity head;

S_{mid} is the midsection area.

Conversion to the body coordinate system is accomplished just as for the wing (see Chapter XII).

§21.2. Lift of Bodies of Revolution

The lift of a body of revolution immersed in a flow at some angle of attack can be determined if we know the pressure distribution on the surface of the body. We see from Figure 21.2 that the pressure distribution along the meridional section of a body of revolution (curve 2) in an incompressible fluid stream is qualitatively very similar to the pressure distribution over a wing profile (curve 1) of the same relative thickness and at the same angle of attack. However,

the underpressure on the body of revolution is considerably less than that on the wing, which is a result of the three-dimensional nature of the flow around the body of revolution.

The flow around a body of revolution can be compared with the flow around a wing of very low aspect ratio, for which we know that the underpressure on the upper surface, other conditions being the same, is always less than that on a wing of large aspect ratio because of the air crossflow around the wingtips from the high-pressure region into the low-pressure region. Thus, the lift and drag variation of a body of revolution is in the first approximation qualitatively very similar to wing lift and drag variation at both small and large values of M_∞.

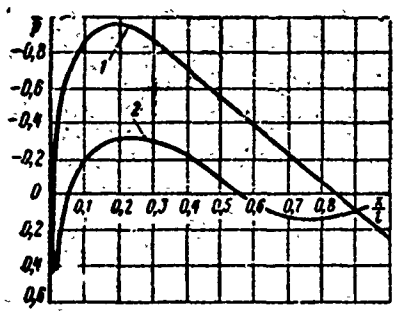

Figure 21.2. Pressure distribution along wing profile (1) and meridional section of body of revolution (2) for low M_∞.

Since the underpressure on a body of revolution is less than that on a wing, for the same M_∞ the compressibility effect is less in the case of flow around a body of revolution. M_{cr} for the body of revolution is considerably higher than for the wing.

There are certain differences in the flow around a body of revolution in comparison with the flow around a wing, and these differences unquestionably affect the magnitudes of the body of revolution lift and drag. When air flows past a body of revolution at the angle of attack α, flow separation takes place on the upper surface of the body (Figure 21.3). The normal force Y_n which arises in this case can be found from the formula

$$Y_n = c_{yn} S q \frac{V_n^2}{2}, \tag{21.8}$$

where $V_n = V_\infty \sin \alpha$, $c_{yn} = c_{x\ cyl}$, i.e., the coefficient c_{yn} is equal to the drag coefficient of a cylinder in transverse flow, S is the

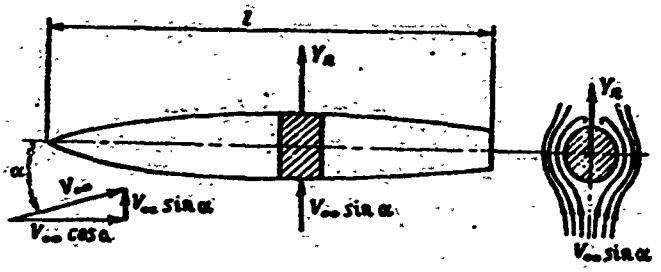

Figure 21.3. Normal force caused by crossflow on body of revolution.

area of the body of revolution in plan view.

Experimental data show that flow separation usually takes place on the cylindrical and aft portions of the body of revolution. Therefore, in the present case the area S is equal to the sum of the areas of the cylindrical and aft parts of the body in plan view.

A characteristic feature of the flow about a body of revolution with a base section ($n_{aft} \neq 0$), but without an engine jet leaving the base, is the appearance of base drag. This drag arises as a result of the pressure reduction behind the base, which takes place because of the presence of friction between the outer flow past the base and the flow behind the base. The friction creates an ejecting effect.

The degree of pressure reduction depends in considerable measure on the structure and thickness of the boundary layer leaving the aft portion of the body of revolution. The pressure reduction behind the base is greater for a turbulent boundary layer than for a laminar layer of the same thickness because of the greater ejecting capability of the turbulent boundary layer in comparison with the laminar layer.

This difference decreases as the role of the inertial forces increases in comparison with the viscous forces, i.e., with increase of the Reynolds number. The pressure reduction behind the base decreases with increase of the boundary layer thickness. If the pressure reduction behind the base is known, the drag force is found from the formula

$$X_{\text{дон}} = (p_{\infty} - p_{\text{дон}}) S_{\text{дон}}, \qquad (21.9)$$

where p_{base} is the pressure behind the base;
p_{∞} is the freestream pressure.

When a supersonic stream flows around a body of revolution, there is an additional effect on the base pressure of the expansion of the supersonic flow leaving the aft part of the body of revolution. As the flow expands, the pressure in the stream decreases. Consequently, the base pressure decreases when a supersonic stream flows around a body of revolution. Equalization of the supersonic stream at some distance from the base leads to the formation of a trailing shock wave.

The wind coordinate system is usually used in calculating the trajectories of flight vehicles. In this case the lift coefficient of the body of revolution is

$$c_y = c_{y1} \cos\alpha - c_{x1} \sin\alpha. \qquad (21.10)$$

Here the lift coefficient c_{y1} of the body of revolution in the body coordinate system is found from the formula

$$c_{y1} = c_{y\,\text{нос}} + c_{y\,\text{цил}} + c_{yn} + c_{y\,\text{корм}}, \qquad (21.11)$$

where $c_{y\ nose}$ is the lift coefficient of the nose part of the body of revolution;

$c_{y\ cyl}$ is the lift coefficient of the cylindrical part of the body of revolution;

c_{yn} is the lift coefficient of the cylindrical and aft parts owing to the presence of flow separation at large angles of attack [see (21.8)];

$c_{y\ aft}$ is the lift coefficient of the aft part of the body of revolution.

We know from experimental data that the cylindrical part adjacent to the nose part of the body of revolution creates a lift force. The magnitude of this force is small and is not identified separately, but is rather combined with the lift of the nose part. Then (21.11) takes the form

$$c_{y1}=c_{y\,нос}+c_{y\,п}+c_{y\,корм}. \tag{21.12}$$

The formula for determining the lift coefficient c_{y1}, referred to the midsection area, can be represented in the following form in accordance with linear theory

$$c_{y1}=c^{\alpha}_{y1}\cdot\alpha, \tag{21.13}$$

where

$$c^{\alpha}_{y1}=\frac{\partial c_{y1}}{\partial\alpha}.$$

Experiment shows that the coefficient c^{α}_{y1} depends not only on α, but also on the nature of the boundary layer, the Mach number M_{∞}, the fineness ratio λ of the body of revolution, and several other factors.

The derivative c^{α}_{y1} can be represented in the form of the sum

$$c^{\alpha}_{y1}=c^{\alpha}_{y\,нос}+c^{\alpha}_{yп}+c^{\alpha}_{y\,корм}, \tag{21.14}$$

where $c^{\alpha}_{y\ nose}$ is the derivative of the nose lift coefficient with respect to angle of attack (with account for the cylindrical part);

c^{α}_{yn} is the derivative of the normal force coefficient of the cylindrical and aft parts with respect to angle of attack;

$c^{\alpha}_{y\ aft}$ is the derivative of the lift coefficient of the aft part with respect to angle of attack.

The lift coefficient of the nose part of the body of revolution is found by solving the linearized equation for the disturbed flow

$c_{x\,cyl} = 0.35$ for the turbulent boundary layer;
$c_{x\,cyl} = 1.2$ for the laminar boundary layer.

The following formula has been obtained theoretically for the lift coefficient of the aft part

$$c_{y\,корм} = -2\sin\alpha\cos\alpha(1-\eta^2_{корм}). \qquad (21.19)$$

In reality the value of $c_{y\,aft}$ is considerably smaller than the theoretical value.

The derivative of the lift coefficient of the aft part of the body of revolution is found from the empirical formula

$$c^{\alpha}_{y\,корм} = -2\zeta(1-\eta^2_{корм}). \qquad (21.20)$$

The correction coefficient ζ depends on Re, M_∞, and the form of the aft part, and accounts for the lift coefficient reduction because of thickening and separation of the boattail ($\zeta = 0.15 - 0.20$).

According to (21.14) the sum of $c^{\alpha}_{y\,nose}$, c^{α}_{yn}, $c^{\alpha}_{y\,aft}$ equals c^{α}_{yl}. Substituting into (21.13) the value of c^{α}_{yl}, we obtain the expression for determining the lift coefficient of the body of revolution

$$c_{yl} = [c^{\alpha}_{y\,нос} + 0{,}624\lambda^2 c_{x\,цил}\alpha^2 - 2\zeta(1-\eta^2_{корм})]\,\alpha. \qquad (21.21)$$

Considering that for small angles of attack $\alpha^2 \to 0$, we have

$$c_{yl} = [c^{\alpha}_{y\,нос} - 2\zeta(1-\eta^2_{корм})]\,\alpha. \qquad (21.22)$$

If the body cross section is oval rather than circular, the calculation is made using the formula

$$c_{y\,ов} \approx c_y \frac{\pi B^2}{4S_{мид}}, \qquad (21.23)$$

where c_y is found from (21.22);

B is the midsection width;

S_{mid} is the midsection area, to which the lift coefficient $c_{y\,cv}$ is referred.

If an air intake is located in the nose part of the body, the coefficient of the additional lift which arises with engine operation at design power is

$$\Delta c_y = 2\varkappa \frac{S_{in}}{S_{mid}}, \tag{21.24}$$

where S_{in} is the air intake area.

§21.3. Drag of Bodies of Revolution

The drag coefficient of a body of revolution for $\alpha = 0$ can be represented as the sum of three terms

$$c_{x0} = c'_{xp} + c_{x\,base} + c_{xf},$$

where c'_{xp} is the drag coefficient which depends on the distribution of the normal pressure forces over the surface of the body;

$c_{x\,base}$ is the base drag coefficient;

c_{xf} is the friction drag coefficient.

At subsonic speeds the coefficient c'_{xp} is comparatively small and is neglected. However at transonic and supersonic speeds the coefficient c'_{xp} increases rapidly, since in this case it is determined primarily by the system of compression shocks at the surface of the body of revolution. In this case the quantity c'_{xp} is called the wave drag coefficient and the formula for the drag coefficient takes the form

$$c_{x0} = c_{xp} + c_{x\,base} + c_{xf}. \tag{21.25}$$

The friction drag coefficient of the body of revolution is defined similarly to the friction drag coefficient of a wing. In this case, just as for the other coefficients, the friction drag coefficient is

referred to the midsection area S_{mid}

$$c_{xf} = c_f \eta_c \eta_M \frac{S_{wet}}{S_{mid}}, \qquad (21.26)$$

where S_{wet} is the surface area of the body of revolution wetted by the flow (the so-called "wetted" area);

η_c is a coefficient accounting for the fineness ratio of the body of revolution;

η_M is a coefficient accounting for the compressibility of air;

c_f is the friction drag coefficient of a flat plate for $Re = \frac{VL_T}{\nu}$.

In view of the fact that Re is very large for a fuselage (because of the high flight speeds and the large fuselage length of modern transport and passenger airplanes), the boundary layer can be considered turbulent. Increase of the fuselage fineness ratio leads to decrease of its relative thickness, and in this case the fuselage drag differs less and less from the drag of a flat plate, i.e., with increase of the fineness ratio the coefficient η_c decreases, approaching unity. A curve of η_c versus body of revolution fineness ratio is shown in Figure 21.5.

The wave drag coefficient c_{xw} can be written as the sum of the wave drag coefficient $c_{xw\ nose}$ of the nose part of the body of revolution and the wave drag coefficient $c_{xw\ aft}$ of the aft part of the body (for $\alpha = 0$, $c_{xw\ cyl} = 0$). Curves of $c_{x\ B\ nose} = f(M_\infty)$ for bodies of revolution with parabolic nose are shown in Figure 21.6. The segments of the curves in the range $M_\infty < 1.6$ (dashed) are plotted on the basis of experimental data; the segments in the range $M_\infty > 1.6$ (continuous) are plotted on the basis of theoretical calculation. Curves of the relation $c_{x\ B\ aft} = f(M_\infty)$ for the aft part of the body of revolution with parabolic generators are shown in Figure 21.7. The curve segments for $M_\infty > 1.6$ are calculated values; those for $M_\infty < 1.6$ are approximate.

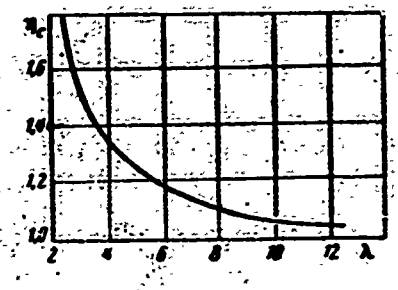

Figure 21.5. - Correction factor n_c versus fineness ratio of body of revolution.

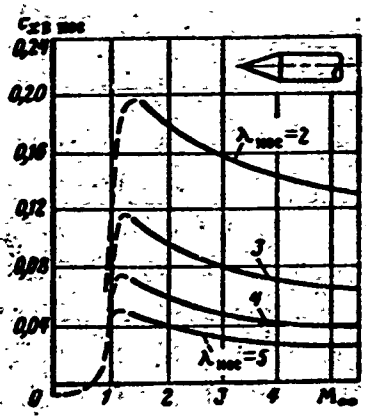

Figure 21.6. Wave drag coefficient of nose section of conical body of revolution versus M_∞.

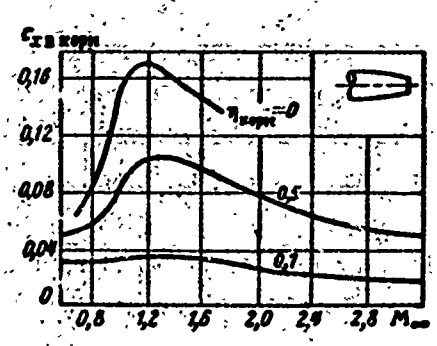

Figure 21.7. Wave drag coefficient of parabolic boattail versus M_∞ ($\lambda_{aft} = 2$).

Considering the expression (21.9) for base drag, the base drag coefficient can be found from the formula

$$c_{x\,\text{дон}} = \frac{X_{\text{дон}}}{S_{\text{мид}}\frac{\varrho V_\infty^2}{2}} = \frac{p_\infty - p_{\text{дон}}}{\frac{\varrho V_\infty^2}{2}} \frac{S_{\text{дон}}}{S_{\text{мид}}} = -\bar{p}_{\text{дон}} \left(\frac{d_{\text{дон}}}{D_{\text{мид}}}\right)^2. \tag{21.27}$$

In the particular case in which $d_{base} = D_{mid}$, the base drag coefficient equals the pressure coefficient.

Sometimes the ratio p_{base}/p_∞ is used in place of $\bar{p}_{base}$ in (21.27). The connection between these quantities is given by the relation

$$\bar{p}_{\text{дон}} = \frac{p_{\text{дон}} - p_\infty}{\frac{\varrho V_\infty^2}{2}} = \frac{p_{\text{дон}} - p_\infty}{k\frac{p_\infty M_\infty^2}{2}} = \left(\frac{p_{\text{дон}}}{p_\infty} - 1\right)\frac{2}{kM_\infty^2}. \tag{21.28}$$

With account for (21.28) the formula for $c_{x\,base}$ can be written as

$$c_{x\,\text{дон}} = -\left(\frac{p_{\text{дон}}}{p_\infty} - 1\right)\frac{2}{kM_\infty^2}\left(\frac{d_{\text{дон}}}{D_{\text{мид}}}\right)^2. \tag{21.29}$$

The results of experimental data analysis have made it possible to obtain the following approximate relation for the base drag

coefficient for subsonic and transonic speeds

$$c_{x\,дон} = \frac{0.029}{\sqrt{c_{xf}}}\left(\frac{d_{дон}}{D_{мид}}\right)^3. \qquad (21.30)$$

For supersonic speeds the base drag coefficient is found from the formulas

$$c_{x\,дон} = \frac{0.085k(2-k)}{M_\infty^2}\bar{S}_{дон}; \qquad (21.31)$$

$$c_{x\,дон} = \frac{0.085}{M_\infty^2}\bar{S}_{дон}, \qquad (21.32)$$

where

$$k = \frac{M_\infty}{\lambda_э}; \quad \lambda_э = \sqrt{\frac{\lambda_{корм}}{\bar{S}_{дон}}}; \quad \bar{S}_{дон} = \frac{S_{дон}}{S_{мид}}.$$

Formula (21.31) corresponds to values k < 1; formula (21.32) corresponds to k > 1.

REVIEW QUESTIONS

1. How does the lift force arise on a body of revolution (on its nose, cylindrical, and aft parts)?

2. Write expressions for the lift, lift coefficient, and derivative c_y^α of a body of revolution.

3. How is base drag created? How is base drag determined?

4. On what factors do the pressure drag and friction drag of bodies of revolution depend and how do they vary with change of the flight speed?

PROBLEMS

1. The angle of attack of an airplane flying at H = 2000 m and V = 900 km/hr is 0.07 rad. Find the fuselage lift force if we know

that the wing incidence angle (angle between the wing chord and the fuselage longitudinal axis) is 0.017 rad and the fuselage has the following geometric characteristics: fuselage length L = 32 m, nose length l_{nose} = 8 m, length of cylindrical part l_{cyl} = 16 m, diameter of cylindrical part d_{cyl} = 4 m, base diameter d_{base} = 1 m, the generatrix of the nose and aft sections is a straight line.

Solution. Since the fuselage angle of attack

$$\alpha_\phi = \alpha_{кр} - \varphi_{кр} = 0{,}053 \text{ rad}$$

c_{yl} for the fuselage is found from (21.22). Let us find the quantities appearing in (21.22). We take $\zeta \approx 0.17$. Using (21.4), we have

$$\eta_{корм} = \frac{1}{4} = 0{,}25.$$

To determine $c_{y\,nose}^{\alpha}$ we find:

a) at $H = 2000$ м $a = 333{,}3$ м/сек;

b) $V = \frac{900}{3{,}6} = 250$ m/sec; $M_\infty = \frac{250}{333{,}3} = 0{,}752$;

c) $\lambda_{нос} = \frac{l_{нос}}{D_{мид}} = \frac{8}{4} = 2$;

d) $\sqrt{\frac{1 - M_\infty^2}{\lambda_{нос}}} = \sqrt{\frac{1 - 0{,}752^2}{2}} = 0{,}466$;

e) $\frac{\lambda_{мид}}{\lambda_{нос}} = \frac{4}{2} = 2$, since $\lambda_{мид} = \frac{l_{мид}}{D_{мид}} = 4$;

f) $c_{y\,нос}^{\alpha} = f\left(\sqrt{\frac{1 - M_\infty^2}{\lambda_{нос}}},\ \frac{\lambda_{мид}}{\lambda_{нос}}\right)$;

$$c_{y\,нос}^{\alpha} = 2{,}06; \quad \frac{c_{y\,нос}^{\alpha}}{57{,}3} = 0{,}36.$$

From (21.22) we have

$$c_{yl} = [2{,}06 - 2 \cdot 0{,}17 (1 - 0{,}0625)] \frac{3}{57{,}3} = 0{,}0923.$$

Then

$$Y_1 = c_{yl} S_{мид} \frac{\rho V_\infty^2}{2} = 0{,}122 \frac{\pi}{4} 4^2 \cdot \frac{1 \cdot 250^2}{2} = 36200 \text{ N}$$

CHAPTER XXII

TAIL AND CONTROL SURFACE AERODYNAMIC CHARACTERISTICS

§22.1 Tail Aerodynamic Characteristics

In order to provide motion stability and flight controllability, flight vehicles are equipped with special surfaces which have the same form as the wing and are termed the tail.

The tail, located at the aft or forward end of the fuselage, usually includes stationary parts, fin and stabilizer, and movable parts, elevator and rudder (Figure 22.1). The fin and rudder constitute the vertical tail, and the stabilizer and elevator constitute the horizontal tail.

In most cases the horizontal tail of supersonic airplanes is all-moving, i.e., without a stationary stabilizer.

The types of tails used are quite varied. Some of the most typical horizontal tail shapes are shown in Figure 22.2. Swept and triangular tails are used for high-speed airplanes. The aerodynamic

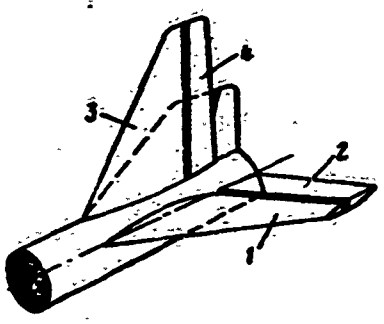

Figure 22.1. Horizontal and vertical tail;
1 - stabilizer; 2 - elevator; 3 - fin; 4 - rudder.

characteristics of the swept and triangular tails differ from the characteristics of the unswept tail, just as the aerodynamic characteristics of wings of similar form differ from one another.

Relatively small forces act on the tail; however, because of the long arm relative to the airplane center-of-gravity these forces create moments which are capable of balancing the overall moment from all the other parts of the airplane: wing, fuselage, nacelles, and so on.

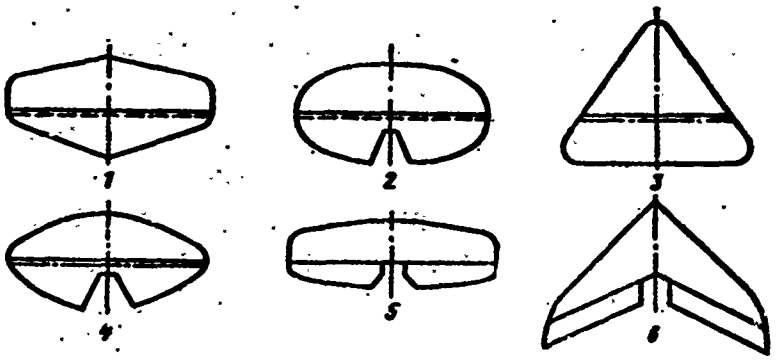

Figure 22.2. Characteristic horizontal tail planforms:
1, 4, 5 - trapezoidal; 2 - elliptical; 3 - triangular; 6 - swept.

The lifting properties of the tail are determined by the lift coefficient increment caused by change of the angle of attack or magnitude of the control surface deflection

$$\frac{dc_y}{d\alpha}; \quad \frac{dc_y}{d\delta_p}.$$

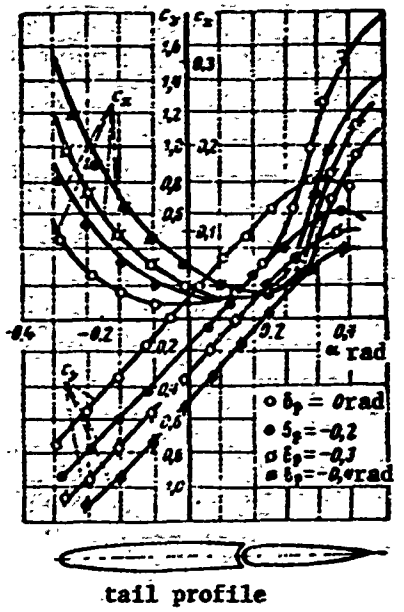

Figure 22.3. Aerodynamic characteristics of isolated tail.

The lift and drag coefficients of an isolated tail tested in TsAGI wind tunnels ($\bar{c}$ = 8%; λ = 3; η = 2; control surface area is 40% of the overall tail area) are shown in Figure 22.3.

We note that the control surface effectiveness decreases when it is deflected to large angles (for δ_c = 0.6-0.7 rad the lift does not increase because of flow separation from the surface of the tail). The control surfaces of swept and triangular tails retain their effectiveness better at high deflection angles in comparison with straight tails.

For linear variation of the lift coefficient, the dependence of c_y on the angle of attack α and on the control surface deflection angle δ_c is expressed by the formula

$$c_y = \frac{\partial c_y}{\partial \alpha}(\alpha + n\delta_p), \tag{22.1}$$

where the control surface effectiveness coefficient

$$n = \frac{\partial \alpha}{\partial \delta_p} = \frac{\frac{\partial c_y}{\partial \delta_p}}{\frac{\partial c_y}{\partial \alpha}}. \tag{22.2}$$

The quantities $\partial c_y/\partial\alpha$ and $\partial c_y/\partial\delta_c$ are smaller for swept tails than for straight tails. Experiments show that the quantity $\partial c_y/\partial\alpha$ for the unswept tail depends very little on the tail profile and can be expressed by the approximate formula

$$\frac{\partial c_y}{\partial \alpha} = \frac{0{,}085\lambda}{1{,}73 + \lambda}. \tag{22.3}$$

The control surface effectiveness coefficient n for subsonic speeds can be found from the formula

$$n \approx \sqrt{\frac{S_t}{S_{ca}}}, \qquad (22.4)$$

where S_t is the tail area;

S_c is the control surface area.

The presence on the control surface of cutouts and aerodynamic balance provisions (special provisions used to reduce the forces on the flight controls) has a considerable effect on the tail lift coefficient c_y, tending to reduce its value.

The coefficient decreases markedly at transonic speeds and in the presence of local compression shocks. In this case the lift coefficient changes very little with change of δ_c. To increase the control surface effectiveness at transonic speeds, the relative thickness of the tail profiles can be reduced (to increase M_{cr}) or the area of the all-movable tail is increased, which is more effective.

At supersonic speeds the control surface effectiveness coefficient is found from the formula

$$n \approx \frac{S_t}{S_{ca}}.$$

§22.2. Aileron Aerodynamic Characteristics

The ailerons are deflecting wing trailing edges, located at the wing tips and used to provide transverse controllability of the airplane. The aileron chord usually amounts to 0.15-0.30 of the wing chord. Ailerons of various types are shown in Figure 22.4.

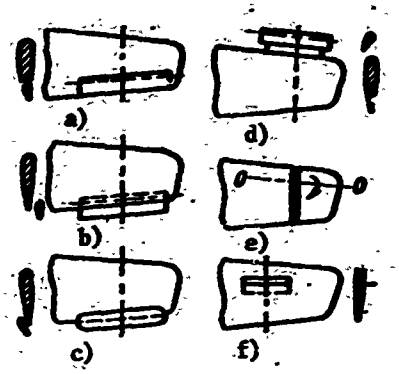

Figure 22.4. Ailerons:
a - conventional; b - below-wing; c - above-wing; d - fore-wing; e - tip; f - plate (spoiler).

The aerodynamic coefficients characterizing the ailerons are

$$m_x=\frac{M_x}{qSl};\quad m_y=\frac{M_y}{qSl}, \qquad (22.5)$$

where M_x, M_y are moments about the x and y axes;

m_x, m_y are the moment coefficients;

$q=\frac{\rho V^2}{2}$ is the dynamic pressure;

S is the wing area.

Curves of relations $m_x = f(\alpha)$ and $m_y = f(\alpha)$ for a trapezoidal wing with conventional ailerons are shown in Figure 22.5. We see from the curves that at normal flight angles of attack m_x is nearly constant and decreases sharply near the stall angle of attack; m_y increases gradually at the operational angles of attack.

§22.3. Control Surface Hinge Moments and Aerodynamic Balancing

The magnitude of the pilot forces applied to the flight controls (stick and pedals) depends on the control system and the magnitude of the aerodynamic forces, which create moments about the rudder, elevator and aileron hinges. The moment of the aerodynamic forces about the control surface axis of rotation is termed the hinge moment M_h (Figure 22.6).

The force on the flight control

$$P=-k_h M_h, \qquad (22.6)$$

where M_h is the magnitude of the control surface hinge moment;

k_h is the control system gear ratio.

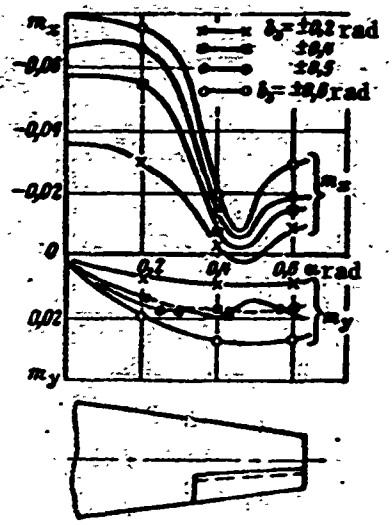

Figure 22.5. Curves of $m_x = f(\delta_a, \alpha)$ and $m_y = f(\delta_a, \alpha)$ for trapezoidal wing with conventional aileron.

For the elevator the coefficient

$$k_m = \frac{d\delta_{el}}{dx}, \qquad (22.7)$$

where $d\delta_{el}$ is the elevator angular displacement (in rad);

dx is the stick linear displacement.

For airplanes with conventional controls, the coefficient k_h has the following values; elevator 1.5-2.0, rudder 3.5-5.5, ailerons 0.5.

The hinge moment is found from the formula

$$M_m = m_m \frac{\rho V^2}{2} S_c b_c, \qquad (22.8)$$

where m_h is the dimensionless hinge moment coefficient;

S_c and b_c are, respectively, the area and MAC of the control surface (aileron).

Here the dynamic pressure $\rho V^2/2$ is measured at the control surface location.

To find the magnitude of the hinge moment, we must know the magnitude of the coefficient m_h. Curves of the relation $m_h = f(\delta_c, \alpha)$ for the elevator and rudder and of the relation $m_h = f(\delta_a, \alpha)$ for the ailerons based on experimental data are shown in Figure 22.7.

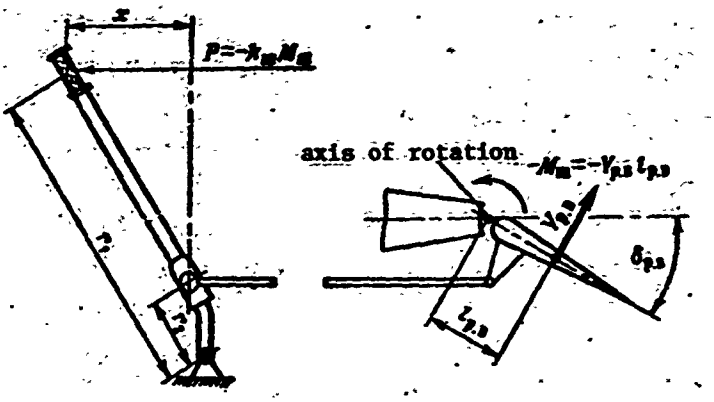

Figure 22.6. Hinge moment on control surface when stick is deflected.

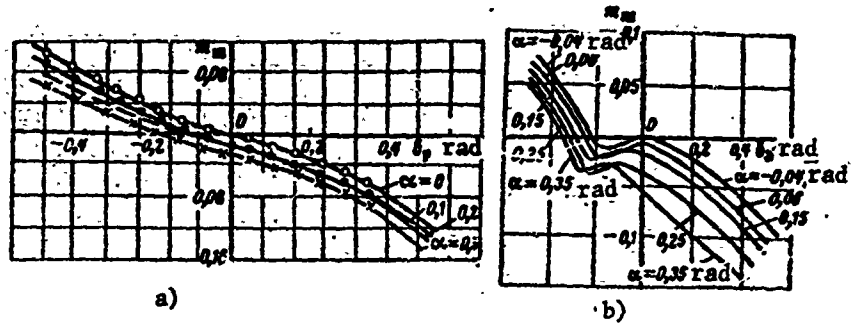

Figure 22.7. Curves of $m_h = f(\delta_c, \alpha)$ and $m_h = f(\delta_a, \alpha)$:
a - elevator and rudder; b - ailerons.

With increase of the flight speed and airplane size, there is an increase of the hinge moments and therefore of the forces required to control the airplane. One important technique for reducing the magnitude of the forces is the use of aerodynamic balancing. The principle involved in the action of the horn and overhanging aerodynamic balances is quite similar. They differ only in the location of the portion of the surface which extends ahead of the control surface axis of rotation.

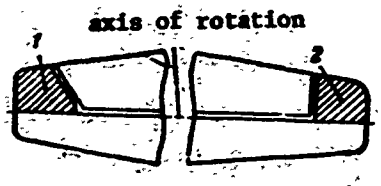

Figure 22.8. Horn balance:
1 - semihorn balance;
2 - horn balance.

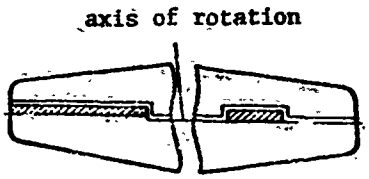

Figure 22.9. Overhanging balance.

Figure 22.8 shows the horn balance, while Figure 22.9 shows an overhanging balance, which is more widely used than the horn balance on present-day airplanes. When the control surface is deflected, an aerodynamic force arises on the balance and creates a moment about the axis of rotation which is opposite to the direction of the hinge moment and reduces its magnitude.

In addition to the horn and overhanging balances, in order to reduce the magnitude of the forces on the flight controls use is made of trim tabs , geared tabs, and flying tabs, which are small control surfaces mounted near the aft end of the main control surfaces.

The trim tab (Figure 22.10) is controlled manually or electrically from the cockpit; it deflects in the direction opposite the main control surface deflection. Deflection of the trim tab creates a hinge moment whose magnitude depends on the deflection angle. This moment reduces or may even balance the hinge moment of the main control surface.

The geared tab (Figure 22.11), in contrast with the trim tab, is not controlled from the cockpit. Its deflection is provided by a rigid rod which links the tab with a fitting on the stabilizer, fin, or wing. When the main control surface is deflected, the geared tab is automatically deflected in the direction opposite that of the main control surface, reducing the control hinge moment.

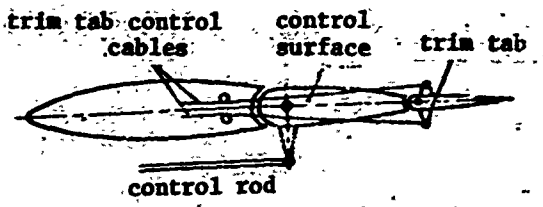

Figure 22.10. Trim tab.

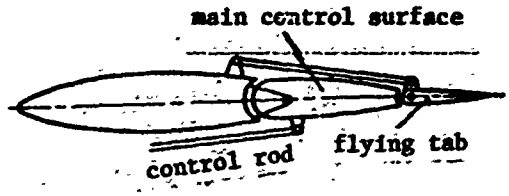

Figure 22.11. Geared tab.

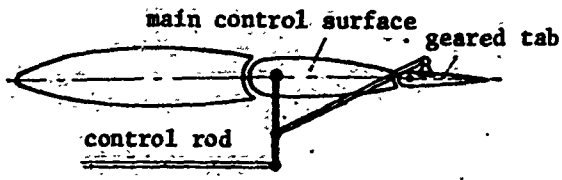

Figure 22.12. Flying tab.

The flying tab (Figure 22.12) is also used at the present time on many airplanes (particularly heavy airplanes). The flying tab is connected by rigid linkage with the flight control stick and is designed to deflect the main control surface. The control linkage is hinged to the main control surface and does not transmit any forces to the latter. When the stick is deflected, the flying tab deflects. The moment which it creates leads to deflection of the main control surface. The main control surface deflection angle is determined by the flying tab deflection angle, i.e., by the stick deflection angle.

Review Questions

1. Write the formula expressing lift coefficient dependence on angle of attack and control surface deflection angle.

2. Write the formula for determining the control surface effectiveness coefficient for subsonic and supersonic speeds.

3. Explain the purpose of the ailerons and write the formulas for the aerodynamic coefficients characterizing the ailerons.

4. How does the flight control stick force depend on the magnitude of the hinge moment? Write the formula expressing this dependence.

5. Explain the purpose and principle of operation of the horn and overhanging balances.

6. Explain the purpose and operation of the trim tab.

7. Sketch the operation of a flying tab.

CHAPTER XXIII

AIRPLANE AERODYNAMIC CHARACTERISTICS

§23.1. Aerodynamic Interference

In addition to the wing and fuselage, the airstream flowing around an airplane encounters the tail, engine pods, nacelles, antennas, and other parts of the airplane. The wing creates the major share of the airplane lift force. The other parts of the airplane, while having little effect on the magnitude of the lift force, increase the airplane drag to a considerable degree and therefore are termed non-lifting components.

It has been found that bodies positioned close to one another in an airstream exert a mutual influence on the nature of the flow around them. The result is change of the flow pattern and the shape of the streamlines, vortical wake, and disturbances caused by each element of the airplane separately, which leads to redistribution of the pressure forces. As a result of the mutual influence of the airplane parts or so-called interference, the sum of the drags of the wing, fuselage, and other parts taken individually (isolated) is not equal to the total drag of the airplane. This conclusion is valid for all aerodynamic forces and moments.

To determine the aerodynamic characteristics of an airplane, we must solve the complex problem of accounting for the mutual influence (interference) of the airplane parts. Interference may be positive, reducing the drag and increasing the aerodynamic efficiency, or negative, increasing the drag and reducing the aerodynamic efficiency of the airplane.

At subsonic speeds the airplane is subjected to additional resistance, owing primarily to fuselage influence on the circulation distribution along the wing span, which in turn affects wing induced drag. Moreover, the presence of nacelles and also various cutouts and openings in the wing disrupt the circulation distribution over the wing and create additional drag.

The fuselage and wing meet as two curvilinear surfaces and form a V-shaped diverging channel (diffuser), in which the flow expands far faster than when flowing around an isolated wing. The intense expansion of the air flow leads to accelerated increase of the boundary layer thickness and premature boundary layer separation in the regions where the wing joins the fuselage or nacelle (Figure 23.1), which causes deterioration of the airplane aerodynamic characteristics, i.e., drag increases and lift decreases. Figure 23.2 shows the influence of wing-fuselage relative positioning on the interference drag, which is given in percent of the overall drag of these components.

The greatest diffusor effect is obtained on airplanes with wings located at the bottom of the fuselage (low-wing configuration), particularly when the fuselage section is circular. The diffusor effect is less on midwing airplanes. "Fillets" are usually used to reduce the harmful effect of interference in the areas where the wing and fuselage join (Figure 23.3).

The interference between the wing and fuselage and between the wing and engine nacelles becomes more unfavorable at transonic flight speeds because of air compressibility. As the flight speed approaches

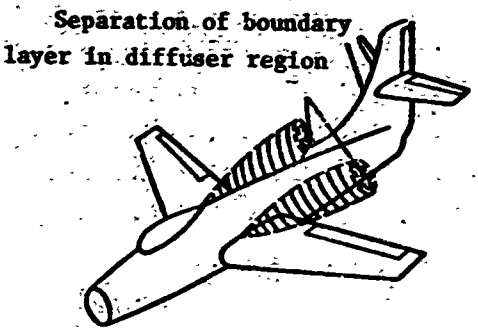

Figure 23.1. Increase of boundary layer thickness and premature flow separation at wing-fuselage junction.

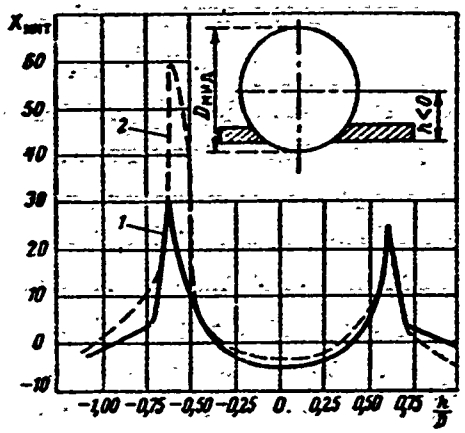

Figure 23.2. Effect of relative location of wing and fuselage on interference drag: 1 - for $c_y = 0$ ($c_{x\ air} = c_{x\ min}$); 2 - for $c_y = 0.115$.

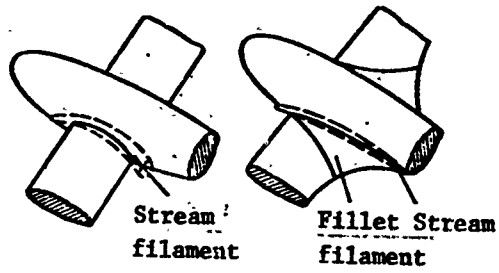

Figure 23.3. Diffuser effect at wing-fuselage junction.

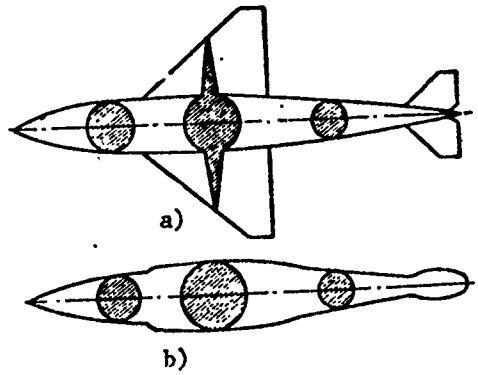

Figure 23.4. Illustration of "area rule."

the speed of sound, the local velocities on the fuselage, nacelles, and, most of all, on the wing increase near the thickest parts of these bodies (at the midsections and at locations where surfaces join). Therefore, the airplane critical Mach number M_{cr} is lower than the critical Mach numbers of the wing, fuselage, nacelles, and so on taken separately, i.e., shock stall begins earlier on the airplane. With increase of M_∞, flow separation starts earlier at the wing-fuselage juncture, and after appearance of compression shocks on the wing there may be earlier and stronger shock stalling, associated with flow separation.

In the transonic speed range the airplane drag approaches the drag of a body of revolution along whose length the cross section

areas are equal to the corresponding overall areas of the airplane cross sections. Therefore, to reduce negative interference for $M > M_{cr}$ an attempt is made to avoid coincidence of the maximal thicknesses and convexities of individual components of the airplane. In this situation a midwing configuration is more favorable, and it is recommended that the engine nacelles be located ahead of or behind the wing on special pylons. These measures to reduce airplane drag in the transonic region speed range are taken with account for the "area rule."

Figure 23.4 shows a plan view of an airplane and several cross sections, as well as a body of revolution with equivalent areas of the corresponding sections. In the case shown the body of revolution is not well streamlined. In accordance with the area rule, for reduction of the wave drag it is necessary that the overall cross section areas of the airplane vary along its length as for a body of revolution of minimal drag, or at least smoothly. Therefore it is obvious that the fuselage must have smaller cross section area in the wing region, i.e., it must have a "waist." Figure 23.5 shows the effect of the "area rule" for a flight vehicle.

To analyze the influence of wing-fuselage interference on the lift force, we shall examine the flow around a fuselage with a thin wing attached to the fuselage (Figure 23.6). The stream approaching the fuselage is deflected downward below the fuselage and upward along the sides. Consequently, the fuselage causes an upwash, increasing the wing angle of attack α and lift force. This leads to increase of the pressure below the wing and increase of the suction above the wing. This favorable effect of fuselage influence occurs at supersonic flight speeds. This effect is less marked at subsonic speeds.

There is also a reverse influence of the wing on the fuselage. If the wing creates a lift force, there is a low-pressure region above the wing and a high-pressure region below the wing, which extend correspondingly to the upper and lower surfaces of the fuselage. Therefore, even if the velocity vector is directed parallel to the fuselage

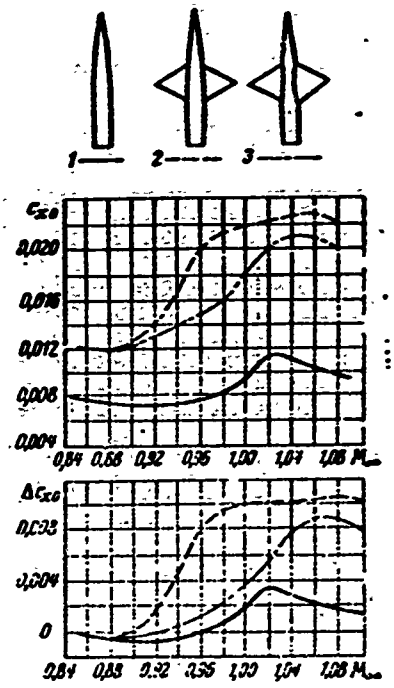

Figure 23.5. Effect of area rule application: 1 - fuselage alone; 2 - cylindrical fuselage plus wing; 3 - fuselage plus wing with use of "area rule".

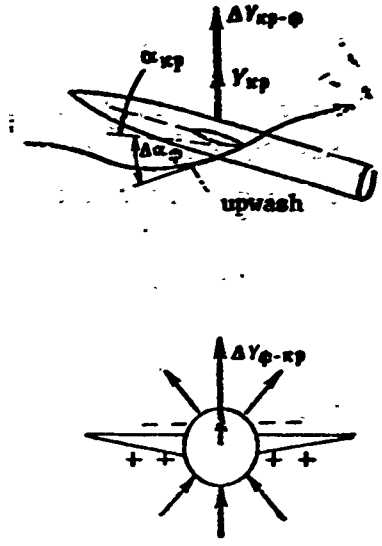

Figure 23.6. Illustrating effect of wing-fuselage mutual influence on pressure distribution.

axis, a lift force will develop on the fuselage because of the pressure difference.

§23.2. Airplane Lift Force

For subsonic airplanes the influence of interference on the magnitude of the lift force of the various parts of the airplane is such that the lift force created by the fuselage and other parts of the airplane is practically equal to the magnitude by which the wing lift is reduced because of the wing area occupied by the fuselage, engine nacelles, and so on. Therefore, in calculations we can assume that

$$Y_{сам}=Y_{кр} \tag{23.1}$$

and

$$c_{y\,cm}=c_{y\,sp}.$$

We note that when using (23.1) a fictitious part of the wing area (within the fuselage) is included in the lifting surface area. For supersonic speeds, this assumption may lead to significant errors.

Assuming that the wing, fuselage, and tail make the major contribution to the lift force at supersonic speeds, we first determine the lift of the wing-fuselage combination and then add the tail lift. Since wing-fuselage interference affects the mutual increase of their lift, we can write

$$Y_{sp\text{-}\phi}=Y_{sp}+Y_{\phi}+\Delta Y_{sp}+\Delta Y_{\phi}.$$

We ascribe the wing lift increase ΔY_w and the fuselage lift increase ΔY_f entirely to the wing, i.e., we write

$$Y_{sp\text{-}\phi}=Y_{\phi}+Y_{sp}k,$$

where k > 1 is the interference coefficient.

In order to account separately for the influence of angle of attack α and wing incidence angle ϕ (this may be done if the angles α and ϕ are small), we write the expression for the lift of the wing-fuselage combination in the form

$$Y_{sp\text{-}\phi}=Y_{\varphi}+Y_{\alpha}, \qquad (23.2)$$

where Y_{ϕ} is the lift of the wing-fuselage combination for $\alpha = 0$ and $\phi \neq 0$

Y_{α} is the lift of the wing-fuselage combination for the angle of attack $\alpha \neq 0$ and $\phi = 0$.

Hereafter we shall measure the angle of attack not from the wing chord plane, as we have done previously, but rather from the fuselage axis.

The lift owing to angle of attack

$$Y_\alpha = Y_{\phi=0} + Y_{w\phi=0} k_\alpha \qquad (23.3)$$

where k_α is the interference coefficient accounting for the lift increase of the wing and fuselage for $\phi = 0$, $\alpha \neq 0$, (Figure 23.7).

For $\alpha = 0$, $\Delta Y_w = 0$ and the lift on the wing owing to the incidence angle ϕ only is

$$Y_\varphi = Y_{w\varphi=0} k_\varphi \qquad (23.4)$$

where k_ϕ is the interference coefficient accounting for the mutual influence of the fuselage and wing for $\alpha = 0$ and $\phi \neq 0$ (see Figure 23.7)

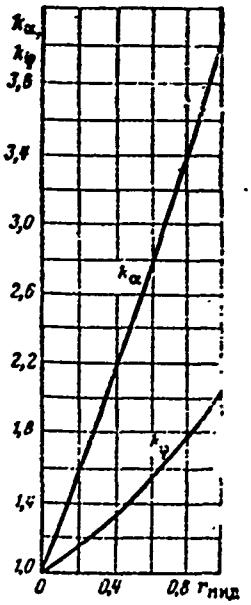

Figure 23.7. Curves for determining interference coefficients k_α and k_ϕ.

Now, substituting into (23.2) the values of Y_α and Y_ϕ from (23.3) and (23.4), we obtain

$$Y_{кр\text{-}\phi} = Y_{\phi=0} + Y_{w\phi=0} k_\alpha + Y_{w\varphi=0} k_\varphi. \qquad (23.5)$$

The wings of supersonic airplanes are usually assembled from symmetric profiles and the fuselage is nearly a body of revolution; therefore we can write the relations

$$c_{y\,\phi=0} = c_{y\phi}^{\alpha}\alpha; \quad c_{y\,w\phi=0} = c_{y}^{\alpha}\alpha; \quad c_{y\,w\varphi=0} = c_{y}^{\alpha}\varphi.$$

With account for these formulas for the coefficients, using (23.5) we obtain the expression for the lift coefficient of the wing-fuselage combination

$$c^{\alpha}_{y\,кр\text{-}ф} = c^{\alpha}_{y\,ф}\frac{S_{миф}}{S}\alpha + c^{\alpha}_{y\,кр}[k_{\alpha}\alpha + k_{\bar{\varphi}}\bar{\varphi}]\frac{S_{кр}}{S}. \qquad (23.6)$$

where S_{wi} is the area of the lifting part of the wing.

Considering the horizontal tail, we obtain

$$c_{y\,кр\text{-}ф} = c^{\alpha}_{y\,кр}[k_{\alpha}\alpha + k_{\bar{\varphi}}\bar{\varphi}]\frac{S_{кр}}{S} + c^{\alpha}_{y\,ф}\frac{S_{миф}}{S}\alpha + c_{y\,г.о}\frac{S_{г.о}}{S}. \qquad (23.7)$$

The coefficient $c_{y\ ht}$ is found just as the coefficients of the other components were found, except that here the angle of attack α is reduced by the magnitude of the downwash angle.

§23.3. Airplane Drag

The total airplane drag is found as the sum of the drags of its parts, with the influence of wing-fuselage interference taken into account in determining the wing drag

$$c_{x\,кр} = c_{x\,изол.кр}\left(1 - k_{инт}\frac{S_{кр.ф}}{S}\right). \qquad (23.8)$$

where $S_{w.f}$ is the wing area occupied by the fuselage;
k_{int} is the interference coefficient.

The larger the portion of the wing occupied by the fuselage, the less wing surface is exposed to the stream, and therefore the total airplane drag is reduced. As for the negative effects associated with the mutual influence of the wing and fuselage, they are taken into account in (23.8) by the interference coefficient. For a low-wing configuration k_{int} = 0.25-0.6, for the mid-wing k_{int} = 0.85, and for the high-wing arrangement it is equal to one.

If the wing, fuselage, engine nacelles, vertical tail, and horizontal tail are exposed to the flow, the airplane drag can be written in the form

$$X_{сам} = X_{кр} + X_{ф} + X_{г.о} + X_{в.о} + X_{г.к}$$

or

$$c_{x0}q_\infty S = c_{x0ф}q_\infty S + c_{x0ф}q_\infty S_{ммя.ф} + c_{x0г.о}q_{г.о}S_{г.о} + \\ + c_{x0в.о}q_{в.о}S_{в.о} + c_{x0г.кл}q_{г.к}S_{ммя.г.кл}$$

After transformation we obtain

$$c_{x0см} = c_{x0ф} + c_{x0ф}\frac{S_{ммя.ф}}{S} + c_{x0г.о}\frac{S_{г.о}}{S}\frac{q_{г.о}}{q_\infty} + \\ + c_{x0в.о}\frac{S_{в.о}}{S}\frac{q_{в.о}}{q_\infty} + c_{x0г.к}\frac{S_{ммя.г.к}}{S}\frac{q_{г.к}}{q_\infty},$$

or

$$c_{x0} = \frac{\sum_{k=1}^{n} c_{x0k}S_k q_k}{Sq_\infty}. \qquad (23.9)$$

Here the ratios q_{ht}/q_∞ and so on of the dynamic heads account for the flow deceleration ahead of the installed airplane components.

Usually the following notation is used to obtain a simpler form of the computational relations

$$k_{г.о} = \frac{q_{г.о}}{q_\infty}; \quad k_{в.о} = \frac{q_{в.о}}{q_\infty} \quad \text{etc.}$$

where k_{ht}, k_{vt}, and so on are dimensionless velocity coefficients.

The magnitude of the velocity coefficient equals one if the undisturbed stream approaches the given airplane component; the coefficient is less than one if the stream is decelerated ahead of the various airplane components and, finally, it is greater than one if the airplane component is located, for example, in the airplane propeller slipstream. The values of these coefficients are determined experimentally.

The calculation is usually summarized in a table — the drag summary. If all the flight regimes are performed with $M_\infty < M_{cr}$, the magnitude of c_{x0} is nearly independent of M_∞. For transonic and supersonic airplanes the quantity c_{x0} must be calculated for the entire range of M_∞.

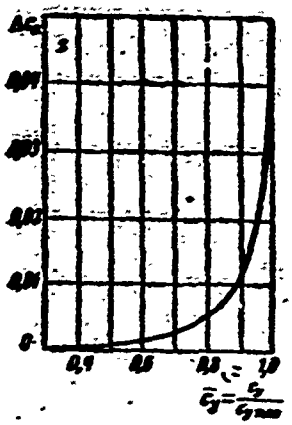

Figure 23.8. Curve for determining additional separation drag.

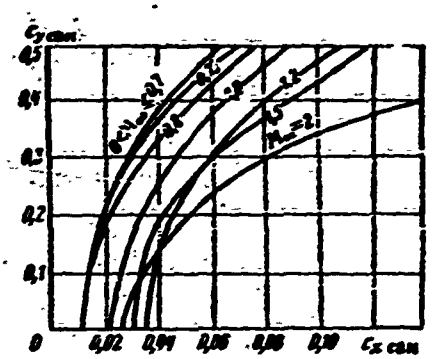

Figure 23.9. Supersonic airplane polars for different M_∞.

The airplane induced drag at subsonic speeds is found from the formula

$$c_{xi}=\frac{c_y^2}{\pi\lambda_{эф}}. \tag{23.10}$$

In this formula we have used, in place of the wing geometric aspect ratio, the so-called effective aspect ratio λ_{eff}, which accounts for interference between the airplane components. The value of λ_{eff} is found from the empirical relation

$$\lambda_{эф}=\frac{\lambda}{1+\frac{S_0}{S}}, \tag{23.11}$$

where S_0 is the wing area occupied by the fuselage, engine nacelles, landing gear, and so on.

At supersonic speeds, when the suction forces are small, it is more convenient to find the induced drag coefficient from the formula

$$c_{xi}=\frac{c_y^2}{c_y^\alpha}. \tag{23.12}$$

The quantity c_y^α can be calculated by differentiating (23.7)

$$c_y^\alpha=\frac{\partial c_y}{\partial\alpha}=c_{y\,кр}^\alpha k_a\frac{S_к}{S}+c_{y\,ф}^\alpha\frac{S_{мид.ф}}{S}+c_{y\,г.о}^\alpha\frac{S_{г.о}}{S}. \tag{23.13}$$

The total airplane drag coefficient is found from the relation

$$c_x = c_{x0} + c_{xi} + \Delta c_x. \qquad (23.14)$$

The quantity Δc_x accounts for the appearance and development of the phenomena induced by interference as the wing lift force increases (Figure 23.8). A typical high-speed airplane polar is shown in Figure 23.9.

REVIEW QUESTIONS

1. What is the essence of aerodynamic interference and its effect on drag?

2. Write the formula for the magnitude of the upwash angle induced on the wing by the fuselage and analyze this expression.

3. Compare airplane lift with wing lift and give an analysis.

PROBLEMS

1. Find the wave drag coefficient of a subsonic airplane if

$\lambda_{э\phi}=8{,}4$	$k_{г.о}=0{,}8;$
$c_{x0м.кр}=0{,}008;$	$k_{в.о}=0{,}92;$
$c_{x\phi}=0{,}076;$	$k_{инт}=0{,}5;$
$c_{x0г.о}=0{,}0096;$	$S=140\ м^2;$
$c_{x0в.о}=0{,}0092;$	$S_{мид.\phi}=9{,}6\ м^2;$
$c_{x0г.в}=0{,}041;$	$S_{г.о}=27{,}8\ м^2;$
$c_{y\,max}=1{,}4;$	$S_{в.о}=17\ м^2;$
$c_y=0{,}8;$	$S_{г.в}=1{,}1\ м^2.$

The wing area occupied by the fuselage amounts to 20% of the entire wing area.

Solution. According to (23.14)

$$c_x = c_{x0} + c_{xi} + \Delta c_x.$$

It follows from (23.8) that

$$c_{x0\,\text{тр}}=c_{x0\,\text{тр.пр}}\left(1-k_{\text{отн}}\frac{S_{\text{пр}\Phi}}{S}\right)=0{,}003(1-0{,}5\cdot 0{,}2)=0{,}0072.$$

Then from (23.9)

$$c_{x0}=0{,}0072+\frac{0{,}076\cdot 9{,}6+0{,}0096\cdot 27{,}8\cdot 0{,}8+0{,}0092\cdot 17\cdot 0{,}92+0{,}041\cdot 1{,}1}{140}=$$

$$=0{,}0072+\frac{0{,}73+0{,}213+0{,}144+0{,}0451}{140}=0{,}0072+0{,}0081=0{,}0153.$$

According to (23.10)

$$c_{xi}=\frac{c_y^2}{\pi\lambda_{\text{эф}}}=\frac{0{,}8^2}{\pi\cdot 8{,}4}=\frac{0{,}64}{\pi\cdot 8{,}4}=0{,}0243.$$

After determining

$$\bar{c}_y=\frac{c_y}{c_{y\,\max}}=\frac{0{,}8}{1{,}4}=0{,}571,$$

we use Figure 23.8 to find the value of Δc_x

$$\Delta c_x\approx 0{,}0015.$$

Thus the total drag coefficient

$$c_x=c_{x0}+c_{xi}+\Delta c_x=0{,}0153+0{,}0243+0{,}0015=0{,}041.$$

CHAPTER XXIV

AERODYNAMICS OF FLIGHT AT HYPERSONIC SPEEDS AND HIGH ALTITUDES

§24.1. Concepts of Hypersonic Flow and Rarefied Gas Aerodynamics (Hyper- and Super-aerodynamics)

Hypersonic flow theory deals with the solution of several important scientific and practical problems in aviation and rocketry and is in the process of intensive development at the present time. This theory includes, specifically, questions of the determination of the aerodynamic characteristics of guided missiles and other flight vehicles which are of interest in connection with orbital flight. Therefore, along with the study of the aerodynamics of flight at conventional supersonic speeds, exceeding by a few times the speed of sound, the need arises to study the aerodynamics of flows with high supersonic (hypersonic — from the Greek word "hyper", meaning "extremely" or "above") speeds — speeds several times the speed of sound (M_∞ = 5 - 10 or more). At these speeds features characteristic of hypersonic flow show up: first, the aerodynamic characteristics associated with high Mach numbers and, second, the physical or chemical characteristics associated with high flow energy.

In certain cases the aerodynamic effects lead to simplification of the solution of the aerodynamic problems associated with the motion of flight vehicles at high supersonic speeds; in other cases they lead to considerable complication. The linearization of the equations of motion, which is a very effective method in studying conventional supersonic flows, is not applicable for hypersonic flow.

The physical or chemical effects in hypersonic flows are associated with the formation of high-temperature regions. The latter arise when the gas stream passes through strong compression shocks, in which the kinetic energy of the directed motion is transformed into thermal energy.

It is well-known that air at normal temperature consists of approximately 78% nitrogen, 21% oxygen, 1% argon, and other gases. When heated, air can reach temperatures at which the vibrations of the nitrogen and oxygen molecular atoms become significant. At still higher temperature ($\sim$ 2500° K) and at moderate pressures, dissociation of the oxygen molecules begins. At temperatures above 4000° K part of the nitrogen molecules dissociates; at temperatures above 7000° K partial ionization of the nitrogen and oxygen atoms is observed; at still higher temperatures ionization of the nitrogen molecules may begin. At the same time the reverse reaction takes place — recombination, as a result of which oxygen and nitrogen molecules are formed. At these temperatures the specific heats are no longer constant and independent of the temperature, and we can no longer use the results obtained for constant ratio of the specific heats at constant pressure and volume. In this connection, the need arises to study the properties of air flows under such conditions.

So far we have considered air to be a continuous medium, since this assumption did not introduce noticeable error into the studies.

A quite different picture is observed when the gas is highly rarefied. In this case, the gas cannot be considered a continuous

medium, since its density is so small that the molecules rarely interact with one another. For example, the density of air at an altitude of 60 km is 10^3 times less than at sea level and at an altitude of 100 km it is 10^6 times less. Therefore, during flight in the upper layers of the atmosphere we must consider its discrete molecular structure. Here the gas can be considered an assemblage of molecules moving in all possible directions, constantly colliding with one another and with the surface of the immersed body.

Along with the aerodynamics of hypersonic velocities, which examines air as a continuum, a significant role is also played by rarefied gas aerodynamics — superaerodynamics.

Special flight vehicles have been designed to carry out studies at high altitudes and speeds, and their characteristics are presented in Table 24.1. We see from the table that considerable aerodynamic heating is unavoidable at hypersonic speeds. The flight speed is determined not only on the basis of creating the required lift force but also on the basis of permissible flight vehicle kinetic heating.

TABLE 24.1

Vehicle type	Altitude km	Mach number	Trajectory inclination, rad	Heat flux from aerodynamic heating, kW/m^2	Heating duration, sec
Ballistic rocket (range 300 km)	60	15	0.665	8600	-
ICBM (range 10,000 km)	60	23	0.4	32 000	15
Hypersonic glider	36	5-10	0	54	1800-7200
Vehicle descending from satellite orbit	75	20	0-0.175	1000-10,750	120-300
Experimental vehicle	75	10-25	0-0.175	1000-10,750	120-180

§24.2. Aerodynamic Characteristics of Bodies in Hypersonic Flow

In the case of hypersonic flow around bodies, we must take into account the most significant differences between this flow and supersonic flow around the bodies. For example, in the case of hypersonic flow around bodies the bow shock wave approaches very close to the body surface. On the other hand, with increase of M_∞ there is an increase of the boundary layer thickness (see Chapter XIII, §13.3). The interaction of the shock wave with the boundary layer takes place in the presence of high temperatures, which leads to considerable increase of the friction coefficient.

For the approximate calculation of the pressure distribution for hypersonic flow around bodies, use is made of the Newton hypothesis, based on the impact theory of hydrodynamic drag. According to this hypothesis, the approaching stream particles remain undisturbed until they collide with the surface of the body. Upon impact the particles lose the normal component of their momentum, after which they travel tangent to the surface without further change of velocity. The lost normal momentum component creates an impulse of the pressure force on the body, defined by the equality

$$p - p_\infty = \rho_\infty V_\infty^2 \sin^2\theta, \qquad (24.1)$$

where θ is the angle between the tangent to a surface element and the flow direction.

In fact, through unit area taken on a plane parallel to the inclined face (Figure 24.1) there passes per unit time the air mass $\rho_\infty V_\infty \sin\theta$, having the normal velocity component $V_\infty \sin\theta$; therefore in the direction normal to the inclined surface, the momentum decreases by the magnitude $\rho_\infty V_\infty^2 \sin^2\theta$.

It is easy to obtain from (24.1) the expression for the pressure coefficient

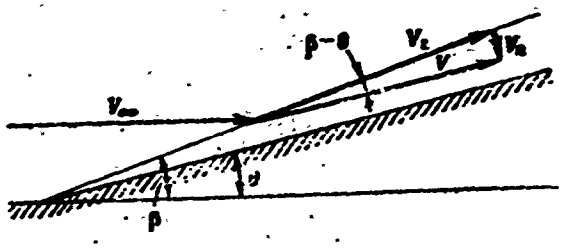

Figure 24.1. Illustration for determining flow parameters behind oblique compression shock at hypersonic speed.

$$\bar{p}=\frac{p-p_\infty}{q}=2\sin^2\theta, \tag{24.2}$$

and for thin bodies, when the angle θ is small

$$\bar{p}=2\theta^2. \tag{24.2'}$$

Formula (24.2) defines the pressure on the surface of the body sufficiently exactly if the body curvature and the disturbed flow regions are small in the flow direction. The use of this formula for hypersonic flow around bodies assumes that the bow wave coincides with the surface of the body. This is not exactly so, but for large freestream Mach numbers it yields an acceptable error.

We note that calculation using the Newton formula describes quite exactly the flow near a body in the limiting case when $k = \frac{c_p}{c_v} \to 1$ and $M_\infty \to \infty$. For this case the pressure coefficient at the stagnation point $\bar{p}_{max} = 2$. Experiment shows that for $k = 1.33$ and $M_\infty = 15$, $\bar{p}_{max} = 1.75$.

Considering that the shock surface does not coincide with the body, it is more correct to use the modified Newton formula

$$\bar{p}=\bar{p}_{max}\sin^2\theta, \tag{24.3}$$

where $\bar{p}_{max}$ is the pressure coefficient at the stagnation point. Formula (24.1) can be transformed to

$$p=p_\infty\left(1+\frac{\varrho_\infty}{p_\infty}V_\infty^2\sin^2\theta\right).$$

Then, considering that $a_\infty^2=k\frac{p_\infty}{\varrho_\infty}$ and $M_\infty^2=\frac{V_\infty^2}{a_\infty^2}$, we obtain the expression for finding the pressure on the surface of the body

$$p=p_\infty(1+kM_\infty^2\sin^2\theta). \tag{24.4}$$

According to Newtonion theory, the pressure on an elementary body area depends only on the attitude of this elementary area with respect to the approaching flow and is independent of the shape of the remainder of the body. Therefore, body drag is determined only by the shape of the forebody, since this is the only part which collides with the approaching flow particles. The pressure on the aft region, which does not collide with the approaching flow particles, must be equal to zero.

For hypersonic flow past a cone with apex angle 2 β_c at the angle of attack $\alpha < \beta_c$, using the pressure distribution pattern, we obtain the expressions for the normal and axial component coefficients in the form

$$\begin{aligned} c_N&=\cos^2\beta_\kappa\sin^2\alpha;\\ c_R&=2\sin^2\beta_\kappa+\sin^2\alpha(1-3\sin^2\beta_\kappa). \end{aligned} \tag{24.5}$$

As the angle of attack $\alpha \to 0$ we obtain from (24.5) the formula for the cone wave drag coefficient

$$c_R=c_{Rx\,0}=2\sin^2\beta_\kappa. \tag{24.6}$$

To obtain the overall cone drag coefficient, it is obviously necessary to combine the wave drag and friction drag coefficients.

§24.3. Oblique Compression Shock at Hypersonic Speeds

To find the gas parameters behind an oblique compression shock, we examine hypersonic flow past a concave corner with angle less than π.

As $M_1 \to \infty$ it follows from (10.34') that

$$\operatorname{tg}(\beta-\theta)\to\frac{k-1}{k+1}\operatorname{tg}\beta.$$

For large M_1 the difference $\beta - \theta$ is small (see Figure 24.1), particularly for small θ, and therefore, replacing $\operatorname{tg}(\beta-\theta)$ by $\beta-\theta$ in (10.34') we obtain

$$\beta-\theta=\frac{\frac{2}{k+1}+\frac{k-1}{k+1}M_1^2\sin^2\beta}{M_1^2\sin\beta\cos\beta}. \tag{24.7}$$

Considering that at hypersonic speeds the compression shock is very close to the body surface, for small flow turning angles θ we can assume that $\sin\beta\approx\beta$, and $\cos\beta\approx 1$. Then (24.7) takes the form

$$\beta-\theta=\frac{2+(k-1)M_1^2\beta^2}{(k+1)M_1^2\beta},$$

or, after transformations,

$$(M_1\beta)^2-\frac{k+1}{2}(M_1\beta)(M_1\theta)-1=0. \tag{24.8}$$

The quantities $M_1\theta$ and $M_1\beta$ are called the hypersonic similarity parameters and are denoted respectively by

$$K_a=M_1\theta;$$
$$K_c=M_1\beta.$$

With account for these notations (24.8) can be written as

$$K_c^2-\frac{k+1}{2}K_cK_\alpha-1=0. \tag{24.9}$$

Solving this quadratic equation and considering that the negative sign is meaningless, since K_c is a positive quantity, we obtain

$$K_c=\frac{k+1}{4}K_\alpha+\sqrt{1+\left(\frac{k+1}{4}K_\alpha\right)^2}, \tag{24.10}$$

or, after transformations

$$\frac{K_c}{K_\alpha}=\frac{\beta}{\theta}=\frac{k+1}{4}+\sqrt{\frac{1}{K_\alpha^2}+\left(\frac{k+1}{4}\right)^2}. \tag{24.11}$$

For some fixed (small) angle θ and M_1 which increases without bound $K_\alpha\to\infty$. Then we obtain from (24.11)

$$\frac{\beta}{\theta}=\frac{k+1}{2}. \tag{24.12}$$

Setting $\sin\beta\approx\beta$ for small values of θ and assuming that $M_1\beta=K_c$, we obtain from (10.30)

$$\frac{p}{p_1}=\frac{2k}{k+1}K_c^2-\frac{k-1}{k+1}. \tag{24.13}$$

We find the pressure coefficient

$$\bar{p}=\frac{p-p_1}{q_1}=\frac{p_1}{q_1}\left(\frac{p}{p_1}-1\right),$$

or, with account for (5.19)

$$\bar{p}=\frac{2}{kM_1^2}\left(\frac{p}{p_1}-1\right).$$

Substituting herein the value of p/p_1 from (24.13), we obtain

$$\bar{p}=\frac{4}{M_1^2}\cdot\frac{K_c^2-1}{k+1}. \tag{24.14}$$

Dividing both sides of (24.14) by θ^2 and considering that $M_1\theta=K_\alpha$, we have

$$\frac{\bar{p}}{\theta^2}=\frac{4}{k+1}\frac{K_c^2-1}{K_c^2}. \tag{24.15}$$

It follows from (24.9) that

$$K_c^2-1=\frac{k+1}{2}K_cK_\infty$$

then

$$\frac{\bar{p}}{\theta^2}=2\frac{K_c}{K_\infty}.$$

Substituting into this expression the value of $\frac{K_c}{K_\infty}$ from (24.11), we obtain

$$\frac{\bar{p}}{\theta^2}=\frac{k+1}{2}\left\{1+\sqrt{1+\left[\frac{4}{(k+1)K_\infty}\right]^2}\right\}. \tag{24.16}$$

From this equation we have as $M_1\to\infty(K_\infty\to\infty)$

$$\bar{p}=(k+1)\theta^2. \tag{24.17}$$

Hence for:

$k=1$ $\quad\bar{p}=2\theta^2$;

$k=1{,}2$ $\quad\bar{p}=2{,}2\theta^2$;

$k=1{,}4$ $\quad\bar{p}=2{,}4\theta^2$.

Consequently, we can conclude that in hypersonic flow the pressure coefficient behind a compression shock for small turning angles θ is proportional to the square of θ. We can find similarly the other gas parameters behind the oblique compression shock for hypersonic velocities.

§24.4. Profile Aerodynamic Characteristics at Hypersonic Speeds

In accordance with hypersonic flow theory there are two similarity parameters for affinely similar bodies

$$K_c = M_\infty \bar{c} \qquad \text{and} \qquad K_\alpha = M_\infty \alpha, \tag{24.18}$$

where $\bar{c}$ is the profile relative thickness;
α is the angle of attack.

The criterion K_α may be written in the form

$$K_\alpha = M_\infty \alpha = M_\infty \bar{c} \frac{\alpha}{\bar{c}},$$

or

$$K_\alpha = K_c \frac{\alpha}{\bar{c}}, \tag{24.19}$$

where $\alpha/\bar{c}$ is the so-called corrected angle of attack. Expression (24.19) establishes the connection between the similarity criteria.

For hypersonic flow past a flat plate at the angle of attack α the lift and drag coefficients are found from the formulas

$$\left.\begin{aligned} c_y &= f(K_\alpha)\alpha^2, \\ c_{x_w} &= f(K_\alpha)\alpha^3, \end{aligned}\right\} \tag{24.20}$$

where

$$f(K_\alpha) = 2\frac{K_c}{K_\alpha} + \frac{2}{kK_\alpha^2}\left[1 - \left(1 - \frac{k-1}{2}K_\alpha\right)^{\frac{2k}{k-1}}\right].$$

With increase of the parameter $M_\infty\alpha$ the coefficients c_y and $c_{x\,w}$ increase, and in the limiting case when $M_\infty\alpha \to \infty$ we obtain

$$\left.\begin{aligned} c_y &= (k+1)\alpha^2, \\ c_{x_w} &= (k+1)\alpha^3. \end{aligned}\right\} \tag{24.21}$$

We see from these formulas that as $M_\infty\alpha \to \infty$ the coefficient c_y is proportional to α^2 and the coefficient $c_{x\,w}$ is proportional to α^3.

Using the hypersonic similarity criteria, we can write for an arbitrary profile

$$\left.\begin{aligned} c_y &= F_1\left(K_{\bar{c}};\ \frac{\alpha}{\bar{c}}\right)\bar{c}^2, \\ c_{x\omega} &= F_2\left(K_{\bar{c}};\ \frac{\alpha}{\bar{c}}\right)\bar{c}^3, \\ c_m &= F_3\left(K_{\bar{c}};\ \frac{\alpha}{\bar{c}}\right)\bar{c}^3. \end{aligned}\right\} \qquad (24.22)$$

The form of the functions F_1, F_2, F_3 depends on the profile shape. The polars for triangular and rhombic profiles, calculated using hypersonic gas flow theory (the polars are plotted in the similarity parameters $c_y/\bar{c}^2$ and $c_x/\bar{c}^3$), are shown in Figure 24.2. If we denote the limiting values of these coefficients as $M_\infty \to \infty$ by $c_{y\infty}$, $c_{x\ \omega\infty}$, $c_{m\infty}$, we can write

$$\left.\begin{aligned} c_y &= c_{y\infty} + \Delta c_y, \\ c_{x\omega} &= c_{x\omega\infty} + \Delta c_{x\omega}, \\ c_m &= c_{m\infty} + \Delta c_m, \end{aligned}\right\} \qquad (24.23)$$

where Δc_y, $\Delta_{x\omega}$ and Δc_m are corrections which depend on M_∞.

If we assume that each term of the right side of (24.23) has a factor which depends on the angle of attack, then these expressions by analogy with (24.22) can be written as

$$\left.\begin{aligned} c_y &= \bar{c}_{y\infty}(k+1)\bar{c}^2 + \Delta\bar{c}_y \frac{\bar{c}^2}{\bar{c}M_\infty}, \\ c_{x\omega} &= \bar{c}_{x\ w\infty}(k+1)\bar{c}^3 + \Delta\bar{c}_{x\omega}\frac{\bar{c}^3}{\bar{c}M_\infty}, \\ c_m &= \bar{c}_{m\infty}(k+1)\bar{c}^2 + \Delta\bar{c}_m \frac{\bar{c}^2}{\bar{c}M_\infty}. \end{aligned}\right\} \qquad (24.24)$$

The quantities $\bar{c}_{y\infty}$, $\Delta\bar{c}_p$, $\bar{c}_{x\ \omega\infty}$, $\Delta c_{x\ \omega}$, $\bar{c}_{m\infty}$ and $\Delta\bar{c}_m$ are found from curves. Curves showing the variation of $\bar{c}_{x\ w\infty}$ and $\Delta\bar{c}_{x\ w}$ with $\alpha/\bar{c}$ for various profile shapes are shown in Figures 24.3 and 24.4. Using the curves and Formulas (24.24), we can find the aerodynamic coefficients c_y, $c_{x\ w}$, c_m for given $\bar{c}$, α, M_∞. We see from analysis of these figures that c_y and $c_{x\ w}$ increase rapidly with increase of $\alpha/\bar{c}$ for all the profiles.

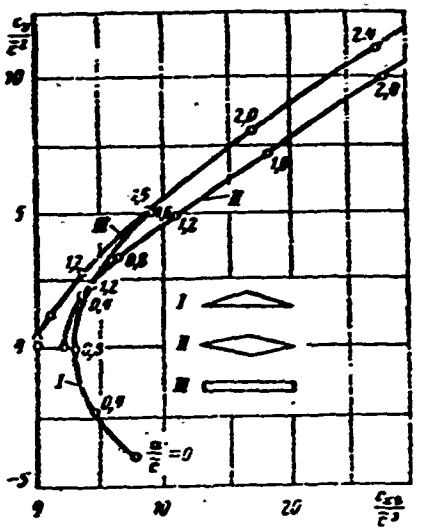

Figure 24.2. Polars of triangular and rhombic profiles and flat plate calculated using hypersonic gas flow theory.

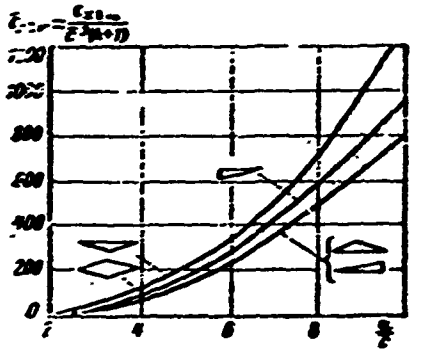

Figure 24.3. Coefficient $\bar{c}_{x\,w\infty}$ versus corrected angle of attack $\alpha/\bar{c}$ for different profiles.

In conclusion we note that the aerodynamic coefficients of the profile and wing are practically identical in hypersonic flow.

§24.5. Rarefied Gas Aerodynamics

We noted previously that under rarefied gas conditions we must take account of its molecular structure, which may be expressed by the molecular free path from one collision to another.

Since the individual molecule chaotic motion velocities may vary over wide ranges, the free path of different molecules is not the same. Therefore, we introduce the concept of the mean free path, which is the basic parameter for rarefied gas flow.

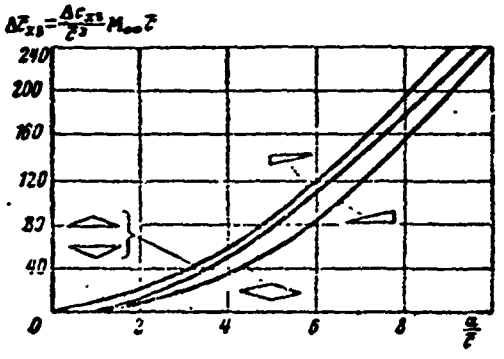

Figure 24.4. Coefficient $\Delta\bar{c}_{x\,w}$ versus corrected angle of attack for different profiles.

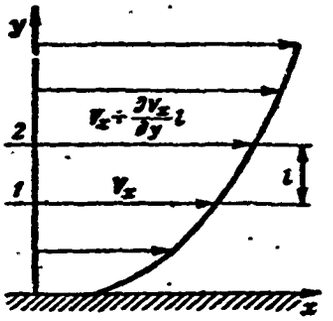

Figure 24.5. Illustration used to derive formula for finding molecular mean free path.

Let us examine the interaction of two air layers in a boundary layer which are separated by a distance equal to the mean free path length l (Figure 24.5).

If the average velocity component along the x axis of the air molecules of layer 1 is denoted by V_x, the average velocity component of the molecules of layer 2 will be $V_x+\frac{\partial V_x}{\partial y}l$.

As a result of chaotic motion the molecules will displace from layer 1 into layer 2 and vice versa. If we assume that the displacement takes place from layer 1 into layer 2, then the mass m of molecules flowing through unit area of layer 1 during unit time will be proportional to the average chaotic motion velocity and the gas density. Denoting the coefficient of proportionality by k_1 and the average chaotic motion velocity of the molecules by V, we obtain for the mass m

$$m=k_1\varrho V.$$

The momentum change is

$$m\frac{\partial V_x}{\partial y}l \quad \text{or} \quad k_1\varrho V\frac{\partial V_x}{\partial y}l. \tag{a}$$

The impulse of the friction force during unit time will be determined using the Newton formula

$$\tau=\mu\frac{\partial V_x}{\partial y}. \tag{b}$$

Equating (a) and (b) and considering that $\nu=\frac{\mu}{\rho}$, we obtain the molecular mean free path:

$$l=\frac{\nu}{k_1V}.$$

According to the kinetic theory of gases, the coefficient of proportionality $k_1 = 0.499$.

The velocity V is found from the formula of kinetic theory of gases

$$V=a\sqrt{\frac{8}{\pi k}}. \tag{24.25}$$

where $k = c_p/c_v$;
a is the speed of sound.

With account for this formula the mean free path is

$$l=1{,}255\sqrt{k}\frac{\nu}{a}. \tag{24.26}$$

We note that the molecular mean free path changes very significantly with increase of the altitude: at sea level the mean free path is millionths of a centimeter. At an altitude of 120 km it is several meters, and at an altitude of 200 km it is hundreds of meters.

If the molecular mean free path is divided by the characteristic flow dimension (for example, the body length L), we obtain the so-called Knudsen number

$$\mathrm{Kn}=\frac{l}{L}.$$

Substituting herein l from (24.26) and considering that the Reynolds number $\mathrm{Re} = VL/\nu$, we obtain

$$\mathrm{Kn}=1{,}255\sqrt{k}\frac{\mathrm{M}}{\mathrm{Re}}. \tag{24.27}$$

To characterize the degree of rarefaction of the medium in the boundary layer, we use the ratio of the molecular mean free path to the boundary layer thickness δ:

$$\mathrm{Kn}_\delta=\frac{l}{\delta}.$$

With account for this, Expression (24.27) takes the form

$$Kn_\delta = 1{,}255\sqrt{k}\frac{M}{Re}\frac{L}{\delta}. \qquad (24.28)$$

The boundary layer thickness depends on the flow nature and Re; consequently Kn_δ will depend on M and Re. Since the following relation holds for large Re in the laminar boundary layer

$$\frac{\delta}{L}\sim\frac{1}{\sqrt{Re}},$$

the Knudsen number is

$$Kn_\delta\sim\frac{M}{\sqrt{Re}}. \qquad (24.29)$$

For very small values of Re (approximately < 100) we can write in place of (24.29)

$$Kn_\delta\sim\frac{M}{Re}. \qquad (24.30)$$

It follows from (24.27), (24.29), 24.30) that the degree of rarefaction of the medium is characterized by the ratio M/Re or $\frac{M}{\sqrt{Re}}$ which is called the rarefaction parameter.

Depending on Kn, the gas flow can be divided into three basic regions: continuum flow, slip flow, and free molecular flow.

1. For $\frac{l}{\delta}<0{,}01$ or $M/\sqrt{Re} < 0.01$ the molecular mean free path is less than 1% of the boundary layer thickness. In this case we can consider the flow to be continuous, i.e., we have the region of conventional gasdynamics (Figure 24.6).

2. For $0{,}01<\frac{l}{\delta}<1$ the molecular mean free path is small in comparison with the body dimension, but is comparable with the thickness δ. In this case we have slip flow. Here the flow velocity at the wall is not equal to zero.

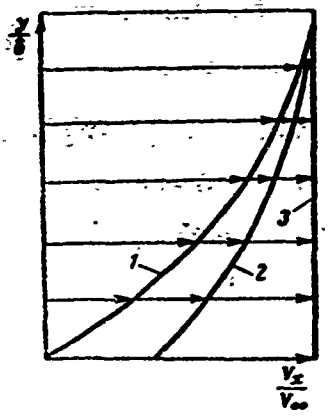

Figure 24.6 Velocity distributions along normal to surface:

1 - continuum flow;
2 - slip flow;
3 - free molecular flow.

3. For $\frac{l}{\delta} > 1$ the molecular mean free path is greater than or commensurate in magnitude with the boundary layer thickness δ. In this case we have the free molecular flow region. In this region the elementary particles do not interact with one another, and there is essentially no boundary layer. The interaction force between the flow and the body is the overall impulse of the air particle impacts on the surface of the body. The kinetic theory of gases examines this question in detail.

REVIEW QUESTIONS

1. What is the difference between hypersonic flow and conventional supersonic flows.

2. Define the pressure coefficient for hypersonic flows, specifically at the stagnation point.

3. Find the magnitude of the wave drag coefficient for hypersonic flow past a cone with angle $\beta_c = 0.175$ rad.

4. Determine the gas parameters behind an oblique compression shock.

5. Write and analyze the formulas for the aerodynamic coefficients.

6. List the salient features of rarefied gas aerodynamics. Characterize the mean free path as a gas flow parameter.

7. Give the definition of the Knudsen number and write its formula. Explain how the nature of the flow depends on the Knudsen number.

PROBLEMS

1. Find the wave drag of the rocket of Figure 24.7 at the altitude H using the Newtonian representation for gas particle interaction, and compare the drag for the same rocket nosecone fineness ratio if the nosecone shape is specified respectively by the equations

$$y_1=0{,}2x;\quad y_2=0{,}2\sqrt{x_{нос}x}.$$

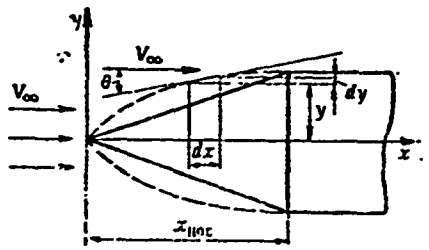

Figure 24.7. Illustration for Problem No. 1.

The freestream direction coincides with the rocket axis. The freestream velocity is such that $M_\infty \gg 1$. the mass density at the altitude H is ρ. The nosecone length is $x_{nose} = 5$ m.

Solution. We see from Figure 24.7 that the mass flux to the segment $2\pi ydy$ is

$$dm=2\pi\rho V_\infty ydy=2\pi\rho V_\infty yy'dx,$$

where

$$y'=\frac{dy}{dx}.$$

The drag on the segment $2\pi ydy$ resulting from gas particle momentum change is

$$dX=2\pi\rho V_\infty^2\sin^2\vartheta yy'dx.$$

Integrating this expression, we obtain the rocket drag

$$X=2\pi\rho V_\infty^2\int_0^{x_{noc}}\sin^2\theta yy'\,dx.$$

Since $\sin^2\theta=\frac{y'^2}{1+y'^2}$, then

$$X=2\pi\rho V_\infty^2\int_0^{x_{noc}}\frac{yy'^3}{1+y'^2}dx.$$

We find correspondingly

$$X_1=2\pi\rho V_\infty^2\int_0^{x_{noc}}\frac{16\cdot10^{-4}x\,dx}{1,04}=$$

$$=\frac{16\cdot10^{-4}}{1,04}\pi\rho V_\infty^2x_{noc}^2;$$

$$X_2=4\pi\rho V_\infty^2\cdot10^{-4}x_{noc}^2\int_0^{x_{noc}}\frac{dx}{x+10^{-2}x_{noc}}=$$

$$=4\cdot10^{-4}\pi\rho V_\infty^2x_{noc}^2\ln101.$$

Hence we have

$$\frac{X_1}{X_2}=\frac{16\cdot10^{-4}}{1,04\cdot4\cdot10^{-4}\ln101}=0,834.$$

2. Find how much the pressure ratio across the compression shock and the shock halfangle change for symmetric flow past a wedge of infinite length and halfangle $\theta = 0.175$ rad when the Mach number changes from $M_\infty = 10$ to $M_\infty = 20$.

Answer: $\Delta\beta=0,0392$ rad, $\Delta\bar{p}=1,05\theta^2$.

CHAPTER XXV

PROPELLERS

§25.1. Principles of Air Propeller Operation, Their Geometric and Kinematic Characteristics

The thrust required for flight on airplanes with an airscrew propulsor is created by accelerating a mass of air in the aft direction by means of the propeller. The greater the speed and mass of the air accelerated in the aft direction, i.e., the greater the momentum, the larger is the thrust force. On the propeller driven airplane the thrust is created by the propeller; it is the propulsor. The propeller transforms the engine power into the work which is performed in moving the airplane.

A propeller can be used for purposes other than creating thrust, i.e., as the airplane propulsor: with the aid of a propeller the mechanical energy of the engine can be transformed into kinetic energy of moving air (operation in the fan regime); it is also possible to transform the energy of the moving air into energy of the rotating propeller (operation in the windmill regime).

In aerodynamics courses the propeller is examined only as a creator of thrust, i.e., as a screw propeller which transforms engine work into thrust work. The power on the propeller shaft, defined by the product $M\Omega$ (M is torque; Ω is angular velocity), is transformed into the useful power PV_∞ (P is thrust, V_∞ is airplane flight velocity).

The propeller effectiveness is evaluated by the efficiency

$$\eta=\frac{PV_\infty}{M\Omega}.$$

Modern propellers have high efficiency, reaching 83-86% at subcritical flight speeds. For fixed engine power N, the thrust $P = \eta N/V$ decreases with increase of the flight speed to the degree that airplanes with airscrew propulsors become inferior in economy to airplanes with turbojet engines.

The basic working element of the air propeller is the blade. Propeller blade shapes can be quite varied — from rectangular to scimitar. The profiles from which the blade is made up vary from the blade root to its tip. The propeller blade is characterized by several geometric dimensions, which are termed the geometric characteristics.

The propeller diameter D (2R) is the diameter of the circle described by the blade tips as it rotates. Other conditions being the same, the magnitude of the propeller diameter has a marked influence on the efficiency and is determined by aerodynamic calculation. In selecting the propeller diameter, account is taken of geometric considerations since, for example, the propeller dimensions affect landing gear height. The diameter must be considered in the layout of multiengine airplanes in order to avoid deterioration of the operating conditions of neighboring propellers.

The solidity σ is the ratio of the area of the blade projections on the propeller plane of rotation to the area swept by the blades as the propeller rotates.

The blade width b is the blade section chord length. The chord varies along the blade length (Figure 25.1). For subsonic propellers the maximal width is usually located at about half the blade length.

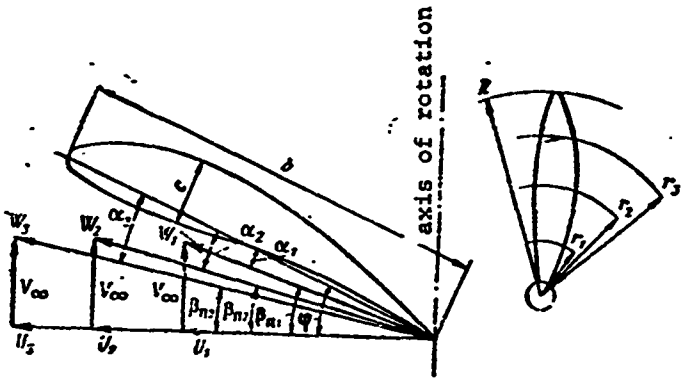

Figure 25.1. Geometric and kinematic characteristics of blade profile.

The blade thickness c is the maximal thickness of the blade profile at a given section. The blade thickness decreases from the blade root toward its tip, reaching 4 - 7% of the chord at the tip. The blade thickness at the middle sections amounts to 10 - 16% and at the roots sections is 25 - 30%.

The blade section incidence angle ϕ is the angle formed by the section chord with the propeller plane of rotation (Figure 25.2).

As the propeller rotates, air flows around each blade section and, just as in the case of the airplane wing, a lift force is developed. The blade operating conditions are more complex than those of the wing, since both translational and rotational motions are performed simultaneously. The section angle of attack α is the angle between the profile chord and the resultant velocity W (see Figure 25.1), in the first approximation equal to the vector sum of the axial velocity (flight velocity V_∞) and the linear rotational velocity U. The linear rotational velocity increases with increase of the distance from the axis of rotation; therefore

the flow conditions around the blade section vary along the blade. The angle of attack increases with increase of the linear rotational velocity (see Figure 25.1). Therefore, for constant angular velocity the section angle of attack will be larger, the farther the section is located from the axis of rotation.

Since the blade section angle of attack depends on the distance from the axis of rotation, to obtain the same operating conditions of all sections the blade must be made with lengthwise twist, so that the blade section angles of attack will be approximately the same at any distance from the axis of rotation.

The blade twist is the variation of the section incidence angle along the blade length. Usually this variation is measured relative to the incidence angle of a reference section located at the distance 0.75 R from the axis of rotation. Therefore the blade twist is characterized by the difference $\phi - \phi_{0.75}$, where ϕ is the incidence angle of the section in question, located at the distance r from the axis of rotation.

Under operational conditions the reference section is frequently located at some distance other than 0.75 R, which however is quite definite for each propeller type. The reference section is denoted by a brightly painted line.

For constant linear velocity of rotation, the angle of attack will obviously depend on the axial velocity. With increase of the axial velocity the angle of attack decreases and may become negative (Figure 25.2). A negative angle of attack can also be obtained as a result of decrease of the blade incidence angle ϕ.

In order to ensure optimal operating conditions in all flight regimes, modern propellers are equipped with a system for rotating the blades. Such propellers are termed variable pitch propellers (VPP), in contrast with the fixed pitch propellers (FPP) which were used in the early stages of aviation development.

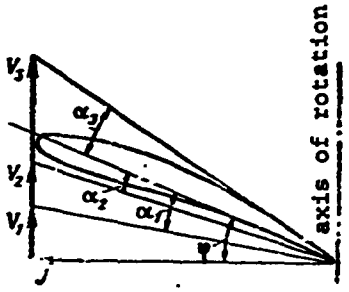

Figure 25.2. Effect of flight speed on blade section angle of attack.

The nonrotating propeller, just like any body in an airstream, has drag, which will be minimal if the blades are set so their chords are approximately parallel to the flight velocity. This blade position is termed <u>feathered</u>.

As a rule, in aerodynamic calculations the geometric characteristics are used in relative rather than absolute form, i.e., in calculations we use the quantities

$$\bar{b}=\frac{b}{D};\ \bar{c}=\frac{c}{b};\ \bar{r}=\frac{r}{R}=\frac{2r}{D}.$$

These quantities are often specified in percent. For each propeller blade the characteristics are represented graphically as a function of the relative radius (Figure 25.3).

The kinematic characteristics of the propeller make it possible to describe the nature of the air flow around the blade and its individual sections.

The <u>propeller pitch</u> H is the distance measured in the axial direction which the blade element travels in a single revolution if it advances in the surrounding medium considered as a solid body.

The <u>propeller advance</u> H_a is the distance which the propeller actually travels in the air in a single revolution. As a result of the compliance of the air, the propeller will travel in a single revolution a distance which is, as a rule, not equal to the propeller pitch. With the propeller operating under static conditions, the propeller advance is equal to zero.

The advance ratio λ is the ratio of the propeller advance to its diameter

$$\lambda=\frac{H_a}{D}.$$

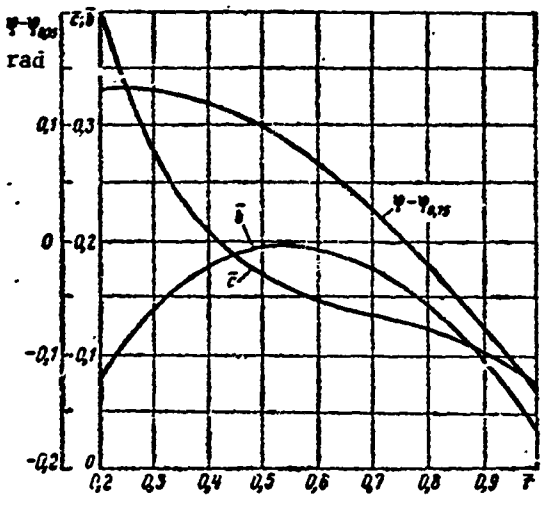

Figure 25.3. Variation of geometric characteristics along blade length.

Since in a single revolution the propeller travels the distance $H_a = V_\infty/n_s$, where n_s is the number of revolutions per second, then

$$\lambda=\frac{V_\infty}{Dn_c}. \qquad (25.1)$$

The absolute velocity W is equal to the geometric sum of the axial velocity V_∞ and the linear rotational velocity U. The linear rotational velocity for the blade section located at the distance r can be found from the formula

$$U=2\pi r n_c,$$

or, introducing the dimensionless radius, we have

$$U=\pi D n_c \bar{r}.$$

Then the absolute velocity for this section

$$W=\sqrt{V_\infty^2+U^2}=Dn_c\sqrt{\lambda_2+\pi^2\bar{r}^2}.$$

The inflow angle β_{in} is the angle between the absolute velocity and the blade rotation plane (see Figure 25.1). We see from the figure that

$$\operatorname{tg}\beta_a=\frac{V_\infty}{U}.$$

Using (25.1) and expressing the circumferential velocity in terms of the distance to the axis of rotation and n_s, we obtain

$$\operatorname{tg}\beta_{in}=\frac{\lambda}{\pi r}. \qquad (25.2)$$

For the section located at the distance 0.75 R

$$\beta_{in}=\operatorname{arctg}\frac{\lambda}{0.75\pi}.$$

The section angle of attack $\alpha = \phi = \beta_{in}$ is also a kinematic characteristic. We see from the formulas obtained above that the kinematic characteristics are functions of the advance ratio.

§25.2. Ideal Propeller Theory. Propeller Operation in Shroud

Ideal propeller theory is approximate, is based on the general theorems of mechanics, and is not related with blade geometry; therefore it cannot be used for design. However, this theory makes it possible to estimate power and thrust and also permits clarification of the effect of forward speed on propeller thrust and efficiency.

The air is assumed to be an inviscid medium, i.e., there are no friction losses. The airstream contracts along its entire length, but the contraction is most intense in the region just ahead of the propeller disk and immediately behind the disk. In practice we can consider that the contraction region is bounded by the distance $\pm$ D from the propeller plane of rotation.

We denote the velocity of the undisturbed flow ahead of the propeller by V_∞, the axial component in the propeller plane of rotation by $V_1 = V_\infty + v_1$, the axial component far behind the propeller by $V_2 = V_\infty + v_2$ (Figure 25.4). The induced velocities v_1 and v_2 are the deviations from the undisturbed flow velocity caused by propeller operation.

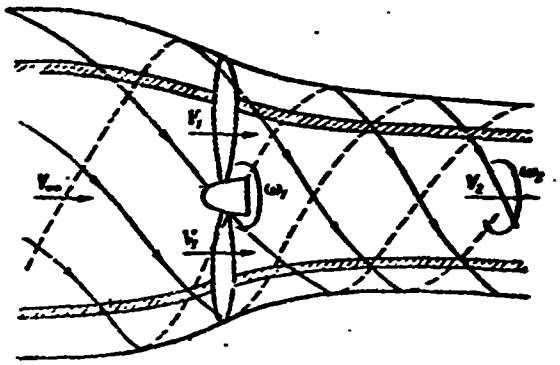

Figure 25.4. Illustrating ideal propeller analysis.

The magnitude of the thrust can be calculated by applying the momentum theorem in the projection on the propeller axis of rotation

$$P=m(V_2-V_\infty)=mv_2, \qquad (25.3)$$

where m is the air mass flow per second through the surface swept by the propeller.

The propeller entrains the air, forcing it to rotate. The rotational velocity of the air far ahead of the propeller is zero. We assume, and this is not far from true, that within the airstream passing through the propeller the air rotates in each individual cross section following the solid body law, with the angular velocities being different at different cross sections. We denote the angular velocity in the plane of the propeller by ω_1 and that far behind the propeller by ω_2.

The power, i.e., the energy imparted per second by the propeller to the surrounding medium, can be calculated as the change of the kinetic energy of the air flowing inside the body of revolution

$$N=\frac{mV_2^2}{2}+J_2\frac{\omega_2^2}{2}-\frac{mV_\infty^2}{2}=\frac{m}{2}(V_2^2-V_\infty^2)+J_2\frac{\omega_2^2}{2}, \qquad (25.4)$$

where J_2 is the moment of inertia of the airstream which has passed through the propeller at a large distance from the plane of rotation.

It follows from (25.4) that the power imparted by the propeller to the flow is expended on increasing the kinetic energy in the translational motion parallel to the propeller axis and on creating the kinetic energy of rotation, i.e., we can represent the propeller power as the sum of the "axial" power N_{ax} and the "circumferential" power N_{cir}.

The magnitude of the "axial" power is

$$N_{oc}^{\cdot}=\frac{m}{2}(V_2^2-V_\infty^2)=m(V_2-V_\infty)\frac{V_2+V_\infty}{2},$$

or, with account for (25.3),

$$N_{oc}^{\cdot}=P\frac{V_2+V_\infty}{2}. \tag{25.5}$$

On the other hand, the magnitude of the "axial" power equals the product of the propeller thrust P by the axial velocity V_1 of the air in the propeller plane of rotation

$$N_{oc}^{\cdot}=PV_1. \tag{25.5'}$$

Comparing (25.5) and (25.5'), we obtain

$$V_1=\frac{V_2+V_\infty}{2}.$$

But

$$V_2=V_\infty+v_2;\quad V_1=V_\infty+v_1.$$

Then

$$v_1=\frac{v_2}{2}. \tag{25.6}$$

The "circumferential" power, expended by the propeller on rotation of the air, is equal to the product of the angular velocity ω_1 in the propeller plane of rotation by the torque M_t, which rotates the propeller, i.e.,

$$N_{окр}^{\cdot}=M_k\omega_1.$$

Thus, the total power imparted to the air by the propeller can be expressed in the form of the sum

$$N=PV_1+M_k\omega_1.$$

The power delivered by the engine to the propeller is defined by the product of the torque M_t and the propeller angular velocity of rotation Ω

$$N=M_t\Omega. \tag{25.7}$$

This means that

$$M_t\Omega=PV_1+M_t\omega_1.$$

Hence

$$PV_1=M_t(\Omega-\omega_1). \tag{25.8}$$

We find the propeller efficiency by dividing the useful power PV_∞ by the power expended, defined by (25.7)

$$\eta_p=\frac{PV_\infty}{M_t\Omega}=\frac{PV_\infty}{PV_1}\frac{PV_1}{M_t\Omega}=\frac{V_\infty}{V_1}\frac{PV_1}{M_t\Omega}.$$

Substituting herein the value of PV_1 from (25.8) we obtain

$$\eta_p=\frac{V_\infty}{V_1}\frac{\Omega-\omega_1}{\Omega}. \tag{25.9}$$

We call the first factor in the right side of (25.9) the <u>axial</u> efficiency and the second factor the <u>circumferential</u> efficiency. On the basis of the meaning of the quantities appearing (25.9), we can draw some conclusions.

First, the smaller the air rotational velocity ω_1 in comparison with the propeller rotational velocity Ω, the higher is the propeller circumferential efficiency. We could prevent entrainment of the air into rotational motion by the installation of so-called guide vanes. However this is not advantageous for the airplane, since along with increase of the circumferential efficiency there would be reduction of the propeller thrust owing to the friction forces on the surface

of the guide vanes. A real increase of the circumferential efficiency is achieved in installations with coaxial propellers, rotating in opposite directions. In this case the rotation of the air behind the first propeller is utilized usefully by the second propeller.

Second, the propeller efficiency can be increased by reducing the velocity V_1 in the propeller plane of rotation. However, we must remember that reduction of the velocity V_1 always leads to reduction of propeller thrust. This follows from (25.3) and (25.6). Reduction of the axial efficiency is a sort of payment for the creation of thrust. The higher the velocity v_2, the larger is the thrust. However the propeller efficiency will be lower, since the propeller creates thrust by forcing air aft with a velocity exceeding the inflow velocity. The axial efficiency may be increased by increasing propeller diameter with simultaneous reduction of the induced velocity. However the propeller diameter can be increased only up to certain limits for structural reasons. Moreover, increase of the propeller diameter is limited by increase of the profile losses.

Thus, (25.9) can be rewritten in the form

$$\eta_в = \eta_{ос}' \eta_{окр}', \tag{25.9'}$$

where

$$\eta_{ос}' = \frac{V_\infty}{V_1} = \frac{1}{1 + \frac{v_2}{2V_\infty}}; \quad \eta_{окр}' = \frac{\Omega - \omega_1}{\Omega}. \tag{25.10}$$

Since $\eta_{ax} < 1$ and $\eta_{cir} < 1$,

$$\eta_{ос}' < 1 \text{ и } \eta_{окр}' < 1, \text{ то}$$

$$\eta_в = \eta_{ос}' \eta_{окр}' < 1.$$

To clarify the influence of flight velocity V_∞ on propeller axial efficiency η_{ax} and thrust P, we shall analyze the effect of flight velocity on the magnitude of the induced velocity v_2.

Substituting the thrust from (25.3) into (25.5'), we obtain

$$N_{oc}^{\cdot}=mv_2V_1.$$

Now we express the mass flow per second in terms of the density ρ, area F swept by the propeller, and velocity V_1 in the propeller plane

$$m=\varrho FV_1,$$

then

$$N_{oc}^{\cdot}=\varrho Fv_2V_1^2.$$

Hence

$$V_1=\sqrt{\frac{N_{oc}}{\varrho Fv_2}}.$$

Considering that according to (25.6)

$$V_1=V_\infty+v_1=V_\infty+\frac{v_2}{2},$$

we obtain

$$V_\infty+\frac{v_2}{2}=\sqrt{\frac{N_{oc}}{\varrho Fv_2}}. \tag{25.11}$$

We see from this relation that for constant power N_{ax} the induced velocity v_2 varies monotonically with change of V_∞ and approaches zero with unrestricted increase of the flight velocity V_∞. Now, using (25.10), we can draw a conclusion on the influence of flight velocity on the axial efficiency.

For $V_\infty = 0$ we obtain $\eta_{ax} = 0$, since in this case no useful work is performed; as $V_\infty \to \infty$ $v_2 \to 0$ and $\eta_{ax} \to 1$, i.e., the propeller axial efficiency increases with increase of the flight velocity, approaching unity.

$$V_1=\frac{V_\infty+V_2}{2}=\frac{V_\infty}{2}(1+\sqrt{1+B}). \tag{25.14}$$

Substituting this value of V_1 into (25.10), we obtain the expression for propeller axial efficiency in terms of disk loading factor

$$\eta_{ax}=\frac{V_\infty}{V_1}=\frac{2}{1+\sqrt{1+B}}. \tag{25.15}$$

Formulas (25.13) - (25.15) show that the velocities V_1 and V_2 increase and the axial efficiency decreases with increase of the disk loading factor, i.e., the nonproductive energy expenditures increase with increase of the thrust.

Curves showing the dependence of the axial efficiency (η_{ax}), ideal propeller efficiency ($\eta_p = \eta_{ax}\eta_{cir}$), and real propeller efficiency (η_{real}) on flight speed are shown in Figure 25.5(1) (we see from this figure that at high flight speeds the primary role is played by the profile drag, which defines the limit of ideal propeller theory applicability).

Let us analyze the operation of a propeller in a shroud (Figure 25.6). We assume that the stream does not contract behind the shroud and the stream velocity does not increase. Usually straightening vanes are installed in the shroud behind the propeller to eliminate rotation of the air in the slipstream. As in the preceding problem, we assume the air to be inviscid and neglect friction losses.

We find the propeller thrust from the momentum change law

$$P=m(V_1-V_\infty), \tag{25.16}$$

where m is the air mass flowrate.

The power if found as the difference of the airstream kinetic energies ahead of and at some distance behind the propeller (sections

*Footnote (1) appears on page 299

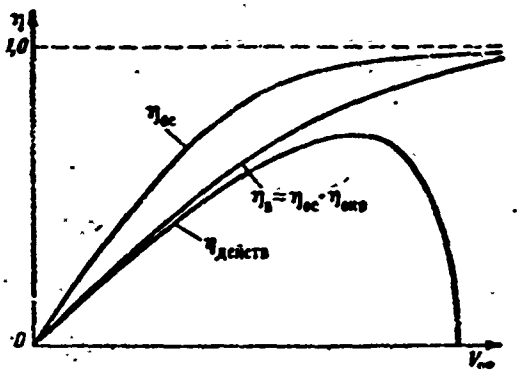

Figure 25.5. Variation of axial efficiency and efficiency of ideal and real propellers with flight speed.

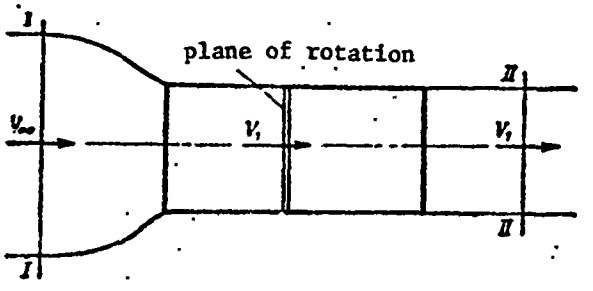

Figure 25.6. Illustrating analysis of shrouded ideal propeller operation.

I and II in Figure 25.6)

$$N=\frac{mV_1^2}{2}-\frac{mV_\infty^2}{2}=\frac{m}{2}(V_1^2-V_\infty^2). \qquad (25.17)$$

Now we can calculate the axial efficiency η_{sh} of the shrouded propeller

$$\eta_{sh}=\frac{PV_\infty}{N}.$$

Substituting the thrust from (25.16) and power from (25.17), we obtain

$$\eta_{ax}=\frac{\rho(V_1-V_\infty)V_\infty}{\frac{\rho}{2}(V_1^2-V_\infty^2)}=\frac{2V_\infty}{V_1+V_\infty}. \qquad (25.18)$$

In order to compare the axial efficiency η_{ax} of the free propeller and that η_{sh} of the shrouded propeller, we divide η_{sh} by η_{ax}, using (25.18) and (25.10)

$$\frac{\eta_{sh}}{\eta_{ax}}=\frac{2V_1}{V_1+V_\infty}. \qquad (25.19)$$

Since $V_1 > V_\infty$, it follows from (25.19) that $\eta_{sh} > \eta_{ax}$.

Consequently, the efficiency of the shrouded propeller is higher than that of the free propeller. However, this difference is significant only for low freestream velocities V_∞. The larger V_∞, the smaller this difference will be. Therefore, operation of the propeller in a shroud is used only when V_∞ is small, specifically on hydrogliders, aerosleds, and recently on certain vertical takeoff vehicles.

§25.3. Isolated Blade Element Theory

In isolated blade element theory the propeller blade is considered as a wing and the following assumptions are made:

1. The blade element operates alone (neighboring elements have no effect on its operation). This assumption makes it possible to examine the blade element as a wing element of infinite span, i.e., we can neglect induced drag.

2. The action of the flow on the blade element traveling along a helical line is the same as that on an element traveling translationally with the same absolute velocity.

We use two concentric surfaces with center at the axis of rotation to cut out a blade element of length dr at the distance r

from the axis of rotation (Figure 25.7). The absolute velocity of the air relative to the blade is defined by the relation obtained above.

$$W=Dn_c\sqrt{\lambda^2+\pi^2\bar{r}^2}.$$

Then we have the following expression for the elementary blade element lift force

$$dY=c_y\frac{\varrho W^2}{2}b\,dr=\frac{c_y}{2}\varrho D^2n_c^2(\lambda^2+\pi^2\bar{r}^2)\bar{b}\,dr.$$

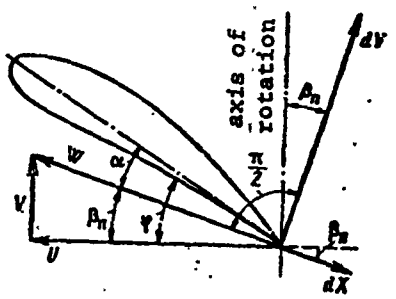

Figure 25.7. Forces acting on blade element.

Since

$$b=\bar{b}D;\quad dr=\frac{D}{2}d\bar{r},$$

where

$$\bar{b}=\bar{b}(\bar{r}),$$

we obtain

$$dY=\frac{c_y}{4}\varrho D^4n_c^2(\lambda^2+\pi^2\bar{r}^2)\bar{b}\,d\bar{r}.$$

The elementary lift force dY is perpendicular to the absolute velocity W.

We have similarly for the elementary drag of the blade element

$$dX=\frac{c_x}{4}\varrho D^4n_c^2(\lambda^2+\pi^2\bar{r}^2)\,\bar{b}\,d\bar{r}.$$

It is obvious that the sum of the projections of dY and dX on the axis of rotation equals the thrust dP created by the blade element

$$dP=dY\cos\beta_n-dX\sin\beta_n,$$

or, substituting the values of dY and dX, we obtain

$$dP=\frac{1}{4}\varrho D^4 n_c^2(\lambda^2+\pi^2\bar{r}^2)(c_y\cos\beta_a-c_x\sin\beta_a)\bar{b}\,d\bar{r}. \qquad (25.20)$$

The sum of the projections of dY and dX on the plane of rotation, multiplied by the linear velocity of rotation, is equal to the elementary power dN. Since $\omega = 2\pi n_s$, we have

$$dN=(dY\sin\beta_a+dX\cos\beta_a)2\pi n_c r,$$

or substituting the values of dY and dX and considering that $r = \bar{r}D/2$, we obtain

$$dN=\frac{\pi}{4}\varrho D^5 n_c^2(\lambda^2+\pi^2\bar{r}^2)(c_y\sin\beta_a+c_x\cos\beta_a)\bar{b}\bar{r}\,d\bar{r}. \qquad (25.21)$$

Integrating (25.20) and (25.21) in the limits from $\bar{r}_0$ to 1, where $\bar{r}_0$ is the dimensionless radius of the propeller hub, we obtain the expressions for finding propeller thrust P and power N

$$P=\frac{k}{4}\varrho D^4 n_c^2\int_{\bar{r}_0}^{1}(\lambda^2+\pi^2\bar{r}^2)(c_y\cos\beta_a-c_x\sin\beta_a)\bar{b}\,d\bar{r}; \qquad (25.22)$$

$$N=\frac{k}{4}\pi\varrho D^5 n_c^3\int_{\bar{r}_0}^{1}(\lambda^2+\pi^2\bar{r}^2)(c_y\sin\beta_a+c_x\cos\beta_a)\bar{b}\bar{r}\,d\bar{r}, \qquad (25.23)$$

where k is the number of propeller blades.

Isolated blade element theory does not permit determining sufficiently exactly the values of P and N, since this theory does not consider the influence of tip effects, which are similar to the tip effects on the airplane wing. However, this theory makes it possible to obtain the basic similarity laws which can be used for testing propellers and in selecting propellers for an airplane.

Propeller thrust and power with account for tip effects are determined with the aid of propeller vortex theory, developed by Zhukovskiy. In accordance with this theory the propeller blades are

replaced by a system of bound and free rotating vortices. This technique makes it possible to construct more precisely the velocity field and therby define more correctly all the kinematic characteristics and operating regime of the propeller.

§25.4. Propeller Aerodynamic Similarity Conditions and Aerodynamic Characteristics

Various theories make it possible to determine with some degree of precision the basic propeller characteristics — thrust, power, and efficiency. However, the final conclusion on the magnitude of the propeller parameters is made on the basis of experiment, since all the factors influencing propeller operation under actual conditions cannot be taken into account in the theoretical calculations.

Experimental studies are conducted in wind tunnels on models whose geometric dimensions are usually smaller than those of the full-scale propellers. Therefore the need arises to find the conditions under which geometrically similar propellers can be considered aerodynamically similar. We need aerodynamic similarity criteria in order to be able to convert from model to full-scale parameters in a valid fashion.

The similarity criteria can be obtained from analysis of the theoretical relations obtained, for example, with the aid of isolated blade element theory. The formulas (25.22), (25.23) for determining thrust and power, obtained with the aid of this theory, contain the quantities $\bar{r}$ and $\bar{b}$, which are the same for geometrically similar propellers. The inflow angle β_{in}, which appears in the trigonometric functions, depends on the propeller advance ratio λ and is defined by (25.2)

$$\beta_{in}=\operatorname{arctg}\frac{\lambda}{\pi\bar{r}}.$$

For the same blade incidence angles ϕ, the aerodynamic coefficients c_y and c_x, other conditions being the same, will depend on the angle

of attack α, which if we neglect tip effects is equal to the difference of the incidence and inflow angles, i.e., $\alpha = \phi = \beta_{in}$. This means that the angle of attack, and therefore the lift and drag coefficients as well, of the blade element depend on the advance ratio λ.

Thus, the integrals in (25.22) and (25.23), being dimensionless, are in the final analysis functions of the advance ratio and these expressions can be written as

$$P = f_1(\lambda)\rho n_c^2 D^4;$$
$$N = f_2(\lambda)\rho n_c^2 D^5.$$

Denoting $f_1(\lambda) = \alpha$ and $f_2(\lambda) = \beta$, we obtain

$$P = \alpha\rho n_c^2 D^4; \tag{25.24}$$
$$N = \beta\rho n_c^3 D^5. \tag{25.25}$$

The coefficients α and β are called respectively the thrust and power coefficients.

We can obtain the following expression for the propeller efficiency by using (25.1)

$$\eta = \frac{PV_\infty}{N} = \frac{\alpha\rho n_c^2 D^4 \lambda n_c D}{\beta\rho n_c^3 D^5},$$

or

$$\eta = \frac{\alpha\lambda}{\beta}. \tag{25.26}$$

Since the thrust coefficient α and the power coefficient β depend on the advance ratio λ, the propeller efficiency is also a function of the advance ratio.

Consequently, the condition for aerodynamic similarity of geometrically similar propellers is equality of the advance ratios

λ of these propellers. Here we must recall that the aerodynamic coefficients c_y and c_x also depend on the friction forces and elasticity of the air. Therefore equality of the Reynolds and Mach numbers for the actual and scale propellers is also a necessary condition for complete aerodynamic similarity.

If the Reynolds number is not large, the friction forces will not depend on the air viscosity and will be proportional to the squares of the relative velocities (regime of self-similar flow around the blades with respect to Reynolds number). In this case equality of the Reynolds numbers for the two similar blades is not required.

Theory and experiment show that with increase of the flight speed at constant rpm, and this means with increase of the advance ratio λ, propeller thrust decreases.

The variation of the power transmitted by the propeller from the engine to the air is approximately the same as that of the thrust. The graphical dependence of the thrust α and power b coefficients on the advance ratio λ for fixed blade incidence angle is called the propeller operating characteristic (Figure 25.8).

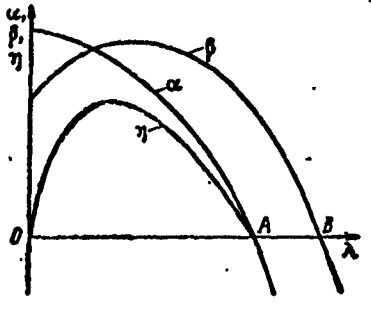

Figure 25.8. Propeller operating characteristics with ϕ = constant.

In Figure 25.8 we can identify three zones, corresponding to qualitatively different propeller operating regimes. In the region of λ values corresponding to the segment OA on the abscissa axis, the thrust is positive. At the ends of this segment the efficiency is zero, since at the coordinate origin the translational velocity is zero and at point A the thrust is zero, i.e., in both cases the propeller does not perform useful work.

The segment AB of the abscissa axis corresponds to the regimes in which the thrust is negative but power is positive. These are called the negative thrust regimes.

The regimes corresponding to negative thrust and power are located to the right of point B. Here the propeller is rotated by the airstream and does not require energy from the engine. These are termed autorotation regimes.

The propeller characteristics depend on the blade incidence angle. Therefore in laboratory propeller testing a series of operating characteristics is recorded at different incidence angles.

For convenience in use for design purposes, the curves of power coefficient and efficiency versus advance ratio λ for different incidence angles ϕ (the curves for the thrust coefficient ϕ are not presented since they are rarely used in design) are presented on a single plot, called the propeller aerodynamic characteristic (Figure 25.9).

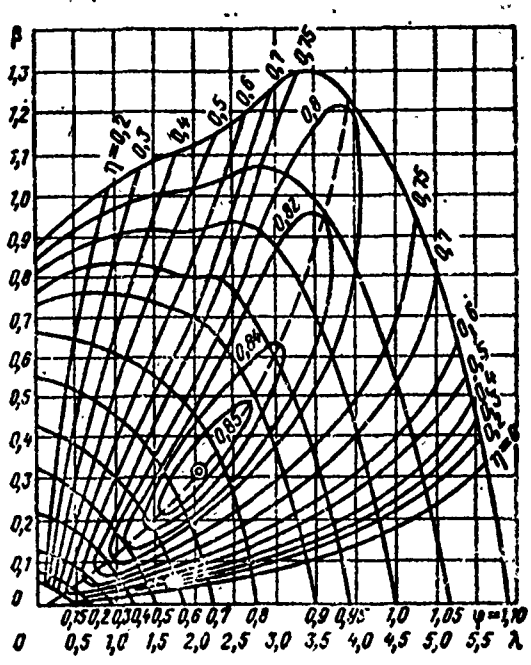

Figure 25.9. Propeller aerodynamic characteristics.

In calculating airplane takeoff distances, we must know how the propeller thrust varies as a function of velocity during the ground run, and therefore special curves are plotted of the thrust coefficient for different propeller operating conditions $\alpha = f(\phi,\lambda)$ for small values of the advance ratio (Figure 25.10).

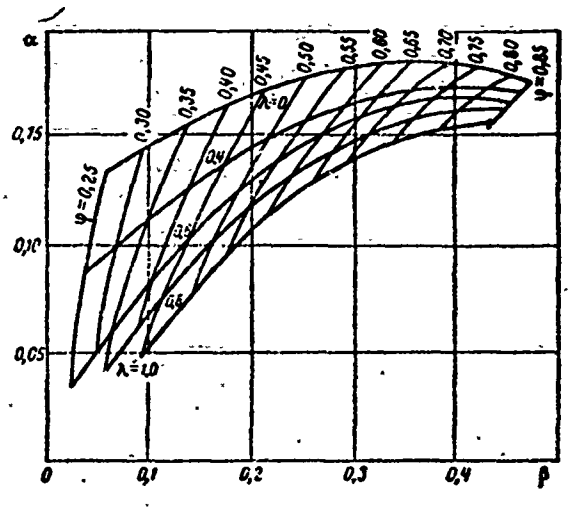

Figure 25.10. Propeller thrust characteristics.

§25.5. Mutual Influence of Propeller and Airplane. Influence of Air Compressibility on Propeller Efficiency

The influence of the propeller on the airplane shows up in the fact that the portion of the wing behind the propeller is located in a region of velocities which are greater than the flight velocity; therefore the drag and lift on this portion of the wing increase. Particularly marked is the lift increase at low flight speeds. In this case the velocity behind the propeller exceeds considerably the airplane flight speed.

Denoting the wing area in the propeller slipstream by S_{slip} and that outside the slipstream by S_{out} and the corresponding lift forces by Y_{slip} and Y_{out}, we obtain

$$Y = Y_{\text{обд}} + Y_{\text{необд}}.$$

We denote the lift coefficient with account for the propeller influence by $c_{y\ slip}$. Then expressing the forces in terms of the coefficients, we obtain the expression

$$c_{y\,\text{обд}} \frac{\rho V_\infty^2}{2} S = c_y \frac{\rho V_\infty^2}{2} S_{\text{необд}} + c_y \frac{\rho V_2^2}{2} S_{\text{обд}},$$

or, considering that $S_{out} = S - S_{slip}$, where S is the wing area, we have

$$c_{y\,обд} = c_y\left(1 - \frac{S_{slip}}{S} + \frac{S_{обд}}{S}\frac{V_2^2}{V_\infty^2}\right).$$

According to (25.13)

$$V_2 = V_\infty\sqrt{1+B}.$$

Then

$$\Delta\bar{c}_{y\,обд} = \frac{\Delta c_{y\,обд}}{c_y} = \frac{c_{y\,обд} - c_y}{c_y} = \frac{S_{обд}}{S}B. \qquad (25.27)$$

In (25.27) no account is taken for the angle of attack reduction at the wing sections behind the propeller. Therefore the experimentally determined lift force increment is less than that given by (25.27). Figure 25.11 shows curves of $\Delta\bar{c}_{y\,slip}$ versus the disk loading factor B for different $\bar{S}_{slip} = S_{slip}/S$, plotted on the basis of experimental data.

The wing drag increase behind the propeller is usually taken into account by reducing the propeller thrust by the magnitude of the drag increase, i.e., in place of the propeller thrust developed in the presence of the body behind the propeller we introduce into the aerodynamic calculation the effective thrust

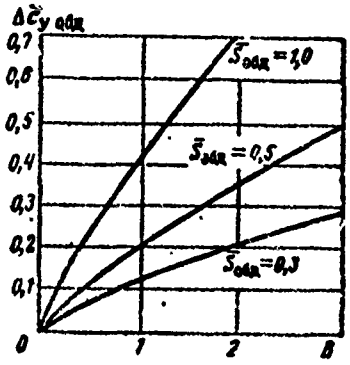

Figure 25.11. Effect of propeller slipstream over wing on lift force.

$$P_{эф} = P - \Delta Q,$$

where ΔQ is the body drag increase owing to the propeller slipstream.

The corresponding effective efficiency is

$$\eta_{эф} = \frac{P_{эф}V_\infty}{N}.$$

The influence of the engine nacelle on propeller operation shows up in partial retardation of the airstream ahead of the nacelle. The larger the nacelle transverse dimension, the lower the velocity will be in the propeller rotation plane. The result of this is reduction of the velocity V_2 at a large distance from the plane of rotation, and along with this the propeller thrust and efficiency decrease.

The influence of the engine nacelle is usually accounted for by a correction factor, used to multiply the propeller efficiency.

The aerodynamic characteristics are usually plotted with account for the mutual influence of the propeller and the engine nacelle with which the propeller tests were conducted in the wind tunnel. Therefore the propeller efficiency found from the characteristic curves already accounts for the mutual influence of the engine nacelle and the propeller on the model. Consequently, in determining the correction to the propeller efficiency we must consider the differences in the relative dimensions of the full-scale engine nacelle and the model nacelle.

The compressibility of the air begins to have an effect at high flight speeds. For the propeller the maximal velocity is observed at the blade tips, where the absolute air velocity relative to the blade is

$$W_{\text{конц}}=Dn_c\sqrt{\lambda^2+\pi^2}=\lambda Dn_c\sqrt{1+\frac{\pi^2}{\lambda^2}}=V_\infty\sqrt{1+\frac{\pi^2}{\lambda^2}},$$

and

$$M_{\text{конц}}=M_\infty\sqrt{1+\frac{\pi^2}{\lambda^2}}.$$

We know that the coefficients c_y and c_x increase with increase of the velocity (M_∞) for subsonic flow conditions. The rate of increase increases with approach of M_∞ to M_{cr}. When local supersonic

velocities and shock waves appear on the blade, the drag increases markedly and the propeller efficiency decreases. Sonic velocities at the propeller blade tips are reached at quite moderate flight speeds. For example, for the AV-681 propeller on the Il-18 airplane at V_∞ = 630 km/hr, H = 8000 m, n = 1075 rpm, and D = 4.5 m we have:

flight speed 175 m/sec;

linear rotational speed at the blade tips (absolute) 254 m/sec;

resultant velocity of blade tips 310 m/sec;

blade tip Mach number 1.01.

We note that shock stall is possible not only at the blade tip but also in the root region (Figure 25.12), in spite of the fact that the resultant velocity in this region is lower than that at the tip because of closeness to the axis of rotation. This is explained by the fact that the relative blade thickness is very large (reaching 30% or more) in the root region, and in this region the shock stall occurs at comparatively low Mach numbers.

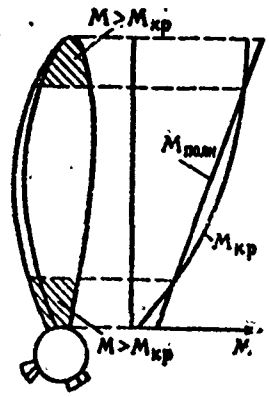

Figure 25.12. Regions of shock stall on blade.

The marked reduction of the efficiency because of the onset of shock stall is one of the basic reasons for not using propellers on high speed airplanes.

The propeller is selected for each type of airplane in the design process. The propeller diameter is selected on the basis of the most characteristic operating regime. The design condition may be the flight condition at maximal speed, maximal range, takeoff, and so on. For transport airplanes the design regime is most frequently that of maximal range.

In selecting the propeller type and diameter, we must know the engine power and rpm at the design flight conditions, i.e., at the design altitude and flight speed. In the design process we select the propeller type and diameter to ensure a propeller efficiency close to the maximal value in flight at the design conditions. The propeller efficiency may be lower in other flight conditions.

The prop diameter is determined approximately as follows. Excluding the diameter D from (25.1) and (25.25), we have

$$\beta=\lambda^5\frac{Nn_c^2}{\rho V_\infty^5}.$$

In this relation all the quantities other than the power coefficient and the advance ratio λ must be given. On the propeller aerodynamic characteristics (see Figure 25.9) the relationship between λ and β is represented in the form of a fifth degree parabola. On this parabola we find the point corresponding to the maximal efficiency, and after finding for this point the value of λ we find the propeller diameter from (25.1)

$$D=\frac{V_\infty}{\lambda n_c}.$$

If the parabola lies far from the maximal efficiency values, the propeller rpm must be changed or propellers of a different series must be investigated.

This method yields the prop diameter in the first approximation. More exact methods which make it possible to account for the influence of compressibility, mutual influence of the prop and airplane, and so on are presented in the specialized literature.

§25.6. Propeller Operation in the Negative Thrust and Autorotation Regimes

The negative thrust regime may be observed with the airplane in a dive, when as a result of the airplane speed increase along

its trajectory the blades are subjected to flow at a negative angle of attack (Figure 25.13). The negative thrust regime is also created during rollout of the airplane after landing. During the approach, when the landing speed is reached the power levers are retarded to the flight idle position and the blade incidence angle decreases to values on the order of 0.20-0.30 rad. If the power lever is moved to ground idle immediately after touchdown, the incidence angle decreases to zero and a large negative thrust is created.

In case of failure of an engine and of the feathering system in flight, the prop control system drives the prop to small incidence angles. Large negative thrust is created, exceeding by two or three times the positive thrust with normal engine operation. In this case the prop continues to turn under the action of the approaching airstream.

The reasons for autorotation can be clarified by analyzing the nature of the forces acting on the prop blade when it is at comparatively small incidence angle and has high axial velocity (Figure 25.14). The blade angle of attack is negative. The resultant aerodynamic force R, equal to the vector sum of the lift Y and the drag X, when projected on the plane of rotation yields the component F directed in the direction of rotation of the prop. The force F, multiplied by its arm relative to the prop hub axis, yields a moment which accelerates the prop in the previous direction.

Consequently, the aerodynamic forces not only do not retard the prop, they begin to accelerate it and prop autorotation begins. In the autorotation regime the prop takes energy from the kinetic energy of the airplane, i.e., it has a retarding action. The power required to rotate the prop with the engines off is very large, since the engine compressor and turbine are rotated along with the prop.

The rpm and retarding action will be maximal at incidence angles 0.17 - 0.26 rad (10-15°). At larger and smaller incidence

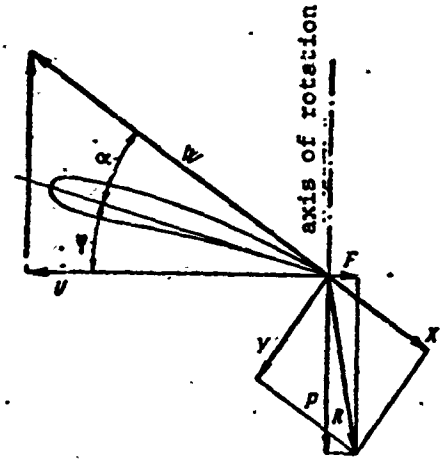

Figure 25.13. Prop blade operation in negative thrust regime.

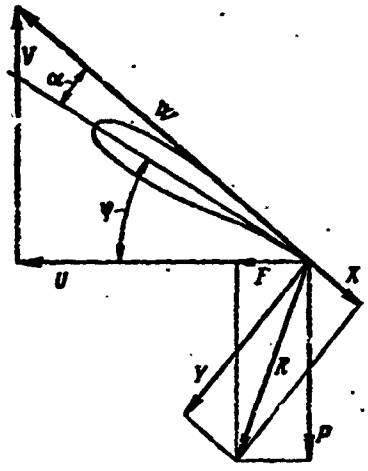

Figure 25.14. Prop blade operation in autorotation regime.

angles the drag force and rpm decrease and the prop will stop.

Feathering systems are used to reduce prop drag in case of engine failure on airplanes. The feathering systems drive the props to the feathered position, in which the prop drag becomes minimal and the prop does not turn. The automatic system is activated when the engine power drops off in case of engine failure.

Review Questions

1. Explain the necessity for using prop blade geometric twist.

2. Why is the prop efficiency always less than one even in an inviscid medium? How can the prop efficiency be increased under these conditions?

3. Under what conditions can negative thrust be obtained if the direction and speed of rotation remain unchanged and the blade incidence angle is not negative?

4. How will the blade incidence angle and angle of attack change during airplane takeoff acceleration for constant prop rotational speed?

Problem

1. On the prop aerodynamic characteristics (see Figure 25.9) indicate all the variable pitch prop (N = const, n = const) and fixed pitch prop (ϕ = const) regimes if the props operate in the regimes $\beta = 0.315$; $\lambda = 2.05$, respectively. For which of these props will the range of advance ratio values be larger for efficiencies exceeding 0.8?

Answer

The horizontal line $\beta = 0.315$ corresponds to the variable pitch prop regimes in Figure 25.9.

The line for $\phi = 0.76$ rad corresponds to the fixed pitch prop operating regimes.

FOOTNOTES

1. on page 282 — As can be seen in Figure 25.5, at high flight velocities the profile drag plays a decisive role, which predetermines the limits of applicability of the ideal propeller theory.

CHAPTER XXVI

AERODYNAMICS OF HELICOPTER MAIN ROTOR

§26.1. Main Rotor Operation

In contrast with the airplane propeller, the helicopter rotor not only performs the functions of a propulsor but also equalizes the helicopter weight in flight (therefore it is termed the lifting rotor). At the same time the helicopter rotor provides flight stability and controllability and also provides for safe descent in case of engine failure.

Depending on the aerodynamic arrangement of the helicopter, there are many different lifting rotor designs which make it possible for it to perform its varied functions.

In order to provide maneuverability, the main rotor thrust vector must vary over a wide range, both in absolute magnitude and in direction. This problem can be solved in various ways. However, the most widely used rotors are those in which the blade plane of rotation can change its attitude with respect to the shaft axis. This capability is provided by hinged mounting of the main rotor blades to the hub and the use of a special mechanism, the so-called tilt control, first suggested in 1910 by Academician B. N. Yur'yev.

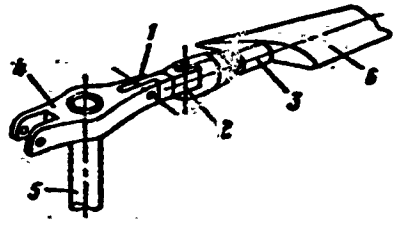

Figure 26.1. Main rotor blade mounting: 1 - horizontal hinge; 2 - vertical hinge; 3 - axial hinge; 4 - hub; 5 - shaft; 6 - blade.

Figure 26.1 shows a schematic of the hinged mounting of a main rotor blade on the hub. The horizontal hinge 1 provides for variation of the blade inclination with respect to the plane of rotation. Moreover, the horizontal hinge results in zero bending moment at the blade root relative to this hinge. During rotation the blade is subject to the action of the aerodynamic force Y and the centrifugal force F_{cent} (Figure 26.2) and automatically takes an equilibrium position in which the resultant force vector F passes through the hinge axis.

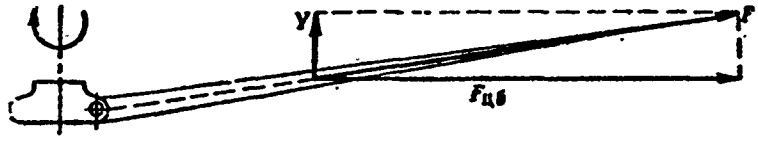

Figure 26.2. Blade equilibrium position.

The vertical hinge 2 relieves the root part of the blade of the moment created by the drag and centrifugal forces.

As a result of the presence of the horizontal and vertical hinges, the rotor blades perform continuous oscillatory motions in flight under the action of the moments, which vary in magnitude. The main rotor design includes stops which limit blade rotation, for example, the stops which limit blade droop when the rotor is stopped.

The axial hinge 3 makes it possible to change the blade incidence angle in flight in order to vary the thrust force.

The tilt control controls the blade incidence angles on the operating rotor as a function of their position, which is characterized by the azimuth angle ψ (Figure 26.3). If the blade incidence angles

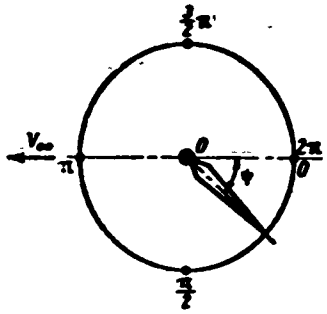

Figure 26.3. Blade azimuthal positions.

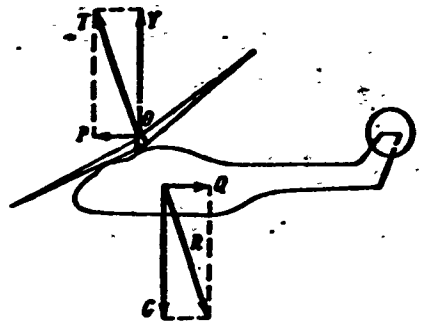

Figure 26.4. Forces acting on helicopter in flight.

are increased for values of ψ close to 0 and reduced for values of ψ close to π, then as a result of lift force variation the blade plane of rotation is tilted forward, the rotor thrust force T creates the horizontal component P, and the helicopter begins to move forward (Figure 26.4). If we reduce the blade incidence angles for values of ψ close to $3\pi/2$ and increase them for ψ close to $\pi/2$, then the helicopter begins to move to the right.

A schematic of the tilt control is shown in Figure 26.5. Tilting of the outer bearing ring 1 with the aid of the control stick 2 causes tilt of the inner ring 3, which rotates together with the blades and is connected with them by the rods 4. Displacement of the rods 4 leads to corresponding cyclic variation of the blade incidence angle.

The collective pitch lever 5 can be used to change the incidence angle by the same amount simultaneously for all the blades (regardless of their azimuthal position), which is achieved by varying the magnitude of the thrust force without altering its direction.

To obtain more uniform main rotor operation, the number of blades is usually more than two. The blades have rectangular or trapezoidal planform with small taper ratio. As a rule the blades are twisted to reduce the incidence angle toward the blade tip.

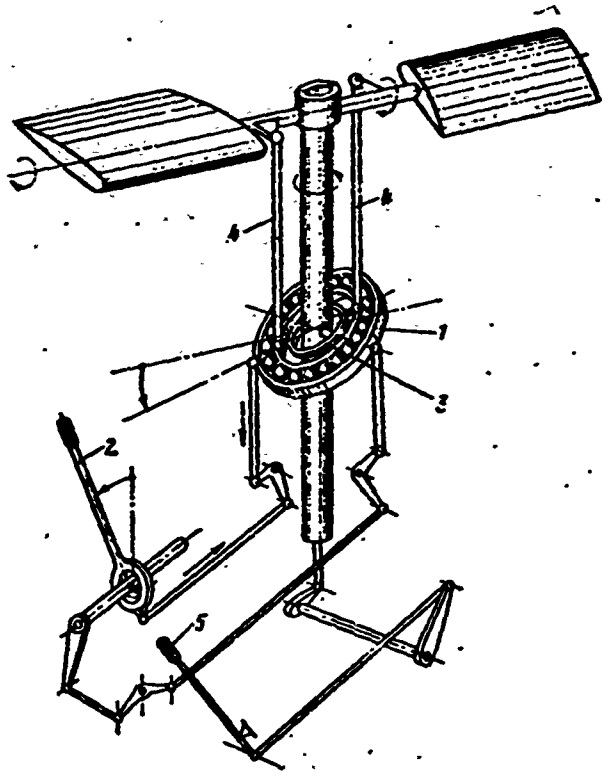

Figure 26.5. Tilt control: 1 - outer bearing ring; 2 - control stick; 3 - inner bearing ring; 4 - rods; 5 - collective pitch lever.

§26.2. Effect of Oblique Flow on Rotor Aerodynamics

The helicopter main rotor blade plane of rotation forms some angle with the flight direction during flight. This angle is called the rotor angle of attack. In conventional flight the angle of attack is negative (Figure 26.6). For angles of attack $\alpha = \mp \pi/2$, corresponding to helicopter vertical climb and descent, the helicopter rotor encounters the air in the axial direction. For α which differs from $\pm \pi/2$ the rotor operates in the so-called oblique flow regime. We note that the airplane propeller may also operate in this regime; however, the angle of attack of the airplane propeller in this case is very close to $-\pi/2$.

Oblique flow leads to change of the rotor blade operating conditions with variation of the azimuth angle ψ. Let us resolve the

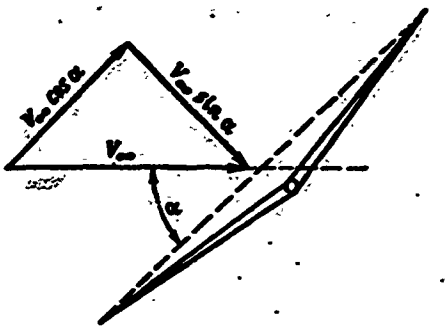

Figure 26.6. Main rotor angle of attack. Axial and transverse flow through rotor.

flight velocity V_∞ into the axial component $V_\infty \sin\alpha$ and the component $V_\infty \cos\alpha$ in the plane of rotation (see Figure 26.6).

Oblique flow through the rotor can be represented as the sum of the axial (with velocity $V_\infty \sin\alpha$) and transverse (with velocity $V_\infty \cos\alpha$) flows. The tangential velocity U_t at some blade element (Figure 26.7) owing to the transverse flow is equal to

$$U_t = \omega r + V_\infty \cos\alpha \sin\psi. \qquad (26.1)$$

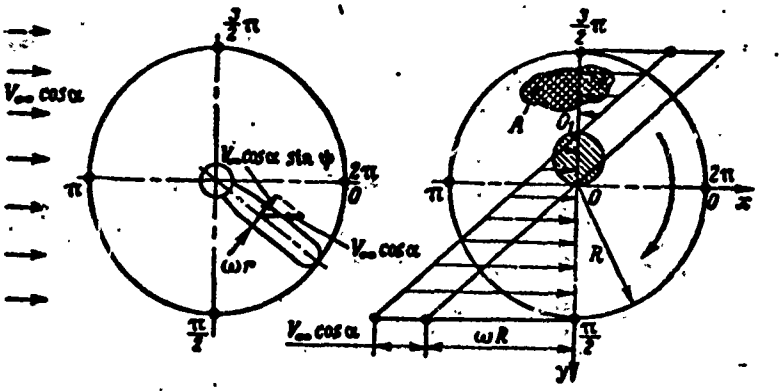

Figure 26.7. Tangential velocities on main rotor blades.

The velocity U_t depends on the azimuthal position of the element. Figure 26.7 shows the variation of U_t along the blade for $\psi = \pi/2$ and $\psi = 3\pi/2$. We see from the figure that on the segment OO_1 the blade elements encounter the air with their trailing edge. Consequently, a reverse flow zone is obtained in the case of oblique flow over the rotor. It can be shown that this zone is a circle (shaded in the figure). In the reverse flow zone the lift force on the blade elements

has a direction opposite the direction of the lift on the elements located outside this zone, i.e., negative thrust is developed in this zone. The higher the velocity $V_\infty \cos \alpha$, the larger is the reverse flow zone and the more markedly the rotor effectiveness decreases. The formation of the reverse flow zone is one of the factors limiting helicopter flight speed.

The blade element absolute velocity

$$W = \sqrt{V_\infty^2 \sin^2 \alpha + (\omega r + V_\infty \cos \alpha \sin \psi)^2}.$$

The inflow angle at the blade element is defined by the expression

$$\operatorname{tg} \beta_a = \frac{V_\infty \sin \alpha}{\omega r + V_\infty \cos \alpha \sin \psi}.$$

Hence we see that the resultant absolute velocity and inflow angle for a given blade element depend on the azimuth angle ψ. The resultant velocity reaches its maximal value at $\psi = \pi/2$ and minimal value at $\psi = 3\pi/2$. The inflow angle is minimal at $\psi = \pi/2$, and reaches a maximum at $\psi = 3\pi/2$.

The reduction of the inflow angle, as the azimuth angle ψ varies from 0 to $\pi/2$, causes increase of the blade element angles of attack. Since in this case there is an increase of the absolute velocity, the lift force also increases with variation of ψ from 0 to $\pi/2$.

The lift increment, in turn, leads to upward rotation of the blade about the horizontal hinge (the so-called flapping motion). The blade flaps upward in that period when it moves against the transverse flow. Downward blade flapping motion is obtained when the blade travels in the direction of the transverse flow.

As a result of the flapping motion, an additional axial velocity component V_{fl} appears on the blade elements; therefore the blade angle of attack α_r decreases for values of ψ close to $\pi/2$, while it increases for values of ψ close to $3\pi/2$ (Figure 26.8). At high flight speeds

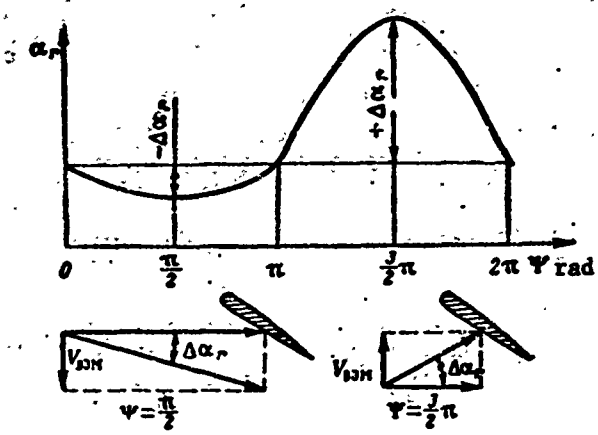

Figure 26.8. Azimuthal variation of blade section angle of attack because of blade flapping motion.

the angle of attack increase at $\psi = 3\pi/2$ can become significant and flow separation takes place. The flow separates from the blades at that moment when they occupy azimuthal positions close to $\psi = 3\pi/2$ (zone A in Figure 26.7).

Because of flow separation, and also because of the presence of the region of reversed flow over the blade, the rotor plane of rotation "tilts" in the direction of $\psi = 3\pi/2$. The appearance of flow separation at high speeds is also a factor limiting helicopter flight speed.

§26.3. Rotor Dynamic Similarity Conditions in Forward Flight

The problems of main rotor modeling are of great importance. Oblique flow through the rotor, the very complex blade motion in which flapping motion about the horizontal hinge is also imposed on the rotational motion, the lead-lag motion about the vertical hinge, the cyclic variation of the incidence angle as commanded by the tilt control — all this complicates not only the theoretical analysis of the main rotor but also its experimental study. If we take into account the deformational motions of the blade as it bends and twists (the deformations must be considered because of the large rotor diameters and the comparatively low stiffness of the rotor blades), and also the necessity for ensuring similarity of the blade inertial characteristics, since their motion takes place with acceleration, the entire complexity of the problem of modeling the helicopter main rotor becomes clear.

Let us examine very briefly the dynamic similarity conditions for lifting rotors. As always, geometric similarity of the rotors must be satisfied first of all in order to obtain dynamic similarity. In comparison with conventional propellers, here we must satisfy several additional requirements with respect to similar positioning of the blade hinge axes, and also similarity of the tilt control system elements.

The kinematic conditions for dynamic similarity of rotors in forward flight can be obtained by examining separately rotor operation with purely axial flow and with purely transverse flow.

In the axial direction the rotor operates with the velocity $V_\infty \sin \alpha$. We have for the advance ratio

$$\lambda = \frac{V_\infty \sin \alpha}{nD}. \qquad (26.2)$$

On the basis of the arguments of §25.4, we conclude that for aerodynamic similarity of the rotor it is necessary to observe equality of the rotor advance ratios.

In the case of purely transverse flow over dynamically similar rotors, it is obvious that the velocity patterns must be geometrically similar. Specifically, the blade reverse flow zones must be commensurate with the disks, which leads to the following relation (see Figure 26.7)

$$\frac{O_1O}{R} = \frac{V_\infty \cos \alpha}{\omega R} = \mu = \text{const}. \qquad (26.3)$$

The quantity μ is termed the main rotor operating regime characteristic. It shows what part of the blade operates under reversed flow conditions (if $\mu = 0.2$, this means that 20% of the blade operates with reversed flow). Large values of μ lead to rotor efficiency loss and vibrations. In addition to equality of the advance ratios, equality of the μ characteristics must be satisfied for dynamic similarity of rotors operating in forward flight.

The main rotor operating regime characteristic μ and the advance ratio λ are connected by the relation

$$\mu = \frac{V_\infty \cos\alpha}{\pi n D} = \frac{V_\infty \sin\alpha}{nD} \frac{\cos\alpha}{\pi \sin\alpha} = \lambda \frac{\operatorname{ctg}\alpha}{\pi}. \qquad (26.4)$$

We see from (26.4) that in place of equality of μ we can take equality of the angles of attack α as the additional condition for dynamic similarity.

Thus, while for rotors in axial flow the condition for dynamic similarity involves equality of the advance ratios, in the case of forward flight equality of λ and μ or of λ and α must be ensured for dynamic similarity of the rotors.

For the main rotor in forward flight the blade incidence angle (pitch) usually varies as a function of blade azimuthal position. This pitch variation is specified by the tilt control deflection angle. Along with geometric similarity of the blade retention and the tilt control elements, to ensure identical blade pitch variation we must obviously ensure equality of the tilt control deflection angles. The requirement for identity of blade cyclic pitch change complicates markedly the modeling of rotors and the use of data from flow testing of a series of rotors.

In practical calculations, we normally use rotor aerodynamic characteristics obtained under forward flight conditions with fixed blade pitch, with the pitch not varying as the blade moves in azimuth. Theory shows that the constant-pitch rotor is dynamically similar to a rotor with varying pitch if their angles of attack differ by some quantity defined by a special calculation (this question is examined in detail in the specialized textbooks). Such a rotor with constant pitch but set at some different angle of attack is termed the <u>equivalent rotor</u>. The introduction of the equivalent rotor concept makes it possible to make extensive use of the results of flow testing of a series of lifting rotors.

To ensure dynamic similarity of lifting rotors, it is necessary to observe equality of the Reynolds numbers

$$\mathrm{Re}=\frac{R^2\omega}{\nu}.$$

For the lifting rotors, just as for conventional propellers, there is a self-similar regime with respect to Reynolds numbers. If both rotors operate in the self-similar region, there is no need to observe equality of the Reynolds numbers.

For high Mach numbers it is necessary to ensure equality of the Mach numbers $M=\frac{\omega R}{a}$.

Since lifting rotors have very long and flexible blades (bending is measured in tens of centimeters and twisting reaches 0.05-0.1 rad), for their similarity it is necessary to satisfy the deformation similarity condition. This condition is satisfied with equality of the Cauchy numbers

$$C=\frac{\rho V^2}{E},$$

where E is the modulus of elasticity of the blade material.

§26.4. Lifting Rotor Aerodynamic Characteristics

Let us analyze the aerodynamic characteristics of the main rotor. Assume a main rotor operates at the angle of attack α (Figure 26.9). The resultant aerodynamic force R acting on the rotor can be resolved into components in the wing or body coordinate systems.

In the body coordinate system we obtain the component T perpendicular to the plane of rotation — the rotor thrust, and the component H in the rotor plane of rotation — the rotor longitudinal force.

In the wind coordinate system Y is the rotor lift and X is the rotor propulsive force. For simplicity we shall not consider the lateral components of the force R, which are associated with tilting of the rotor plane of rotation in the direction of the azimuth values

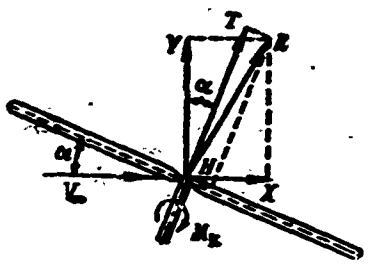

Figure 26.9. Projections of main rotor resultant aerodynamic force on directions of wind and body axes.

$\psi = 3\pi/2$ (see §26.2). These components are considered in the solution of helicopter flight stability and controllability problems.

In accordance with the aerodynamic similarity laws, we can write the expressions for the components of the force R

$$T = c_T \frac{1}{2} \varrho (\omega R)^2 \pi R^2;$$

$$H = c_H \frac{1}{2} \varrho (\omega R)^2 \pi R^2;$$

$$Y = c_y \frac{1}{2} \varrho (\omega R)^2 \pi R^2;$$

$$X = c_x \frac{1}{2} \varrho (\omega R)^2 \pi R^2.$$

Here c_T, c_H, c_y, and c_x — the coefficients of the corresponding forces — are dimensionless quantities which depend on the rotor dynamic similarity parameters under forward flight conditions.

Using the equivalent rotor concept, in approximate calculations we consider that the aerodynamic coefficients are determined by the value of the advance ratio λ, angle of attack α, Reynolds and Mach numbers, in addition to the basic geometric parameters (number z_b of blades, solidity σ, relative profile thickness $\bar{c}$, blade incidence angle ϕ).

The expression for the torque on the rotor shaft is

$$M_к = c_{mк} \frac{1}{2} \varrho (\omega R)^2 \pi R^3,$$

where c_{mt} is the torque coefficient.

The set of coefficients c_T, c_H, and c_{mt} in the body frame or c_y, c_x and c_{mt} in the wind frame defines the aerodynamic efficiency of the lifting rotor and are called its aerodynamic characteristics.

The aerodynamic coefficients in the two coordinate systems are connected with one another by the relations (see Figure 26.9)

$$c_T = c_y \cos\alpha + c_x \sin\alpha;$$
$$c_H = c_x \cos\alpha - c_y \sin\alpha.$$

In calculations of helicopter flight characteristics, we frequently use dimensionless coefficients, obtained by dividing the above coefficients by the solidity σ

$$t = \frac{c_T}{\sigma} = \frac{T}{\frac{1}{2}\rho\sigma\pi R^2(\omega R)^2};$$

$$h = \frac{c_H}{\sigma} = \frac{H}{\frac{1}{2}\rho\sigma\pi R^2(\omega R)^2};$$

$$t_y = \frac{c_y}{\sigma} = \frac{Y}{\frac{1}{2}\rho\sigma\pi R^2(\omega R)^2};$$

$$t_x = \frac{c_x}{\sigma} = \frac{X}{\frac{1}{2}\rho\sigma\pi R^2(\omega R)^2};$$

$$m_x = \frac{c_{mx}}{\sigma} = \frac{M_x}{\frac{1}{2}\rho\sigma\pi R^3(\omega R)^2}.$$

The solidity σ is the ratio of the total area of the blade projections on the plane of rotation to the area of the circle described by the blade tips.

REVIEW QUESTIONS

1. Explain the purpose of the three-hinge helicopter main rotor blade mounting.

2. What helicopter operating conditions are accounted for by the rotor operating regime characteristic μ?

3. What helicopter rotor similarity criteria are used in modeling?

PROBLEMS

1. Find the boundary shape and location of the zone of reversed flow over helicopter blades.

Solution. At the boundary of the reversed flow zone the magnitude of the velocity component U_t, defined by (26.1), equals zero. Then

$$\omega r + V_\infty \cos\alpha \sin\phi = 0. \tag{a}$$

Converting to Cartesian coordinates (see Figure 26.7), we obtain

$$r = \sqrt{x^2+y^2}, \quad \sin\phi = \frac{y}{\sqrt{x^2+y^2}}.$$

After substitution into (a) and algebraic transformations, we have

$$x^2 + \left(y + \frac{V_\infty \cos\alpha}{2\omega}\right)^2 = \left(\frac{V_\infty \cos\alpha}{2\omega}\right)^2. \tag{b}$$

Equation (b) describes the boundary of the reversed flow zone, which is a circle with diameter $\frac{V\cos\alpha}{\omega}$ and center at the point with the coordinates $\left(0;\ -\frac{V\cos\alpha}{2\omega}\right)$.

2. Find the angle of attack of a helicopter main rotor if the advance ratio $\lambda = 0.5$ and rotor operating regime characteristic $\mu = 0.2$ are known.

Answer:

$$\alpha = \operatorname{arctg}\frac{\lambda}{\pi\mu} \approx 0{,}92 \text{ rad}.$$

REFERENCES

1. Абрамович Г. Н., Прикладная газовая динамика, ГИТТЛ, 1956.
2. Александров В. Л., Воздушные винты, Оборонгиз, 1951.
3. Аржаников Н. С., Мальцев В. Н., Аэродинамика, Оборонгиз, 1956.
4. Аржаников Н. С., Садекова Г. С., Аэродинамика больших скоростей, изд-во «Высшая школа», 1965.
5. Байдаков В. Б., Иванов-Эмин Л. Н., Аэромеханика летательных аппаратов, изд-во «Машиностроение», 1965.
6. Бай Ши-и, Введение в теорию течения сжимаемой жидкости, ИЛ, 1962.
7. Безбородов Г. Ф., Логинов Е. Ф. и др., Гражданская авиация СССР 1917—1967, «Транспорт», 1967.
8. Биркгоф Г., Гидродинамика, ИЛ, 1963.
9. Вулис Л. А., Термодинамика газовых потоков, Энергоиздат, 1950.
10. Гаухман Р. Н., Касторский В. Е., Логачев Ю. Т., Аэродинамика, ч. I, РИИГА, 1965.
11. Гессоу А. и Мейерс Г., Аэродинамика вертолета, Оборонгиз, 1954.
12. Голубев В. В., Лекции по теории крыла, ГИТТЛ, 1949.
13. Горлин С. М., Слезингер И. И., Аэродинамические измерения, изд-во «Наука», 1964.
14. Гофман М. Л., Основы аэродинамики скоростного самолета, Редиздат Аэрофлота, 1958.
15. Гошек И., Аэродинамика больших скоростей, ИЛ, 1954.
16. Гудерлей К. Г., Теория околозвуковых течений, ИЛ, 1960.
17. Дородницын А. А., Пограничный слой в сжимаемом газе, Прикладная математика и механика, т. VI, вып. 6, 1942.
18. Жуковский Н. Е., Избранные сочинения т. 1, 2, ГИТТЛ, 1948.
19. Загордан А. М., Элементарная теория вертолета, Воениздат, 1960.
20. Закс. Н. А., Основы экспериментальной аэродинамики, Оборонгиз, 1953.
21. Зауер Р., Течение сжимаемой жидкости, ИЛ, 1954.
22. Изаксон А. М., Советское вертолетостроение, изд-во «Машиностроение», 1964.
23. Калихман Л. Е., Турбулентный пограничный слой на криволинейной поверхности, обтекаемой газом, Оборонгиз, 1956.
24. Карафоли Е., Аэродинамика крыла самолета, изд-во АН СССР, 1956.
25. Кочин Н. Е., Кибель И. А., Розе Н. В., Теоретическая гидромеханика, ч. I, II, Гостехиздат, 1948, 1949.
26. Краснов Н. Ф., Аэродинамика тел вращения, изд-во «Машиностроение», 1964.

27. Курант Р., Фридрихс К., Сверхзвуковое течение и ударные волны, ИЛ, 1950.
28. Ламб Г., Гидродинамика, ГИТТЛ, 1947.
29. Ландау Л. Д., Лифшиц Е. Л., Механика сплошных сред, ГИТТЛ, 1954.
30. Лебедев А. А., Стражева И. В., Сахаров Г. И., Аэромеханика самолета, Оборонгиз, 1955.
31. Лебедев А. А., Чернобровкин Л. С., Динамика полета, Оборонгиз, 1962.
32. Левинсон Я. И., Аэродинамика больших скоростей, Оборонгиз, 1950.
33. Лин Дзя-цзяо, Турбулентные течения и теплопередача, ИЛ, 1963.
34. Липман Г. В. и Пакет А. Е., Введение в аэродинамику сжимаемой жидкости, ИЛ., 1949.
35. Липман Г. В., РошкоА., Элементы газовой динамики, ИЛ, 1950.
36. Лойцянский Л. Г., Ламинарный пограничный слой, ГИФМЛ, 1962.
37. Лойцянский Л. Г., Механика жидкости и газа, ГИТТЛ, 1957.
38. Мартынов А. К., Экспериментальная аэродинамика, Оборонгиз, 1958.
39. Мельников А. П., Аэродинамика больших скоростей, Воениздат, 1961.
40. Мизес А., Теория полета, ИЛ, 1949.
41. Милн-Томсон Л. М., Теоретическая гидромеханика, изд-во «Мир», 1964.
42. Миль М. Л. и др. Вертолеты, расчет и проектирование, ч. I, «Машиностроение», 1966.
43. Мхитарян А. М., Аэромеханика и динамика полета летательных аппаратов, ч. I. II, КИИГА, Киев, 1965, 1969.
44. Остославский И. В., Аэродинамика самолета, Оборонгиз, 1957.
45. Остославский И. В., Стражева И. В., Динамика полета. Траектории летательных аппаратов, Оборонгиз, 1963.
46. Остославский И. В., Титов В. М., Аэродинамический расчет самолета, Оборонгиз, 1947.
47. Патрашев А. Н., Гидромеханика, Военмориздат, 1953.
48. Пейн П. Р., Динамика и аэродинамика вертолета, Оборонгиз, 1963.
49. Повх И. Л., Техническая гидромеханика, изд-во «Машиностроение», 1964.
50. Прандтль Л., Гидроаэромеханика, ИЛ, 1949.
51. Прицкер Д. М., Турьян В. А., Аэромеханика, Оборонгиз, 1960.
52. Путята В. И., Сидляр М. М., Гидромеханика, Киевский Госуниверситет, Киев, 1963.
53. Пэнкхерст Р., Холдер Д., Техника эксперимента в аэродинамических трубах, ИЛ, 1955.
54. Седов Л. И., Методы подобия и размерности в механике, изд-во «Наука», 1965.
55. Седов Л. И., Плоские задачи гидродинамики и аэродинамики, ГИТТЛ, 1950.
56. Фабрикант Н. Я., Аэродинамика, изд-во «Наука», 1964.
57. Ферри А., Аэродинамика сверхзвуковых течений, ГИТТЛ, 1952.
58. Франкль Ф. И., Карпович Е. А., Газодинамика тонких тел, Гостехиздат, 1948.
59. Хилтон У. Ф., Аэродинамика больших скоростей, ИЛ, 1955.
60. Хоуарт Л. и др., Современное состояние аэродинамики больших скоростей, ИЛ, 1955.
61. Христианович С. А., О сверхзвуковых течениях газа. Труды ЦАГИ, вып. 543, 1941.

62. Христианович С. А. и др., Прикладная газовая динамика, ГИТТЛ, 1948.
63. Чаплыгин С. А., Избранные работы по теории крыла, ГИТТЛ, 1949.
64. Черный Г. Г., Течения газа с большой сверхзвуковой скоростью, ГИФМ, 1959.
65. Чертов А. Г., Международная система единиц измерения, Росвузиздат, 1963.
66. Шлихтинг Г., Теория пограничного слоя, ИЛ, 1956.
67. Эммонс, Основы газовой динамики, ИЛ, 1963.
68. Юрьев Б. Н., Воздушные винты, Госмашлитиздат, 1933.
69. Юрьев Б. Н., Аэродинамический расчет вертолетов, Оборонгиз, 1956.
70. Юрьев Б. Н., Экспериментальная аэродинамика, Оборонгиз, 1936 (ч. I), 1938 (ч. II).
71. Яцунович М. С., Практическая аэродинамика соосного вертолета, Оборонгиз, 1963.

SYMBOL LIST

Russian	Typed	Meaning
ЛАМ	lam	laminar
ТУР	turb	turbulent
ТР	fr	friction
КР	cr	critical
В	u	upper
Н	l	lower
П	f	forward
З	a	aft
КР	st	stall
Д	p	pressure
МеСТ	loc	local
СР	av	average
ГОЛ	head	head
ХВ	tail	tail
ПРОФИЛЯ	profile	profile
КОНТУРа	contour	contour
НС	incom	incompressible
СЖ	com	compressible
Т	t	turbulent
В	w	wave
КОНЦ	t	tip
К	r	root
ИСТ	true	true
Л	lt	left
П	rt	right
Ц	r	root (centerplane)
КР	w	wing
СеЧ	sec	section
НВ	opt	optimal
СК	yaw	yawed
ПР	str	straight

Russian	Typed	Meaning
СТР	sw	swept
ТРЯСКИ	buffet	buffet
Щ	f	flap
З	f	flap
ПРОФ	profile	prof
ИЗ.КР	is.w	isolated wing
НОС	nose	nose
ЦИЛ	cyl	cylindrical
МИД	mid	midsection
КОРМ	aft	aft
ДОН	base	base
Т	b	body
ОВ	ov	oval
ВХ	in	inlet
СМ	wet	wetted
Ф	f	fuselage
Э	e	effective
Р	c	control surface
ОП	t	tail
Э	a	aileron
Ш	h	hinge
Р.В	el	elevator
СаМ	air	airplane
ИНТ	int	interference
К	wi	wing
Г.О	ht	horizontal tail
ИЗ	is	isolated
В.О	vt	vertical tail
Г.Д	nac	engine nacelle
ЭФ	eff	effective
К	c	cone
КОН	c	cone
П	in	inflow

Russian	Typed	Meaning
С	s	second
ОС	ax	axial
ОКР	cir	circumferential
К	t	turning
В	p	prop
ДэйСМВ	real	real
К	sh	shrouded
ОбД	slip	slipstream
НеОбД	out	outside
ПОЛН	res	resultant
Цб	cent	centrifugal
ВЗМ	fl	flapping
Л	b	blade